



IntechOpen

Quantum Dots

Theory and Applications

Edited by Vasilios N. Stavrou



QUANTUM DOTS - THEORY AND APPLICATIONS

Edited by **Vasilios N. Stavrou**

Quantum Dots - Theory and Applications

<http://dx.doi.org/10.5772/59735>

Edited by Vasilios N. Stavrou

Contributors

Sergey Ivanovich Pokutnyi, Tetyana Torchynska, Safwan S.A, Witold Jacak, Gordey Lesovik, Valerii Vinokur, Ivan Sadovskyy, Akos Nemcsics

© The Editor(s) and the Author(s) 2015

The moral rights of the and the author(s) have been asserted.

All rights to the book as a whole are reserved by INTECH. The book as a whole (compilation) cannot be reproduced, distributed or used for commercial or non-commercial purposes without INTECH's written permission.

Enquiries concerning the use of the book should be directed to INTECH rights and permissions department (permissions@intechopen.com).

Violations are liable to prosecution under the governing Copyright Law.



Individual chapters of this publication are distributed under the terms of the Creative Commons Attribution 3.0 Unported License which permits commercial use, distribution and reproduction of the individual chapters, provided the original author(s) and source publication are appropriately acknowledged. If so indicated, certain images may not be included under the Creative Commons license. In such cases users will need to obtain permission from the license holder to reproduce the material. More details and guidelines concerning content reuse and adaptation can be found at <http://www.intechopen.com/copyright-policy.html>.

Notice

Statements and opinions expressed in the chapters are these of the individual contributors and not necessarily those of the editors or publisher. No responsibility is accepted for the accuracy of information contained in the published chapters. The publisher assumes no responsibility for any damage or injury to persons or property arising out of the use of any materials, instructions, methods or ideas contained in the book.

First published in Croatia, 2015 by INTECH d.o.o.

eBook (PDF) Published by IN TECH d.o.o.

Place and year of publication of eBook (PDF): Rijeka, 2019.

IntechOpen is the global imprint of IN TECH d.o.o.

Printed in Croatia

Legal deposit, Croatia: National and University Library in Zagreb

Additional hard and PDF copies can be obtained from orders@intechopen.com

Quantum Dots - Theory and Applications

Edited by Vasilios N. Stavrou

p. cm.

ISBN 978-953-51-2155-8

eBook (PDF) ISBN 978-953-51-5766-3

We are IntechOpen, the world's leading publisher of Open Access books Built by scientists, for scientists

3,800+

Open access books available

116,000+

International authors and editors

120M+

Downloads

151

Countries delivered to

Our authors are among the
Top 1%

most cited scientists

12.2%

Contributors from top 500 universities



WEB OF SCIENCE™

Selection of our books indexed in the Book Citation Index
in Web of Science™ Core Collection (BKCI)

Interested in publishing with us?
Contact book.department@intechopen.com

Numbers displayed above are based on latest data collected.
For more information visit www.intechopen.com



Meet the editor

Dr. Vasilios N. Stavrou is currently an Adjunct Member at the Hellenic Naval Academy, Pireus, Greece. He received his MSc and PhD in Theoretical Solid State Physics from the University of Essex in England, in 1995 and 1999 respectively. As a postdoctoral researcher, he worked at the following institutes: Deutsche Forschungsanstalt fuer Luft und Raumfahrt e.V (German Aerospace Research Center) in Germany; State University of New York (SUNY) at Buffalo, USA; and University of Iowa, USA. His research interests are related to quantum computing, spintronics, decoherence in quantum dots, diluted magnetic semiconductors, and phonon models in low dimensional structures among others. The results of his work have been published in reputable journals and were also presented at a number of International Conferences.

Contents

Preface XI

Section 1 Theory 1

Chapter 1 **Theory of Excitons and Excitonic Quasimolecules Formed from Spatially Separated Electrons and Holes in Quasi-Zero-Dimensional Nanostructures 3**

Sergey I. Pokutnyi and Włodzimierz Salejda

Chapter 2 **Excitons and Trions in Semiconductor Quantum Dots 27**

S. A. Safwan and N. El-Meshed

Chapter 3 **On the 'Three-Orders Time-Limit' for Phase Decoherence in Quantum Dots 47**

Witold Aleksander Jacak

Chapter 4 **Charge States in Andreev Quantum Dots 85**

Ivan A. Sadovskyy, Gordey B. Lesovik and Valerii M. Vinokur

Section 2 Applications 117

Chapter 5 **Quantum Dots Prepared by Droplet Epitaxial Method 119**

Ákos Nemcsics

Chapter 6 **Physical Reasons of Emission Varying in CdSe/ZnS and CdSeTe/ZnS Quantum Dots at Bioconjugation to Antibodies 151**

Tetyana V. Torchynska

Preface

Semiconductor quantum dots are small devices in which carriers exhibit strong three dimensional confinement and show discrete energy spectrum. Their tunable optical and electronic properties enable them to be used in several optoelectronic / electronic devices such as quantum bits, sensors, and lasers among others. In this book, a few theoretical aspects and applications are included.

The current book is divided in two sections. In the first section, fundamental theories on excitons, trions, phase decoherence, and charge states are presented. Several applications of quantum dots are included in the second section.

As the editor of this book project, I would like to thank all the authors for their contributions and efforts to bring the up-to-date research of their high quality work.

Lastly, I gratefully acknowledge the InTech team for their support during the preparation of the book.

Dr. Vasilios N. Stavrou
Hellenic Naval Academy
Pireaus, Greece

Theory

Theory of Excitons and Excitonic Quasimolecules Formed from Spatially Separated Electrons and Holes in Quasi-Zero-Dimensional Nanostructures

Sergey I. Pokutnyi and Włodzimierz Salejda

Additional information is available at the end of the chapter

<http://dx.doi.org/10.5772/60591>

Abstract

The theory of an exciton formed from a spatially separated electron and a hole is developed within the framework of the modified effective mass method. The effect of significantly increasing the exciton binding energy in quantum dots of zinc selenide, synthesized in a borosilicate glass matrix and relative to that in a zinc selenide single crystal is revealed. It is shown that the short-wavelength shift of the peak of the low-temperature luminescence spectrum of samples containing zinc selenide quantum dots, observed under experimental conditions, is caused by quantum confinement of the ground-state energy of the exciton with a spatially separated electron and hole.

A review devoted to the theory of excitonic quasimolecules (biexcitons) (made up of spatially separated electrons and holes) in a nanosystem that consists of ZnSe quantum dots synthesized in a borosilicate glass matrix is developed within the context of the modified effective mass approximation. It is shown that biexciton (exciton quasimolecule) formation has a threshold character and is possible in a nanosystem, where the spacing between quantum dots' surfaces is larger than a certain critical arrangement. An analogy of the spectroscopy of the electronic states of superatoms (or artificial atoms) and individual alkali metal atoms theoretically predicted a new artificial atom that was similar to the new alkali metal atom.

Keywords: Excitons, exciton binding energy, quantum dots, excitonic quasimolecules, spatially separated electrons and holes, superatoms

1. Introduction

Quasi-zero-dimensional semiconductor nanosystems consisting of spherical semiconductor nanocrystals, i.e., quantum dots with radii of $a = 1-10$ nm and containing cadmium sulphide and selenide, gallium arsenide, germanium, silicon, and zinc selenide in their volume, and synthesized in a borosilicate glass matrix currently attract particular research attention due to their unique photoluminescent properties, i.e., the ability to efficiently emit light in the visible or near infrared ranges at room temperature [1-10]. The optical and electro-optical properties of such quasi-zero dimensional nanosystems are to a large extent controlled by the energy spectrum of the spatially confined electron-hole pair (exciton) [4-16].

In most theoretical models for calculating the energy spectra of quasiparticles in quantum dots (QDs), the effective mass approximation is used, which was considered applicable for QDs by analogy with bulk single crystals [11-13]. However, the problem concerning the applicability of the effective mass approximation to the description of semiconductor QDs remains unsolved [4-18].

In [14], a new modified effective mass method is proposed to describe the exciton energy spectrum in semiconductor QDs with radii of $a \approx a_{ex}$ (a_{ex} is the exciton Bohr radius in the semiconductor material contained in the QD volume). It was shown that, within a model in which the QD is represented as an infinitely deep potential well, the effective mass approximation can be applied to the description of an exciton in QDs with radii a comparable to the exciton Bohr radius a_{ex} , assuming that the reduced effective exciton mass is a function of the radius a , $\mu = \mu(a)$.

In the adiabatic approximation and within the modified effective mass method [14], an expression for the binding energy of an exciton, whose electron and hole move within the semiconductor QD volume, was derived in [15]. In [15], the effect of significantly increasing the exciton binding energy in cadmium selenide and sulphide QDs with radii a , comparable to the exciton Bohr radii a_{ex} and relative to the exciton-binding energy in cadmium selenide and sulphide single crystals (by factors of 7.4 and 4.5, respectively) was also detected.

In the experimental study [7], it was found that excess electrons produced during interband excitation of the cadmium sulphide QD had a finite probability of overcoming the potential barrier and penetrating into the borosilicate glass matrix, into which the QD is immersed. In experimental studies [10, 19] (as well as in [7]) using glass samples with cadmium-sulphide and zinc selenide QDs, it was found that the electron can be localized in the polarization well near the outer QD surface, while the hole moves within the QD volume.

In [10, 19], the optical properties of borosilicate glass samples containing QD zinc selenide were experimentally studied. The average radii of such QDs were in the range $a \approx 2.0-4.8$ nm. In this case, the values of a are comparable to the exciton Bohr radius $a_{ex} \approx 3.7$ nm in a ZnSe single crystal. At low QD concentrations, when the optical properties of the samples are mainly controlled by those of individual QDs in the borosilicate glass matrix, a shift of the peak of the

low temperature luminescence spectrum to the short wavelength region (with respect to the band gap E_g of the zinc selenide-single crystal) was observed. The authors of [10] assumed that this shift was caused by quantum confinement of the energy spectra of the electron and the hole localized near the spherical surface of the QD. In this case, the following problem remained open: the quantum confinement of the state of which electron and hole (the hole moving in the QD volume and the electron localized at the outer spherical QD-dielectric matrix interface or the electron and hole localized in the QD volume) caused such a shift in the luminescence spectrum peak?

The use of semiconductor nanosystems as the active region of nanolasers is prevented by the low binding energy of the QD exciton [8, 9, 13]. Therefore, studies directed at the search for nanostructures in which a significant increase in the binding energy of QD excitons can be observed are of importance.

Currently, the theory of exciton states in quasi- zero- dimensional semiconductor nanosystems has not been adequately studied. In particular, no theory exists for an exciton with a spatially separated electron and hole in quasi- zero- dimensional nanosystems. Therefore, in this study, we developed the theory of an exciton formed from a spatially separated electron and hole (the hole is in the semiconductor QD volume and the electron is localized at the outer spherical surface of the QD-dielectric matrix interface) [20-22]. It was shown that the short wavelength shift of the peak of the low temperature luminescence spectrum of samples containing zinc selenide QDs, observed under the experimental conditions of [10], was caused by quantum confinement of the ground state energy of the exciton with a spatially separated electron and hole. The effect of significantly increasing the binding energy of an exciton (with a spatially separated electron and hole) in a nanosystem containing zinc selenide QDs, compared with the binding energy of an exciton in a zinc selenide single crystal (by a factor of 4.1-72.6), was detected [20-22].

In [10, 19], a shift of the spectral peak of the low temperature luminescence was also observed for samples with a QD concentrations from $x = 0.003$ -1%. It was noted [10, 19] that at such a QD content in the samples, the interaction between charge carriers localized above the QD surfaces must be taken into account. Therefore, in [23, 24], we develop the theory of excitonic quasimolecules (biexcitons) (formed from spatially separated electrons and holes) in a nanosystem, which consists of ZnSe QDs synthesized in a borosilicate glass matrix.

2. Spectroscopy of excitons in Quasi - Zero - Dimensional nanosystems

Let us consider the simple model of a quasi-zero-dimensional system, i.e., a neutral spherical semiconductor QD of the radius a , which contains semiconductor material with the permittivity ϵ_2 in its volume, surrounded by a dielectric matrix with permittivity ϵ_1 . A hole h with the effective mass m_h moves in the QD volume, while an electron e with the effective mass $m_e^{(1)}$ lies in the matrix (r_e and r_h are the distances from the QD centre to the electron and hole). Let

we assume that the QD valence band is parabolic. Let us also assume that there is an infinitely high potential barrier at the spherical QD-dielectric matrix interface; therefore, the hole h cannot leave the QD volume and the electron e cannot penetrate into the QD volume in the model under study [20-22].

The characteristic dimensions of the problem are the quantities:

$$a_h = \varepsilon_2 \hbar^2 / m_h e^2, \quad a_{ex} = \varepsilon_2 \hbar^2 / \mu e^2, \quad a_e = \varepsilon_1 \hbar^2 / m_e^{(1)} e^2, \quad (1)$$

where a_h and a_{ex} are the hole and exciton Bohr radii in the semiconductor with the permittivity ε_2 , e is the elementary charge, $\mu = m_e^{(2)} m_h / (m_e^{(2)} + m_h)$ is the reduced effective mass of the exciton, $m_e^{(2)}$ is the effective mass of an electron in the semiconductor with permittivity ε_2 and a_e is the electron Bohr radius in the dielectric matrix with the permittivity ε_1 . The fact that all characteristic dimensions of the problem are significantly larger than the interatomic distances a_0 ,

$$a, a_e, a_h, a_{ex} \gg a_0$$

allows us to consider the electron and hole motion in the quasi-zero-dimensional nanosystem in the effective mass approximation [11-13].

We analysed the conditions of carrier localization in the vicinity of a spherical dielectric particle of the radius a with the permittivity ε_2 in [25-27]. In this instance, the problem of the field induced by the carrier near a dielectric particle immersed in a dielectric medium with the permittivity ε_1 was solved in a final analytical form and analytical expressions for the potential energy of the interaction of the carrier with the spherical interface of two media are presented.

Solving the Poisson equation with usual electrostatic boundary conditions

$$\begin{aligned} \phi(r', j | \mathbf{r}, i) \Big|_{r'=a} &= \phi(r', j) \Big|_{r'=a'} \\ \varepsilon_1 \frac{\partial \phi(r', j | \mathbf{r}, i)}{\partial r'} \Big|_{r'=a} &= \varepsilon_2 \frac{\partial \phi(r', j)}{\partial r'} \Big|_{r'=a'} \end{aligned} \quad (2)$$

the potential $\phi(r', j | \mathbf{r}, i)$ at the observation point \mathbf{r}' in a medium with the permittivity ε_j , induced by the charge e at the point \mathbf{r} in a medium with the permittivity ε_i , can be presented as a sum of the potentials induced by the image point charge $e'(\mathbf{r}_{ij} | \mathbf{r})$ at the point $\mathbf{r}_{ij} = (a/r)^2 \mathbf{r} \delta_{ij} + \mathbf{r}(1 - \delta_{ij})$ and the linear distribution with the density $\rho_{ij}(y, r)$ of the image charge along a straight line passing through the centre of the dielectric particle with the radius a and the charge at the point r [25-27]:

$$\phi(\mathbf{r}', j | \mathbf{r}, i) = \frac{e}{\varepsilon_j |\mathbf{r}' - \mathbf{r}|} + \frac{e'(\mathbf{r}_{ij} | \mathbf{r})}{\varepsilon_j |\mathbf{r}' - \mathbf{r}_{ij}|} + \frac{1}{\varepsilon_j} \int_0^\infty \frac{dy \rho_{ij}(y, \mathbf{r})}{|\mathbf{r}' - y(\mathbf{r} / r)|}$$

where

$$\begin{aligned} \mathbf{r}_{11} &= (a^2/r^2)\mathbf{r}, e'(\mathbf{r}_{11} | \mathbf{r}) = -\beta(a/r)e & \text{a} \\ \rho_{11}(y, r) &= \beta\alpha(a^2/ry)^{(1-\alpha)}(e/a)\theta((a^2/r) - y); \\ \mathbf{r}_{22} &= (a^2/r^2)\mathbf{r}, e'(\mathbf{r}_{22} | \mathbf{r}) = \beta(a/r)e & \text{b} \\ \rho_{22}(y, r) &= \beta(1-\alpha)(a^2/ry)^\alpha(e/a)\theta(y - (a^2/r)); \\ \mathbf{r}_{12} &= r, e'(\mathbf{r}_{12} | \mathbf{r}) = \beta e & \text{c} \\ \rho_{12}(y, r) &= \beta(1-\alpha)(r/y)^\alpha(e/r)\theta(y - r); \\ \mathbf{r}_{21} &= r, e'(\mathbf{r}_{21} | \mathbf{r}) = -\beta e & \text{d} \\ \rho_{21}(y, r) &= \beta\alpha(r/y)^{(1-\alpha)}(e/r)\theta(r - y) \end{aligned} \quad (3)$$

where $\theta(x)$ is the Heaviside unit-step function,

$$\beta = \frac{(\varepsilon_2 - \varepsilon_1)}{(\varepsilon_2 + \varepsilon_1)}, \alpha = \frac{\varepsilon_1}{(\varepsilon_2 + \varepsilon_1)} \quad (4)$$

Using expressions (3)-(3d), the energy $U(\mathbf{r}_e, \mathbf{r}_h, a)$ of the polarization interaction of the electron and hole with the spherical QD-matrix interface at the relative permittivity $\varepsilon = (\varepsilon_2/\varepsilon_1) \gg 1$ can be presented as an algebraic sum of the energies of the interaction of the hole and electron with self- $V_{hh}(\mathbf{r}_h, a)$, $V_{ee}(\mathbf{r}_e, a)$ and "foreign" $V_{eh}(\mathbf{r}_e, \mathbf{r}_h, a)$, $V_{he}(\mathbf{r}_e, \mathbf{r}_h, a)$ images, respectively [15, 16, 26-28]:

$$U(\mathbf{r}_e, \mathbf{r}_h, a, \varepsilon) = V_{hh'}(\mathbf{r}_h, a, \varepsilon) + V_{ee'}(\mathbf{r}_e, a, \varepsilon) + V_{eh'}(\mathbf{r}_e, \mathbf{r}_h, a, \varepsilon) + V_{he'}(\mathbf{r}_e, \mathbf{r}_h, a, \varepsilon), \quad (5)$$

where

$$V_{hh'}(\mathbf{r}_h, a, \varepsilon) = \frac{e^2\beta}{2\varepsilon_2 a} \left(\frac{a^2}{a^2 - r_h^2} + \varepsilon \right), \quad (6)$$

$$V_{ee'}(\mathbf{r}_e, a, \varepsilon) = -\frac{e^2\beta}{2\varepsilon_1 a} \cdot \frac{a^4}{r_e^2(r_e^2 - a^2)}, \quad (7)$$

$$V_{he'}(\mathbf{r}_e, \mathbf{r}_h, a, \varepsilon) = \frac{e^2\beta}{2\varepsilon_2 a} \cdot \frac{a^2}{r_e \left| r_h - (a/r_e)^2 r_e \right|}, \quad (8)$$

$$V_{eh}(\mathbf{r}_e, \mathbf{r}_h, a, \varepsilon) = -\frac{e^2 \beta}{2\varepsilon_1 a} \cdot \frac{a^2}{r_h \left| \mathbf{r}_e - (a/r_h)^2 \mathbf{r}_h \right|}. \quad (9)$$

In the studied simple model of a quasi-zero-dimensional nanostructure within the above approximations and in the effective mass approximation using the triangular coordinate system [14-16], $r_e = |\mathbf{r}_e|$, $r_h = |\mathbf{r}_h|$, $r = |\mathbf{r}_e - \mathbf{r}_h|$, with the origin at the centre of the QD, the exciton Hamiltonian (with a spatially separated hole moving within the QD volume and an electron in the dielectric matrix) takes the following form [20-22, 29-32]:

$$\begin{aligned} H(\mathbf{r}_e, \mathbf{r}_h, \mathbf{r}, a) = & -\frac{\hbar^2}{2m_e^{(1)}} \left(\frac{\partial^2}{\partial r_e^2} + \frac{2}{r_e} \cdot \frac{\partial}{\partial r_e} + \frac{r_e^2 - r_h^2 + r^2}{r_e r} \cdot \frac{\partial^2}{\partial r_e \partial r} \right) - \\ & -\frac{\hbar^2}{2m_h^{(1)}} \left(\frac{\partial^2}{\partial r_h^2} + \frac{2}{r_h} \cdot \frac{\partial}{\partial r_h} + \frac{r_h^2 - r_e^2 + r^2}{r_h r} \cdot \frac{\partial^2}{\partial r_h \partial r} \right) - \frac{\hbar^2}{2\mu_0} \left(\frac{\partial^2}{\partial r^2} + \frac{2}{r} \cdot \frac{\partial}{\partial r} \right) + \\ & + V_{eh}(\mathbf{r}) + U(\mathbf{r}_e, \mathbf{r}_h, a, \varepsilon) + V_e(r_e) + V_h(r_h) + E_g, \end{aligned} \quad (10)$$

where the first three terms are the operators of the electron, hole and exciton kinetic energy, E_g is the band gap in the semiconductor with the permittivity ε_2 and $\mu_0 = m_e^{(1)} m_h^{(1)} / (m_e^{(1)} + m_h^{(1)})$ is the reduced effective mass of the exciton (with a spatially separated hole and electron). In the exciton Hamiltonian (10), the polarization interaction energy $U(\mathbf{r}_e, \mathbf{r}_h, a, \varepsilon)$ (5) is defined by formulas (6)-(9) and the electron-hole Coulomb interaction energy $V_{eh}(r)$ is described by the following formula:

$$V_{eh}(r) = -\frac{1}{2} \left(\frac{1}{\varepsilon_1} + \frac{1}{\varepsilon_2} \right) \frac{e^2}{r} \quad (11)$$

In the exciton Hamiltonian (10), the potentials

$$\begin{aligned} V_h(r_h) &= \begin{cases} 0, & r_h \leq a \\ \infty, & r_h > a' \end{cases} \\ V_e(r_e) &= \infty, \quad r_e \leq a \end{aligned} \quad (12)$$

describe the quasiparticle motion using the models of an infinitely deep potential well.

As the QD radius a increases (so that $a \gg a_{ex}^0$), the spherical interface of the two media (QD-matrix) passes to the plane <semiconductor material with the permittivity>-matrix interface. In this case, the exciton with the spatially separated electron and hole (the hole moves within the semiconductor material and the electron lies in the borosilicate glass matrix) becomes two-dimensional [20-22].

The primary contribution to the potential energy of the Hamiltonian (10) describing exciton motion in a nanosystem containing a large-radius QD, $a \gg a_{ex}^0$ is made by the electron-hole Coulomb interaction energy $V_{eh}(r)$ (11). The energy of the hole and electron interaction with self- $V_{hh}(r_h, a, \epsilon)$ (6), $V_{ee}(r_e, a)$ (7) and “foreign” $V_{eh}'(r_e, r_h, a)$ (9), $V_{he}(r_e, r_h, a)$ (8) images make a significantly smaller contribution to the potential energy of the Hamiltonian (10). In the first approximation, this contribution can be disregarded. In this case, only the electron-hole Coulomb interaction energy (11) remains in the potential energy of the Hamiltonian (10) [20-22]. The Schrodinger equation with such a Hamiltonian describes a two-dimensional exciton with a spatially separated electron and hole (the electron moves within the matrix, and the hole lies in the semiconductor material with the permittivity ϵ_2), the energy spectrum of which takes the following form [33, 34]:

$$E_n = -\frac{Ry_{ex}^0}{(n + 1/2)^2}, \tag{13}$$

$$Ry_{ex}^0 = \frac{(\epsilon_1 + \epsilon_2)^2}{4\epsilon_1^2\epsilon_2^2} \left(\frac{\mu_0}{m_0} \right) Ry_0$$

where $n = 0, 1, 2, \dots$ is the principal quantum number of the exciton and $Ry_0 = 13.606$ eV is the Rydberg constant. The Bohr radius of such a two-dimensional exciton is described by the following formula:

$$a_{ex}^0 = \frac{2\epsilon_1\epsilon_2\hbar^2}{\epsilon_1 + \epsilon_2\mu_0e^2}, \tag{14}$$

and the binding energy of the ground state of such a two-dimensional exciton, according to (13), is written as:

$$E_{ex}^0 = -4Ry_{ex}^0 \tag{15}$$

The binding energy (15) of the exciton ground state is understood as the energy required for bound electron and hole state decay (in a state where $n = 0$).

To determine the ground-state energy of an exciton (with a spatially separated electron and hole) in a nanosystem containing QDs of the radius a , we applied the variational method. When choosing the variational exciton wave function, we used an approach similar to that developed in [14]. Let us write the variational radial wave function of the exciton ground-state (1s electron state and 1s hole state) in the nanosystem under study in the following form [20-22]:

$$\begin{aligned} \psi_0(\mathbf{r}_e, \mathbf{r}_h, r, a) = & A \exp\left(-\frac{\mu(a)}{\mu_0} \frac{r}{a_{ex}^0}\right) \frac{(a^2 - r_h^2)}{a^2} \\ & \times \frac{(r_e^2 - a^2)}{a^2} \frac{r}{a} \left| \mathbf{r}_e - \left(\frac{a}{r_h}\right)^2 \mathbf{r}_h \right| \frac{r_h}{a^2} \left| \mathbf{r}_h - \left(\frac{a}{r_e}\right)^2 \mathbf{r}_e \right| \frac{r_e}{a^2} \end{aligned} \quad (16)$$

Here, the coefficient A is determined from the condition of normalization of the exciton wave function (16):

$$\int_a^\infty r_e dr_e \int_0^a r_h dr_h \int_r^{r_e+r_h} \psi_0^2(\mathbf{r}_e, \mathbf{r}_h, r, a) r dr = 1$$

and the effectively reduced exciton mass $\mu(a)$ is the variational parameter.

As the QD radius a increases (so that $a \gg a_{ex}^0$), a two-dimensional exciton is formed in the nanosystem. This leads to the variational exciton wave function (16) containing the Wannier-Mott two-dimensional exciton wave eigenfunction [33, 34]. Furthermore, the polynomials from r_e and r_h enter the exciton variational function (16), which make it possible to eliminate singularities in the functional $E_0(a, \mu(a))$ in the final analytical form.

To determine the exciton ground-state energy $E_0(a, \varepsilon)$ in the nanosystem under study using the variational method, we wrote the average value of the exciton Hamiltonian (10) in wave functions (16) as follows:

$$\begin{aligned} E_0(a, \mu(a)) = & \psi_0(\mathbf{r}_e, \mathbf{r}_h, r, a) | H(\mathbf{r}_e, \mathbf{r}_h, r, a) | \psi_0(\mathbf{r}_e, \mathbf{r}_h, r, a) = \\ & \int_a^\infty dr_e \int_0^a dr_h \int_r^{r_e+r_h} dr r r_e r_h \psi_0(\mathbf{r}_e, \mathbf{r}_h, r, a) H(\mathbf{r}_e, \mathbf{r}_h, r, a) \psi_0(\mathbf{r}_e, \mathbf{r}_h, r, a) \end{aligned} \quad (17)$$

The dependence of the energy $E_0(a)$ of the exciton ground state ($n_e = 1, l_e = m_e = 0; n_h = 1, l_h = m_h = 0$) (n_e, l_e, m_e and n_h, l_h, m_h are the principal, orbital and magnetic quantum numbers of the electron and hole, respectively) on the QD radius, a is calculated by minimizing the functional $E_0(a, \mu(a))$ (17):

$$\frac{\partial E_0(a, \mu(a))}{\partial \mu(a)} = F(\mu(a), a) \quad (18)$$

Without writing cumbersome expressions for the first derivative of the functional $\partial E_0(a, \mu(a)) / \partial \mu(a) = F(\mu(a), a)$, we present the numerical solution to the equation $F(\mu(a), a) = 0$ (18) in tabulated

form. This follows from the table that the solution to this equation is the function $\mu(a)$, which monotonically varies weakly within the limits [20-22]:

$$0.304 \leq \mu(a) / m_0 \leq 0.359 \quad (19)$$

as the QD radius a varies within the range

$$2.0 \leq a \leq 29.8 \text{ nm} \quad (20)$$

(m_0 is the electron mass in a vacuum). In this case, the reduced exciton effective mass $\mu(a)$ (19) in the nanosystem differs slightly from the effective mass of an exciton (with a spatially separated hole and electron) $\mu = 0.304m_0$ by the value $(\mu(a) - \mu_0)/\mu_0 \leq 0.18$ when the QD radii vary within the range (20).

Simultaneously substituting the values of the variational parameter $\mu(a)$ (19) from Table 1 with the corresponding QD radii from the range (20) into the functional $E_0(a, \mu(a))$ (17), we obtain the exciton ground-state energy $E_0(a, \epsilon)$ (17) as a function of the QD radius a [20-22].

$a, \text{ nm}$	$\mu(a)/m_0$
2.0	0.359
3.0	0.352
4.0	0.345
5.0	0.338
6.0	0.331
8.0	0.325
10.0	0.319
15.0	0.313
20.0	0.308
29.8	0.304

Table 1. Variational parameter $\mu(a)$ as a function of the zinc selenide QD radius a .

The results of the variational calculation of the energy of the ground state of an exciton $E_0(a, \epsilon)$ (17) in the nanosystem under study containing zinc selenide QDs of the radius a (20) are shown in the Figure 1 [20-22]. Here, the values of function $\mu(a)$ (19) and the results of the variational calculation of the exciton ground-state energy $E_0(a, \epsilon)$ (17) are obtained for a nanosystem containing zinc selenide QDs, synthesized in a borosilicate glass matrix, as studied in the experimental works [10, 19].

In the experimental work [10], borosilicate glass samples doped with zinc selenide with concentrations ranging from $x = 0.003\text{-}1\%$, obtained by the sol-gel method, were studied. According to X-ray diffraction measurements, the average radii a of ZnSe QDs formed in the

samples were within $a \approx 2.0\text{-}4.8$ nm. In this case, the values of \tilde{a} were comparable to the exciton Bohr radius $a_{ex} \approx 3.7$ nm in a zinc selenide single crystal. At low QD concentrations ($x = 0.003$ and 0.06%), their interaction can be disregarded. The optical properties of such nanosystems are primarily controlled by the energy spectra of electrons and holes localized near the spherical surface of individual QDs synthesized in the borosilicate glass matrix.

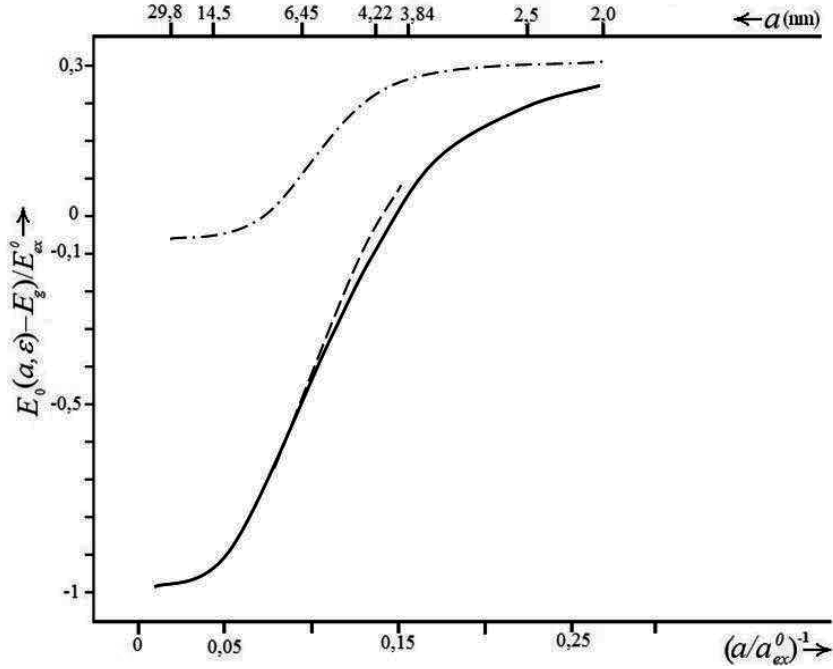


Figure 1. Dependences of the exciton ground state-energy ($E_0(a, \varepsilon) - E_g$) (17) (solid curve) and the binding energy of the exciton ground state ($E_{ex}(a, \varepsilon) - E_g$) (21) (dashed curve) on the zinc selenide QD radius a in the model of an exciton with a spatially separated electron and hole. The dash-dotted curve is the dependence of the exciton ground-state energy ($E_0(a, \varepsilon) - E_g$) on the zinc selenide QD radius a in the exciton model, in which the electron and hole move within the zinc selenide QD volume [16]. $E_g = 2.823$ eV is the band gap in a zinc selenide single crystal; $E_{ex}^0 = 1.5296$ eV (15) and $a_{ex}^0 = 0.573$ nm (14) are, respectively, the binding energy of the ground state and the Bohr radius of a two-dimensional exciton with a spatially separated electron and hole.

In [10, 19], a peak in the low-temperature luminescence spectrum at an energy of $E1 \approx 2.66$ eV was observed at the temperature $T = 4.5$ K in samples with $x = 0.06\%$; this energy is lower than the band gap of a zinc selenide single crystal ($E_g = 2.823$ eV). The shift of the peak of the low-temperature luminescence spectrum with respect to the band gap of the ZnSe single crystal to the short-wavelength region is $\Delta E1 = (E1 - E_g) \approx -165$ meV. The authors of [10] assumed that the shift $\Delta E1$ was caused by quantum confinement of the energy spectra of electrons and holes localized near the spherical surface of individual QDs, and that it was associated with a decrease in the average radii a of zinc-selenide QDs at low concentrations ($x = 0.06\%$). In this case, the problem of the quantum confinement of which electron and hole states (the hole

moving within the QD volume and the electron localized at the outer spherical QD-dielectric matrix interface or the electron and hole localized in the QD volume) caused such a shift of the luminescence-spectrum peak remained open.

Comparing the exciton ground-state energy ($E_0(a, \varepsilon) - E_g$) (17) with the energy of the shift in the luminescence-spectrum peak $\Delta E1 \approx -165$ meV, we obtained the average zinc selenide QD radius $a1 \approx 4.22$ nm (see Figure 1) [20-22]. The QD radius $a1$ may be slightly overestimated, since the variational calculation of the exciton ground-state energy can yield slightly overestimated energies [33, 34]. The determined average QD radius $a1$ was found to be within the range of the average radii of zinc selenide QDs ($a \approx 2.0-4.8$ nm) studied under the experimental conditions of [10, 19].

It should be noted that the average Coulomb interaction energy $\bar{V}_{eh}(a, \varepsilon) = \langle \psi_0(\mathbf{r}_e, \mathbf{r}_h, r, a) | V_{eh}(r) | \psi_0(\mathbf{r}_e, \mathbf{r}_h, r, a) \rangle$ between the electron and hole primarily contributed to the ground-state energy (17) of the exciton in the nanosystem containing zinc selenide QDs with radii $a1$ comparable to the exciton Bohr radius in a zinc-selenide single crystal ($a_{ex} \approx 3.7$ nm). In this case, the average energy of the interaction of the electron and hole with self- and "foreign" images,

$$\begin{aligned} & (\bar{V}_{ee'}(a, \varepsilon) + \bar{V}_{hh'}(a, \varepsilon) + \bar{V}_{eh'}(a, \varepsilon) + \bar{V}_{he'}(a, \varepsilon)) = \\ & = \langle \psi_0(\mathbf{r}_e, \mathbf{r}_h, r, a) | V_{ee'}(\mathbf{r}_e, a, \varepsilon) + V_{hh'}(\mathbf{r}_h, a, \varepsilon) + V_{eh'}(\mathbf{r}_e, \mathbf{r}_h, a, \varepsilon) + V_{he'}(\mathbf{r}_e, \mathbf{r}_h, a, \varepsilon) | \psi_0(\mathbf{r}_e, \mathbf{r}_h, r, a) \rangle \end{aligned}$$

yielded a significantly smaller contribution to the exciton ground-state energy (17),

$$0.04 \leq \left[[V_{ee'}(a, \varepsilon) + V_{hh'}(a, \varepsilon) + V_{eh'}(a, \varepsilon) + V_{he'}(a, \varepsilon)] / E_0(a, \varepsilon) \right] \leq 0.12 [20-22].$$

Thus, the short-wavelength shift $\Delta E1$ of the low temperature luminescence spectrum peak is caused by renormalization of the electron-hole Coulomb interaction energy $V_{eh}(r)$ (11), as well as renormalization of the energy $U(\mathbf{r}_e, \mathbf{r}_h, r, a, \varepsilon)$ (5) of the polarization interaction of the electron and hole with the spherical QD-dielectric matrix interface, which is associated with spatial confinement of the quantization region by the QD volume. In this case, the hole moves within the QD volume and the electron is localized at the outer spherical QD-dielectric matrix interface.

The binding energy of the ground state of an exciton (with a spatially separated electron and hole) $E_{ex}(a, \varepsilon)$ in a nanosystem containing zinc selenide QDs of the radius a is the solution to the radial Schrodinger equation with a Hamiltonian containing, in contrast to Hamiltonian (10), only the terms $V_{he'}(\mathbf{r}_e, \mathbf{r}_h, a, \varepsilon)$ (8) and $V_{eh'}(\mathbf{r}_e, \mathbf{r}_h, a, \varepsilon)$ (9) in the polarization interaction energy $U(\mathbf{r}_e, \mathbf{r}_h, a, \varepsilon)$ (5), which describe the energies of the hole and electron interaction with "foreign" images, respectively [15, 27, 28]. Therefore, the exciton ground-state binding energy $E_{ex}(a, \varepsilon)$ is defined by the expression [20-22]:

$$E_{ex}(a, \varepsilon) = E_0(a, \varepsilon) - \left\langle \psi_0(r_e, r_h, r, a) \left| \left(V_{hh'}(r_h, a, \varepsilon) + V_{ee'}(r_e, a, \varepsilon) \right) \right| \psi_0(r_e, r_h, r, a) \right\rangle, \quad (21)$$

where the term $\langle \psi_0(r_e, r_h, r, a) | (V_{hh'}(r_h, a, \varepsilon) + V_{ee'}(r_e, a, \varepsilon)) | \psi_0(r_e, r_h, r, a) \rangle$ describes the average energy of hole and electron interaction with self-images.

Since the average energies of the interaction of the hole with its image and the average energies of the interaction of the electron with its image deliver contributions that take opposing signs to expression (21), they significantly compensate for each other. Therefore, the binding energies of the exciton ground state $E_{ex}(a, \varepsilon)$ (21) slightly differs from the corresponding total energies of the exciton ground state $E_0(a, \varepsilon)$ (17). This difference,

$$\Delta = \left| \left(E_{ex}(a, \varepsilon) - E_0(a, \varepsilon) \right) / E_{ex}(a, \varepsilon) \right|,$$

varies within $\Delta \leq 4\%$, as QD radii a varies within the range $3.84 \leq a \leq 8.2$ nm (see Figure 1) [20-22].

Figure 1 shows the dependences of the total energy $E_0(a, \varepsilon)$ (17) and the binding energy $E_{ex}(a, \varepsilon)$ (21) of the ground state of the exciton with a spatially separated electron and hole on the QD size for a nanosystem containing zinc selenide QDs of the radius a . We can see that the bound states of electron-hole pairs arise near the spherical surface of the QD, starting from the QD critical radius $a \geq a_c^{(1)} \approx 3.84$ nm. In this case, the hole is localized near the QD inner surface and the electron is localized at the outer spherical QD-dielectric matrix interface. Starting from the QD radius $a \geq a_c^{(1)}$, the electron-hole pair states are in the region of negative energies (counted from the top of the band gap E_g for a zinc selenide single crystal), which corresponds to the electron-hole bound state [20-22, 29-23]. In this case, the electron-hole Coulomb interaction energy $V_{eh}(r)$ (11) and the energy $U(r_e, r_h, r, a, \varepsilon)$ (5) of the polarization interaction of the electron and hole with the spherical QD-dielectric matrix interface dominate the energy of the quantum confinement of the electron and hole in the nanosystem under study.

The total energy $|E_0(a, \varepsilon)|$ (17) and the binding energy $|E_{ex}(a, \varepsilon)|$ (21) of the ground state of the exciton with a spatially separated electron and hole increases with QD radius a . In the range of radii

$$4.0 \leq a \leq 2.8 \text{ nm} \quad (22)$$

the binding energy $|E_{ex}(a, \varepsilon)|$ (21) of the exciton ground state significantly (by a factor of 4.1-76.2) exceeds the exciton binding energy in a zinc selenide single crystal, $E_{ex}^0 \approx -21.07$ meV. Starting from the QD radius $a \geq a_c^{(2)} \approx 29.8$ nm, the total energies (17) and binding energies (21) of the exciton ground state asymptotically tend to the value $E_{ex}^0 = -1.5296$ eV, which characterizes the binding energy of the ground state of a two-dimensional exciton with a spatially separated electron and hole (see the figure 1) [20-22, 29-32].

The obtained values of the total energy $E_0(a, \varepsilon)$ (17) of the exciton ground state in the nano-system satisfy the inequality

$$(E_0(a, \varepsilon) - E_g) \ll \Delta V(a) \quad (23)$$

where $\Delta V(a)$ is the potential-well depth for the QD electron. For a large class of II-VI semiconductors in the region of QD sizes, $a \geq a_{ex}^0$, $\Delta V(a) = 2.3-2.5$ eV [7]. Satisfaction of condition (23) likely makes it possible to disregard the effect of the complex structure of the QD valence band on the total energy (17) and the binding energy (21) of the exciton ground state in the nano-system under study when deriving these quantities.

The effect of a significant increase in the binding energy $|E_{ex}(a, \varepsilon)|$ (21) of the exciton ground state in the nanosystem under study, according to formulas (5) to (9), (11), (13) to (15), (17) and (21) is controlled by two factors [20-22, 29-32]: (i) a significant increase in the energy of the electron-hole Coulomb interaction $|V_{eh}(r)|$ (11) and an increase in the energy of the interaction of the electron and hole with "foreign" images $|V_{eh}(r_{er}, r_{hr}, r, a, \varepsilon)|$ (9), $|V_{he}(r_{er}, r_{hr}, r, a, \varepsilon)|$ (8) (the "dielectric enhancement" effect [34]); (ii) spatial confinement of the quantization region by the QD volume. In this case, as the QD radius a increases, starting from $a \geq a_c^{(2)} \approx 52$ $a_{ex}^0 \approx 29.8$ nm, the exciton becomes two-dimensional, with a ground-state energy of E_{ex}^0 (15), which exceeds the exciton binding energy E_{ex} in the zinc selenide single crystal by almost two orders of magnitude:

$$\left(\left| \frac{E_{ex}^0}{E_{ex}} \right| \approx 72.6 \right).$$

The "dielectric enhancement" effect is caused by the following factor. When the matrix permittivity ε_1 is significantly smaller than the QD permittivity ε_2 , the most important role in the electron-hole interaction in the nanosystem under study is fulfilled by the field induced by these quasiparticles in the matrix. In this case, electron-hole interaction in the nanosystem appears to be significantly stronger than in an infinite semiconductor with the permittivity ε_2 [34].

In [16], in the nanosystem experimentally studied in [10], an exciton model in which the electron and hole move within the zinc selenide QD volume was studied. Using the variational method, within the modified effective mass method, the dependence of the exciton ground-state energy $E_0(a, \varepsilon)$ on the QD radius a in the range (20) was obtained in [16] (see Figure 1). It was shown that, as the QD radius increased, starting from $a \geq a_c = 3.90$ $a_{ex}^0 = 1.45$ nm, a bulk exciton appeared in the QD; its binding energy,

$$\overline{E}_{ex}^0 = -\frac{\hbar^2}{2\mu(\overline{a}_{ex}^0)^2} \quad (24)$$

was 21.07 meV ($\mu = 0.132m_0$ and $\overline{a}_{ex}^0 = 3.7$ nm are the reduced effective mass and Bohr radius of the exciton in the zinc-selenide forming the QD volume). The bulk exciton in the QD is understood as an exciton whose structure (reduced mass, Bohr radius and binding energy) in the QD does not differ from the structure of an exciton in an infinite semiconductor material. As the QD radius a increases ($a \geq a_c$), the exciton ground-state energy $E_0(a)$ asymptotically follows the binding energy of the bulk exciton (24) (see Figure 1) [20-22, 29-32].

Thus, using the exciton model, in which an electron and hole move in the QD volume, it is impossible to interpret the mechanism of the appearance of the nanosystem luminescence-spectrum peak with the shift $\Delta E1 \approx -165$ meV, obtained in [10, 19].

A comparison of the dependences of the exciton ground-state energy $E_0(a)$ in the nanosystem [10], obtained using two-exciton models (see Figure 1) (the electron and hole move within the zinc selenide QD volume [16]) (model I); the hole moves within the zinc selenide QD volume and the electron is localized in the boron silicate glass matrix near the QD spherical surface (model II), allowing for the following conclusion. In model I, as the QD radius a increases, starting from $a \geq a_c \approx 14.5$ nm, the exciton ground-state energy $E_0(a)$ asymptotically follows the binding energy of the bulk exciton $\overline{E}_{ex}^0 \approx -21.07$ meV (24). In model II, as the QD radius increases, starting from $a \geq a_c^{(2)} \approx 29.8$ nm, the exciton ground-state energy (17) asymptotically follows $E_{ex}^0 = -1.5296$ eV (15) (characterizing the binding energy of the ground state of a two-dimensional exciton with a spatially separated electron and hole), which is significantly lower than $\overline{E}_{ex}^0 \approx -21.07$ meV [20-22, 29-32].

3. Excitonic quasimolecules formed from spatially separated electrons and holes

We considered a model nanosystem [23, 24] that consisted of two spherical semiconductor QDs, A and B , synthesized in a borosilicate glass matrix with the permittivity ϵ_1 . Let the QD radii be a and the spacing between the spherical QD surfaces be D . Each QD is formed from a semiconductor material with the permittivity ϵ_2 . For simplicity, without loss of generality, we assumed that holes h (A) and h (B) with the effective masses m_h were in the QD (A) and QD (B) centres and the electrons $e(1)$ and $e(2)$ with the effective masses $m_e^{(1)}$ were localized near the spherical QD(A) and QD (B) surfaces, respectively. The above assumption was reasonable, since the ratio between the effective masses of the electron and hole in the nanosystem was much smaller than unity: $((m_e^{(1)}/m_h) \ll 1)$. Let us assume that there was an infinitely high potential barrier at the spherical QD-matrix interface. Therefore, in the nanosystem, holes did not leave the QD bulk and electrons did not penetrate into the QDs.

In the context of the adiabatic approximation and effective mass approximation, using the variational method, we obtained the total energy $E_0(\tilde{D}, \tilde{a})$ and the binding energy $E_e(\tilde{D}, \tilde{a})$ of the biexciton singlet ground state (the spinning of the electrons $e(1)$ and $e(2)$ were antiparallel) in such a system as functions of the spacing between the QD surfaces D and the QD radius a [23, 24]:

$$E_0(\tilde{D}, \tilde{a}) = 2E_{ex}(\tilde{a}) + E(\tilde{D}, \tilde{a}), \quad (25)$$

Here, the binding energy $E_{ex}(\tilde{a})$ (17) of the ground state of the exciton (formed from an electron and a hole spatially separated from the electron) localized above the QD(A) (or QD(B)) surface was determined in [23, 24] (by the parameters $\tilde{a} = (a/a_{ex}^0)$ ($a_{ex}^0 = 3.7$ nm and the exciton Bohr radius in a single crystal ZnSe, $\tilde{D} = (D/a_{ex}^0)$). For the nanosystem under study, the values of the binding energies $E_{ex}(\tilde{a})$ were calculated in [23, 24] for use in the experimental conditions of [10, 19].

The results of the variational calculation of the binding energy $E_e(\tilde{D}, \tilde{a})$ of the biexciton singlet ground state in the nanosystem of ZnSe and QDs with an average radii of $\tilde{a}_1 = 3.88$ nm, synthesized in a borosilicate glass matrix, are shown in [23, 24]. Such a nanosystem was experimentally studied in [10, 19]. In [10, 19], the borosilicate glassy samples doped with ZnSe to the content x from $x = 0.003$ -1% were produced using the sol-gel technique. At a QD content of $x = 0.06$ %, one must take into account the interaction of charge carriers localized above the QD surfaces.

The binding energy $E_e(\tilde{D}, \tilde{a})$ of the biexciton singlet ground state in the nanosystem of ZnSe QDs with average radii of $\tilde{a}_1 = 3.88$ nm has a minimum of $E_e^{(1)}(D_1, \tilde{a}_1) \approx -4, 2$ meV (at the spacing $D_1 \cong 3.2$ nm) [23, 24]. The value of $E_e^{(1)}$ corresponds to the temperature $T_c \approx 49$ K. In [23, 24], it follows that a biexciton (excitonic quasimolecule) is formed in the nanosystem, starting from a spacing between the QD surfaces of $D \geq D_c^{(1)} \cong 2, 4$ nm. The formation of such a excitonic quasimolecule (biexciton) is of the threshold character and possible only in a nanosystem with QDs with average radii \tilde{a}_1 , such that the spacing between the QD surfaces D exceeds a certain critical spacing $D_c^{(1)}$. Moreover, the exciton quasimolecule (biexciton) can exist only at temperatures below a certain critical temperature, i.e., $T_c \approx 49$ K [23, 24].

As follows from the results of variational calculation [23, 24], the binding energy of an exciton (formed from an electron and a hole spatially separated from the electron) localized above the surface of the QD(A) (or a QD(B)) with an average radius of $\tilde{a}_1 = 3, 88$ nm is $E_{ex}(\tilde{a}_1) \cong -54$ meV. In this case, the energy of the biexciton singlet ground state $E_0(\tilde{D}, \tilde{a})$ (25) takes the value $E_0(\tilde{D}, \tilde{a}) = -112$ meV.

From the results of variational calculation [23, 24], of the biexciton (exciton quasimolecule) binding energy $E_e(\tilde{D}, \tilde{a})$, it follows that the major contribution to the binding energy (25) is

made by the average energy of the exchange interaction of the electrons $e(1)$ and $e(2)$ alongside holes $h(A)$ and $h(B)$. At the same time, the energy of the Coulomb interaction makes a much smaller contribution of the biexciton binding energy $E_e(\bar{D}, \bar{a})$ (25).

The major contribution to the exchange is interaction energy, created by the energy of the exchange interaction of the electron $e(1)$ with the holes $h(B)$, as well as of the electron $e(2)$ with the holes $h(B)$, and of the electron $e(2)$ with the holes $h(A)$. The major contribution to the Coulomb is interaction energy, created by the energy of the Coulomb interaction of the electron $e(1)$ with the holes $h(B)$, as well as of the electron $e(2)$ with the holes $h(A)$ [23, 24].

As the spacing D between the QD(A) and QD(B) surfaces is increased, starting from $D \geq D_c^{(2)} \cong 16,4$ nm, the average Coulomb interaction energy substantially decreases. In addition, because of the decrease in the overlapping of the electron wave function, the average exchange interaction energy also substantially decreases. Consequently, the average Coulomb interaction energy and the average energy of the exchange interaction of the electrons $e(1)$ and $e(2)$ with the holes $h(A)$ and $h(B)$ sharply decrease in comparison with the exciton binding energy $E_{ex}(\bar{a})$ (17) [23, 24], resulting in decomposition of the biexciton in the nanosystem into two excitons (formed of spatially separated electrons and holes) localized above the QD(A) and QD(B) surfaces.

4. Theory of new superatoms — Analogue atoms from the group of alkali metals

The idea of superatoms (or artificial atoms) is essential for the development of mesoscopic physics and chemistry [20-22, 29, 30]. Superatoms are nanosized quasi-atomic nanostructures formed from spatially separated electrons and holes (the hole in the volume of the QD and the electron is localized on the outer spherical quantum dot matrix dielectric interface) [20-22, 29, 30]. This terminology can be accepted as correct, given the similarities between the spectra of discrete electronic states of atoms and superatomic atoms, and the similarities in terms of their chemical activities [20-22, 29, 30].

In [20-22], within the framework of the modified effective mass method [14], the theory of artificial atoms formed from spatially separated electrons and holes (holes moving in the volume of a semiconductor (dielectric) QD and an electron localized on the outer spherical interface between the QD and a dielectric matrix) is developed. The energy spectrum of superatoms (excitons of spatially separated electrons and holes) from QD radius $a \geq ac$ (about 4 nm) is fully discrete [20-22, 29, 30]. This is referred to as a hydrogen-superatom and is localized on the surface of a valence electron QD. The energy spectrum of the superatom consists of a quantum-dimension of discrete energy levels in the band gap of the dielectric matrix. Electrons in superatoms are localized in the vicinity of the nucleus (QD). The electrons move in well-defined atomic orbitals and serve as the nucleus of QD, containing in its volume semiconductors and insulators. Ionization energy superatoms take on large values (of the

order of 2.5 eV), which is almost three orders of magnitude higher than the binding energy of the excitons in semiconductors [20-22, 29, 30].

We will briefly discuss the possible physical and chemical effects that are relevant for the results of this paper. In our proposed [20-22, 29, 30] model of a hydrogen superatom localized on the surface of the QD is a valence electron. In quasi-atomic structures of the outer valence, electrons can participate in a variety of physical and chemical processes, similar to the atomic valence electrons in atomic structures. Artificial atoms have the ability to connect to the electron orbitals of electrons N (where N can vary from one to several tens). At the same time, the number of electrons N can take values of the order of a few tens or even surpass the serial numbers of all the known elements found in Mendeleev's table [20-22, 29, 30]. This new effect allows for attaching to the electronic orbitals of artificial atoms N electrons, causing a high reactivity and opening up new possibilities for superatoms related to their strong oxidizing properties, increasing the possibility of substantial intensity in photochemical reactions during catalysis and adsorption, as well as their ability to form many new compounds with unique properties (in particular, the quasi-molecule and quasicrystals) [24, 29, 30]. Therefore, studies aimed at the theoretical prediction of the possible existence of artificial new atoms (not listed in the Mendeleev table) and to their study in terms of experimental conditions are very relevant.

Quantum discrete states of the individual atoms of alkali metals are determined by the movement of only one, i.e., the outermost valence electron, around a symmetric atomic core (containing the nucleus and the remaining electrons) [35]. In the hydrogen superatom formed quantum-energy spectra of discrete energy levels of the valence electron [20-22, 29, 30]. Thus, the observed similarity of the spectra of discrete electronic states and individual superatoms alkali metal atoms, as well as the similarity of their chemical activity [20-22, 29, 30, 35].

In Section 4, on the basis of a spectroscopic analogy of electronic states of artificial atoms and individual alkali metal atoms, a new artificial atom is theoretically predicted, which is similar to the new alkali metal atom.

In [20-22, 29, 30], a new model of an superatom is proposed, which is a quasi-zero-dimensional nanosystem consisting of a spherical QD (nucleus superatom) with radius a and which is included within its scope as a semiconductor (dielectric) with a dielectric constant ϵ_2 , surrounded by a dielectric matrix with a dielectric constant ϵ_1 . A hole h with the effective mass m_h moves in the QD volume, while an electron e with the effective mass $m_e^{(1)}$ lies in the dielectric matrix. In such a nanostructure, the lowest electronic level is situated in the matrix and the humble hole level is the volume QD. Large shift of the valence band (about 700 meV) is the localization of holes in the volume QD. A large shift of the conduction band (about 400 meV) is a potential barrier for electrons (electrons move in the matrix and do not penetrate into the volume QD). The Coulomb interaction energy of an electron and a hole, and the energy of the electron polarization interaction with the surface section (QD-matrix) (since the permittivity ϵ_2 is far superior to QD permittivity ϵ_1 matrix) cause localization of the electron in the potential well above the surface of QD [20-22, 29, 30].

With increasing radius a QD, so that $a \gg a_{ex}^0$ (where a_{ex}^0 (14) two-dimensional Bohr radius of the electron) spherical surface section (QD- matrix) transforms into a flat surface section. In this artificial atom, electrons localized on the surface (QD-matrix) become two-dimensional. In this case, the potential energy in the Hamiltonian describing the motion of an electron in a superatom, the main contribution to the energy of the Coulomb interaction $V_{eh}(r)$ (11) between an electron and a hole [20-22]. Polarization interaction energy of the electron and the hole with a spherical surface section (QD-matrix) delivers a much smaller contribution to the potential energy of the Hamiltonian and thus, contributions to a first approximation can be neglected [20-22]. In this regard, the two-dimensional electron energy spectrum En in the artificial atom takes the form (13).

Depending on the binding energy $E_{ex}(a,\varepsilon)$ of an electron in the ground state superatom (QD containing zinc-selenide radius a and surrounded by a matrix of borosilicate glass [10]) as obtained in [20-22] by the variational method, it follows that the bound state of an electron occurs near the spherical interface (QD-matrix), starting with the value of the critical radius QD $a \geq a_c^{(1)} = 3.84$ nm, when this hole moves in the volume QD and the electron is localized on the surface of the spherical section (QD-matrix). In this case, the Coulomb interaction energy $V_{eh}(r)$ (11) between the electron and the hole, and the energy of the polarization interaction of electrons and holes with a spherical surface section (QD-matrix) prevail over the size quantization of the energy of electrons and holes in the artificial atom. Thus, [20-22] found that the occurrence of superatoms had a threshold and was only possible if the radius of QD $a \geq a_c^{(1)} = 3.84$ nm.

With the increasing radius of a QD scan, an increase in the binding energy of the electron in the ground state superatom was observed. In the range of radii $4.0 \leq a \leq 29.8$ nm, the binding energy of the electron in the ground state superatom significantly exceeded (in (4,1-76,2) times) the value of the exciton binding energy $\tilde{E}_{ex}^0 \approx 21.07$ meV in a single crystal of zinc-selenide [20-22]. Beginning with a radius QD $a \geq a_c^{(2)} = 29.8$ nm, the energy of the ground state of an electron in a superatom asymptotically follow the value $E_{ex}^0 = -1.5296$ eV, which characterized the energy of the ground state of two-dimensional electrons in an artificial atom (15) [20-22].

The effect of significantly increasing the energy of the ground state of an electron in a superatom was primarily determined by two factors [20-22]: 1) a significant increase in the Coulomb interaction energy $|V_{eh}(r)|$ (2) electron-hole (the "dielectric enhancement" [34]); 2) the spatial limitations on the quantization volume QD, while with an increasing radius of a QD, since the radius of QD $a \geq a_c^{(2)} = 52a_{ex}^0 = 29.8$ nm, superatoms became two-dimensional with a binding energy of the ground state E_{ex}^0 (15), the value of which exceeded the exciton binding energy in a single crystal of zinc-selenide by two orders. The effect of "dielectric enhancement" as a result of the dielectric constant ε_1 of the matrix was much lower than the dielectric constant of QD ε_2 , which played an essential role in the interaction between the electron and the hole in the superatom playing field produced by these quasi-particles in a matrix. Thus, the interaction between the electron and the hole in the superatom was significantly larger than in a semiconductor permittivity ε_2 [34].

Quantum discrete states of the individual atoms of alkali metals were determined by the movement of only one, the outermost valence electron, around a symmetric atomic core

(containing the nucleus and the remaining electrons) [35]. Where large distances were the case between r electron and the nucleus (so that $r \gg a_0$, where $a_0 = 0.053$ nm – the Bohr radius of the electron in a hydrogen atom), the field of the atomic core was described by the Coulomb field [35]:

$$V(r) = -\left(\frac{Ze^2}{r}\right), \quad (26)$$

determining the interaction of the valence electron with the atomic core (Z – serial number of the atom in the periodic table of Mendeleev). The energy spectrum of a single atom of an alkali metal hydrogen-described spectrum [35] is given as follows:

$$E_{n^*} = -\frac{Ry^*}{(n^*)^2}, \quad Ry^* = Z^2 Ry_0 \quad (27)$$

where $n^* = (n + y)$ and effective quantum number ($n = 1, 2, 3, \dots$ the principal quantum number); the amendment y depended on the orbital quantum number l . Amendments to y were due to the fact that the valence electron moved in the Coulomb field of the atomic core, where the nuclear charge was screened by core electrons. Amendment y corrections were determined by comparing the spectrum of (6) with its experimental values. The value of $y < 0$ and was numerically closer to the atomic core suitable valence electron orbit. The number of possible orbits of the valence electron in a single alkali metal atom such as a hydrogen atom, and [35].

The similarity of the individual series of neutral alkali metal atoms with the hydrogen Balmer series suggests that the energy spectra of neutral alkali metal atoms can be labelled valence electron radiation in transition from higher levels to the level of principal quantum number $n = 2$ [35].

In a single atom of an alkali metal valence electron moving in the Coulomb field of the atomic core (26) having the same functional dependence on r as the Coulomb field (11), in which the valence electron in hydrogen-like model of artificial atom. This leads to the fact that the energy spectra of the valence electron in a single atom of an alkali metal (27) and in the artificial atom (13) describe the spectrum of hydrogen-type. At the same time, the number of possible quantum states of valence electrons in a hydrogen-like artificial atom model is the same as the number of quantum states of discrete valence electrons in a single atom of an alkali metal [20-22, 29, 30].

Table 2 shows the position of the valence electron energy levels in the atoms of alkali metals (K, Rb, Sc) [35] and the new artificial atom X, as well as the level shifts of the valence electron ($\Delta E_{Rb}^K, \Delta E_{Sc}^{Rb}, \Delta E_x^{Sc}$) relative to the adjacent level. Assume that the shift of the energy level E_x artificial atom X (relative to the energy level E_{sc} of the atom Sc) will be the same as the shift of the energy level E_{Rb} of the atom Rb (relative energy level E_{sc} of the atom Sc), (i.e., $\Delta E_x^{Sc} = \Delta E_{Sc}^{Rb}$). In this case, the level of the valence electron artificial atom will be $E_x = -593$ meV. Using the dependence of the binding energy $E_{ex}(a, \varepsilon)$ of the ground state of an electron in an artificial

atom [20-22] (QD containing zinc-selenide radius a and surrounded by a matrix of borosilicate glass [10]), we found the radius QD zinc-selenide $a_1 = 5.4$ nm, which corresponded to the $E_x = -593$ meV. It should be noted that the energy levels of a valence electron in the individual atoms of alkali metals (K, Rb, Sc) [35] and the new artificial atom X are located in the infrared spectrum.

Alkali metal atoms selected	Valence electron energy levels (meV)	Level shifts of the valence electron (meV)
K	-7 21.1	
Rb	-7 11.2	1 0
Sc	-652	5 9
X	-5 93	5 9

Table 2. Position of energy levels of the valence electron in some alkali metal atoms (K, Rb, Sc) and a new artificial atom, X. Level shifts of the valence electron ($\Delta E_{Rb}^K, \Delta E_{Sc}^{Rb}, \Delta E_x^{Sc}$) are relative to the adjacent level.

Thus, we propose a new model of an artificial atom that is a quasi-atomic heterostructure consisting of a spherical QD (nucleus superatom) radius a and which contains in its scope, zinc-selenide, surrounded by a matrix of borosilicate glass (in volume QD, h hole effectively moves mass $m_{h,e}$ and the electron effective mass $m_e^{(1)}$ is located in the matrix), thus allowing for finding a new artificial atom X (absent in the Mendeleev periodic system), which is similar to a new single alkali metal atom. This new artificial atom of a valence electron can participate in various physical [20-22, 29, 30] and chemical [30, 35] processes that are analogous to atomic valence electrons in atomic systems (in particular, the selected alkali metal atoms [35]). Such processes are unique as a result of the new properties of artificial atoms: strong oxidizing properties that increases the possibility of substantial intensity in photochemical reactions during catalysis and adsorption, as well as their ability to form a plurality of the novel compounds with unique properties (in particular, the quasi-molecule and the quasicrystals [23, 24]).

The application of semiconductor nanoheterostructures as the active region nanolasers prevents small exciton binding energy in QD. Therefore, studies aimed at finding nanoheterostructures, which will yield a significant increase in the binding energy of the local electronic states in QDs, are relevant [20-22]. The effect of significantly increasing the energy of the electron in a hydrogen superatom [20-22, 29, 30] allows for better experimental detection of the existence of such superatoms at room temperatures and will stimulate experimental studies of nanoheterostructures containing superatoms, which can be used as active region nanolasers when working with optical transitions.

5. Conclusions

The theory of an exciton with a spatially separated electron and hole was developed within the framework of the modified effective mass method [14], in which the reduced effective exciton mass is a function of the semiconductor QD radius a . The average zinc-selenide QD

radius was determined by comparing the dependence of the exciton ground-state energy (17) on the QD radius, obtained by the variational method within the modified effective mass method [14] and using the experimental peak of the low-temperature luminescence spectrum [10, 19]. It was shown that the short-wavelength shift of the peak of the low-temperature luminescence spectrum of the samples containing zinc selenide QDs, which was observed under the experimental conditions noted in [10, 19], was caused by renormalization of the electron-hole Coulomb interaction energy (11), as well as the energy created by the polarization interaction (5) of the electron and hole with the spherical QD-dielectric matrix interface, related to spatial confinement of the quantization region by the QD volume. In this case, the hole moves in the QD volume and the electron is localized at the outer spherical QD-dielectric matrix interface [20-22, 29-32].

To apply semiconductor nanosystems containing zinc-selenide QDs as the active region of lasers, it is required that the exciton binding energy $|E_{ex}(a, \epsilon)|$ (21) in the nanosystem be at the order of several kT_0 and at room temperature T_0 (k is the Boltzmann constant) [13]. Nanosystems consisting of zinc-selenide QDs grown in a borosilicate glass matrix can be used as the active region of semiconductor QD lasers. In the range of zinc selenide QD radii a (22), the parameter $|E_{ex}(a, \epsilon)/kT_0|$ take on significant values ranging from 3.1 to 56 [20-22, 29-32].

The effect of significantly increasing the binding energy (21) of the exciton ground state in a nanosystem containing zinc selenide QDs with radii a (22) was detected; compared to the exciton binding energy in a zinc selenide single crystal, the increase factor was 4.1-72.6. [20-22, 29-32]. It was shown that the effect of significantly increasing the binding energy (21) of the exciton ground state in the nanosystem under study was controlled by two factors [20-22, 29-32]: (i) a substantial increase in the electron-hole Coulomb interaction energy (11) and an increase in the energy of the interaction of the electron and hole with "foreign" images (8), (9) (the "dielectric enhancement" effect [34]); (ii) spatial confinement of the quantization region by the QD volume; in this case, as the QD radius a increased, starting from $a \geq a_c^{(2)} \approx 29.8$ nm, the exciton became two-dimensional with a ground-state energy (15), which exceeded the exciton binding energy in a zinc selenide single crystal by almost two orders of magnitude.

A review devoted to the theory of excitonic quasimolecules (biexciton) (made up of spatially separated electrons and holes) in a nanosystem that consists of ZnSe QDs synthesized in a borosilicate glass matrix was developed within the context of the modified effective mass approximation. Using the variational method, we obtained the total energy and the binding energy of the biexciton singlet ground state in such a system as functions of the spacing between the QD surfaces and the QD radius. It was established that, in a nanosystem composed of ZnSe QDs with the average radii \bar{a}_1 , the formation of a biexciton (exciton quasimolecule) was of the threshold character and possible in a nanosystem where the spacing D between the QD surfaces is defined by the condition $D_c^{(1)} \leq D \leq D_c^{(2)}$ [23, 24]. Moreover, the exciton quasimolecule (biexciton) can exist only at temperatures below a certain critical temperature, i.e., $T_c \approx 49$ K [23, 24]. It was established that the spectral shift of the low temperature luminescence peak [10, 19] in such a nanosystem resulted due to quantum confinement of the energy of the biexciton singlet ground state.

Thus, we propose a new model of an artificial atom, which is a quasi-atomic heterostructure consisting of a spherical QD (nucleus superatom) with radius a and which contains in its scope zinc selenide, surrounded by a matrix of borosilicate glass (in volume QD moves h hole effective mass m_h , e and the electron effective mass $m_e^{(1)}$ is located in the matrix), and which is allowed to find a new artificial atom X (absent in the Mendeleev periodic system), which is similar to a new single alkali metal atom. This new artificial atom of valence electron can participate in various physical [20-22, 29, 30] and chemical [30, 35] processes that are analogous to atomic valence electrons in atomic systems (in particular, the selected alkali metal atoms [35]). Such processes are unique due to the new properties of artificial atoms: strong oxidizing properties that increase the possibility of substantial intensity in photochemical reactions during catalysis and adsorption, as well as their ability to form plurality among novel compounds with unique properties (in particular, the quasi-molecule and the quasicrystals [23, 24]).

Author details

Sergey I. Pokutnyi^{1*} and Włodzimierz Salejda^{1*}

*Address all correspondence to: Pokutnyi_Sergey@inbox.ru; Wlodzimierz.Salejda@pwr.edu.pl

1 Chuiko Institute of Surface Chemistry, National Academy of Sciences of Ukraine, Kyiv, Ukraine

2 Technical University of Wrocław, Wrocław, Poland

References

- [1] Ekimov, A., Onushchenko, A., (1981). Size quantization of electrons in microcrystals. *Journal Experimental Theoretical Physics Letters*. 34, 345-348.
- [2] Ekimov, A., Onushchenko, A., (1984). Size quantization of electrons in semiconductor microcrystals. *Journal Experimental Theoretical Physics Letters*. 40, 1136-1139.
- [3] Ekimov, A., Efros, A., (1985). Excitons in semiconductor microcrystals. *Solid State Communication*. 56, 921-924.
- [4] Ekimov, A., Onushchenko, A., Efros, A., (1986). Size quantization of electron-hole pairs in nanocrystals. *Journal Experimental Theoretical Physics Letters*. 43, 376-379.
- [5] Chepik, D., Efros, A., Ekimov, A., (1990). Spectroscopy of excitons in semiconductor nanocrystals. *Journal of Luminescence*. 47, 113-118.

- [6] Ekimov, A., Hache, F., Schanne-Klein, M., (2003). Optical properties semiconductor quantum dots. *Journal Optical Society American*. B 20, 100 -108.
- [7] Grabovskis, V., Dzenis, Y., Ekimov, A., (1989). Photoluminescences of excitons in semiconductor nanocrystals. *Physics Solid State*. 31, 149 -152.
- [8] Alferov, J.I., (2002). Progress development in semiconductor nanostructures. *Physics Uspekhi*. 172, 1068 - 1074.
- [9] Alferov, J.I., (1998). Optical properties in semiconductor nanostructures. *Semiconductors*. 32, 1-8.
- [10] Bondar, V.N., Brodin, M.S., (2010). Optical properties semiconductor quantum dots. *Semiconductors*. 44, 884-890.
- [11] Efros, A.L., Efros, Al. L., Interband absorption light in semiconductor sphere. (1982). *Sov. Phys. Semiconductors*. 16, 955- 962.
- [12] Pokutnyi, S.I., (2004). Size quantization Stark effect in semiconductor quantum dots. *J. Appl. Phys*. 96, 1115-1122.
- [13] Pokutnyi, S.I., (2005). Optical nanolaser heavy hole transitions in quasi-zero- dimensional semiconductors nanosystems. *Physics Lett. A*. 342, 347-352.
- [14] Pokutnyi, S.I., (2007). Exciton states in semiconductor quantum dots in the framework of the modified effective mass method. *Semiconductors*. 41, 1323-1331.
- [15] Pokutnyi, S.I., (2010). Exciton states in semiconductor quantum dots. *Semiconductors*. 44, 488-493.
- [16] Pokutnyi, S.I., (2012). Exciton states in semiconductor nanosystems. *Semiconductors*. 46, 174-184.
- [17] Soloviev, V., Eeichofer, A., (2001). Approximation of effective mass in nanosystems. *Physica Status Solidi B*. 224, 285-291.
- [18] Yeh, C., Zhang, S., Zunger, A., (2004). The effective mass method in nanosystems. *Physical Review B*. 62, 14408-14416.
- [19] Bondar, N., Brodyn, M., (2010). Spectroscopy of semiconductor quantum dots. *Physics E*. 42, 1549-1555.
- [20] Pokutnyi, S.I., (2013). Binding energy of the exciton of a spatially separated electron and hole in quasi-zero-dimensional semiconductor nanosystems. *Technical Physics Letters*. 39, 233-235.
- [21] Pokutnyi, S.I., (2013). On an exciton with a spatially separated electron and hole in quasi-zero-dimensional semiconductor nanosystems. *Semiconductors*. 47, 791 -798.

- [22] Pokutnyi, S.I., (2014). Theory of excitons formed from spatially separated electrons and holes in quasi-zero-dimensional semiconductor nanosystems. *SOP Transactions Theoretical Physics*. 1, 24 -35.
- [23] Pokutnyi, S.I., (2013). Biexcitons formed from spatially separated electrons and holes in quasi-zero-dimensional semiconductor nanosystems. *Semiconductors*. 47, 1626-1635.
- [24] Pokutnyi, S.I., (2014). Quasi-zero-dimensional nanostructures: Excitonic quasimolecules. *J. Appl. Chem*. 2, 1- 4.
- [25] Efremov, N.A., Pokutny, S.I., (1985). Macroscopic local charge states in ultradisersion media. *Sov. Phys. Solid. State*. 27, 27- 35.
- [26] Efremov, N.A., Pokutny, S.I., (1990). Energy spectrum of exciton in spherical particle. *Sov. Phys. Solid. State*. 32, 955- 964.
- [27] Pokutnyi, S.I., (1992). Size quantization of electron-hole pair in semiconductor quantum dots. *Physics Lett. A*. 168, 433-438.
- [28] Pokutnyi, S.I., (2011). Theory of exciton states in semiconductor nanosystems. *Physics Express*. 1, 158-164.
- [29] Pokutnyi, S.I., Gorbyk, P.P., (2013). Superatoms in quasi-zero-dimensional nanostructures (review). *Progr. Phys. Metal*. 14, 144 - 168.
- [30] Pokutnyi, S.I., Gorbyk, P.P., (2013). Superatoms in quasi-zero-dimensional nanosystems. *J. Appl. Chem*. 1, 44 - 47.
- [31] Pokutnyi, S.I., (2012). Exciton states in quasi-zero-dimensional semiconductor nanosystems: Theory. *Phys. Express*. 2, 20 - 26.
- [32] Pokutnyi, S.I., (2013). Exciton states in quasi-zero-dimensional nanostructures. *J. Appl. Chem*. 1, 5 - 18.
- [33] Lozovik, Y., Nishanov, V., (1976). Exciton Wannier-Mott near the interface. *Physics Solid State*. 18, 1905-1911.
- [34] Keldysh, L., (1979). The interaction of the electrons in a thin films. *Journal Experimental Theoretical Physics Letters*. 29, 621-624.
- [35] Frish, S.E., (1963). Optical spectra of atoms. Nauka, Moscow [in Russian].

Excitons and Trions in Semiconductor Quantum Dots

S. A. Safwan and N. El-Meshed

Additional information is available at the end of the chapter

<http://dx.doi.org/10.5772/61177>

Abstract

We aim from this chapter to declare for the readers, what are the exciton and trions in quantum dot and we will present complete theoretical discussion for the behavior of exciton ,its bound state ,binding energy and its stability in quantum dot with different sizes and different confinement potentials .The charged complex particles as negative and positive trions will be investigated theoretically using variational procedure in both strong and weak confinement regime . Good agreement with experimental data was found and discussed.

Keywords: quantum dot, exciton, trion, binding energy

1. Introduction

During the optical excitation of carriers in a semiconductor, the minimum energy required to form free carriers is called the band gap. The energy below that value cannot excite free carriers. However, low-temperature absorption studies of semiconductors have shown excitation just below the band gap [1]. This excitation is associated with the formation of an electron and an electron hole bound to each other, otherwise called an exciton. It is an electrically neutral quasiparticle like in a hydrogenic state. At low temperatures, the bound states are formed and the Coulomb interaction between the electron and the hole becomes prominent [2]. The negative trion (X^-) is created due to the additional electron bound to a pre-existing exciton and if a hole is bound to an exciton, a positive trion (X^+) is created. Both the negative and positive trions are complex electronic excited states of the

semiconductors and therefore, the 3-body problem is raised. Although Lampert [3] in 1958 originally and theoretically predicted the negative trion in semiconductors, K.Kheng et al. experimentally achieved a negative trion in Cd Te/Cd Zn Te quantum well [4].

The rapid progress of semiconductor technology in the recent years has allowed the fabrication of low dimension electronic nanostructures. Such nanostructures confine charged particles in all three space dimensions. In low dimensional, especially in quantum dots [5,6] (three dimension confinement), the picture is different because it is below a nanometer wide, a few nanometers thick, and in various shapes. The quantum confinement increases highly, and this quantum confinement leads to more stability of the excitons and trions by increasing their binding energy. The stability of such particles remains up to room temperature. A proper identification of the (X-) was not achieved until the early 1990's in remotely doped, high-quality quantum-well (QW) structures [7-9]. Since then, extensive work has been carried out on (X-) inside the two-dimensional (2D) [wide quantum wells [7-11]] and quantum dots, which the first observations of the QD-confined charged excitons (trions) were performed on ensembles of the QDs [12]. There are many theoretical studies devoted to excitons [13-15] and trions [16-25] in quantum dot. Most of such studies have treated and considered the spherical[26-28], lens shaped [29,30], square flat plated [31,32], and cylindrical [33,34] quantum dots.

In the present chapter, we study the influence of the 3-D quantum confinement on the binding energy of the exciton (X), negative trion (X-), and the positive trion (X⁺) in a semiconductor cylindrical quantum dot manufactured in GaAs surrounded by Ga_{1-x}Al_xAs. Using a variational approach and the effective mass approximation with finite confinement – potential. There have been concerns as to whether the effective mass approximation could still be valid in the quantum dot limit when the size of the exciton could be similar to the average lattice constants of bulk semiconductor [35].

2. Theoretical model

Within the effective mass approximation and non-degenerated band approximation, we can describe the exciton and trions in the following semiconductor structure: a symmetric cylindrical QD of radius R and height L made of GaAs surrounded by Ga_{1-x}Al_xAs. In our model, the electrons and the holes are placed in the external potential $V_e(r_e, z_e)$ and $V_h(r_h, z_h)$, respectively and coupled via Coulomb potential. We choose the potential in GaAs (well) to be zero and equals V_e or V_h in the barrier material.

2.1. Exciton

The Hamiltonian of an exciton confined in cylindrical QD, using the relative coordinate $r = |\vec{r}_e - \vec{r}_h|$, can be written as[36]:

$$\begin{aligned}
 H = & \frac{-\hbar^2}{2m_e^*} \left\{ \frac{\partial^2}{\partial r_e^2} + \frac{1}{r_e} \frac{\partial}{\partial r_e} + \frac{r_e^2 - r_h^2 + r^2}{r_e r} \frac{\partial^2}{\partial r_e \partial r} + \frac{\partial^2}{\partial z_e^2} \right\} \\
 & \frac{-\hbar^2}{2m_h^*} \left\{ \frac{\partial^2}{\partial r_h^2} + \frac{1}{r_h} \frac{\partial}{\partial r_h} + \frac{r_h^2 - r_e^2 + r^2}{r_h r} \frac{\partial^2}{\partial r_h \partial r} + \frac{\partial^2}{\partial z_h^2} \right\} \\
 & \frac{-\hbar^2}{2\mu} \left\{ \frac{\partial^2}{\partial r^2} + \frac{1}{r} \frac{\partial}{\partial r} \right\} + V_e(r_e, z_e) + V_h(r_h, z_h) - \frac{e^2}{\epsilon_0 \epsilon \sqrt{(r_e - r_h)^2 + (z_e - z_h)^2}}
 \end{aligned} \tag{1}$$

Where m_e^* and m_h^* is the effective mass of the electron and the hole, respectively, μ is the reduced mass of exciton $\mu = m_e m_h / (m_e + m_h)$, and (r_e, z_e) and (r_h, z_h) are the spatial coordinates of the electrons and hole in the cylindrical frame, respectively. The first three terms of equation (1) represent the kinetic energy of the electron, hole, and exaction's center of mass existing in the structure under consideration. The last three terms represent the confinement potentials followed by the Coulomb interaction term. ϵ is the relative static dielectric constant for the used material and ϵ_0 is the permittivity of free space. We can write the expressions of $V_e(r_e, z_e)$ and $V_h(r_h, z_h)$ as:

$$V(r_i, z_i) = \begin{cases} 0 & r_i \leq R \text{ and } |z_i| \leq L \\ V_0 & r_i > R \text{ and } |z_i| > L \end{cases} \tag{2}$$

Here the indices i stand for the electron (e) or the hole (h).

The Schrödinger equation for the exciton in the quantum dot is:

$$H\Psi(r_e, r_h, r, z_e, z_h) = E\Psi(r_e, r_h, r, z_e, z_h) \tag{3}$$

By choosing the following trial wave function, it takes into account the electron-hole correlation and the Ritz variation principle that are used to solve this equation. Thoroughly, we are able to determine the exciton ground state (E_{ex}),

$$\Psi(r_e, r_h, r, z_e, z_h) = f(r_e) f(r_h) g(z_e) g(z_h) \exp\left(-\alpha \sqrt{(r_e - r_h)^2 + (z_e - z_h)^2}\right) \tag{4}$$

The variation parameter α is determined by minimizing the value of the exciton energy:

$$E_{ex}(\alpha) = \langle \Psi | H | \Psi \rangle / \langle \Psi | \Psi \rangle, \tag{5}$$

The binding energy of the exciton is given by:

$$E_b = E_e + E_h - E_{ex} \quad (6)$$

Where $f(r_e)$, $f(r_h)$, $g(z_e)$, $g(z_h)$ and E_e , E_h are the ground wave functions and energies of both the electron and the hole [37].

2.2. Negative trion

The negative trion (X-) is created when an additional electron is bound to a pre-existing exciton (X). The negative trion Hamiltonian in a cylindrical coordinate can be written as:

$$\begin{aligned} H = & \frac{-\hbar^2}{2m_e^*} \left\{ \frac{\partial^2}{\partial r_{e_1}^2} + \frac{1}{r_{e_1}} \frac{\partial}{\partial r_{e_1}} + \frac{\partial^2}{\partial z_{e_1}^2} \right\} \frac{-\hbar^2}{2m_e^*} \left\{ \frac{\partial^2}{\partial r_{e_2}^2} + \frac{1}{r_{e_2}} \frac{\partial}{\partial r_{e_2}} + \frac{\partial^2}{\partial z_{e_2}^2} \right\} \\ & \frac{-\hbar^2}{2m_h^*} \left\{ \frac{\partial^2}{\partial r_h^2} + \frac{1}{r_h} \frac{\partial}{\partial r_h} + \frac{\partial^2}{\partial z_h^2} \right\} + V_{e_1}(r_{e_1}, z_{e_1}) + V_h(r_h, z_h) + V_{e_2}(r_{e_2}, z_{e_2}) \\ & + \frac{e^2}{4\pi\epsilon_0\epsilon} \left[\frac{1}{\sqrt{(r_{e_1} - r_{e_2})^2 + (z_{e_1} - z_{e_2})^2}} - \frac{1}{\sqrt{(r_{e_1} - r_h)^2 + (z_{e_1} - z_h)^2}} - \frac{1}{\sqrt{(r_{e_2} - r_h)^2 + (z_{e_2} - z_h)^2}} \right] \end{aligned} \quad (7)$$

The first three terms of equation (7) represent the kinetic energy terms of the three particles existing in the structure under consideration. The second three terms represent the confinement potentials followed by the three Coulomb interaction terms. We use equation (2) for expressions of $V_e(r_e, z_e)$ and $V_h(r_h, z_h)$.

The present model is fully three dimensional and is applicable to the confinement potentials of finite range and depth, i.e., it is adequate for QD nano-crystals embedded in an insulating medium, e.g. GaAs [38] and InAs [39, 40]. The quantum well potential given above does not commute with the kinetic energy operator at the center of the mass motion. Therefore, the Hamiltonian (7) cannot be separated from the center of the mass and Hamiltonians of the relative motion.

The full three dimension Schrödinger equation for the negative trion in quantum dot is:

$$H \Psi(r_{e_1}, r_{e_2}, r_h, z_{e_1}, z_{e_2}, z_h) = E \Psi(r_{e_1}, r_{e_2}, r_h, z_{e_1}, z_{e_2}, z_h) \quad (8)$$

Hence, the ground state wave function for the negative trion confined in the cylindrical quantum dot has dependent on the six coordinate parameters appearing in equation (8). Here, we adopt the variation approach to estimate the ground state of the negative trions (X-), their binding energy, and their wave functions. We choose the following trial wave function:

$$\Psi_{trion} = f(r_{e_1})f(r_{e_2})f(r_h)g(z_{e_1})g(z_{e_2})g(z_h)\phi(r_{e_1}, r_{e_2}, r_h, z_{e_1}, z_{e_2}, z_h) \quad (9)$$

Where, $f(r_{e_1}), f(r_{e_2}), f(r_h), g(z_{e_1}), g(z_{e_2})$ and $g(z_h)$ are the single particle eigenfunctions [37], and the trial wave function ϕ describes the internal motion of the trions (X-) defined as:

$$\phi(r_{e_1}, r_{e_2}, r_h, z_{e_1}, z_{e_2}, z_h) = \exp \left[-\left(\beta_1 \sqrt{(r_h - r_{e_1})^2 + (z_h - z_{e_1})^2} \right) - \left(\beta_2 \sqrt{(r_h - r_{e_2})^2 + (z_h - z_{e_2})^2} \right) - \left(\beta_3 \sqrt{(r_{e_1} - r_{e_2})^2 + (z_{e_1} - z_{e_2})^2} \right) \right]$$

Here β_1, β_2 and β_3 are the variation parameters. The form of the wave function given in equation (9) satisfies not only the strong interaction region requirements (such as in a very narrow quantum dots), but also yields the correct results near the bulk limits (weak interaction region).

$$\text{Let } \chi_{e_1} = \frac{r_{e_1}}{R}, \chi_{e_2} = \frac{r_{e_2}}{R}, \chi_h = \frac{r_h}{R} \text{ and } \varsigma_{e_1} = \frac{z_{e_1}}{L}, \varsigma_{e_2} = \frac{z_{e_2}}{L}, \varsigma_h = \frac{z_h}{L},$$

where $0 \leq \chi_i \leq 1$ and $-1 \leq \varsigma_i \leq 1$. Now, we rewrite the arguments of the negative trion wave functions in terms of χ ’s, and ς ’s and define, $\chi_1 = |\chi_h - \chi_{e_1}|$, $\chi_2 = |\chi_{e_2} - \chi_h|$, $\chi_3 = |\chi_{e_1} - \chi_{e_2}|$ and $\varsigma_1 = (\varsigma_h - \varsigma_{e_1})$, $\varsigma_2 = (\varsigma_{e_2} - \varsigma_{h_1})$, $\varsigma_3 = (\varsigma_{e_1} - \varsigma_{e_2})$,

By using the new variables, the trial wave function can be expressed as follows:

$$\Psi_{trion}(\chi_{e_1}, \chi_{e_2}, \chi_h, \varsigma_{e_1}, \varsigma_{e_2}, \varsigma_h) = f(\chi_{e_1})f(\chi_{e_2})f(\chi_h)g(\varsigma_{e_1})g(\varsigma_{e_2})g(\varsigma_h) \times \exp \left[-\left(\beta_1 \sqrt{R^2 \chi_1^2 + L^2 \varsigma_1} \right) - \left(\beta_2 \sqrt{R^2 \chi_2^2 + L^2 \varsigma_2} \right) - \left(\beta_3 \sqrt{R^2 \chi_3^2 + L^2 \varsigma_3^2} \right) \right] \quad (10)$$

The ground state energy of the charged exciton system is given by:

$$\langle E_{trion}(\beta_1, \beta_2, \beta_3) \rangle = \frac{\langle \Psi_{trion} | H | \Psi_{trion} \rangle}{\langle \Psi_{trion} | \Psi_{trion} \rangle} \quad (11)$$

Following some tedious algebra to minimize the above equation with respect to the variational parameters β_1, β_2 and β_3 , we obtained the ground state energy of the negative trion. The variational method is used to calculate the ground state of the negative and positive trions.

The integral form of the nominator in the R.H.S of equation (11) is:

$$\langle \Psi_{trion} | H | \Psi_{trion} \rangle = \int_{-\infty}^{\infty} \int_{-\infty}^{\infty} \int_{-\infty}^{\infty} \int_0^{\infty} \int_0^{\infty} \int_0^{\infty} \int_0^{\infty} \Psi^* H \Psi r_{e_1} dr_{e_1} r_{e_2} dr_{e_2} r_h dr_h dz_{e_1} dz_{e_2} dz_h \quad (12)$$

Considering the following mathematical formula which is proven in Appendix:

$$-\int_0^{\infty} \Psi^* \left\{ \frac{d^2}{dr^2} + \frac{1}{r} \frac{d}{dr} \right\} \Psi r dr = \int_0^{\infty} \left(\frac{d\Psi}{dr} \right)^2 r dr \quad (13)$$

The equation (12) is presented in terms of χ 's, and ζ 's as:

$$\begin{aligned} & \langle \Psi_{trion} | H | \Psi_{trion} \rangle = \\ & = \int_{-1}^1 \int_{-1}^1 \int_{-1}^1 \int_0^1 \int_0^1 \int_0^1 f^2(\chi_{e_1}) f^2(\chi_{e_2}) f^2(\chi_h) g^2(\zeta_{e_1}) g^2(\zeta_{e_2}) g^2(\zeta_h) [\varphi(\chi_{e_1}, \chi_{e_2}, \chi_h, \zeta_{e_1}, \zeta_{e_2}, \zeta_h)]^2 \\ & \times \left\{ \frac{\hbar^2}{2m_e^* R^2} \left[\left(\frac{f'(\chi_{e_1})}{f(\chi_{e_1})} \right) + \frac{\beta_1 R^2 \chi_1}{\sqrt{R^2 \chi_1^2 + L^2 \zeta_1^2}} - \frac{\beta_3 R^2 \chi_3}{\sqrt{R^2 \chi_3^2 + L^2 \zeta_3^2}} \right]^2 \right. \\ & + \frac{\hbar^2}{2m_e^* R^2} \left[\left(\frac{f'(\chi_{e_2})}{f(\chi_{e_2})} \right) - \frac{\beta_2 R^2 \chi_2}{\sqrt{R^2 \chi_2^2 + L^2 \zeta_2^2}} + \frac{\beta_3 R^2 \chi_3}{\sqrt{R^2 \chi_3^2 + L^2 \zeta_3^2}} \right]^2 \\ & + \frac{\hbar^2}{2m_h^* R^2} \left[\left(\frac{f'(\chi_h)}{f(\chi_h)} \right) - \frac{\beta_1 R^2 \chi_1}{\sqrt{R^2 \chi_1^2 + L^2 \zeta_1^2}} + \frac{\beta_2 R^2 \chi_2}{\sqrt{R^2 \chi_2^2 + L^2 \zeta_2^2}} \right]^2 \\ & + \frac{\hbar^2}{2m_e^* L^2} \left[\left(\frac{g'(\zeta_{e_1})}{g(\zeta_{e_1})} \right) + \frac{\beta_1 L^2 \zeta_1}{\sqrt{R^2 \chi_1^2 + L^2 \zeta_1^2}} - \frac{\beta_3 L^2 \zeta_3}{\sqrt{R^2 \chi_3^2 + L^2 \zeta_3^2}} \right]^2 \\ & + \frac{\hbar^2}{2m_e^* L^2} \left[\left(\frac{g'(\zeta_{e_2})}{g(\zeta_{e_2})} \right) - \frac{\beta_2 L^2 \zeta_2}{\sqrt{R^2 \chi_2^2 + L^2 \zeta_2^2}} + \frac{\beta_3 L^2 \zeta_3}{\sqrt{R^2 \chi_3^2 + L^2 \zeta_3^2}} \right]^2 \\ & + \frac{\hbar^2}{2m_h^* L^2} \left[\left(\frac{g'(\zeta_h)}{g(\zeta_h)} \right) - \frac{\beta_1 L^2 \zeta_1}{\sqrt{R^2 \chi_1^2 + L^2 \zeta_1^2}} + \frac{\beta_2 L^2 \zeta_2}{\sqrt{R^2 \chi_2^2 + L^2 \zeta_2^2}} \right]^2 \\ & + V_{e_1}(\chi_{e_1}, \zeta_{e_1}) + V_{e_2}(\chi_{e_2}, \zeta_{e_2}) + V_h(\chi_h, \zeta_h) \\ & \left. + \frac{e^2}{4\pi\epsilon\epsilon_0} \left[\frac{1}{\sqrt{R^2 \chi_3^2 + L^2 \zeta_3^2}} - \frac{1}{\sqrt{R^2 \chi_1^2 + L^2 \zeta_1^2}} - \frac{1}{\sqrt{R^2 \chi_2^2 + L^2 \zeta_2^2}} \right] \right\} \\ & \times R^6 L^2 \chi_{e_1} d\chi_{e_1} \chi_{e_2} d\chi_{e_2} \chi_h dx_h d\zeta_{e_1} d\zeta_{e_2} d\zeta_h y_h \end{aligned} \quad (14)$$

The denominator in the R.H.S (normalization term) of equation (11) is:

$$\begin{aligned} \langle \Psi_{trion} | \Psi_{trion} \rangle = & \int_{-1}^1 \int_{-1}^1 \int_{-1}^1 \int_0^1 \int_0^1 \int_0^1 \left(f^2(\chi_{e_1}) f^2(\chi_{e_2}) f^2(\chi_h) g^2(\varsigma_{e_1}) g^2(\varsigma_{e_2}) g^2(\varsigma_h) \right) \\ & \times [\varphi(\chi_{e_1}, \chi_{e_2}, \chi_h, \varsigma_{e_1}, \varsigma_{e_2}, \varsigma_h)]^2 \times R^6 L^2 \chi_{e_1} d\chi_{e_1} \chi_{e_2} d\chi_{e_2} \chi_h d\chi_h d\varsigma_{e_1} d\varsigma_{e_2} d\varsigma_h \end{aligned} \quad (15)$$

Substituting equations (14) and (15) in equation (11), we get the ground state energy of the trion (E_{trion}).

2.3. Positive trion

The positive trion (X^+) is created when an additional hole is bound to a pre-existing exciton (X), the positive Trion Hamiltonian can be obtained from equations (7) and (8) by interchanging the indices $e_2 \leftrightarrow h$ and ascribing the indices 1 and 2 to the holes.

$$\begin{aligned} H = & \frac{-\hbar^2}{2m_e^*} \left\{ \frac{\partial^2}{\partial r_e^2} + \frac{1}{r_e} \frac{\partial}{\partial r_e} + \frac{\partial^2}{\partial z_e^2} \right\} \\ & \frac{-\hbar^2}{2m_h^*} \left\{ \frac{\partial^2}{\partial r_{h_1}^2} + \frac{1}{r_{h_1}} \frac{\partial}{\partial r_{h_1}} + \frac{\partial^2}{\partial z_{h_1}^2} \right\} \\ & \frac{-\hbar^2}{2m_h^*} \left\{ \frac{\partial^2}{\partial r_{h_2}^2} + \frac{1}{r_{h_2}} \frac{\partial}{\partial r_{h_2}} + \frac{\partial^2}{\partial z_{h_2}^2} \right\} \\ & + V_e(r_e, z_e) + V_{h_1}(r_{h_1}, z_{h_1}) + V_{h_2}(r_{h_2}, z_{h_2}) \\ & + \frac{e^2}{4\pi\epsilon_0\epsilon} \left[\frac{1}{\sqrt{(r_{h_1} - r_{h_2})^2 + (z_{h_1} - z_{h_2})^2}} - \right. \\ & \left. - \frac{1}{\sqrt{(r_{h_1} - r_e)^2 + (z_{h_1} - z_e)^2}} - \frac{1}{\sqrt{(r_{h_2} - r_e)^2 + (z_{h_2} - z_e)^2}} \right] \end{aligned} \quad (16)$$

By the same mathematical method that was done with the negative trion, we can have the energy of a positive trion (E_{trion}).

The binding energy of the charged exciton (negative or positive trion) is defined as:

$$E_b = E_i + E_{ex} - E_{trion} \quad (17)$$

Where E_i is the ground state energy of the free electron or the free hole [27], E_{ex} is the ground state energy of the exciton in the quantum dot as presented by equation (5), and E_{trion} is the ground state energy of the negative or positive trion calculated from equation (11).

3. Results and discussion

Applying this methodology for the GaAs cylindrical QD, we consider the following values of the confinement potential [13]: $V_o^e=0.57(1.155x+0.37x^2)eV$ for the electron and $V_o^h=0.43(1.155x+0.37x^2)eV$ for the hole. In our calculation, the Al concentration in the barrier material $Al_xGa_{1-x}As$ is taken as x . Furthermore, we used the following material parameters[13]: the relative dielectric constant for GaAs is $\epsilon=12.58$ and the effective masses are $m_e^*=0.067m_o$, $m_h^*=0.34m_o$ for the electron and the isotropic hole mass, respectively, where m_o is the mass of the free electron.

Figure (1) shows the calculated the exciton binding energy for the ground state as a function of the quantum dot radius for three different values of the width $L/2 = 4, 7,$ and 10 nm. The calculated values show the presence of the well-known peaks of the binding energy curves in nanostructures, which depend strongly on the QD radius (R values), but its dependence on the QD width ($L/2$ values) is not strong. These results are in a good consistence with the previous data obtained by Le Goff and Stebe [41].

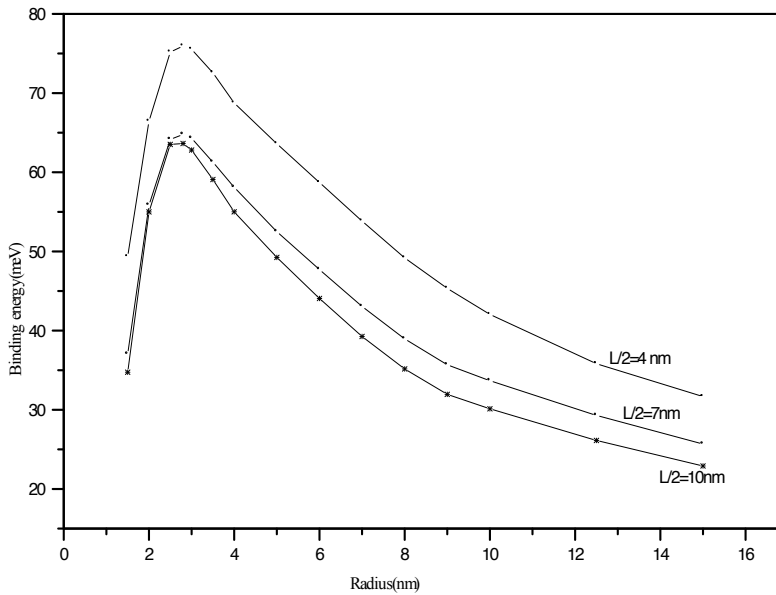


Figure 1. The binding energy of the exciton as a function of R . The Three curves are at different values of QD disc width L (as indicated).

Here, we would like to add that the peak positions of the binding energy as a function of $L/2$ also occur at almost one value of $R = 3$ nm. We notice the sudden decrease of the exciton binding energy with the decrease in radius values. When R increases from 7-10 nm, the binding energy changes almost by 10 meV, and changes almost by half this value if the disc width $L/2$ increases from 7-10 nm.

Figure (2) displays the variation of the exciton binding energy as a function of R, but for two different values of Al concentration ($x=0.15, 0.4$). Here, a right shift of the peak position by almost 1nm and by 20 meV in height is observed when the quantity of Al increases by a ratio of 0.25. The height of the peak translated to higher values by increasing the barrier height (large x), which is due to the more confinement of the particles. Here, the position of the exciton binding energy peaks can be estimated to occur around $L/2 \cong 4\text{nm}$ and $R \cong 3\text{nm}$ or a diameter $\cong 6\text{nm}$ for the quantum dot disc.

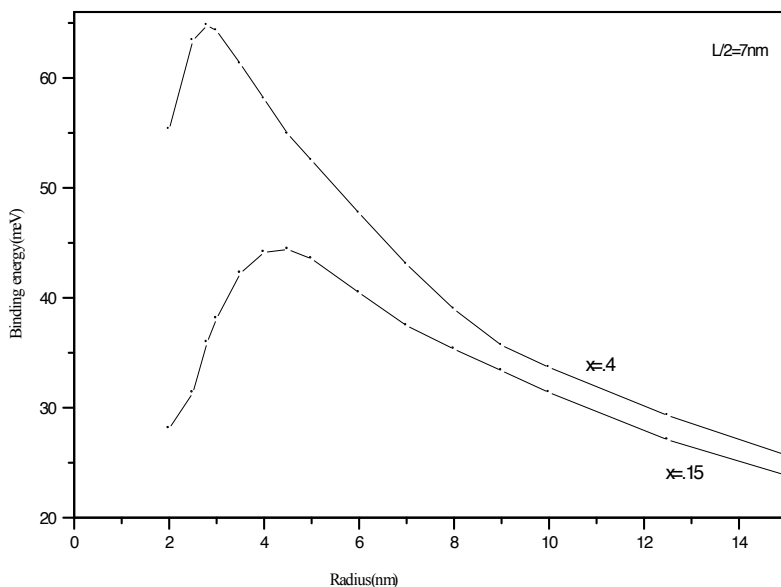


Figure 2. The variation of the exciton binding energy with R, At two different values of Al concentration, $x=0.15$, and 0.4

It has been shown in reference (35) that there is a scaling rule for circular and square quantum wires of the form $L/2R = 0.9136$ such that a square wire of width L is equivalent to a circular wire of diameter $2R$ if the ratio of 0.9136 is achieved. Using this scaling rule, the critical confinement width for a quantum square wire of width $L=5.4\text{nm}$ is equivalent to the present quantum disc with a radius $R \cong 3\text{nm}$. From the behavior of the binding energy positions discussed above, we may conclude that the bulk effect sets in along one spatial axis around $L/2 \cong 4.5$ to 6nm , fairly independently of the confinement conditions. The present results should be useful for designers of nanoscale devices.

Concerning the discussion above about the quantum size effect, we present in figure (3) the exciton binding energy (E_b) and the corresponding exciton energy $\langle H \rangle$ as a function of the disc radius R at two different values of $L/2 = 4, 7$, and 10nm .

In figure (3-a), there is no intersection between the exciton energy and the exciton binding energy ($\langle H \rangle / E_b > 1$) all the time so the exciton stability is small. At the intersection point figures

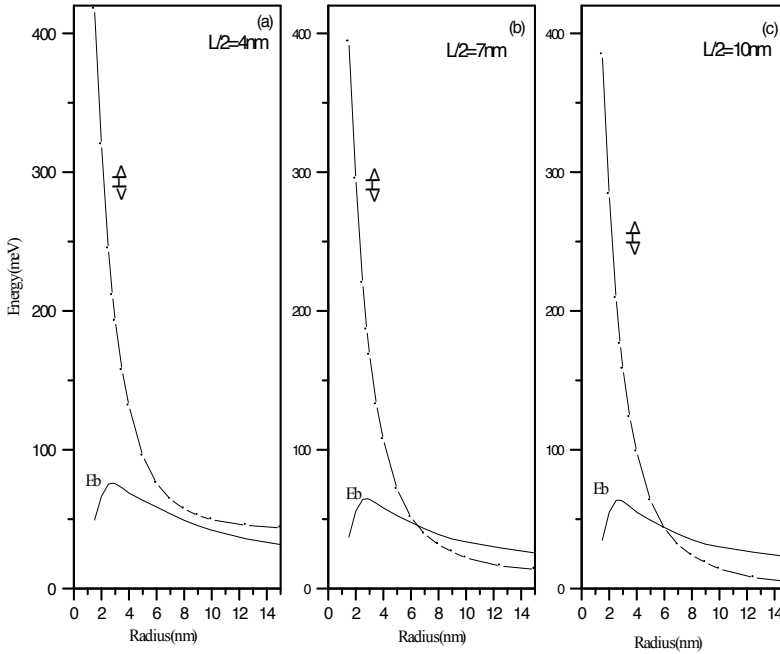


Figure 3. The exciton energy ($\langle H \rangle$) and the exciton binding energy (E_b) versus the radius R . a) at $L=4\text{nm}$, b) at $L=7\text{nm}$, c) $L=10\text{nm}$.

(3-b and 3-c), we have the binding energy equal to the expectation value of the Hamiltonian and equal to half the free particles energy ($E_e + E_h$). Before the intersection point where $\langle H \rangle / E_b > 1$, the exciton state directs to annihilation faster than after the intersection point where $\langle H \rangle / E_b < 1$. The crossover of the binding energy curve with the Hamiltonian curve confirms our above discussion. In order to obtain a large exciton binding energy, we should choose quantum dots with radius from 3nm to 10nm. However, if the radii of quantum dots are beyond the nanostructure scale, the principle of quantum theory is unavailable and the electronic properties of dots belong to the region of bulk materials.

One of main goals of this chapter is to estimate the best theoretical model with an available data to fit, and to clarify the paradoxes about the trion binding energy, which are discussed in previous researches. Since the available existing experimental data are given in the work of Backer et al. [42], to match our parameters with theirs we therefore used the anisotropic hole effective mass (hole effective mass in the z -direction (m_{hz}^*) is different from its value in the in-plane direction (m_{hxy}^*), such as: $m_{hz}^* = 0.377m_0$ and $m_{hxy}^* = 0.112m_0$). The results of the charged exciton binding energies as a function of the half-height ($L/2$) of the QD are shown in Figure (4) and are evaluated at $x = 0.3$ with a QD radius (R) equal to 15 nm. The curves with solid squares and solid circles correspond to our theoretical calculations of the negatively charged exciton binding energy (E_b^-) and positively charged exciton (E_b^+), respectively, whereas, the opened square points and opened circle points indicate the experimental values of the binding

energies [42] of the negative and positive trion, respectively. For each curve, we see that the binding energy increases as the dot half height decreases, which leads to the trions being more stable at small QD (strong confinement regime). When the half-height becomes greater than the effective electron Bohr radius for Ga As ($a_b=9.933$ nm), the binding energy of X^- decreases rapidly and reaches values less than the binding energy of X^+ . At a small QD size, the gain of the binding energy as a function of the size of QD comes from the Coulomb interaction related to the distances of the interparticles where the Coulomb interaction between the electrons (V_{ee}) in X^- is larger than the Coulomb interaction between the holes (V_{hh}) in X^+ , and the Coulomb interaction at this size is more effective than the massive localization of the system, so $E_b^- > E_b^+$. Our theoretical values for both trions are shifted approximately by 0.3 meV (7%) from the experimental value.

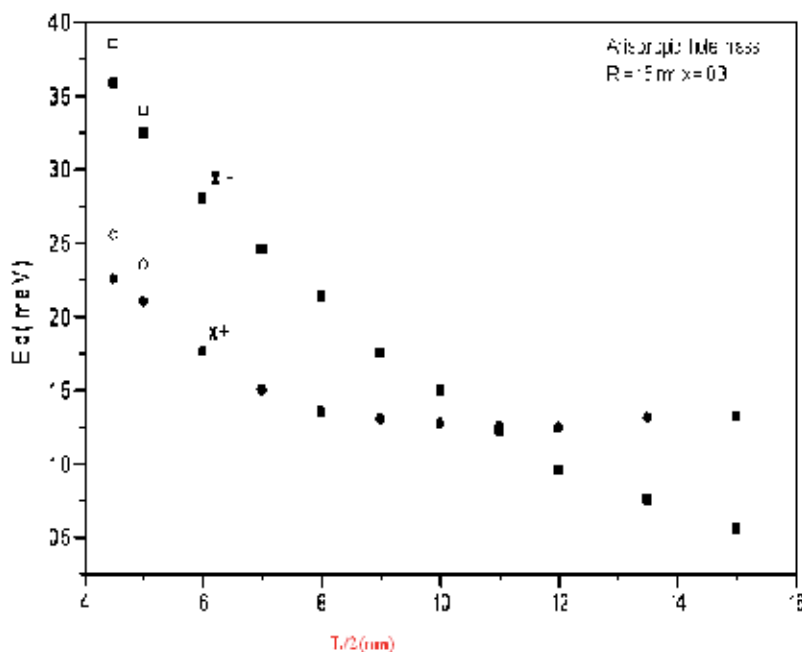


Figure 4. Trion binding energy (E_b) as a function of QD half-height ($L/2$) at radius $R=15$ nm, for an anisotropic effective hole mass. The closed circles and closed squares represent the theoretical results of (E_b^+) and (E_b^-), respectively. The experimental data for (E_b^+) and (E_b^-) are indicated by open circles and open squares, respectively.

In table (1), we summarize our theoretical results, compared with the experimental data and other theoretical data calculated by using the Path Integral Monte Carlo method (PIMC) (Ref (42)). Table (1-a) and Table (1-b) show the negative and the positive trion data, respectively.

We refer the acceptable agreement between our theoretical and the experimental data to the following two issues. The first issue is that we considered a theoretical model that solved a full

L/2 (nm)	Ours $E_b(x)$ meV	Exp. (meV) Ref [42]	Value(%) shift from Exp.	PIMC (meV) Ref [42]	Value(%) shift from Exp.
4.5	3.6	3.9	7.69%	2.9	25.6%
5	3.25	3.4	4.41%	2.5	26.47%
(a)					
L/2 (nm)	Ours $E_b(X)$ meV	Exp. (meV) Ref [42]	Value (%) shift from Exp.	PIMC (meV) Ref [42]	Value(%) shift from exp.
4.5	2.27	2.6	12.69%	2.25	13.46%
5	2.22	2.4	7.5%	2.0	8.33%
(b)					

Table 1. (a): The negative trion results; (b): The positive trion results.

3-D confinement of the trions inside the QD; the second issue is the choice of the trial wave function, which describes correctly the internal motion of the trion. Let us discuss the binding energy of the charged excitons confined inside a cylindrical QD, with an isotropic hole effective mass ($m_h^* = 0.34 m_0$).

We have calculated the negatively charged exciton binding energy (E_b^- , solid squares) and the positively charged exciton binding energy (E_b^+ , solid circles) as a function of the QD half-height. The results are shown in figure (5) and are calculated at $x = 0.3$ and $R=15\text{nm}$. Also, we obtained a more stable negative trion system than the positive trion system at small QD. Besides, E_b^- crosses down E_b^+ at a larger value of the QD half-height ($L/2=15\text{nm}$) than in the case of an anisotropic hole effective mass ($L/2=11\text{nm}$).

Now, we come to the second goal of our work on trions, which concerns the paradoxes existing in most of the previous papers. In Refs (42, 43, and 44), the authors obtained a higher binding energy of the negative trion than the positive one over all of the QD dimensions they examined. On other hand, the demonstrated data in Refs (18 and 38) showed that the binding energy of the negative trion is less than the binding energy of the positive trion. In Ref (18), the author introduced the correlated hyperspherical harmonics as basic functions to solve the hyper angular equation for negative and positive trions in a harmonic quantum dot. He introduced, as an approximation of the center of mass coordinates, to reduce the variables and consequently simplified the calculations. In Ref (38), the authors formulated the Hartree-Fock approximation using a calculation method, which is based on the quantum adiabatic theorem, to study the stability of the charged excitons in QD. Again, we see that the standard tools of the condensed-matter physics, like the many body techniques relying on the Hartree-Fock approximation, are often not sufficient since the exchange and correlation energies can not be negligible [45]. The full three dimensional calculation is introduced by Szafran et al. [23] for a trion confined in a spherical quantum dot, and the authors found that the binding energy of the negative trion is less than the binding energy of the positive trion at a large radius and vice versa at a small radius. Generally, this agrees with our view. The results shown in figure

(5) coincide with the results given in Refs. 42, 44, and 45. Here, $E_b^- > E_b^+$ as long as the QD size is small. Also, our results are qualitatively similar to those obtained by the authors in Refs. 18 and 38 in the case of a large QD size where they showed that $E_b^+ > E_b^-$ as given in figure (6).

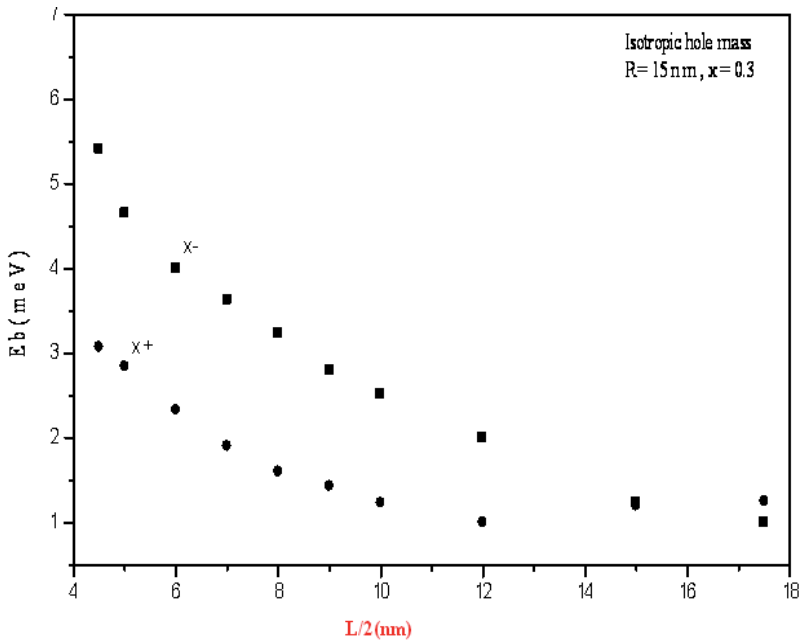


Figure 5. The variation of trion binding energy (E_b) calculated as a function of QD half-height ($L/2$) at a radius of $R=15$ nm, for an isotropic hole mass. The closed circles correspond to E_b^+ of positive trion and the closed squares correspond to E_b^- of negative trion.

The possibility to observe negative or positive trions depends on its stability against dissociation into an exciton and free electron or hole. The corresponding sufficient stability condition for the charged excitons is [38] $E_b^\pm \geq 0$. Concerning the stability of X^- and X^+ in the case of isotropic and anisotropic hole effective mass, from figures (4) and (5), we observe that the positive and negative trions are stable, while from figure (6), X^- is unstable in a large QD ($L > 2a_b$) and X^+ is stable even near the bulk limit.

In order to get a physical insight into the stability of X^+ at large QD size, this can be attributed to its heavy mass. This heavy mass system becomes more localized and stable even inside large QDs. As a result, the positive trions binding energy behavior allowed most of experimentalists to detect X^+ near room temperature in such large dimensional structures.

At last, a comparison between the ground state energy and the binding energy of the positive and negative trions and the excitons is shown in figure (7). In figure (7- a), the ground state energies of the trions X^- , X^+ , and exciton (X) are plotted as a function of the QD half-height ($L/2$) for the isotropic hole mass. Similarly, the binding energies are shown in figure (7-b). From

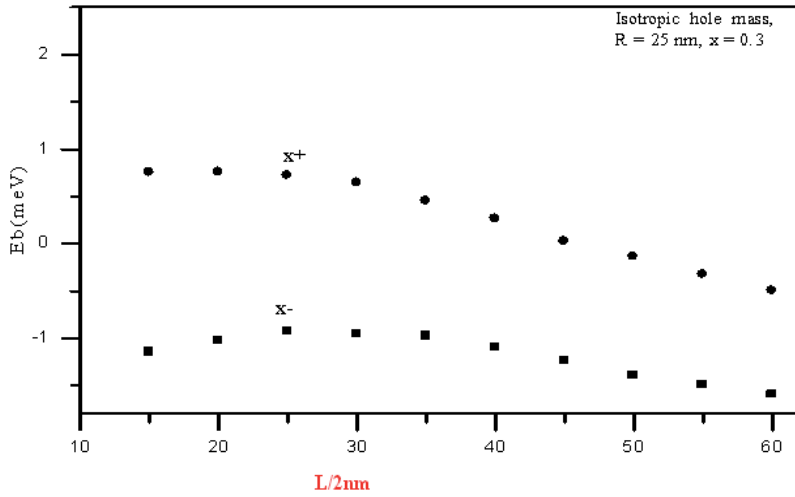


Figure 6. The trion binding energy as a function of $L/2$ at $R=25$ nm for an isotropic effective hole mass. Closed circles correspond to the positive trion and closed squares correspond to the negative trion.

this figure, one can see that the neutral exciton has the lowest ground state energy (E^X) compared to that of the trions (X^- , X^+)(figure7-a).

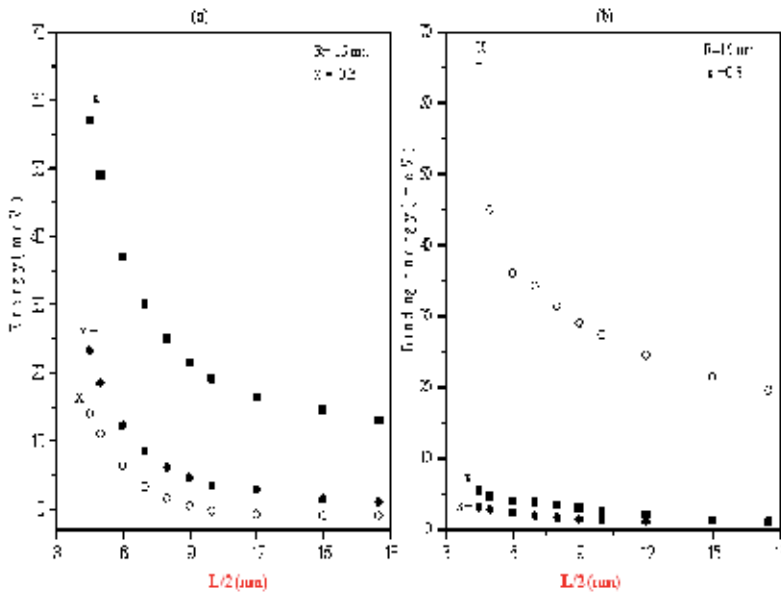


Figure 7. a) Exciton (X) and charged excitons (X^- and X^+) ground state energies as a function of QD half-height L , at radius $R=15$ nm. b) The binding energies of exciton and charged excitons as a function of QD half-height $L/2$.

Also, we notice that it decreases monotonically and not rapidly like the trions ground state energies. In other words, within the examined range of the QD height, we obtained a drop in E^X by 14 meV, while E^{X^+} decreased by 22meV and E^{X^-} decreased by 44meV. By looking at figure (7-b), one can see that the exciton is the most stable system. For small QDs, this stability (or the largest binding energy) of X may be referred as the strong confinement regime of the QD where the exciton is severely restricted in all spatial directions and the quantum confinement are at a maximum for this system. Defining the neutral exciton binding energy (E_b^X) in the same manner as in equation (6) $\{E_b^X = E_e + E_h - E^X\}$, we find that E^X is the lowest but not comparable to the single particles ground state energy. However, for positive and negative trions, their ground state energies compete with the single particle, where E^{X^-} is larger and comparable with E_e , but E^{X^+} competes with E_h , therefore their binding energy is low compared to the neutral exciton. Within the examined QD size, we obtained a drop by 45, 4 and 2 meV in the binding energy of X , X^- , and X^+ , respectively. The decrease of the exciton binding energy seems dramatic, but compared with the trions it is not. The binding energy of the negative trion drops by 80% when the QD half-height changes from 4.5nm to 18nm, while $E_b^{X^-}$ and $E_b^{X^+}$ within the same size range decrease by 70% and 55%, respectively.

4. Conclusion

We have introduced a trial wave function for the positive and negative trions confined in a cylindrical QD. Using the given wave, we obtained a higher binding energy of negative trions than the positive trions inside the QD with a half-height less than the effective Bohr radius and we referred that to the high Coulomb interaction energy between the two electrons compared to the weak Coulomb interaction between two holes at such small QDs. When the half-height of the QD increased to values higher than the Bohr radius, the negative trion binding energy rapidly decreases than the binding energy of the positive trion. An anisotropic hole effective mass state is demonstrated to compare our model with the experimental results. We obtained a good agreement with the experimental results up to 0.3 meV (7%). To improve the stability of the trions (X^- , X^+), in such structures, it is necessary to operate with a special QD size, which permits an enhancement of the binding energy.

5. Appendix

We want to prove the formula that given in equation (13)

$$\langle \psi^* | - \left(\frac{d^2}{dr^2} + \frac{1}{r} \frac{d}{dr} \right) | \psi \rangle = \int_0^\infty \left(\frac{d\psi}{dr} \right)^2 r dr \quad (18)$$

Proof

$$\therefore \langle \psi^* | - \left(\frac{d^2}{dr^2} + \frac{1}{r} \frac{d}{dr} \right) | \psi \rangle = - \int_0^\infty \Psi^* \left\{ \frac{d^2}{dr^2} + \frac{1}{r} \frac{d}{dr} \right\} \psi r dr \quad (19)$$

Let

$$I = - \int_0^\infty \Psi^* \left\{ \frac{d^2}{dr^2} + \frac{1}{r} \frac{d}{dr} \right\} \psi r dr = - \int_0^\infty \Psi^* \frac{1}{r} \frac{d}{dr} \left(r \frac{d}{dr} \right) \psi r dr \quad (20)$$

where ψ is a real eigenfunction.

From equation (3)

$$I = - \int_0^\infty \Psi^* \frac{d}{dr} \left(r \frac{d}{dr} \right) \psi dr \quad (21)$$

But from the integration methods we can use the fact that

$$\int u dv = uv - \int v du \quad (22)$$

Let

$$u = \Psi^* \Rightarrow du = \frac{d\Psi^*}{dr} dr \text{ and } dv = \frac{d}{dr} \left(r \frac{d\psi}{dr} \right) \Rightarrow v = \left(r \frac{d\psi}{dr} \right) \quad (23)$$

By using equation 5 and 6 and substituting in equation 4

$$\therefore I = - \left[\psi^* r \frac{d\psi}{dr} \right]_0^\infty + \int_0^\infty r \frac{d\Psi^*}{dr} \frac{d\psi^*}{dr} dr \quad (24)$$

But $\left[\psi^* r \frac{d\psi}{dr} \right]_0^\infty = 0$ because $\psi(\infty) = 0$ (real eigenfunction condition)

$$\therefore \psi \text{ is a real function } \Rightarrow \psi^* \psi = \psi^2, \frac{d\Psi^*}{dr} \frac{d\psi^*}{dr} \Rightarrow \left(\frac{d\Psi}{dr} \right)^2.$$

This means we can rewrite equation (7) as

$$I = \int_0^{\infty} r \frac{d\Psi}{dr} \frac{d\Psi^*}{dr} dr = \int_0^{\infty} \left(\frac{d\Psi}{dr} \right)^2 r dr \quad (25)$$

From equation 2, 3, and 8, relation 1 is proven.

Author details

S. A. Safwan* and N. El-Meshed

*Address all correspondence to: safwan_s_2000@yahoo.com

The Theoretical Physics Department, National Research Center, Cairo, Egypt

References

- [1] Jacques I. Pankove, *Optical Processes in Semiconductors*, Prentice-Hall, Inc. (1971).
- [2] L.V.Keldy, P.N.Lebedev, *Contemp.Phys.*27,395(1986).
- [3] M.A. Lampert, *Phys. Rev.Lett.*1, 450(1958).
- [4] G. Finkelstein, V.Umansky, and I. Bar-Joseph, *Phys. Rev. B*58, 12637(1998).
- [5] Peter Ramvall, Satoru Tanaka, Philippe Riblet, and Yoshinobu Aoyagi., *Appl.Phys.Lett.* 73,1104(1998).
- [6] L. Esaki, in *physics and Application of Quantum wells and superlattice*, vol 170, of NATO Advanced study institute, series B: physics, edited by E.E, Mendez and K.von klitzing (plenum, new York, 1987).
- [7] K. Kheng, R.T. Cox, Merle Y. d'Aubigne, Franck Bassani, K. Saminadayar and Tatar-enko, *Phys.Rev.Lett.* 71, 1752(1993).
- [8] G. Finkelstein, H. Shtrikman, and I. Bar-Joseph, *Phys. Rev. Lett.*74, 976(1995).
- [9] A. J.Shields M. Pepper, D. A. Ritchie, M. Y. Simmons and G. A. C. Jones, *Phys. Rev. B*51,18049(1995).
- [10] D. Sanvitto, F. Pulizzi, A.J. Shields, P.C. Christianen, S. N. Holmes, M.Y. Simmons, D. A. Ritchie, J. C. Maan, and M. Pepper, *Science* 294, 837(2001).

- [11] G.Eyton, Y. Yayon, M. Rappaport, H. Shtrikman, and I. Bar-Joseph., Phys. Rev. Lett. 81,1666(1998).
- [12] Y. Yayon, M. Rappaport, V. Umansky and I. Bar-Joseph, Phys. Rev. B64, 81308(2001).
- [13] C. F. Lo and R. Sollie, Solid state commun 79,775 (1991)
- [14] S. I. Pokutnil, Fiz Tekh Poluprovodn,Sov.phys. Semicond 25, 381 (1991)
- [15] G. T.Einevoll, Phys. Rev. B45, 3410 (1992).
- [16] M.A. Olshavsky, A. N. Goldstein, and A. P. Alivisatos, J. Am. Chem.Soc.112, 9438 (1990).
- [17] W. Xie, and C. Chen, Physica E 8, 77 (2000).
- [18] W.F. Xie, Phys.Stat.Sol. B226, 247(2001)
- [19] B.Stebe, A.Moradi, and F. Dujardin, Phys. Rev. B61, 7231(2000).
- [20] C.Riva F. M. Peeters, and K. Varga, Phys. Rev. B61, 13873(2000).
- [21] I. Szlufarska, A. Wojs, and J. J. Quinn, Phys. Rev. B63, 085305 (2001).
- [22] W.Y.Ruan, K. S. Chan, and, E. Y. B. Pun, J. Phys.: Condens. Matter 12, 7905(2000).
- [23] B.Szafran, B. Stebe, J. Adamowski, and S. Bednarek, J. Phys.: Condens. Matter 12, 2453 (2000).
- [24] L. C. O. Dacal and J. A.Brum, Phys. Rev. B65,115324 (2002).
- [25] I. M. Kupchak,Yu. V. Kryuchenko, and D. V. Korbutyak, Semiconductor Physics, Quantum Electronics & Optoelectronics, V.9, N1, P 1-8 (2006).
- [26] J.L.Marn, R.Riera, and S.A.Cruz, J. Phys: condens. Matter 10,1349(1998).
- [27] Shudong Wu and Liwan, J. Appl. Phys.111,063711(2012).
- [28] H.Hassanabadi and A.A.Rajabi, Phys. Lett. A373,679,(2009).
- [29] L.C.Lew Yan Voon and M. Willatzen, J. Phys: Condens. Matter 14,13667(2002).
- [30] S.Gaan, Guowei, and R. Feenstra, J. Appl. Phys 108,114315 (2010).
- [31] G. W. Bryant, Phys. Rev. Lett.59, 1140 (1987).
- [32] G. W. Bryant, Phys. Rev. B37, 8763 (1988)
- [33] Y.Kayanuma, Phys. Rev. B44, 13085 (1991).
- [34] V.A. Holovatsky, M.J. Mikhalyova, and M.M. Tkach. J. Phys.: Condens. Matter 3,863(2000).
- [35] J. Marin, L. Riera, and S. A. Cruz, J. phys. Condens matter 10, 1349 (1998).
- [36] Tong San Koh,Yuan Ping, and H.N.Spector, J. Phys.: Condens. Matter 13,1485(2001).

- [37] M.H. Hekmat, Nagwa A. Elmeshad, and S. A. Safwan, *Fizika A* 13, 1(2004).
- [38] S. Baskoutas and A.F. Terzis, *Micro. Eng.* 81, 61(2005).
- [39] A. A. Guzelian, U. Banin, A. V. Kadavanich, X. Peng, and A. P. Alivisatos, *Appl. Phys. Lett.* 69, 1432(1996).
- [40] W. F. Xie and C. Y. Chen, *Solid State Commun.* 107, 439(1998).
- [41] S. Le Goff and B. Stebe, *Phys. Rev.* B47, 1383 (1993).
- [42] A.S.Bracker, E.A. Stinaff, D. Gammon, M. E. Ware, J.G. Tischler, and D. Park, *Phys. Rev.* B72, 035332(2005).
- [43] B.Szafran, B.Stebe, J.Adamowski, and S.Bednarek, *Phys. Rev.* B66, 165331 (2002).
- [44] V.Regelman, D.Gershoni, E.Ehrenfreund, W.V.Schoenfeld, and P.M.Petroff, *Physica*, E13, 114(2002).
- [45] D. Pfannkuche, V.Gudmundsson and P.A.Maksym, *Phys. Rev.* B47, 2244(1993).

On the 'Three-Orders Time-Limit' for Phase Decoherence in Quantum Dots

Witold Aleksander Jacak

Additional information is available at the end of the chapter

<http://dx.doi.org/10.5772/60685>

Abstract

The recent huge increase of the interest in the implementation of quantum information processing (QIP) focused an attention on the semiconductor quantum dots (QDs) as nano-systems with controllable quantum states both in charge and spin degrees of freedom. This creates an opportunity for discussing and modeling of QD-based qubits and quantum-logic gates for prospective quantum computer. Despite of many efforts in this respect the progress is, however, disappointing and the barrier of so-called diVincenzo criteria required to be fulfilled for the QIP technology is not broken and even not approached in any realistic proposal of using QDs for qubits and quantum gates. The reason of this situation is linked with unavoidable restrictions imposed on the coherence and the coherent control of quantum states in QDs, which precludes scalable implementation of qubits and quantum gates based on QDs. The decoherence of charge and of spin degrees of freedom in QDs and QD-systems locates inconveniently straight in the middle of the required six-orders of magnitude diVincenzo window for time scale of the control in comparison to the decoherence rate. This leads to the so-called 'three-orders time-limit' for QIP implementations in QDs. Some advantages of spin degrees of freedom in QDs can be noticed, however. Even though the time scale of the decoherence of spin in of particular practical importance magnetic QDs still is located in the center of six-orders diVincenzo window, the amplitude of the phase decoherence of spin might be frozen on a small level in proximity of the zero temperature. Short critical overview of the dephasing restrictions imposed on the QD technology is the aim of this chapter.

Keywords: quantum dots, quantum information processing (QIP), dephasing

1. Introduction

The notion of a quantum dot [1–3] comprises various nanometre-size semiconductor structures, manufactured by means of different technologies and resulting in spacial

limitations on the carrier dynamics (electrons and holes), as well as excitations of electron-hole pairs (excitons). The Coulomb energy scales with the QD size d as $1/d$ (and is of the order of meV for QDs), while kinetic energy scales as $1/d^2$, which leads to the shell properties of dots, distinct in comparison to atoms (more complicated Hund-type rules for QDs), since both energies remain within mutual proportions of d , which favours Coulomb energy for dots in contrast to atoms [1] at the scale of meV orders. The nanometre-scale limitations on quantum dynamics result in kinetic energy quantization,

$$\Delta E \geq \frac{(\Delta p)^2}{2m^*} \simeq \frac{\hbar^2}{2m^*d^2} \simeq \begin{cases} 10 \text{ meV}, & d \sim 10 \text{ nm}, \\ 1 \text{ eV}, & d \sim 0.1 \text{ nm}. \end{cases} \quad (1)$$

In the case of QDs, quantization energy locates thus within a range accessible for control by means of external fields (electric and magnetic), in contrast to atoms (for the latter, quantum state control by means of external fields requires such values that are beyond the reach of present technologies). This advantage of QDs—which are relatively easy to create due to a variety of existing technologies in addition to their parameters' flexibility and the possibility of immersing them in various media or even creating or modifying them by means of external fields—makes them very promising objects of new nanotechnologies and spintronic practical projects.

Various semiconductor materials may be used to create QDs. Note that insulator or metallic nanoparticles are also manufactured (however, collective electron liquids in metallic nanoparticles manifest distinct physical properties in comparison with semiconductor QDs, which explains why metallic nanostructures are not called QDs). For opto-electronic use, semiconductor dots seem best-suited due to their localization within other nanostructures (e.g., in quantum wells), with well-established technologies for control over such systems. Semiconductor QDs may be manufactured by means of etching technologies after a high-resolution photolithographic process (with the use of an ion or electron beam) has been applied (ordinary optic lithography with a resolution of up to 200-300 nm is not sufficient). Other technologies used here include among others the Stransky-Krastanov dot self-assembling method consisting in the application of epitaxy layers by MBE or MOCVD [MBE, *Molecular Beam Epitaxy*; MOCVD, *Metal Organic Chemical Vapour Deposition*]. Various lattice constants in successive epitaxy layers result in the spontaneous creation of nanocrystals on the ultra-thin so-called 'wetting layer'. Electrical focusing in a quantum well [1, 4, 5] consists of yet another promising technique which, despite being at an early stage (due to a lack of sufficiently precise electrodes), offers the highest dot parameter flexibility and allows for dots to switch on/off within the working time periods of devices based on them [1, 4–6].

The possibility of control over the quantum states of carriers in QDs and their coherent (deterministic, controllable) time evolution are vital for nanotechnological and spintronic applications (especially where this concerns so-called 'single-electron' or 'single-photon' devices) as well as for the quantum processing of information. The absence of decoherence or its significant reduction up to the lowest possible level, at least within the time periods of control realization, is essential for all these applications. However, decoherence is unavoidable due to irreducible dot-environment interactions (there is no means of a dot's total isolation). In the case of nanostructures, QDs offer a new class of physical phenomena

within the decoherence and relaxation range, entirely distinct from analogous processes in bulk materials or in atomic physics. This is due to the characteristic nanoscale-confinement energy, reaching values close to the typical energy parameters of crystal collective excitations (the energy characteristics of band acoustics and optical phonons). This convergence of energy scales results in resonance effects, which is different from what is observed in atomic physics where the scale of the atom-confinement energy is three orders of magnitude higher than the energy of crystal collective excitation, resulting in the weak influence of phonons on atomic states (included as a very small perturbation only). Specific decoherence effects in QDs result from a strong (resonance) coupling effect between the carriers trapped in them and the sea of various types of phonons (as well as with other collective excitations, or with local degrees of freedom, e.g., related to admixtures). This is why the frequently-used notion of an 'artificial atom' in reference to QDs is, to some extent, misleading.

The same reasons are responsible for the fact that QD modeling which does not account for environment-induced collective degrees of freedom may give rise to false conclusions since significant hybridization-induced (decoherence) changes of energy levels can reach up to 10%. This reduces the modeling fidelity if the environmental effects are neglected. Therefore, the current physics of nanostructures should embrace the recognition of the complex decoherence and relaxation effects observed in QDs for trapped carriers' spin and charge, which are essentially different from what is observed in bulk materials and atoms.

2. Limitations on the quantum processing of information

Unavoidable decoherence—uncontrolled quantum information leakage into the surrounding environment due to the system's interaction with the environment—perturbs the ideal quantum procedures which ensure the running of quantum schemes [7–12]. If, however, decoherence is kept below a certain threshold, quantum error corrections can be made by applying so-called 'quantum error correction schemes' [13], which enables the realization of any quantum procedures of a quantum computer or any other deterministic quantum project.

In classical information processing, quantum error correction consists in multiplying classical information and verifying by comparison the multiplied (redundant) classical registers with arbitrary frequency, errors which appear from time to time are identified and corrected immediately. In the quantum case, the multiplication of quantum information is impossible (*No-Cloning theorem*) and quantum error correction is based on a different scheme:

- Seeking more decoherence-resistant areas of the Hilbert space (multi-qubit states which, in a pair of qubits, record symmetrically both "true" and "false" are decoherence-resistant, e.g., singlet-type qubit states; information (or quantum states) symmetrization requires, however, the multiplication of quantum registers, which makes decoherence rise exponentially).
- Attempting the replacement of an information carrier for a more decoherence-resistant one (e.g., temporarily, a state can be teleported onto a more resistant carrier).

In order to satisfy quantum error correction requirements, DiVincenzo formulated a set of conditions [7, 14–16] which allow for the possibility of the implementation of quantum

error correction (the typical decoherence time must be at least of six orders longer than the typical times of quantum procedures). None of the currently suggested solutions for quantum computers have satisfied these time restrictions. This situation may follow from the fact that the same interactions which allow for qubit control (logical operations) are also responsible for decoherence. The stronger (energetically) the interaction is, the faster the logical operations can be carried out. However, the same interaction couples the system with the surrounding environment and produces strong decoherence effects. In nanotechnological and optical projects involving quantum computers (multi-qubit), the difference in the time-rate of quantum operations in relation to decoherence still do not exceed three orders of magnitude.

However, it is expected that further intensive research in this area should result in:

- Finding another method of quantum error correction (despite great efforts, there is still no relevant solution).
- Finding a combined solution with qubit conversion (between a fast, controlled carrier and a decoherence-resistant one—unfortunately, qubit conversion is also inconveniently long-lasting).
- Finding global, topological and thus decoherence-resistant carriers of quantum information in them.
 - Braid groups (and non-Abelian anyons)—herein, the durations of logical operations are expected to be of 30 orders of magnitude greater than those of decoherence processes [17] (however, this is still unclear and it is doubtful if it is experimentally viable).
 - It is hoped that superconductive states may satisfy the DiVincenzo conditions as they have non-local properties to a significant extent.

DiVincenzo criteria, which render a scalable quantum computer project feasible

1	a properly defined qubit—two quantum states separated from the remaining states of the system (by relatively wide energy gaps or by forbidden transitions), so that quantum information entered therein does not leak out
2	the possibility of information recording on the defined qubit—i.e., the possibility of generating any superposition of two qubit states by means of external macroscopically controlled fields (e.g., by Rabi’s oscillations within a realistic range of fields)
3	designing and implementing a universal two-qubit operation, which may enable the performance of any logical quantum operation (a CNOT gate, or any other one, may work as such a universal gate provided there exists an effective means of switching qubit interactions on and off, i.e., the entanglement of two qubits can be controlled
4	ensuring that the time-rate of the performance of logical operations must be at least six order faster than the decoherence time-rate
5	ensuring that output information can be read
6	ensuring that the whole system can be reset
DiVincenzo conditions that enable quantum cryptography	
1	defining a free information carrier—a mobile qubit (e.g., a photon)
2	enabling the maintaining of the quantum properties of mobile qubits at a constant level over long distances
3	enabling the identification of a qubit state (measurement)

In the case of quantum cryptography, equipment requirements [18] are more easily met in respect to decoherence and this is why this quantum technology (public key distribution via a quantum channel) has been used in practice in optical systems [fibre-optical ones over distances of 100 km (up to 1000 km), and outdoors over distances of 2 km].

3. Quantum dots—the prospective technology for quantum gates

The idea of employing quantum evolution for information processing corresponds with the feasibility of the deterministic control over a quantum system in order to execute a previously designed quantum algorithm. However, such a deterministic evolution (also called 'unitary' or 'coherent') requires a totally isolated quantum system. Unfortunately, no quantum system can be totally isolated from the environment. Any quantum system is susceptible to the environment's influence. In consequence, unitary or coherent evolution is perturbed, and quantum information undergoes uncontrollable and irreducible leakage into the environment. Therefore, the feasibility of the construction of a scalable quantum computer is seriously hindered due to decoherence phenomena. The better recognition of decoherence processes in quantum systems may, however, enable the development of new technologies transcending these limitations and facilitating the attainability of quantum gates.

Quantum state decoherence progresses along two channels: relaxation, i.e., quantum state annihilation; and dephasing, i.e., phase relations change within a quantum state description. Relaxation (or 'amplitude decoherence') is related to the decrease in time of the diagonal elements of the quantum state density matrix, whereas dephasing (or 'phase decoherence') corresponds to the reduction of the off-diagonal elements of the density matrix. Both types of decoherence are caused by interaction with the environment and they become more significant the stronger the interaction is.

Solid-state technology (which is promising for new practical realizations of the quantum processing of information using nanometre-scale semiconductor QDs) is burdened mostly with phase decoherence processes. Both the charge (i.e., orbital) and the spin degrees of freedom of quantum states in QDs undergo dephasing due to their environment (however, it should be emphasized that the spin degrees of freedom seem to be more decoherence-resistant than orbital degrees of freedom, since they are less susceptible to direct crystal phonon-induced interaction; however, spin requires much longer periods of time-control than orbital degrees of freedom due to weaker interaction with spin).

Below we present a decoherence analysis, in particular the phase decoherence of the charge (orbital) degrees of freedom and degrees of freedom of spin of excitations localized in QDs, dealing with the issues associated with limitations on the feasibility of QIP.

In the case of semiconductor QDs, decoherence is unavoidable due to strong dot-environment interaction (there are no means for the perfect isolation of a dot). In the case of nanostructures—QDs included—there appears to be a new class of physical phenomena related to decoherence and relaxation, distinct from analogous processes in bulk materials and atomic physics. This is due to characteristic meV-scale energy resulting due to nanoscale confinement, reaching values close to the typical energy parameters of band phonons in the surrounding medium. This coincidence of energy scales results in resonance effects, which is different from what is observed in atomic physics. For atoms, the incommensurability of the atom-confinement energy and phonon energy is of three orders of magnitude, resulting

in a weak phonon impact on atomic states. Specific decoherence effects in QDs result from strong and resonant coupling between the carriers trapped in dots and the sea of various types of collective excitations in the surrounding medium, which highly modifies the QD states. Hybridization-induced changes of energy levels reach up to 10%. Therefore, the decoherence and relaxation effects observed in QDs and for trapped carrier spin or charge (which are essentially different from what is observed in bulk materials and atoms), seem to be of central importance for any possible QD applications, including QIP.

4. Phase decoherence of orbital degrees of freedom in nanostructures

Orbital degrees of freedom pertain to charge-type excitations, such as electrons and holes and charge-balanced electron-hole pairs—excitons. As charge carriers, these excitons interact with the electric field of the electromagnetic wave and so they can be controlled by means of quantum optics methods. Charge-type excitations can be localized in nanometre-scale artificial structures manufactured within various semiconductor heterostructures, namely in QDs. Excitons attract special interest as they can be precisely controlled by an electromagnetic wave within the visible (or near infrared) light range corresponding to the typical energy gap separating electron states from hole states in semiconductors (a typical material is GaAs and QDs will be, e.g., self-assembled structures of GaAs/InAs type). By accommodating the energy of (incident light) photons with the energy of the exciton, an exciton state in the Rabi oscillation regime can be created in which the superposition state of the charge qubit spanned on the states $|1\rangle$ (no exciton in a QD) and $|2\rangle$ (one exciton in a QD) can be selected. The techniques of ultra-high-frequency laser impulses (measured in femtoseconds) and the resulting application of a high intensity beam allowing for high-frequency Rabi oscillations [19] has attracted a lot of interest in QIP research. This interest has been centred on the fact that the lifetime of the excitons in the dots is measured in nanoseconds (this may suggest a difference of six orders of magnitude between the control time and the amplitude decoherence time, which is required by DiVincenzo's criteria [7, 13–16, 20]).

Nevertheless, in QDs the interaction between the excitons (electrons and holes) and phonons of the surrounding crystal is unavoidable and must be accounted for in all considerations, thus diametrically changing this ostensibly convenient situation. Phonons are quanta of the crystal oscillations; acoustical phonons refer to the oscillations of the density type (all the atoms in the unit cell oscillate in the same direction) and optical phonons are related with polarization oscillations (the opposite-sign ions in the unit cell oscillate in the opposite directions; polarization oscillations in such ionic crystals can be excited by means of light, and thus they are called 'optical' phonons). Both types of phonons can interact with charge-type degrees of freedom in QDs. Phonons can be of transversal or longitudinal polarization, but these are the longitudinal modes (LO and LA for optical and acoustic phonons, respectively) that contribute most substantially to the interaction with the electrons/excitons [21].

In polar materials (e.g., GaAs, a weakly polar semiconductor), LO phonon interaction prevails. The interaction of charges with LO phonons is characterized by means of the dimensionless Fröhlich constant [21, 22]. The higher the constant value, the stronger that the interaction is between the charges and the LO phonons, and for the semiconductor GaAs three-dimensional (*bulk*) the constant averages out at around 0.06. For QD GaAs/InAs,

experiments (infrared absorption in a magnetic field and the broadening of the satellite luminescence peak connected to LO phonons, expressed quantitatively via the so-called 'Huang-Rhys factor' [23]) show a double value of the constant, which suggests a substantial increase of the interaction with LO phonons. This phenomenon has been explained [24] with regard to a certain ambiguity [21] in the definition of LO phonon-electron interactions in crystals. The interaction between an LO phonon and an electron leads to the polarization of the crystal lattice by the moving electron. This polarization (i.e., an appropriate packet of optical phonons) is dynamic and leads to a reverse interaction with the polarization-inducing electron. It can be thought of as being composed of two components: an inertial one, which lags behind the moving electron; and a non-inertial one, which accompanies the moving electron. The latter component should be contained in the total crystal field which defines the electron itself (the electron in the crystal is not a free particle and includes, by its definition, the periodic crystal field—thus it can be characterized by the effective mass and quasi-momentum instead of momentum). The necessity of extracting only the inertial part of the polarization from the total interaction of the electron and the LO phonons leads to the above-mentioned ambiguity in the definition of the electron-LO phonon interaction. When the electron is trapped in a QD, it moves with a quasi-classical velocity [25] which exceeds the velocity of a free band electron. Thus, it better escapes from the dynamic polarization, which results in an increase in the inertial part of polarization and the interaction between the electron and LO phonons in QDs. The more localized the electron in a smaller QD, the bigger the quasi-classical velocity of the electron and the bigger the increase in the interaction with LO phonons. The quantitative analysis of the problem agrees well with the experimental data. It should be emphasized, however, that the marked increase in the value of the Fröhlich constant in QDs parallels the increase in the decoherence of electron/exciton states in dots due to the increase in the interaction between the small system of the QD and the sea of LO phonons in the crystal.

The energy scale corresponding to the nanometre localization of electrons (excitons) in QDs ranges from a few to several tens of meV. The same energy scale also characterizes the phonons in crystals, in which the energy of LA phonons ranges from 10 to 20 meV at the edge of the Brillouin zone and the energy of LO phonons at the centre of the Brillouin zone (a gap in the LO phonon spectrum at point Γ [21, 22]) reaches 30 meV. Thus, in the case of QDs we deal with a strong coupling regime for an interaction of QD charge degrees of freedom with phonons (of all types). The same energy scale of both types of excitations—local in QDs and collective in the surrounding crystal—results in the strong mutual hybridization of these excitations or in the dressing of electrons (holes) or excitons with phonons and in the creation of composite particles (quasi-particles)—polarons [21, 22, 26–29].

The creation of polarons in QDs is a strongly decoherent process (much more than it is in bulk materials). The dynamics of this process can be investigated by employing the Green function technique [28]. By means of this technique, the correlation function of the exciton (electron) in the QD can be expressed, which defines the overlap (the scalar product) of the state of the carrier gradually dressed by phonons with the initial state of the bare exciton (or electron) in the dot. Thus, it is possible to quantitatively characterize the leakage of quantum information (fidelity loss) due to the entanglement (in a quantum sense) of the QD's charge with the deformation and polarization degrees of freedom of the whole crystal, which are entirely beyond our control.

The inertia of the crystal lattice is so disadvantageous that it makes it impossible to maintain the coherence of orbital degrees of freedom dynamics (the unitary quantum evolution of the excitations) within the time periods required by the DiVincenzo conditions. The typical times of dressing charge-type excitations with phonons are located within the time-range of single picoseconds, which is the middle of the six-orders time window between the amplitude decoherence time for excitons in QDs and the time-scale of the quickest techniques for their excitation. On both sides of this window, there appear windows of three-orders of magnitude, which precludes the implementation of the quantum error-correction scheme due to the non-fulfilment of the DiVincenzo conditions.

These strongly unfavourable estimations indicate that it may be impossible to scale a quantum computer in a QD technology with only by light control unless more effective quantum error-correction schemes would be proposed [7, 13, 14].

It should be emphasized that LA phonons are of greater importance to the process of dressing the excitons with phonons (polaron decoherence effects), despite the fact that their interaction with excitons is energetically much weaker (at least by one or two orders of magnitude) than in the case of LO phonons. Strong dephasing due to LA phonons corresponds with a wide linear dispersion of acoustic phonons, which in turn leads to a more immediate and significant change in the wave functions of charge-type excitations in QDs than in other phonon modes.

LA phonons-induced decoherence (phase decoherence or dephasing, corresponding to the reduction of the off-diagonal elements of the density matrix [8–12]) is—and as can be shown by means of a microscopic analysis—a relatively fast process and its time-scale is of the order of the ratio of the dot diameter and the sound velocity (it is of the order of picoseconds). Acoustic phonons are especially inconvenient as they are present in any crystal (as well as in any amorphous material), and this is why the above-presented mechanism of decoherence is unavoidable by its nature [strong dephasing also exists at a temperature of 0 K due to phonon emission; at higher temperatures, the dephasing effects are enhanced due to phonon absorption effects, which become more important with the increase in temperature].

Strong decoherence restrictions on the quantum evolution of the charge degrees of freedom in QDs encouraged the researchers to concentrate their attention on the spin degrees of freedom in nanostructures (spin does not interact directly with phonons) instead of pursuing the idea of constructing a quantum computer based on QDs that is only controlled by light [7, 14, 28].

4.1. Phonon-induced dephasing of excitons localized in quantum dots

An exciton created in a QD by means of a non-adiabatic process (in the sub-picosecond order) [4, 5, 30] is a bare particle (an electron-hole pair) which is gradually dressed with phonons until it becomes a polaron. The time within which the polaron is created depends upon the lattice inertia. It is relatively long and its accurate evaluation is an important task. The process of the hybridization of a QD-localized exciton with the collective excitations of the crystal lattice surrounding the QD is, in fact, a time-dependent evolution of a non-stationary state, which at the initial time (the moment of the excitation's creation) is identical with the state of the bare exciton. The bare exciton is not the stationary state of the whole system, the QD exciton and the sea of phonons in the surrounding crystal interacting with it (a polaron represents a stationary state of such a complex system). The

non-stationary initial state (the bare exciton) [the electric field of the e-m wave interacts with the charge and, in consequence, excites a bare electron from the valence band into the QD; the resulting hole is also captured by the QD—a bare QD exciton is thus created] undergoes further non-stationary evolution. In the non-stationary state, the energy is not determined; however, the mean energy is shared over time between the subsystems, the QD and the phonon sea. The mean energy of a bare QD exciton is higher in comparison with the polaron energy (whose energy is lower and therefore the polaron is created by means of interaction with phonons due to energy minimization). The excess energy of the lattice deformation (for acoustical phonons) together with the polarization energy (for optical phonons) is carried outside the QD by the LA and LO phonons, respectively (by their wave packets). A QD polaron is created—a hybridized state of an exciton dressed with an LA and LO phonon cloud [actually, the name of the polaron refers to electrons dressed with LO phonons [22]—a process dominating in strongly polar materials; here, the name refers generally to an electron or exciton dressed with all types of phonons]. The time-scale of QD polaron creation is of the same order as the time that a phonon-wave packet needs to leave the QD area. It should be emphasized that this process is not to be interpreted in terms of Fermi's golden rule [in such an approach, quantum phase transitions resulting from a time-dependent perturbation refer to transitions between stationary states, which is not the case here] [25]. The process of polaron creation is a non-stationary state evolution, in which the elementary processes of phonon absorption or emission contribute in the virtual sense (without energy conservation). Note that the polaron energy is shifted with respect to the bare QD exciton energy by a few meV [28], while the LO phonons energy has a much greater gap, $\hbar\Omega \simeq 36,4\text{meV}$ (in GaAs). The kinetics of polaron creation correspond with the coherent evolution of an entangled state of two interacting systems, namely a QD exciton and the sea of phonons (of various types), and this state is non-separable [28].

The exciton-phonon system is represented by the following Hamiltonian:

$$H = \sum_n E_n a_n^+ a_n + \sum_{\mathbf{q},s} \hbar\omega_s(\mathbf{q}) c_{\mathbf{q},s}^+ c_{\mathbf{q},s} + \frac{1}{\sqrt{N}} \sum_{\mathbf{q},n_1,n_2,s} F_s(n_1, n_2, \mathbf{q}) a_{n_1}^+ a_{n_2} (c_{\mathbf{q},s} + c_{-\mathbf{q},s}^+), \quad (2)$$

where the LO interaction ($s = o$) and the LA interaction ($s = a$) are represented by the following functions:

$$F_o(n_1, n_2, \mathbf{q}) = -\frac{e}{q} \sqrt{\frac{2\pi\hbar\Omega}{v\epsilon}} \int \Phi_{n_1}^*(\mathbf{R}_e, \mathbf{R}_h) \times (e^{i\mathbf{q}\cdot\mathbf{R}_e} - e^{i\mathbf{q}\cdot\mathbf{R}_h}) \Phi_{n_2}(\mathbf{R}_e, \mathbf{R}_h) d^3\mathbf{R}_e d^3\mathbf{R}_h \quad (3)$$

and:

$$F_a(n_1, n_2, \mathbf{q}) = -\sqrt{\frac{\hbar q}{2MC_a}} \int \Phi_{n_1}^*(\mathbf{R}_e, \mathbf{R}_h) \times (\sigma_e e^{i\mathbf{q}\cdot\mathbf{R}_e} - \sigma_h e^{i\mathbf{q}\cdot\mathbf{R}_h}) \Phi_{n_2}(\mathbf{R}_e, \mathbf{R}_h) d^3\mathbf{R}_e d^3\mathbf{R}_h. \quad (4)$$

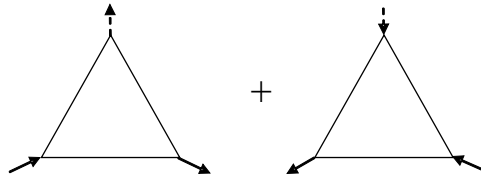


Figure 1. The vertices representing the exciton-phonon interaction; the dotted lines—phonons; the continuous lines—excitons.

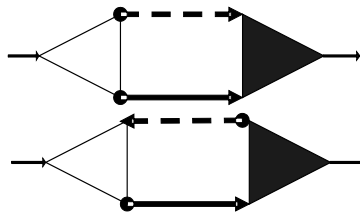


Figure 2. The exciton mass operator (the thick lines represent the full Green functions; the effective vertex of the exciton-phonon interaction is marked [the shaded vertex]).

Here, $c_{\mathbf{q},s}^{(+)}$ denote annihilation (creation) boson operators for LO ($s = o$) and LA ($s = a$) phonons with quasi-momentum \mathbf{q} ; the phonon frequency $\omega_o(\mathbf{q}) \equiv \Omega_{\mathbf{q}} \simeq \Omega - \beta q^2$ (Ω represents an energy gap for LO phonons at Γ point) and $\omega_a(\mathbf{q}) = C_a q$, C_a is the sound velocity (for LA phonons); M represents the mass of ions in the unit cell; $\sigma_{e,h}$ is the deformation potential constant of an electron and hole, respectively; v is the volume of the unit cell; N is the number of cell in the crystal; $\tilde{\epsilon} = (1/\epsilon_\infty - 1/\epsilon_0)^{-1}$ is the effective dielectric constant; $\mathbf{R}_e, \mathbf{R}_h$ represent the coordinates of an electron and hole; $\Phi_n(\mathbf{R}_e, \mathbf{R}_h)$ denotes the QD exciton (electron) wave function and $a_n^{(+)}$ is the exciton or electron annihilation (creation) operator in n -th state (of boson type for excitons and of fermion type for electrons). The interaction between a charge and longitudinal phonon modes is considerably stronger than with transversal modes, which is why only the first ones are further considered [21, 22]. The interaction between an exciton and phonons from both branches (LO and LA) has the simplest linear form with respect to the phonon operators (the third element in the Hamiltonian). It can be represented by means of graphs, as in Fig. 1.

Vertices of this type (as in Fig. 1) result in the mass operators of Green functions, both for the exciton (electron) and the phonon (note that without the linear term with respect to the interaction due to the specific form of the vertices); for the exciton, this is illustrated by the graphs in Fig. 2.

The graphs in Fig. 2 correspond to the complete expressions for the mass operator (thick lines represent the full Green functions; the effective vertex of the exciton-phonon interaction is also marked [the shaded vertex]). It is an accurate form of the mass operator. Within the first approximation, the effective vertex can be replaced with a bare one (it is an approximation with controlled accuracy—the terms of a higher order than the quadratic

with respect to the interaction are omitted [subsequent bare vertices enter the effective vertex]. Given that the charge-phonon interaction is weak, this approximation leads to a small error. The bare vertices of this interaction (the corresponding functions appearing in the Hamiltonian) attain the form (which results from the mechanism of interaction between the charge and LO phonons—by means of polarization, and with LA phonons—by means of deformation) [21, 22] given by the (3, 4) formulae, with the integrals representing the overlap integral of the localized exciton states (initial and final) with the phonon plane wave. These integrals represent the bottleneck effect, typical for QDs [32, 33], resulting from the absence of the translational invariance of a QD system and leading to the non-conservation of the momentum (quasi-momentum). The overlap integral with the plane wave favours the momentum $q \simeq \frac{\hbar}{d}$, where d denotes a QD size. If the exciton is not localized—i.e., is represented by a plane wave—this integral would yield the law of momentum conservation, corresponding to the translational invariance of the system in that case. In the case of a QD-localized exciton, this integral does not become Dirac's delta but rather defines those quasi-momenta \mathbf{q} of phonons which were involved in the interaction. At the same time, the law of conservation of energy holds true for each vertex (i.e., for the interaction process), which results from the unperturbed uniformity of time in the case of QD-localized states. Due to the above functions, the fact of the selection of the fixed values of quasi-momentum for QD-localized exciton (electron) states is called 'the bottle neck effect'. The presence of the above-mentioned integrals results in the elimination of all the phonon modes except for those found within the range of $q \simeq \frac{\hbar}{d}$ (d a QD size, typically of the order of 10 nm); thus, the range of the significant quasi-momentum of a phonon interacting with a QD charge is of the order of 1-10% of the Brillouin zone close to its centre (as illustrated in Fig. 3).

The model (variational) ground state exciton wave function in a parabolic QD assumes the following form (including Coulomb interaction e-h):

$$\Phi_0(\mathbf{r}_e, \mathbf{r}_h) = \frac{1}{(\pi)^{3/2}} \frac{1}{L_e L_h L_z} \exp \left[-\frac{r_{e\perp}^2}{2L_e^2} - \frac{r_{h\perp}^2}{2L_h^2} - \frac{z_e^2 + z_h^2}{L_z^2} \right], \quad (5)$$

where $r_{e,h\perp}$ denotes the positions of the exciton components (e and h) in the xy plane of the QD. The numerically estimated parameters for a QD characterized by the values in Tab. 1 are $L_e = 6.6$ nm, $L_h = 5.1$ nm and $L_z = l_z$ (which agrees sufficiently well with a more accurate numerical calculation and diagonalization [28]). The noticeable difference between the electron and the hole's effective lateral dimensions results from the fact that the e-h Coulomb interaction energy is comparable to the inter-level energy of the heavier holes, while the energy of the lighter electrons is quantized with greater inter-level gaps.

The above form of the ground state QD exciton wave function yields the following phonon coupling functions:

$$\begin{aligned} |F_o(0, 0, \mathbf{k})|^2 &\simeq \frac{\pi e^2 \hbar \Omega k^2}{18 v \epsilon} (L_e^2 - L_h^2)^2 e^{-\alpha k^2} = g_o \frac{k^2}{k_m^2} e^{-\alpha k^2}, \\ |F_a(0, 0, \mathbf{k})|^2 &\simeq \frac{\hbar k}{2 M C_a} (\sigma_e - \sigma_h)^2 e^{-\alpha k^2} = g_a \frac{k}{k_m} e^{-\alpha k^2}, \end{aligned} \quad (6)$$

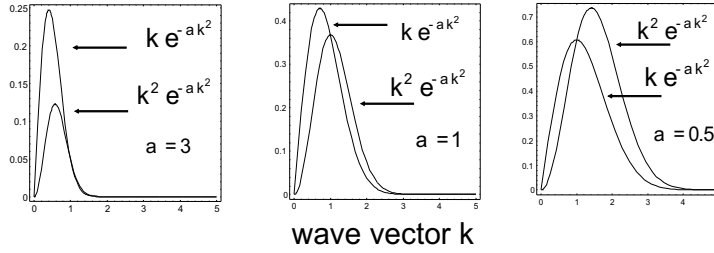


Figure 3. Comparison of the interaction form-factors of the exciton-LO phonon ($\sim k^2 e^{-ak^2}$) and the exciton-LA phonon ($\sim k e^{-ak^2}$) according to the (6) functions for various values of a .

where $k_m = (6\pi^2/v)^{1/3}$ denotes the Debye wave vector ($\simeq 1.1 \cdot 10^{10} \text{m}^{-1}$), $\alpha = l^2/2$, l is the QD size averaged over all directions (this is the averaged ground-state dimension of an exciton), and the same for e and h (l is significantly smaller than the lateral dimensions $L_{e(h)}$ but greater than the vertical one L_z). The exponential factor e^{-ak^2} corresponds to the above-mentioned bottleneck QD effect. These functions are illustrated by the lines in Fig. 3. Both these functions (often called the ‘form-factors’ of the exciton-phonon interaction) assume non-zero values in the vicinity of point Γ and reach the maximum for quasi-momentum $p \simeq \frac{\hbar}{d}$ ($d \sim l$). What matters here is the fact that this behaviour closely corresponds with the bottleneck effect, which replaces the momentum-conservation condition for the system without translational invariance [32, 33].

The bottleneck effect (which seems to limit the importance of phonons in nanostructures) led to an under-evaluation of the phonons’ role in QDs and of their input in the total interaction in nanostructures [32]. This mistaken view often resulted in the underestimation of phonon-induced phenomena in many physical processes in QDs. Despite the fact that the coupling constants (and form-factors including the bottleneck effect) are rather low-valued, the resonant coincidence (proximity) of the energy levels of the quantum states for carriers localized in the QDs and bulk phonon energy characteristics results in a strong increase in the non-perturbative effects of the mutual hybridization of both subsystems (excitons/electrons and phonons), leading to significant polaron-type effects, both for LA and LO phonons. It is a vital process in the case of QDs, for which such hybridization effects result in the change of quantum states by as much as 10% and lead to significant effects regarding time-dependent processes of amplitude decoherence (relaxation, i.e., a decrease in the diagonal elements of the density matrix [27, 34, 35]), and phase decoherence (dephasing, i.e., a decrease in the off-diagonal elements of the density matrix) [8–12]. From the list of parameters for the GaAs/InAs system (Tab. 1), one can notice that the interaction between the exciton and the LO phonons is significantly bigger (by one order of magnitude) than with LA phonons (cf. the values of the parameters g in formulae (6)).

In order to give the description of fidelity loss [8, 13], we will discuss the exciton correlation function $\langle a_{n_1}(t)a_{n_2}^+(0) \rangle$. For $n_1 = n_2$, this corresponds to the overlap of the exciton state at time $t = 0$ with this state at the initial moment $t = 0$ (for $n_1 = n_2 = 0$ —for the ground state of the exciton changing into a polaron after being gradually dressed with LA and LO phonon clouds). The modulus of this correlation function thus gives a measure of

fidelity of the time-dependent (non-stationary) exciton state. The averaging $\langle \dots \rangle$ denotes the temperature-dependent averaging over the phonon states, assuming the exciton vacuum state [36]—that is, without a change of state of a bare exciton—which corresponds to the fact that the great canonical averaging sector without exciton, vacuum, it energetically distant from the next exciton sectors. The energy separation is here of order of 1 eV.

The Fourier transform of the correlation function is called the 'spectral density' [37, 38]:

$$I_{n_1, n_2}(\omega) = \int_{-\infty}^{\infty} \langle a_{n_1}(t) a_{n_2}^+(0) \rangle e^{i\omega t} dt, \quad (7)$$

The spectral density function can be expressed by the imaginary part of the retarded Green function:

$$\text{Im}G_r(n_1, n_2, \omega) = -I(n_1, n_2, \omega)/(2\hbar), \quad (8)$$

where:

$$\begin{aligned} G_r(n_1, n_2, t) &= -\frac{i}{\hbar} \Theta(t) \langle [a_{n_1}(t), a_{n_2}^+(0)]_- \rangle \\ &= \frac{1}{2\pi} \int_{-\infty}^{\infty} G_r(n_1, n_2, \omega) e^{-i\omega t} d\omega, \end{aligned} \quad (9)$$

is the commutation-retarded Green function which describes the linear dielectric response to the electromagnetic wave coupled to an exciton [in the case of the instant creation of an exciton, the time-dependent electromagnetic signal is assumed to be Dirac's delta $\delta(t)$]. In our case, the Green function $G_r(n_1, n_2, t)$ and the correlation function can be obtained by including the interaction between the exciton and the LA and LO phonon sea via the standard temperature-dependent Matsubara-Green function techniques [37, 38]. The advantage of the Matsubara-Green function approach over the others consists of the derivation of the Dyson equation with the mass operator and the possibility of its modelling in terms of Feynman graphs; the causal function technique needs the Tyablikov splitting-type procedures [39] with a relatively lower level of transparency, even though it is fully equivalent to Matsubara attitude. Both these methods lead to the Dyson equation with an appropriate mass operator, which accounts for the interaction of the exciton with the sea of phonons.

In the case of weak exciton-phonon coupling (which is the nature of the case currently being discussed), the mass operator attains the form of [39] as illustrated by the graphs in Fig. 2. For the QD exciton (similarly as for the bulk semiconductor [40]), with an accuracy up to g_s^2 [note that $F_s(n_1, n_2, \mathbf{k}) \sim g_s$ where g_s is an exciton-phonon constant], both real and imaginary parts of the mass operator M are obtained in the following form (for the effective vertex, the components of a higher-order are omitted, i.e., multi-phonon processes are not included):

$$\begin{aligned} \Delta_n(\omega) &= \frac{1}{N} \sum_{\mathbf{k}, s, n_1} |F_s(n, n_1, \mathbf{k})|^2 \\ &\left[\frac{(1+N_{\mathbf{k}, s})[\hbar\omega - E_{n_1} - \Delta_{n_1}(\omega - \omega_s(\mathbf{k})) - \hbar\omega_s(\mathbf{k})]}{[\hbar\omega - E_{n_1} - \Delta_{n_1}(\omega - \omega_s(\mathbf{k})) - \hbar\omega_s(\mathbf{k})]^2 + \gamma_{n_1}^2(\omega - \omega_s(\mathbf{k}))} \right. \\ &\left. + \frac{N_{\mathbf{k}, s}[\hbar\omega - E_{n_1} - \Delta_{n_1}(\omega + \omega_s(\mathbf{k})) + \hbar\omega_s(\mathbf{k})]}{[\hbar\omega - E_{n_1} - \Delta_{n_1}(\omega + \omega_s(\mathbf{k})) + \hbar\omega_s(\mathbf{k})]^2 + \gamma_{n_1}^2(\omega + \omega_s(\mathbf{k}))} \right] \end{aligned} \quad (10)$$

and:

$$\gamma_n(\omega) = \frac{1}{N} \sum_{\mathbf{k},s,n_1} |F_s(n, n_1, \mathbf{k})|^2 \left[\frac{(1+N_{\mathbf{k},s})\gamma_{n_1}(\omega-\omega_s(\mathbf{k}))}{[\hbar\omega-E_{n_1}-\Delta_{n_1}(\omega-\omega_s(\mathbf{k}))-\hbar\omega_s(\mathbf{k})]^2+\gamma_{n_1}^2(\omega-\omega_s(\mathbf{k}))} + \frac{N_{\mathbf{k},s}\gamma_{n_1}(\omega+\omega_s(\mathbf{k}))}{[\hbar\omega-E_{n_1}-\Delta_{n_1}(\omega+\omega_s(\mathbf{k}))+\hbar\omega_s(\mathbf{k})]^2+\gamma_{n_1}^2(\omega+\omega_s(\mathbf{k}))} \right], \quad (11)$$

where: $N_{\mathbf{k},s}$ is the Bose-Einstein distribution function defining the temperature-dependent population of the phonon mode \mathbf{k}, s , $M_{n,n}(\omega) = \Delta_n(\omega) - i\gamma_n(\omega)$, $G_r(n, n, \omega) = [\hbar\omega - E_n - M_{n,n}(\omega) + i\epsilon]^{-1}$ (for $T = 0$, $N_{\mathbf{k},s} = 0$). The above system of equations enables the time-dependent analysis of the dressing of the exciton with a cloud of phonons.

For GaAs in the surrounding medium, the material parameters are taken from Ref. [41], while a InAs/GaAs QD is modelled in terms of parabolic approximation [1] with a curvature $\hbar\omega_0^e = 20$ meV, $\hbar\omega_0^h = 3.5$ meV, $l_e = \sqrt{\frac{\hbar}{m_e^* \omega_0^e}} = l_h = \sqrt{\frac{\hbar}{m_h^* \omega_0^h}} = 7.5$ nm, which results in the identical size of the ground state of the electron and the hole (when the Coulomb interaction is not accounted for); the QD vertical dimension (the QD is significantly flattened) is $l_z^{e(h)} \simeq 2$ nm (with a suitably adjusted parabolic curvature $\omega_z^{e(h)}$) [numerical estimations including particularities of the QD shape show that they only weakly affect the QD structure and the polaron characteristics [28].

For exciton-LO phonon interactions, the Fröhlich constant is of importance [21, 22]:

$$\alpha_e = \frac{e^2}{\epsilon} \sqrt{\frac{m^*}{2\hbar^3 \Omega}}. \quad (12)$$

Its value grows in nanostructures [24, 26], which significantly influences QD polaron-related processes.

In equation (10), the first component provides the main contribution—polaron red-shift resulting from exciton-LO polaron interactions prevails in a polar material (GaAs is a weakly polar material). Note that equations (10)–(11) contain the full Green function (in accordance with the graph in Fig. 2). Taking $\gamma_n(\omega) = 0$ on the right-hand side of equation (10), the first-order approximation for the energy shift is:

$$\Delta_n(\omega) = \frac{1}{N} \sum_{\mathbf{k},n_1} |F_o(n, n_1, \mathbf{k})|^2 \left[\frac{1 + N_{\mathbf{k},o}}{\hbar\omega - E_{n_1} - \Delta_{n_1}(\omega - \Omega) - \hbar\Omega} + \frac{N_{\mathbf{k},o}}{\hbar\omega - E_{n_1} - \Delta_{n_1}(\omega - \Omega) + \hbar\Omega} \right] + \frac{1}{N} \sum_{\mathbf{k},n_1} |F_a(n, n_1, \mathbf{k})|^2 \left[\frac{1 + N_{\mathbf{k},a}}{\hbar\omega - E_{n_1} - \Delta_{n_1}(\omega - C_a k) - \hbar C_a k} + \frac{N_{\mathbf{k},a}}{\hbar\omega - E_{n_1} - \Delta_{n_1}(\omega - C_a k) + \hbar C_a k} \right]. \quad (13)$$

As has already been pointed out, the first term of the equation provides the dominating contribution while the second—of a significantly smaller order of magnitude [due to the smaller value of the LA phonon coupling constant]—can safely be neglected here. However, this term—to a greater extent than the first one—contributes substantially to the derivative $d\Delta/d\omega|_{\omega=E+\Delta}$. The derivative of the first term [$\sim F^2/(\hbar\Omega)^2$] is small due to the gap in dispersion of the LO phonons, but this derivative is important for estimating the residuum of the Green function at its pole—in equation (16). Moreover, in the first term of this equation, the weak dispersion of the LO phonons is neglected due to its insignificant contribution to the energy shift Δ (which has been verified via numerical methods) [28]. The numerical solution of equation (13) for $n = 0$ yields the polaron energy shift $\Delta_0 \sim -5$ meV (for the structure parameters listed in Tab. 1).

For the description of the kinetics of polaron creation, i.e., of the process of the dephasing of an non-adiabatically excited exciton (this is experimentally observed at the picosecond time-scale [30]), the imaginary part of the mass operator and the **out-of-pole** form of the imaginary part of the Green function is of especially importance—it provides complete information about the spectral intensity (not limited to the poles defining the energy and lifetime of quasi-particles, here polarons). The Fourier transform of the spectral intensity yields the unknown correlation function. The imaginary part of the mass operator is given by Eq. (11). Taking $\gamma = 0$ on its right-hand side:

$$\begin{aligned} \gamma_n(\omega) = & \frac{\pi}{N} \sum_{\mathbf{k}, n_1} \{ |F_o(n, n_1, \mathbf{k})|^2 \\ & [(1 + N_{\mathbf{k},o})\delta(\hbar\omega - E_{n_1} - \Delta_{n_1} - \hbar\Omega_{\mathbf{k}}) \\ & + N_{\mathbf{k},o}\delta(\hbar\omega - E_{n_1} - \Delta_{n_1} + \hbar\Omega_{\mathbf{k}})] \\ & + |F_a(n, n_1, \mathbf{k})|^2 [(1 + N_{\mathbf{k},a})\delta(\hbar\omega - E_{n_1} - \Delta_{n_1} - \hbar C_a k) \\ & + N_{\mathbf{k},a}\delta(\hbar\omega - E_{n_1} - \Delta_{n_1} + \hbar C_a k)] \}. \end{aligned} \quad (14)$$

The first term in equation (14) defines the polarization energy transfer to the LO phonon sea, while the second one defines the deformation energy transfer (smaller) to the LA phonon sea during the process of the gradual exciton-dressing with both types of phonon modes. The term γ can be estimated for the ground state of the exciton ($n = 0$) [higher excited levels are neglected]; integrating over \mathbf{k} yields:

$$\begin{aligned} \gamma_0(\omega) \simeq & Ax^3 e^{-\frac{\alpha x^2}{\hbar^2 c_a^2}} [\Theta(x)(1 + N(x)) - \Theta(-x)N(-x)] \\ & + B \left[\Theta(\hbar\Omega - x)(\hbar\Omega - x)^{3/2} e^{-\frac{\alpha(\hbar\Omega - x)}{\hbar\beta}} \Theta(-0.6\hbar\Omega + x)(1 + N(x)) \right. \\ & \left. + \Theta(\hbar\Omega + x)(\hbar\Omega + x)^{3/2} e^{-\frac{\alpha(\hbar\Omega + x)}{\hbar\beta}} \Theta(-0.6\hbar\Omega - x)N(-x) \right], \end{aligned} \quad (15)$$

where $x = \hbar\omega - \tilde{E}_0$, $\tilde{E}_0 = E_0 - \Delta_0$ is the energy of an excited polaron, $N(x) = (e^{\frac{x}{k_B T}} - 1)^{-1}$:

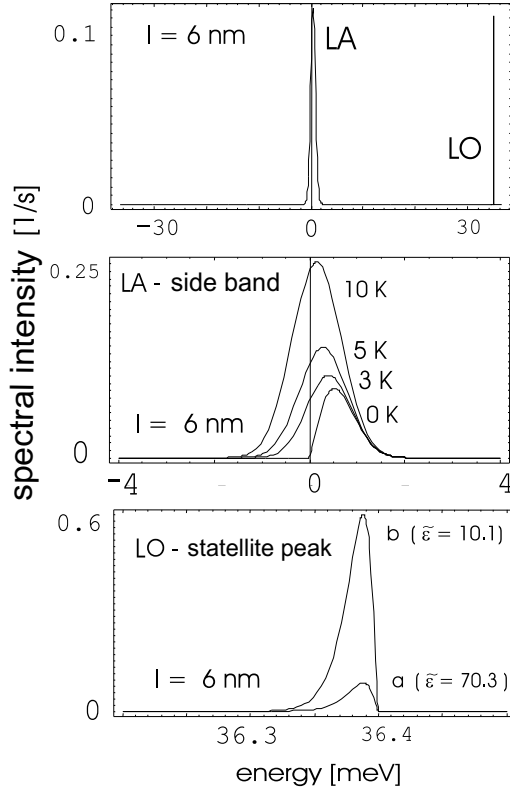


Figure 4. The spectral intensity versus energy ($x = \hbar\omega - \tilde{E}_0^i$) for a QD of a dimension averaged over all directions $l = 6$ nm (upper); the temperature evolution of the side-band due to the LA phonons (middle) and the satellite peak due to the LO phonons (bottom). Only the side-band (due to the LA phonons) increases in value as the temperature rises (within the mentioned range of temperature). LO absorption processes are negligible within this temperature range (the left-hand satellite peak corresponds to LO phonon absorption and is smaller by several orders of magnitude than the right-hand one corresponding to emission of LO phonons; the emission contribution becomes more significant for $T > 80$ K); the satellite peak that is LO phonon-induced increases significantly with the increase in the value of the QD's Fröhlich constant [expressed by the Huang-Rhys factor][23]—Fröhlich constant in *bulk* (a), in a QD (b).

$$A = \frac{(\sigma_e - \sigma_h)^2}{4\pi\rho\hbar^3 C_a^5}, \quad B = \frac{e^2\hbar\Omega(L_e^2 - L_h^2)^2}{36\tilde{\epsilon}2(\hbar\beta)^{5/2}}$$

(LO phonon dispersion as defined in [31] $\Omega_{\mathbf{k}} = \Omega - \beta k^2$ and at the Brillouin zone edge, i.e., for $k = k_m$ attains the value $\Omega_{\mathbf{k}_m} = 0.6\Omega$). The first term of equation (15) corresponds to the LA phonon channel of energy dissipation, while the second one corresponds to the LO phonon dissipation channel. The numerical parameters of this equation for the structure under investigation (Tab. 1) are listed in Tab. 2.

As γ_0 equals 0 at $x = 0$ [which results from equation (15)], this point is understood as the well-defined Green's function pole (it corresponds to a stable quasi-particle—the polaron, this is the exciton dressed in phonon clouds [a generalization of an ordinary electron polaron

dressed only in an LO phonon cloud [22, 34]). The time-dependent evolution of the phonon dressing is given by the correlation function, corresponding to the Green function in the form of:

$$G_r(0,0,\omega) = \frac{1}{\hbar\omega - E_0 - \Delta(\omega) + i\gamma(\omega) + i\epsilon} \quad (16)$$

$$= \frac{a^{-1}}{x + i\gamma'(x) + i\epsilon'}$$

where:

$$a = 1 - \frac{d\Delta(\omega)}{\hbar d\omega} \Big|_{\omega=\tilde{E}_0'} \quad (17)$$

$$= 1 + \frac{1}{N} \sum_{\mathbf{k},s} \left| \frac{F_s(0,0,\mathbf{k})}{\hbar\omega_s(\mathbf{k})} \right|^2 [1 + 2N_s(\mathbf{k})],$$

$\gamma'(x) = \gamma(x)/a$ ($x = \hbar\omega - \tilde{E}_0'$, $\tilde{E}_0' = \tilde{E}_0/a$), $\epsilon = 0+$. The imaginary part of this retarded Green's function (16) attains the form:

$$\text{Im}G_r(0,0,\omega) = -a^{-1}\pi\delta(x) - \frac{a^{-1}\gamma'(x)/x^2}{1 + (\gamma'(x)/x)^2}. \quad (18)$$

The inverse Fourier transform of the spectral intensity (the imaginary part of the retarded Green's function) gives the correlation function in the time domain:

$$I(t) = -2\hbar \frac{1}{2\pi} \int_{-\infty}^{\infty} d\omega \text{Im}G_r(0,0,\omega) e^{-i\omega t},$$

(the indices $n_1 = n_2 = 0$ of function I are suppressed). The first term in (18) yields:

$$I^{(1)}(t) = a^{-1} e^{-i\frac{E_0}{\hbar}t}.$$

Notice that in the second term of equation (18), for temperatures $T < 100$ K, the second term in the denominator can be safely neglected for LA phonons (consistently with the accuracy assumed within the perturbative treatment). This allows us to exchange the order of integration with respect to ω and \mathbf{k} —the inverse Fourier transform can be calculated first and, simultaneously, Dirac's delta can be employed in equation (14). Such integration over frequencies (energy) yields a convenient representation of the correlation function:

$$I^{(2)}(t) = \frac{1}{N} \sum_{\mathbf{k}} \left| \frac{F_a(0,0,\mathbf{k})}{\hbar\omega_a(\mathbf{k})} \right|^2 \times \left\{ [1 + N_s(\mathbf{k})] e^{-i[\tilde{E}_0/\hbar + \omega_s(\mathbf{k})]t} + N_s(\mathbf{k}) e^{-i[\tilde{E}_0/\hbar - \omega_s(\mathbf{k})]t} \right\}. \quad (19)$$

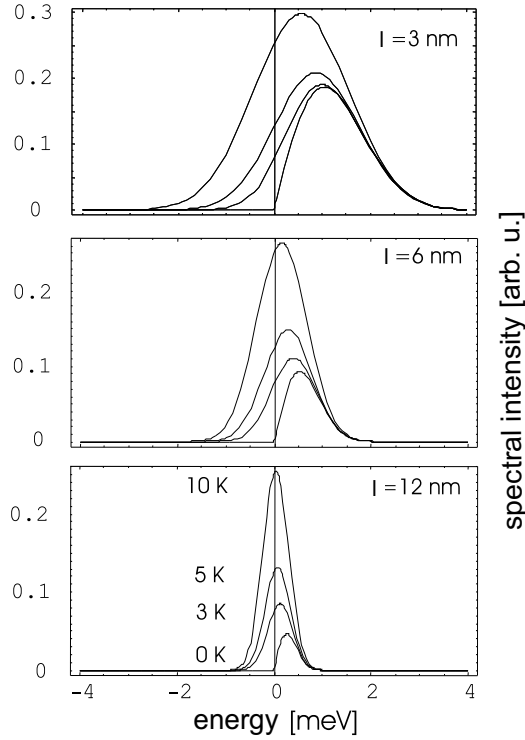


Figure 5. The evolution of the side band due to acoustic phonons (LA) versus the QD's dimension and temperature for $T \geq 0$ K (the same temperatures for each QD dimension $l = 3, 6, 12$ nm).

Notice that, when comparing with Eq. (17), for $t = 0$ this leads to $I^{(1)}(t = 0) = a^{-1}$ and $I^{(2)}(t = 0) = 1 - a^{-1}$, which in effect results in the appropriate normalization of the correlation function.

The spectral intensity and its reverse Fourier transform (its modulus) are plotted in Figs. 4–9 for various temperatures and QD dimensions. The fact that the numerically calculated correlation function agrees well with the experimentally obtained data [30]—cf. Fig. 7 (upper), for a small QD and sub-picosecond excitations, may confirm the validity of the theory developed here. The LA channel (although negligible in terms of energy compared to the LO channel in GaAs) is the fastest and most effective in the dephasing process. The LO channel is slower and accompanied by fast oscillations (beats of ~ 100 fs corresponding to the existence of the LO gap) [the LO channel of dephasing can be significantly intensified due to the anharmonic decay of the LO phonons, e.g., for GaAs/InAs up to 10 ps] [42]. Dephasing produced by LO phonons is significantly weaker than that for LA phonons (contrary to the energy shift). The inclusion of the LO channel results in the weak modification of strong LA dephasing—cf. Figs 8 and 9. Figure 9 (right) presents the type of the scaling of the dephasing time versus a QD dimension—linear for the LA channel and quadratic for the LO channel. This behaviour agrees well with the simple relationship: dephasing time $\simeq \frac{l}{v_g}$, v_g —phonon group velocity, l —QD dimension. For LA phonons $v_g = C_a$, which yields a linear function

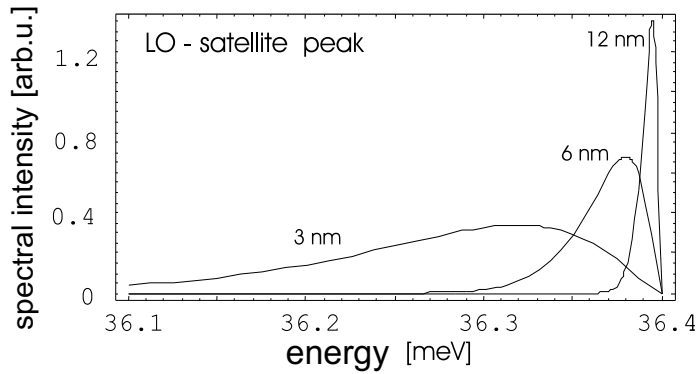


Figure 6. Evolution of the satellite peak (the right-hand one—corresponding to LO phonon emission—versus the QD's dimensions; in practical terms, it is not dependent on temperature for $T < 80$ K.

electron effective mass in GaAs	m_e^*	$0.067m_e$
hole effective mass (heavy) in GaAs	m_h^*	$0.38m_e$
dielectric constant in GaAs (static)	ϵ_0	12.9
dielectric constant in GaAs (dynamic)	ϵ_∞	10.9
electron deformation potential in GaAs	σ_e	6.7 eV
hole deformation potential in GaAs	σ_h	-2.7 eV
LO phonon energy at Γ point in GaAs	$\hbar\Omega$	36.4 meV
density of GaAs	ρ	5.36 g/cm^3
sound velocity (LA) in GaAs	C_a	$4.8 \times 10^5 \text{ cm/s}$
electron confinement energy in a GaAs/InAs dot	$\hbar\omega_0^e$	20 meV
hole confinement energy in a GaAs/InAs dot	$\hbar\omega_0^h$	3.5 meV
lateral dimension of a QD (electron)	$l_e = \sqrt{\frac{\hbar}{m_e^* \omega_0^e}}$	7.5 nm
lateral dimension of a QD (hole)	$l_h = \sqrt{\frac{\hbar}{m_h^* \omega_0^h}}$	7.5 nm
dot height (electron and hole)	$l_z^{e(h)}$	2 nm
Debye wave vector in GaAs	$k_m = \left(\frac{6\pi^2}{v}\right)^{1/3}$	$1.1 \times 10^{10} \text{ m}^{-1}$
Fröhlich constant in a GaAs- <i>bulk</i> (electron)	$\alpha_e = \frac{e^2}{\epsilon} \sqrt{\frac{m_e^*}{2\hbar^3 \Omega}}$	0.07
Fröhlich constant in a GaAs/InAs dot (electron)	$\alpha_e' = \frac{e^2}{\epsilon l} \sqrt{\frac{m_e^*}{2\hbar^3 \Omega}}$	0.15

Table 1. Quantum dot and material parameters for GaAs/InAs

of l , and for LA phonons $v_g = 2\beta k \sim 2\beta/l$, which results in a quadratic dependence on the QD dimension $\sim l^2/(2\beta)$. Conclusive proof of this result follows below.

5. The universal rule for the estimation of the dephasing time of localized excitons in nanostructures

In order to estimate the dephasing time of a QD's (or other nanostructures) localized excitation (e.g., an exciton) due to hybridization with collective excitations in the surrounding

exciton-LA phonon coupling constant	$A = \frac{(\sigma_e - \sigma_h)^2}{4\pi\rho\hbar^2 C_s^2} \simeq 0.29 \text{ meV}^{-2}$
exciton-LO phonon coupling constant	$B = \frac{e^2 \hbar \Omega (L_e^2 - L_h^2)^2}{36\epsilon_2 (\hbar\beta)^{5/2}} \simeq \left(\frac{l nm }{6}\right)^4 6.3 \times 10^5 \text{ meV}^{-1/2}$
lateral exciton dimension (electron)	$L_e \simeq 6.6(l nm /6) \text{ nm}$
lateral exciton dimension (hole)	$L_h \simeq 5.1(l nm /6) \text{ nm}$
mass operator exponent (LA)	$\frac{\alpha}{\hbar^2 C_s^2} \simeq (l nm /6)^2 1.8 \text{ meV}^{-2}$
mass operator exponent (LO)	$\frac{\alpha}{\hbar\beta} \simeq (l nm /6)^2 149 \text{ meV}^{-1}$

Table 2. Parameters of exciton-phonon (LA and LO) interaction for a GaAs/InAs dot

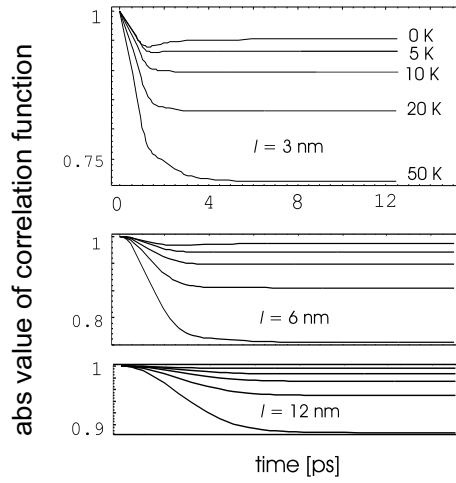


Figure 7. Modulus of the correlation function $|\langle a(t)a^+(0) \rangle|$ (the fidelity measure of the ground excitonic state) versus time for rising temperatures. The three plots correspond to small, medium and large QDs, and contain curves related to the same set of temperatures as given in the upper plot. For the small QD, the experimentally observed fidelity loss for a non-adiabatically excited exciton (for 0.2 ps pulse) [30] is reproduced well in the upper figure.

medium (e.g., with band phonons), a phenomenological picture can be applied that is motivated within the Green function approach [28]. The correlation function:

$$I(t) = \langle a_0(t)a_0^+(0) \rangle = -\frac{\hbar}{\pi} \int d\omega \text{Im} G_r e^{-i\omega t} \quad (20)$$

[where $a^{(+)}$ denotes the QD exciton annihilation (creation) operator] permits a reasonable assumption that the characteristic dephasing time parallels the rapid decrease in the value of its modulus (clearly evident in Figs. 7, 8). The correlation function is an inverse Fourier transform of spectral intensity (cf. Fig. 4), which is expressed via the imaginary part of the retarded one-particle commutation of Green function G_r of the exciton [37, 38]. For a short time-scale (i.e., large values of Fourier frequencies ω), the imaginary part of the retarded Green function is proportional to the imaginary part of the mass operator (due to Eq. (18)),

which is expressed (with multi-phonon effects neglected) by the following formula [37, 38]:

$$\gamma \sim \int dk |F(k)|^2 \delta(\omega - E - \omega(k)), \quad (21)$$

where the interaction vertices assume their general form (the interaction between the QD localized excitation and the non-localized crystal excitations expressed by means of plane waves):

$$F(k) \sim \langle \Psi_0 | e^{ikr} | \Psi_0 \rangle, \quad (22)$$

where $|\Psi_0(r)\rangle$ is a wave function of a QD localized exciton corresponding to its ground state with energy E (for simplicity of description, a single particle-localized excitation is considered here, e.g., an electron [one-dimension picture, $\hbar = 1$]). Thus, the correlation function:

$$I(t) \sim e^{-iEt} \int dr |\Psi_0(r)|^2 \int dk F^*(k) e^{i(kr - \omega(k)t)}, \quad (23)$$

appears to attain the form of a time-dependent overlap of a probability density of a QD localized particle:

$$|\Psi_0(r)|^2, \quad (24)$$

with a collective excitation wave packet (phonons) escaping from the QD-space region:

$$\int dk F^*(k) e^{i\left(r - \frac{\partial\omega(k)}{\partial k}t\right)k} \quad (25)$$

(where k is the centre, $k \sim 1/l$, l is the QD diameter due to the above-mentioned QD bottleneck effect entered here via $F(k)$). The wave packet carries off the excess (deformation or polarization) energy of the particle being dressed to the QD's surrounding region in the crystal with the group velocity $v_g = \frac{\partial\omega(k)}{\partial k}$ (for $k \sim 1/l$). Thus, the dephasing time corresponds to the time for the decrease in value of the modulus $I(t)$, which here is of the order of $\tau \simeq \frac{l}{v_g}$, where l is the QD dimensions averaged over all directions [the QD exciton state dimension] (as illustrated in Fig. 10).

In this representation, the dephasing time is of the order of the proportion of a QD dimension l to the phonon group velocity, i.e., the velocity of the phonon packet carrying off the excess energy from the QD to the surrounding medium (this is the evolution of a non-stationary QD state of a non-adiabatically excited bare exciton). For LA phonons, the group velocity remains constant and equals the sound velocity $v_g = C_a$, which results in a linear dependence of the dephasing time with respect to the QD's dimension,

$$\tau \simeq \frac{l}{C_a};$$

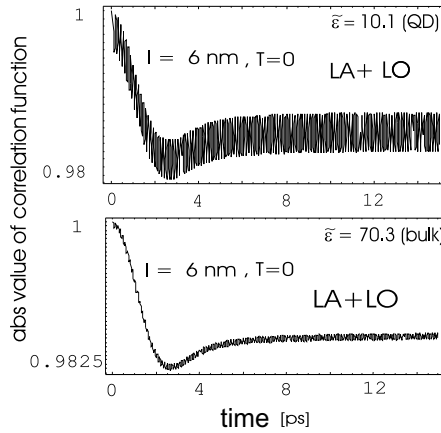


Figure 8. The typical shape of the modulus of the correlation function of an exciton interacting simultaneously with LO and LA phonons. The oscillations, corresponding to the gap in the LO phonon spectrum [the frequency is $\sim 1/\Omega \sim 100$ fs], are significantly stronger for a QD due to the increase in the value of the effective Fröhlich constant (upper).

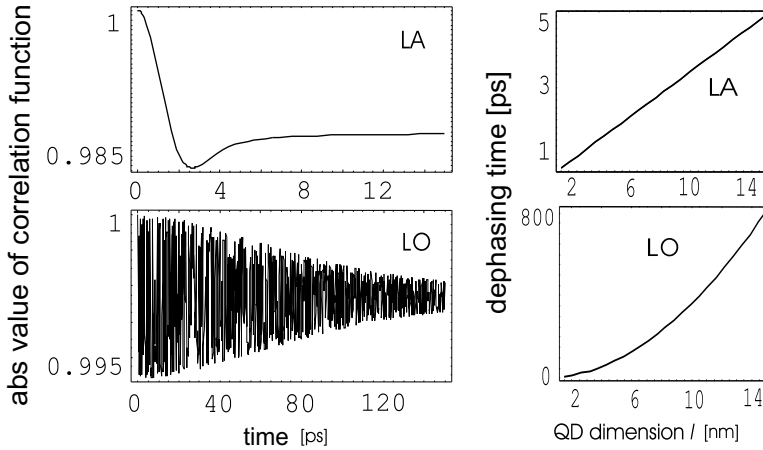


Figure 9. Left: the modulus of the correlation function for, respectively, LA (upper) and LO (lower) phonons only. Right: the exciton dressing time vs the averaged QD dimensions l for the LA channel (upper), the linear dependence, and for the LO channel (lower), which is a quadratic dependence on l .

for optical phonons $v_g = 2\beta k \sim 2\beta/l$ leading to a quadratic dependence of the dephasing time on l ,

$$\tau \simeq \frac{l}{v_g} = l \left(\frac{\partial \epsilon}{\partial p} \right)^{-1} = \frac{\hbar l}{2\beta k} \simeq \frac{\hbar l^2}{2\beta'}$$

as $k \simeq 1/l$ (due to the bottleneck effect on the centre of the wave packet in the momentum space). In the case of LO phonons, the dephasing time-scales quadratically with the dot's dimensions, and thus for the state-of-art structures it attains values much larger than the dephasing time for the LA channel (with the linear scaling) (cf. Fig. 9).

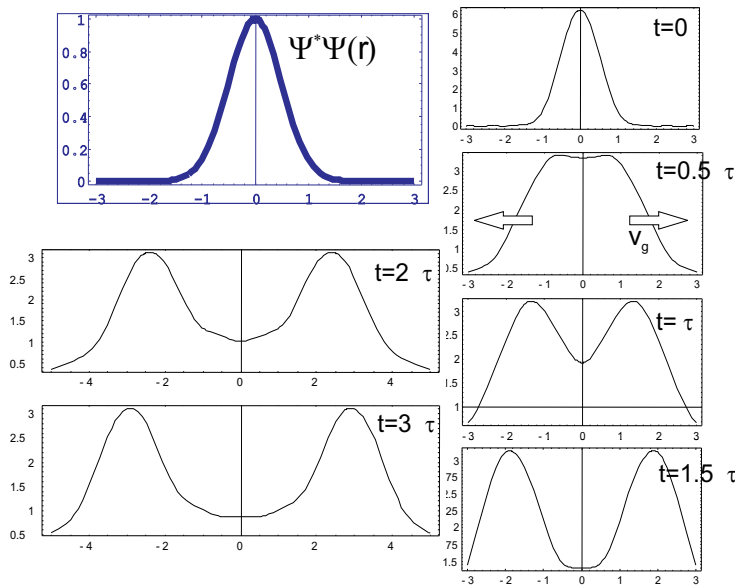


Figure 10. The correlation function's decrease in value corresponds to the decrease in the overlap of the local distribution of a QD particle (exciton) with the phonon (LA) wave packet carrying off the excess energy; the correlation function is the overlap of a QD particle (exciton) probability density, $|\Psi(r)|^2$ (upper left), with the wave packet escaping from the QD-space region $\mathcal{A}(r, t) = \int \int e^{-ikr'} |\Psi(r')|^2 dr' e^{i(r \pm \frac{d\epsilon(k)}{dk} - \text{sign}(k)t)k} dk$ (illustrated here as $\mathcal{A}(r)$ for a sequence of times τ —time-scale of dephasing).

6. Decoherence of the degrees of freedom of spin in quantum dots

Spin do not interact directly with with phonons—the spin of the QD excitations interacts weakly with the lattice oscillations due to their links to orbital (charge) degrees of freedom via:

- spin-orbit coupling [43],
- specific Hund-like rules for multi-electron QDs [1]—the filling of the subsequent shell in the multi-electron QD depends upon the total electron (hole) spin of a given shell [the generalization of singlet and triplet states] which, in effect, link spin and orbital degrees of freedom.

Weak spin coupling with phonons suggests that the spin of a QD electron constitutes a well-isolated quantum system (an insignificant spin-orbit interaction results in an extremely slow spin decoherence, the same is due to weak interaction with nuclear spin) that is suitable for a qubit's definition. One can expect that for spin qubits in QDs, DiVincenzo's conditions would be satisfied [7, 14, 15]. Due to the minor influence of the surrounding medium, the QD's spin coherence is maintained until the time period of order of μs [16]. However, a difficulty arises when Rabi oscillations are implemented (for single qubit operations). Because of the low value of the gyromagnetic factor in semiconductors, qubit spin control (a qubit spanned across two spin orientations in an external constant magnetic field) via Rabi oscillations is extremely slow and the DiVincenzo conditions are again not satisfied (the Pauli term, $g\mu_B s_z B$, leads to very slight Zeeman splitting of only 0.03 meV/T, in GaAs).

For two-qubit operations of spin qubits, no such disadvantage exists—there is an effective procedure for switching spin qubit interactions on and off [15, 16] resulting in qubit entanglement control at the time-scale of picoseconds. The idea of spin interaction control follows from the phenomenon of exchange interaction between two spins, being induced by strong Coulomb interaction [44]. The exchange energy for it is the singlet-triplet energy gap for the spin pair [44], and consequently it is of (several) meV in magnitude, resulting in a picoseconds time-scale for the control of the entanglement of qubits. The scheme of this control relies upon the singlet and triplet states of an electron pair (each electron captured in an individual QD but located closely enough to maintain their quantum indistinguishability [their localized wave functions must overlap]) and their relation with the orbital structure of the corresponding wave functions. Due to the fermionic nature of electrons:

- the singlet state $\frac{1}{\sqrt{2}}(|\uparrow\rangle_1 \otimes |\downarrow\rangle_2 - |\downarrow\rangle_1 \otimes |\uparrow\rangle_2) \iff |0,0\rangle$ corresponds to the symmetric orbital wave function,
- the triplet states $\left\{ \begin{array}{l} |\uparrow\rangle_1 \otimes |\uparrow\rangle_2 \iff |1,-1\rangle \\ \frac{1}{\sqrt{2}}(|\uparrow\rangle_1 \otimes |\downarrow\rangle_2 + |\downarrow\rangle_1 \otimes |\uparrow\rangle_2) \iff |1,0\rangle \\ |\downarrow\rangle_1 \otimes |\downarrow\rangle_2 \iff |1,1\rangle \end{array} \right\}$ correspond to the antisymmetric orbital wave function,

so that the complete spin-orbital wave function remains antisymmetric, as is required for fermions. In the absence of a magnetic field, the singlet state is the ground state [44], but as the field increases in value [i.e., the magnetic field breaks the symmetry of time-reversion], it becomes less energy-efficient and, finally, the triplet state is preferred (with parallel spin orientation) [a parallel spin orientation is also preferred due to the Pauli term, which is, however, of very low value, and its contribution to energy competition is negligible; the triplet spin state is preferred due to the minimization of the energy of Coulomb interaction by the antisymmetric orbital state in the presence of the magnetic field breaking the time-reversion symmetry [44]]. For the critical field (of the order of a few T for QDs), both the singlet and the triplet states have the same energy, which means that the exchange qubit interactions is switched off (the exchange interaction constant is expressed via the difference in the energy value for the singlet and the triplet) [44]. It can be switched on again by varying the value of the applied external magnetic field and shifting the system out of the degeneracy point. The exchange interaction equal to the energy gap between the triplet and singlet states is originated by the relatively strong Coulomb interaction and varies within the range of several meV or more, which allows for the rapid entanglement of qubits.

Let us also mention that the possibility of using the exchange interaction to implement and exert control over single-spin qubits has been investigated, which has resulted in:

- a singlet- and a triplet-defined qubit on a two-electron QD of He-type [45],
- a spin qubit defined by the spin states with $S_z = \pm 1/2$ for three electrons [16] but separated energetically by a strong exchange-like interaction—i.e., a qubit defined by a pair $|1/2, -1/2\rangle_s, |1/2, 1/2\rangle_t$ or a pair $|1/2, 1/2\rangle_s, |1/2, -1/2\rangle_t$ [the spin states of three electrons can be classified according to the spin addition rule: first, two spins of $1/2$ are added, yielding a singlet $|0,0\rangle$ and a triplet: $\left\{ \begin{array}{l} |1,-1\rangle \\ |1,0\rangle \\ |1,1\rangle \end{array} \right\}$ and then the third

spin of 1/2 is added yielding eight three-electron spin states:

$$\left\{ \begin{array}{l} |1/2, -1/2 \rangle_s \quad |1/2, 1/2 \rangle_s \\ |3/2, -3/2 \rangle_t \quad |3/2, -1/2 \rangle_t \quad |3/2, 1/2 \rangle_t \quad |3/2, 3/2 \rangle_t \\ |1/2, -1/2 \rangle_t \quad |1/2, 1/2 \rangle_t \end{array} \right\}.$$

In both cases, however, for the collective qubit's definition, the number of particles must be increased, which results in the enhancement of local decoherence $\sim e^N$ (N —number of qubits). On the other hand, however, it might be conveniently directed towards the application of collective-global (and thus more robust against decoherence) subspaces of the Hilbert space for multi-particle systems for QIP [13].

The scheme for the entangled qubits' control relies upon the symmetry-induced close connection between spin exchange interaction and the orbital (thus, strong) Coulomb interaction of electrons (leading to an energy gap between the singlet and triplet states of an order of magnitude in meV). Due to this strong Coulomb interaction, and following the spin exchange interaction, the time-rates of double-qubit gate unitary operations are of the order of picoseconds, which suggests the convenience of spin degrees of freedom for QIP in QDs. A model of a quantum gate based on the above-mentioned idea was proposed by DiVincenzo [15, 16, 20]. In his model, a pair of H-type QDs (a single qubit spanned across electron spin states $|1/2, -1/2 \rangle$, $|1/2, 1/2 \rangle$) was analysed for two-qubit operations. However, for the implementation of a quantum computer, single-qubit operations are necessary as well, which unfortunately are extremely slow for the defined spin qubit on single-electron spin states. The idea of accelerating single-qubit operations can be associated with the enhancement of the gyromagnetic factor in semiconductor environments with magnetic dopants (as in so-called 'diluted magnetic semiconductors') [46–50] in a magnetically ordered phase. In such materials with low concentrations of magnetic ions (of a few percent range), typically Mn^{2+} ones, phase transition to a magnetically-ordered phase takes place due to the mediating role of band holes [49]. Such a phase transition takes place even at temperatures exceeding 100 K (in Ga(Mn)As) [49, 50] and, additionally, can be controlled via the hole concentration in the semiconductor [47, 48, 51–53]. The magnetic ordering of the material produces an extremely strong Weiss-like magnetic field internally, which acts exclusively on the degrees of freedom of the spin (i.e., it does not act on orbital ones), thus leading to a significant increase in value of the Pauli term, i.e., in the enhancement of the effective gyromagnetic factor. This suggests that single-qubit operations could be accelerated up to the level required by the DiVincenzo criteria in QDs in DMSs (such structures have already become available).

However, introducing an additional spin subsystem (and such is the magnetic dopant part of the semiconductor) causes a new problem. Such a subsystem is a source of collective excitations—spin waves, which interact directly with the qubit spin. In this system, spin waves (magnons) behave like phonons and produce similar spin decoherence effects (as presented for phonons and the charges in the previous paragraphs).

A more detailed analysis of the problem (as will be presented below) shows that spin waves cause harmful decoherence within time-rates of the order of 500-1000 ps, which is a serious negative side-effect threatening the feasibility of the spin logic gate (again, in the centre of the six-order time window between the control time and the amplitude decoherence for spins [54]). It exists, however, the promising opportunity to diminish the amplitude of this spin dephasing, which is in contrast to the phonon-induced effect in the case of spin waves

and can be achieved at very low temperatures, as will be demonstrated in the following paragraphs. The essential elements of the analysis are as follows: (1) the averaging over the random distribution of magnetic admixtures in a DMS [55] yields a spin waves spectrum in a Holstein-Primakoff representation [56, 57] [the averaging restores the effective translational invariance in a randomly doped system [55] and allows for the application of momentum representation]; (2) the determining of the spin wave dispersion in a DMS with respect to the hole and the magnetic dopant concentration; (3) analyzing the structure of the interaction between the spin waves and the spin of a QD exciton. The quadratic dispersion of spin waves found as the result of this analysis turns out to be crucial for the timing of the phase decoherence of spin in QDs. The estimation of the time rate of this process is given as the QD dimension divided by the spin wave group velocity, according to the general rule presented in the paragraph 5, ($v_g = \nabla\epsilon(\mathbf{p}) \sim p \sim \frac{\hbar}{d}$), $\tau \sim \frac{d}{1/d} \sim d^2$; the time-rate scales as the square of the QD dimension (marked as d), similarly as in the case of LO phonons (and similarly as for LO phonons rapidly increases with the dot dimension growth) and for typical dots of dimension of about 10 nm reaches values of the order of 500 ps.

6.1. Dephasing induced by the dressing of QD exciton spin with magnons in a diluted magnetic semiconductor's surroundings

An interesting question arises with regard to the QD spin in the magnetic surroundings when the Pauli term causing the Rabi oscillations for spin can be strengthened due to an increase in the effective gyromagnetic factor. Spin does not interact directly with phonons, and thus it is free from phonon-induced dephasing. Nevertheless, the dephasing role of phonons may be played by spin waves in magnetically-ordered media which, on the other hand, are convenient for accelerating single-qubit QD spin control to the level required by the DiVincenzo conditions. Spin waves (frequently called 'magnons') are collective spin-type excitations in the ferromagnetic or anti-ferromagnetic medium (or in any other magnetically-ordered spin system), and possess similar band properties to phonons in crystalline structures. The spin-exchange interaction between the magnons and the local QD spin (of an exciton trapped in a QD) is relatively strong and causes the dressing of the QD spin with the magnons in a similar fashion to the dressing of the QD charges with phonons. The opportunity for the experimental study of such a spin dressing phenomenon may be linked to the so-called 'diluted magnetic semiconductors' of the type III-V (e.g., Ga(Mn)As) or II-VI (e.g. Zn(Mn)Se). In these magnetically and weakly doped semiconductors, some relatively small part of the cations (usually a few %) is randomly substituted by transition metal ions (typically of Mn). The admixture spins interact with the spins of band holes and as a result the ferromagnetic ordering of the admixture spins is observed. The related Weiss field enhances the effective gyromagnetic factor in the Pauli term, describing the spin action of the external magnetic field conveniently for the acceleration of the control over the local QD spin.

6.2. Spin waves in the diluted magnetic semiconductor

To describe the dephasing of QD spin caused by magnons in DMSs quantitatively, the analytical expression of the spin wave spectrum in the DMS is needed. This can be found in the paper [64]. For the relevant theoretical description of the spin subsystem of the DMS, the model of dopant spin exchange mediated by band holes is utilized [58, 59], assuming

that the $p - d$ exchange between the band holes and the impure magnetic atoms may lead to the ferromagnetic alignment of the magnetic dopants (Mn). Note that the holes taking part in the spin exchange with the dopant Mn ions cause an indirect exchange beyond the weak, direct, short-range and anti-ferromagnetic exchange between the magnetic dopants [48]. The hole-induced indirect coupling, even for low concentrations of holes x_p (lower than the magnetic dopant concentration x) occurs strong and leads to the ferromagnetic ordering of Mn spins even at relatively high temperatures, ~ 110 K in $\text{Ga}_{0.947}\text{Mn}_{0.053}\text{As}$ [58, 60]. Let it be emphasized that, in III(Mn)V DMSs, the Mn atoms of the magnetic dopants are simultaneously shallow acceptor centres, whereas in II(Mn)VI-type DMSs, the Mn dopants are not acceptors and the holes must be supplied by additional p doping.

To briefly sketch the derivation of the magnon spectrum in DMSs, let us set out the Hamiltonian for the DMS system with magnetic dopants Mn^{2+} (with spin $S = 5/2$) in the form:

$$\hat{H} = \hat{H}_s + \hat{H}_p, \tag{26}$$

where \hat{H}_s describes the spin subsystem of the DMS:

$$\hat{H}_s = -2 \sum_{j=1}^{N_p} \sum_{\mathbf{n}} A_p(\mathbf{R}_j - \mathbf{R}_{\mathbf{n}}) \hat{\mathbf{s}}_j \cdot \hat{\mathbf{S}}_{\mathbf{n}}, \tag{27}$$

where $\hat{\mathbf{s}}_j, \mathbf{R}_j$ and $\hat{\mathbf{S}}_{\mathbf{n}}, \mathbf{R}_{\mathbf{n}}$ are operators for the spin and position of the j -th hole and the \mathbf{n} -th impurity atom (in the lattice point $\mathbf{R}_{\mathbf{n}}$; the interstitial positions of the dopants are not accounted for); $A_p(\mathbf{R}_j - \mathbf{R}_{\mathbf{n}})$ is the $p - d$ exchange integral; $A_p(\mathbf{R}) < 0$ (antiferromagnetic) and $|A_p(\mathbf{R})| \sim 1eV$; \mathbf{n} summation goes over lattice points occupied by magnetic dopants; hole concentration $x_p = \frac{N_p}{N}$, magnetic dopant concentration $x = \frac{N_i}{N}$, N_p is the number of band holes which contribute to exchange with the impurity atoms, N_i is the number of magnetic impurities, N is the number of elementary cells and \hat{H}_p is the fermionic Hamiltonian of the holes.

The important property of the considered system is the randomness of the distribution of the magnetic impurity atoms and the acceptors. The averaging over these random distributions conveniently results, however, in the effective restoring of the translational symmetry broken at any particular dopant distribution, though it is again present after averaging. This allows for momentum-representation for collective excitations, which can be utilized in the diagonalization of the spin part of the Hamiltonian. This procedure is originally presented in [64] and results in the explicit form for the low-temperature excitation spectrum of the DMS spin subsystem. This spectrum of magnons in DMSs consists of two branches: the gap-less branch $\varepsilon_1(\mathbf{k})$ and the "optical-type" gapped branch $\varepsilon_2(\mathbf{k})$. The value of the gap is given by the formula $\varepsilon_2(0) = -\tilde{A}_p(0)(x_p + 2Sx)$ ('tilde' denotes the Fourier picture). The energy of the magnon branch $\varepsilon_1(\mathbf{k})$ grows with increasing k , whereas the energy for the branch $\varepsilon_2(\mathbf{k})$ diminishes with increasing k . Within the long-wave limit, i.e., for small k , the spin wave energy spectrum can be written as follows [64]:

$$\begin{cases} \varepsilon_1(\mathbf{k}) = Dk^2, \\ \varepsilon_2(\mathbf{k}) = D_0 - Dk^2, \end{cases} \quad (28)$$

with: $D_0 = -\tilde{A}_p(0)(x_p + 2Sx)$, $D = -\tilde{A}_p(0)\frac{2Sxx_p}{x_p+2Sx}l_{ex}^2$, where l_{ex} expresses the space-range of the exchange interaction.

6.3. Dressing of the QD's local exciton spin by magnons from the surrounding DMS

In analogy to the creation of the polaron in a QD by the dressing of the QD exciton with band phonons, one can observe the formation of the excitonic-magneto-polaron (EMP), i.e., of the localized QD exciton spin dressed with magnons in the surrounding DMS (in the case of the magnetically ordered phase of the DMS at a sufficiently low temperature). Similar to the ordinary polaron, the dephasing of the spin caused by the magnons expresses the inertia of the collective spin wave system. For the non-adiabatically and rapidly excited bare exciton to the QD one deals with a non-stationary state of the whole system of QD with surrounding DMS. Similarly to the dephasing of the QD charge by phonons, in the case of step-by-step formation of the exciton magneto-polaron (EMP) in QD one deals with the outflow of an excess energy to the region outside the QD. This excess energy is linked now with the spin exchange interaction and the carriers for the energy outflow are magnons. The corresponding quantum evolution of the total system is the evolution of the non-stationary state (originally at $t = 0$ defined by the non-stationary initial state of the bare exciton rapidly excited in the QD). During this evolution, the mean energy is shared between the QD and the surrounding magnons in the DMS (the spin wave sea). The final EMP localized in QD and dressed with the cloud of magnons has a lower mean energy than the initial bare exciton. Together with the magnons escaping from the QD region (these ones remove the excess of the spin exchange energy outside the QD), the whole system remains in the non-stationary state, although the local EMP might be treated as the 'stationary' component of the eventual state of the system. In order to estimate the time-rate corresponding to the dressing of the local spin in the QD by magnons resulting in the formation of the EMP, the same rule as that for the QD charge with phonons can be utilized.

In analogy to phonon dressing, one arrives at the formula for the correlation function,

$$I(t) \sim e^{-iEt} \int dr |\Psi_0(r)|^2 \int dk F^*(k) e^{i(kr - \varepsilon(k)t)},$$

describing the time-dependent evolution of the overlap of the local QD particle distribution, $|\Psi_0(r)|^2$, with the wave-packet of the spin waves escaping the dot region step-by-step, $\int dk F^*(k) e^{i\left(r - \frac{\partial \varepsilon(k)}{\partial k} t\right)k}$ (where k corresponds to the centre of the wave-packet being of the order of $\sim 1/l$, as caused by the QD bottleneck effect similar to that for phonons and which is visible from the form of $F^*(k)$). The group velocity of this wave-packet is equal to $v_g = \frac{\partial \varepsilon(k)}{\partial k}$ (at $k \sim 1/l$). Thus, one can conclude that the dephasing time defining the time-scale of the

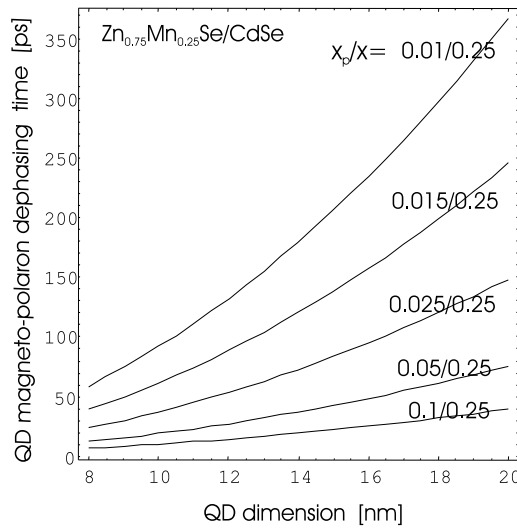


Figure 11. The EMP formation time $\tau = \frac{l}{v_g}$ (the spin dephasing time-rate) for an exciton localized in a QD embedded in a DMS versus the dot dimension for various hole-concentration rates x_p (x is an Mn admixture rate) in the $\text{Zn}_{0.75}\text{Mn}_{0.25}\text{Se}/\text{CdSe}$ DMS/QD structure; the parabolic scaling with the dot dimension is similar to that for LO phonons but distinct from LA phonon wave-packet kinetics.

dressings of the QD spin with magnons and expressed by the function $I(t)$ is given by that according the general rule, $\tau \simeq \frac{l}{v_g}$.

The dressing of the QD exciton spin with magnons is similar to the dressing of the QD charge with LO phonons, since both LO phonons and magnons have a quadratic dispersion. Utilizing now the formulae for magnon energies as given by Eqs. (28), we arrive at the assessment for the time of formation of the EMP in form,

$$\tau \simeq \frac{l}{v_g} = l \left(\frac{\partial \epsilon}{\partial k} \right)^{-1} = \frac{l}{2Dk} \simeq \frac{l^2}{2D}$$

$k \simeq 1/l$ because of above-mentioned QD bottleneck. Note that the derived time for dressing with magnons scales as l^2 . Therefore, it is relatively lengthy for state-of-the-art QD sizes (typically of the order of 10 nm for the diameter). The dephasing time of the exciton spin given by the above estimation depends upon the magnetic admixture and band-hole concentrations in the DMS because of the concentration-dependence of the factor D . To illustrate this behaviour, several examples are presented in Fig. 11.

For the experimentally observed QD in the structure $\text{Zn}(\text{Mn})\text{Se}/\text{CdSe}$ with a dimension of ~ 10 nm and with concentrations of $x = 0.25$, $x_p = 0.025$, one can estimate using the above formula the spin dephasing time as being of the order of 150 ps, which agrees with the timing of the formation of the EMP experimentally observed in $\text{Zn}_{0.75}\text{Mn}_{0.25}\text{Se}/\text{CdSe}$ (note that, for this structure, the time for exciton annihilation is considerably longer, ~ 600 ps, and the complete formation of the EMP can thus be observed) [65–67].

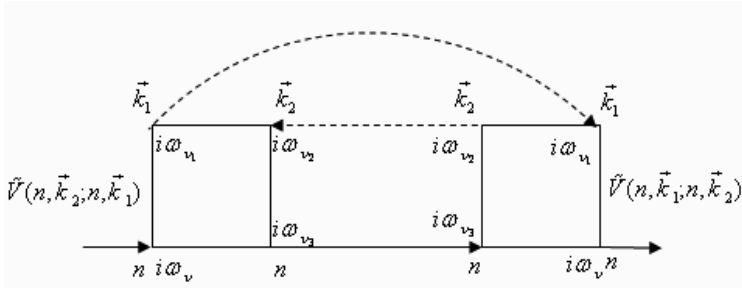


Figure 12. Contribution to the exciton mass operator resulting in the pure dephasing of spin in the state n of an exciton (continuous lines—exciton Green-Matsubara functions, dashed lines—magnon Green-Matsubara functions).

6.4. Explicit form of the interaction of magnons with QD spin causing the spin pure dephasing

An important observation might be made that it is a considerable difference between the phonon- and magnon-assisted dephasing phenomena of charges and spin in QDs, respectively. To demonstrate this difference, it is necessary to analyse the exchange-spin interaction of QD excitons with magnetic admixture spin waves. This interaction can be expressed as follows:

$$\hat{H}_{sd}(\mathbf{R}_e, \mathbf{R}_h) = -2\beta_0 \sum_{\mathbf{n}} A_e(\mathbf{R}_e - \mathbf{R}_n) \hat{\mathbf{s}}_e \cdot \hat{\mathbf{S}}_n - 2\beta_0 \sum_{\mathbf{n}} A_h(\mathbf{R}_h - \mathbf{R}_n) \hat{\mathbf{s}}_h \cdot \hat{\mathbf{S}}_n, \quad (29)$$

where $\hat{\mathbf{s}}_{e(h)}$ is the spin operator of the electron (hole) of the exciton in the QD, \mathbf{R}_n is the position of the magnetic dopant (Mn^{2+}), $\hat{\mathbf{S}}_n$ is the spin operator of the dopant, and the \mathbf{n} summation goes over the lattice sites occupied by magnetic dopants. The term $A_{e(h)}(\mathbf{R}_{e(h)} - \mathbf{R}_n)$ describes the exchange-spin interaction between the electron (hole) spin of the QD exciton and the spin of the dopant, whereas an effective coefficient β_0 accounts for the additional decrease of the exchange integrals due to the dot-structure proximity in real system (β_0 is assumed to be 0.1 as estimated from the experimental data [65, 66]).

For the four-fold spin structure of the QD exciton, we use the notation $(j, n, s_z = \pm \frac{1}{2})$, where $j = 1, 2$ correspond with the anti-parallel and parallel spin alignments of the e-h pair, respectively, and s_z is the spin projection of the electron in the e-h pair. Taking these representations for e-h pair spins $\hat{\mathbf{s}}_{e(h)}$ and the magnon representation (in the Holstein-Primakoff picture) for dopant spins $\hat{\mathbf{S}}_n$ [64], one can rewrite the Hamiltonian (29) in the manner presented below.

By $a_{jns_z}^{(+)}$, we denote the bosonic annihilation (creation) operator of the exciton in the (jns_z) state ($j = 1, 2$ indicates the opposite and the same spin mutual alignment of electron-hole pair creating an exciton, correspondingly; s_z denotes the spin alignment of the electron in electron-hole pair). One can now rewrite the Hamiltonian (29) in the basis of these excitonic states, namely, $\sum_{\mu, \mu'} \langle \mu | H_{sd} | \mu' \rangle a_{\mu}^{\dagger} a_{\mu'}$, where $\mu = (jns_z)$.

Taking the Holstein-Primakoff representation [68] for the spins of dopants and averaging over the dopant random distributions [64] and changing to the magnons— $\hat{a}_i^{(+)}$, $i = 1, 2$

(diagonalization transformation is given explicitly in Ref. 64)—we arrive at the following form of the exchange Hamiltonian (29) [69]:

$$\hat{H}_{sd} = \hat{H}_{sd}^1 + \hat{H}_{sd}^2, \quad (30)$$

$$\begin{aligned} \hat{H}_{sd}^1 = & - \left(\frac{v_0}{(2\pi)^3} \right)^2 2Sx_i\beta_0 \int d^3k_1 \int d^3k_2 [v_{\mathbf{k}_2}\hat{a}_1^+(\mathbf{k}_2) + u_{\mathbf{k}_2}\hat{a}_2^+(\mathbf{k}_2)] \\ & \times [v_{\mathbf{k}_2+\mathbf{k}_1}\hat{a}_1(\mathbf{k}_2 + \mathbf{k}_1) + u_{\mathbf{k}_2+\mathbf{k}_1}\hat{a}_2(\mathbf{k}_2 + \mathbf{k}_1)] \\ & \times \sum_{n,n'} \sum_{s_z=-1/2}^{1/2} s_z \left\{ [F_{nn'}^e(\mathbf{k}_1) - F_{nn'}^h(\mathbf{k}_1)] \hat{a}_{1ns_z}^+ \hat{a}_{1n's_z} \right. \\ & + [F_{nn'}^e(\mathbf{k}_1) + F_{nn'}^h(\mathbf{k}_1)] \hat{a}_{2ns_z}^+ \hat{a}_{2n's_z} \\ & \left. + [F_{nn'}^e(\mathbf{k}_1)\hat{a}_{1ns_z}^+ \hat{a}_{2n's_z} + hc] + [F_{nn'}^h(\mathbf{k}_1)\hat{a}_{1ns_z}^+ \hat{a}_{2n'-s_z} + hc] \right\}, \end{aligned} \quad (31)$$

$$\begin{aligned} \hat{H}_{sd}^2 = & -\sqrt{2Sx_i}\beta_0 \frac{v_0}{(2\pi)^3} \int d^3k \sum_{n,n'} \{ [v_{\mathbf{k}}\hat{a}_1(\mathbf{k}) + u_{\mathbf{k}}\hat{a}_2(\mathbf{k})] \\ & \times [F_{nn'}^e(\mathbf{k}) (\hat{a}_{1n1/2}^+ \hat{a}_{1n'-1/2} \\ & + \hat{a}_{2n1/2}^+ \hat{a}_{2n'-1/2} + \hat{a}_{1n1/2}^+ \hat{a}_{2n'-1/2} + \hat{a}_{2n1/2}^+ \hat{a}_{1n'-1/2}) \\ & + F_{nn'}^h(\mathbf{k}) (\hat{a}_{1n-1/2}^+ \hat{a}_{1n'1/2} \\ & + \hat{a}_{2n1/2}^+ \hat{a}_{2n'-1/2} + \hat{a}_{1n1/2}^+ \hat{a}_{2n'-1/2} + \hat{a}_{2n1/2}^+ \hat{a}_{1n'-1/2})] + hc \}. \end{aligned} \quad (32)$$

In the first part, \hat{H}_{sd}^1 , we can identify the term describing the interaction without any change in the exciton spin (neither the electron nor the hole in the e-h pair). This term thus describes the interaction channel when the spin of the created (annihilated) magnon has to be cancelled by an annihilated (created) magnon (spin is conserved—it is different compared to phonons). It should be emphasized that, in the second part, \hat{H}_{sd}^2 , the exciton spin-flip processes are included only with involvement of a single magnon. Therefore, the term, without any change of the state (the spin state here) and which leads to a pure dephasing of spin, contributes only to \hat{H}_{sd}^1 . The Hamiltonian part \hat{H}_{sd}^2 does not cause any pure dephasing because this part of the interaction does not conserve the exciton state (spin). The term \hat{H}_{sd}^2 always causes an amplitude (diagonal) decoherence as a changing of the exciton spin state.

With the first term in \hat{H}_{sd}^1 , and significantly for the pure dephasing of the QD exciton spin, one can associate the vertex which gives an imaginary part of the mass operator, cf. Fig. 12 (leading to the pure dephasing of the exciton ground state). Note that this is different from that for phonons, cf. Fig. 2.

The imaginary part of the mass operator given by the graph in Fig. 12 can be written as follows:

$$\begin{aligned} \gamma_n(\omega, T) \\ = \pi \sum_{i,j=1}^2 \sum_{\mathbf{k}_1, \mathbf{k}_2} |V(n, \mathbf{k}_1, i; n, \mathbf{k}_2, j)|^2 [n_i(\mathbf{k}_1) + 1] n_j(\mathbf{k}_2) \delta(\omega - E_n - \varepsilon_i(\mathbf{k}_1) + \varepsilon_j(\mathbf{k}_2)), \end{aligned} \quad (33)$$

$n = 0$ comprises here all the exciton ground state quantum numbers $(1, 0, \frac{1}{2})$, and:

$$V(n, \mathbf{k}_1, i; n, \mathbf{k}_2, j)|_{n=0} = \beta_0 2Sx_i \begin{bmatrix} v_{\mathbf{k}_2} v_{\mathbf{k}_1}, v_{\mathbf{k}_2} u_{\mathbf{k}_1} \\ u_{\mathbf{k}_2} v_{\mathbf{k}_1}, u_{\mathbf{k}_2} u_{\mathbf{k}_1} \end{bmatrix} \left(F_{00}^e(\mathbf{k}_1 - \mathbf{k}_2) - F_{00}^h(\mathbf{k}_1 - \mathbf{k}_2) \right),$$

The matrix is addressed to the magnon branches: $\{ij\} = \begin{bmatrix} 11, 12 \\ 21, 22 \end{bmatrix}$, $n_i(\mathbf{k})$ is Bose-Einstein distribution for the i -th magnon branch, $u_{\mathbf{k}}, v_{\mathbf{k}}$ are coefficients of the DMS magnon diagonalization transformation [64], and

$$F_{nn}^{e(h)}(\mathbf{k}) = \tilde{A}_{e(h)}(\mathbf{k}) \int d^3 R_e \int d^3 R_h \Psi_n^*(\mathbf{R}_e, \mathbf{R}_h) e^{i\mathbf{k} \cdot \mathbf{R}_{e(h)}} \Psi_n(\mathbf{R}_e, \mathbf{R}_h),$$

$\tilde{A}_{e(h)}(\mathbf{k}) = \frac{1}{v_0} \int d^3 R A_{e(h)}(\mathbf{R}) e^{-i\mathbf{k} \cdot \mathbf{R}}$, $\Psi_n(\mathbf{R}_e, \mathbf{R}_h)$ is the orbital part of n -th exciton state (for the ground state the trial wave function has been assumed in the form of the Gaussian function, $\Phi_0 = \frac{1}{(\pi)^{3/2}} \frac{1}{L_e L_h L_z} \exp \left[-\frac{r_{e\perp}^2}{2L_e^2} - \frac{r_{h\perp}^2}{2L_h^2} - \frac{z_e^2 + z_h^2}{L_z^2} \right]$, where $r_{e,h\perp}$ are the positions of the electron and hole in the xy plane, $L_{e(h)}$ denotes variational parameters introduced in order to account for e-h Coulomb attraction [64, 70]), $A_{e(h)}(\mathbf{R}) = A_{e(h)} e^{-2R/l_{ex}}$ with the range of the exchange $l_{ex} \sim a$, ($a^3 = v_0$), $\tilde{A}_{e(h)}(\mathbf{k}) = \frac{\tilde{A}_{e(h)}(0)}{[1+k^2 l_{ex}^2/4]^2}$, $\tilde{A}_{e(h)}(0) = \frac{\pi^2}{4} \frac{l_{ex}^3}{v_0} A_{e(h)}$.

The imaginary part of the mass operator can be rewritten in the form:

$$\begin{aligned} \gamma_0(\omega, T) = & \pi \sum_{\mathbf{k}_1, \mathbf{k}_2} |V(\mathbf{k}_1 - \mathbf{k}_2, 0)|^2 \\ & \times \left\{ [n_1(\mathbf{k}_1) + 1] n_1(\mathbf{k}_2) v_{\mathbf{k}_2}^2 v_{\mathbf{k}_1}^2 \delta(\omega - E_0 - \varepsilon_1(\mathbf{k}_1) + \varepsilon_1(\mathbf{k}_2)) \right. \\ & + [n_1(\mathbf{k}_1) + 1] n_2(\mathbf{k}_2) v_{\mathbf{k}_2}^2 u_{\mathbf{k}_1}^2 \delta(\omega - E_0 - \varepsilon_1(\mathbf{k}_1) + \varepsilon_2(\mathbf{k}_2)) \\ & + [n_2(\mathbf{k}_1) + 1] n_1(\mathbf{k}_2) u_{\mathbf{k}_2}^2 v_{\mathbf{k}_1}^2 \delta(\omega - E_0 - \varepsilon_2(\mathbf{k}_1) + \varepsilon_1(\mathbf{k}_2)) \\ & \left. + [n_2(\mathbf{k}_1) + 1] n_2(\mathbf{k}_2) u_{\mathbf{k}_2}^2 u_{\mathbf{k}_1}^2 \delta(\omega - E_0 - \varepsilon_2(\mathbf{k}_1) + \varepsilon_2(\mathbf{k}_2)) \right\}, \end{aligned} \quad (34)$$

with $\varepsilon_1(\mathbf{k}) = Dk^2$, $\varepsilon_2(\mathbf{k}) = D_0 - Dk^2$, $V(\mathbf{k}_1 - \mathbf{k}_2, 0) = \beta_0 2Sx(F_{00}^e(\mathbf{k}_1 - \mathbf{k}_2) - F_{00}^h(\mathbf{k}_1 - \mathbf{k}_2)) = f(\mathbf{k}_1 - \mathbf{k}_2 = \mathbf{k}) = A \frac{e^{-\alpha k^2}}{[1+\kappa k^2]^2}$, $A = \beta_0 2Sx(\tilde{A}_e(0) - \tilde{A}_h(0))$, $\kappa = l_{ex}^2/4$, $\alpha = l^2/2$ (l —the dimension of the exciton in the ground state averaged over all directions [70]). Finally:

$$\begin{aligned} \gamma_0(\omega, T) = & \pi A^2 \sum_{\mathbf{k}_1, \mathbf{k}_2} \frac{e^{-2\alpha(k_1 - k_2)^2}}{[1+\kappa(k_1 - k_2)^2]^4} \\ & \times \left\{ [n_1(k_1) + 1] n_1(k_2) v_{\mathbf{k}_2}^2 v_{\mathbf{k}_1}^2 \delta(\omega - E_0 - D(k_1^2 - k_2^2)) \right. \\ & + [n_1(k_1) + 1] n_2(k_2) v_{\mathbf{k}_2}^2 u_{\mathbf{k}_1}^2 \delta(\omega - E_0 + D_0 - D(k_1^2 + k_2^2)) \\ & + [n_2(k_1) + 1] n_1(k_2) u_{\mathbf{k}_2}^2 v_{\mathbf{k}_1}^2 \delta(\omega - E_0 - D_0 + D(k_1^2 + k_2^2)) \\ & \left. + [n_2(k_1) + 1] n_2(k_2) u_{\mathbf{k}_2}^2 u_{\mathbf{k}_1}^2 \delta(\omega - E_0 - D(k_2^2 - k_1^2)) \right\}, \end{aligned} \quad (35)$$

$$n_1(k) = \frac{1}{e^{Dk^2/kT}-1}, n_2(k) = \frac{1}{e^{(D_0-Dk^2)/kT}-1} \text{ and (for small } k, k/k_{max} \ll 1, k_{max} = \pi/a) u_k^2 = \frac{x_p}{x_p+2Sx} - Bk^2, v_k^2 = \frac{2Sx}{x_p+2Sx} + Bk^2, B = \frac{x_p}{x} \frac{2S-x_p/x}{(2S+x_p/x)^3} 2Sl_{ex}^2, D_0 = -\tilde{A}_p(0)(x_p + 2Sx), D = -\tilde{A}_p(0) \frac{2Sx_p x}{x_p+2Sx} l_{ex}^2.$$

The above formula (35) allows for the calculation of the correlation function $I(t)$ and the estimation of the spin dephasing timing. The results are presented in Fig. 11.

It should be emphasized that due to spin conservation in the vertex, the two magnons must take part simultaneously in the interaction, which is responsible for the dressing of the exciton state with the magnon cloud (i.e., this interaction part, which causes the pure dephasing of the exciton spin). This property leads, however, to the special temperature-dependent factors $[n_i(k_1) + 1]n_j(k_2) \rightarrow 0$ (for $T \rightarrow 0$) which occur in the equation for $\gamma_0(\omega, T)$. These factors tend towards zero with decreasing temperature and completely freezes the pure dephasing of the exciton spin at $T = 0$ (in contrast to the charge dephasing process by phonons, which is maintained strong even at $T = 0$ —this is due to the emission factor $1 + n(k) \rightarrow 1$ for $T \rightarrow 0$, i.e., a non-zero low temperature limit for a triangle-type vertex with phonons). Additionally, let us note that for magnons at low temperatures $n_1 \gg n_2$, and due to the magnon gap, contribute only the terms with $n_1(1 + n_i), (i = 1, 2)$.

7. Magnon-induced versus phonon-induced QD exciton dephasing

Due to the different types of vertex interactions responsible for pure dephasing, namely exciton-phonon (triangle vertex) and exciton-magnon (quadratic vertex), they lead to significantly different phenomena. Spin conservation in the vertex (during interaction) requires the participation of two magnons (the exciton spin state remains unchanged), unlike phonons, in which case single-photon emission or absorption is feasible with the exciton state unchanged. For magnons, magnon emission must be accompanied by magnon absorption (in order to balance the loss of spin in the vertex due to the spin wave emission—equation (33)). Although factors corresponding to the emission (of type $[1 + n]$) assume non-zero values even at $T = 0$ (this is true for phonons as well), the absorption factor (of type n ; the probability of magnon absorption is proportional to the number of magnons) falls to zero for $T \rightarrow 0$, and this is the reason why exciton spin dephasing by magnons becomes smaller and smaller ($\rightarrow 0$) as the temperature falls to $T = 0$ (in the case of phonons, dephasing remains non-zero even at $T = 0$ due to *only* phonon emission, even in a phonon vacuum for $T = 0$). Moreover, for magnons, $n_2 \ll n_1$ in the limit $T \rightarrow 0$ (due to a magnon gap) and therefore at low temperatures only terms with factors $n_1(1 + n_i)$ contribute.

At higher temperatures, when the number of thermodynamic magnons (liable to absorption) increases sufficiently, magnon-induced spin dephasing is as effective as phonon-induced charge dephasing. The difference between both effects presented herein emphasizes the fact that spin is more resistant to DMS-magnon-induced dephasing at low temperatures due to spin conservation constraints in comparison to phonon-induced charge dephasing (which is strong even at $T = 0$).

8. Conclusions

In conclusion, we can state that in the case of QDs we deal with a specific type of phonon-induced phenomenon, which is essentially distinct from the phonon-induced effects

in bulk semiconductors. This difference is caused by the compatibility of the energy scale for carriers trapped in QDs with the band-phonon energy scale. Owing to this energy coincidence, the coupling of carriers in QDs with phonons always meets its strong regime limit. This coupling cannot be treated perturbatively, in general, and the resonance effects are of primary importance, resulting in strong polaron-type modifications of the QD electron and exciton spectra. The typical energy shift due to the formation of electron-polaron is of the order of 10%, while for exciton-polaron it is of the order of 5% with respect to the bare energy levels in QDs treated as separated from the environment. The confinement of carriers, as in the case of QDs, also causes the significant enhancement of the effective Fröhlich constant due to non-adiabatic effects, which additionally strengthens the electron-LO phonon interaction. The dressing of the electrons/holes/excitons in QDs with band phonons from the surrounding crystal induces the dephasing of charge (orbital degrees of freedom) in QDs (the off-diagonal decoherence). The typical time-scale of this dressing process in the case of the formation of an exciton-polaron in QDs turns out to be of the one picosecond time-scale (for a typical QD of 10 nm diameter). This dephasing is caused by the exciton dressing with LA phonons. Worth noting is the observation that the dephasing due to LO phonons is considerably smaller and slower—of the 100 ps scale. This phenomenon is caused by the relatively weak LO phonon dispersion near the Γ point (in the Brillouin zone), in contrast to the dispersion of LA phonons. Nevertheless, the outflow of the excess polarization energy to the space region outside the QD, as a typical process during LO polaron formation, is eventually accelerated by the anharmonic coupling (LO-TA is the most important anharmonic channel in GaAs), which results in a few ps time-scale. It is important to note that these effects of QD-charge dephasing by band phonons refer not only to QDs but also to all nanostructures in solids, because the carrier localization (the space-confinement of trapped carriers) plays the essential role here.

We have observed also that in magnetically-ordered media (like in DMSs), magnons (spin waves) play a similar destructive role to phonons. Spin waves cause the dephasing of the exciton spin in QDs, in a process of the formation of excitons-magnon-polarons by the step-by-step dressing of the local spin of exciton in QD with the magnon cloud from the surrounding magnetically-ordered medium. By using the Green function technique, we have estimated the time for the dressing of the local exciton spin with band magnons in the case of DMSs which surround QDs by analogy to the dressing of QD charge (i.e., QD orbital degrees of freedom) with band phonons from the surrounding crystal. Nevertheless, the significant difference between these two phenomena is observed and elucidated, namely, in the case of spin dressing two magnons are needed (creation and annihilation) owing to the spin conservation in the interaction vertex, which results in the complete freezing (vanishing) of the spin pure dephasing at $T = 0$. This is in contrast to the phonon-induced pure dephasing, which maintains strong even at $T = 0$.

The dephasing scheme for the exciton charge and spin in QD structures is important for the feasibility assessment of QIP implementations in QDs. The picoseconds time-rate for QD charge dephasing probably precludes the feasibility of the implementation of error-correction schemes for all optically-controlled gates in QD technologies. The dressing of a localized spin with magnons in a DMS (i.e., the time corresponding to the formation of EMP in a QD) takes place at a longer time-scale in comparison to dressing charges with phonons, and the related time-scale is of the order of 150-200 picoseconds due to the relatively weak quadratic magnon dispersion, similar to as was the case for LO phonons. Nevertheless, the time-rate for QD spin dephasing induced by magnons in the surrounding DMS is also inconvenient for QIP

applications, similarly to the case of the dephasing of QD charges by phonons. The overall time-scale for QD spin kinetics (QD/DMS-embedded structures) is shifted by three-orders of magnitude to longer periods in comparison to QDs' orbital degrees of freedom, though again with the same inconvenient dephasing time-rate falling right in the middle between the control-timing and the relaxation-timing (which does not allow the satisfaction of the DiVincenzo conditions). In this way, the 'three-orders time-limit' caused by the dephasing phenomena is repeated for spin in the QD/DMS.

The pure dephasing of spin in QD/DMS structures disappears, however, at $T = 0$, and is strongly suppressed in amplitude at low temperatures (in contrast to the charge dephasing), which supports expectations of some advantages of spin degrees of freedom in QDs for QIP applications.

Author details

Witold Aleksander Jacak

Institute of Physics, Wrocław University of Technology, Wrocław, Poland

References

- [1] L. Jacak, P. Hawrylak, A. Wójs, *Quantum Dots*, Springer Verlag, Berlin, 1998
- [2] Y. Masumoto, T. Takagahara, *Semiconductor Quantum Dots*, Springer Verlag, Berlin, 2002
- [3] R. C. Ashoori, *Nature*, **379**, 413 (1996)
- [4] L. Jacak, A. Wójs, P. Machnikowski, *Semiconductor Quantum Dots*, Encyclopedia of Nanoscience and Nanotechnology, American Sc. Publ. 2004, www.aspbs.com/enn
- [5] L. Jacak, P. Machnikowski, *Quantum Dots*, Encyclopedia of Nanoscience and Nanotechnology, American Sc. Publ. 2007
- [6] L. Jacak, J. Krasnyj, M. Korkusiński, A. Wójs, *Phys. Rev. B* **57**, 9069 (1998)
- [7] *Roadmap in Quantum Information*, ARDA Report 2002, www.qist.lanl.gov
- [8] W. Jacak, W. Donderowicz, L. Jacak, *Introduction to Quantum Information Processing*, e-materials, PWr, Wrocław 2004
- [9] M. A. Nielsen, I. L. Chuang, *Quantum Computation and Quantum Information*, Cambridge UP 2000
- [10] D. Aharonov, *Quantum Computation*, quant-ph/98 12037 (1999)
- [11] S. Stenholm, K. A. Suominen, *Quantum Approach to Informatics*, Wiley-Interscience, New Jersey, 2005
- [12] J. Preskill, *Quantum Information and Computation*, <http://www.theory.caltech.edu/preskill/ph229> (1998)

- [13] D. Bouwmeester, A. Ekert, A. Zeilinger, *The Physics of Quantum Information*, Springer-Verlag, Berlin, 2000
- [14] *Quantum Information Processing and Communication—Strategic Report on Current Status*, ICT European Commission (Ed. P. Zoller) 2005, www.cordis.lu/ist/fet/qipc.htm; *Roadmap in Quantum Information*, ARDA Report 2002, www.qist.lanl.gov
- [15] D. P. DiVincenzo, D. Loss, Superlattices and Microstructures **23**, 419 (1998)
- [16] D. Loss, D. P. DiVincenzo, Phys. Rev. A **57**, 120 (1998)
- [17] A. V. Kitaev, Annals Phys. **303**, 2 (2003)
- [18] C. H. Bennett, Phys. Rev. Lett. **68**, 3121, (1992)
- [19] J. M. Kikkawa, D. D. Awschalom, Phys. Rev. Lett. **80**, 4313 (1998)
- [20] D. P. DiVincenzo, D. Bacon, J. Kempe, G. Burkard, K. B. Whaley, Nature **408**, 339 (2000)
- [21] A. C. Davydov, *Solid state theory*, Nauka, Moskwa, 1976
- [22] G. D. Mahan, *Many-particle Physics*, Kluwer, New York, 2000
- [23] K. Huang, A. Rhys, Proc. R. Soc. London (A) **204**, 406 (1950)
- [24] L. Jacak, J. Krasnyj, W. Jacak, Phys. Lett. A **304**, 168 (2002)
- [25] L. D. Landau, E. M. Lifschic, *Quantum Mechanics*, PWN, Warszawa, 1979
- [26] S. Hameau, Y. Guldner, O. Verzelen, R. Ferreira, G. Bastard, J. Zeman, A. Lemaître, J. M. Gerard, Phys. Rev. Lett. **83**, 4152 (1999)
- [27] L. Jacak, J. Krasnyj, D. Jacak, P. Machnikowski, Phys. Rev. B **65** 113305 (2002)
- [28] L. Jacak, J. Krasnyj, W. Jacak, R. Gonczarek, P. Machnikowski, Phys. Rev. B **72**, 245309 (2005)
- [29] O. Verzelen, R. Ferreira, G. Bastard, Phys. Rev. Lett. **88**, 146803 (2002)
- [30] P. Borri, W. Langbein, S. Schneider, U. Woggon, R. L. Sellin, D. Ouyang, D. Bimberg, Phys. Rev. Lett. **87**, 157401 (2001)
- [31] D. Strauch, B. Dorner, J. Phys: Cond. Matt. **2**, 1457 (1990)
- [32] U. Bockelmann, G. Bastard, Phys. Rev. B **42**, 8947 (1990)
- [33] E. A. Muljarov, R. Zimmermann, Phys. Rev. Lett. **98**, 187401 (2007)
- [34] L. Jacak, P. Machnikowski, J. Krasnyj, P. Zoller, Eur. Phys. J. D **22**, 319 (2003)
- [35] L. Jacak, J. Krasnyj, D. Jacak, P. Machnikowski, Phys. Rev. B **67**, 035303 (2003)

- [36] A. Suna, *Phys. Rep.* **135**, A111 (1964)
- [37] A. A. Abrikosov, L. P. Gorkov, I. E. Dzyaloshinski, *Methods of Quantum Field Theory in Statistical Physics*, Dover Publications, New York, 1975
- [38] A. L. Fetter, J. D. Walecka, *Quantum Theory of Many Particle Systems*, PWN, Warszawa, 1982
- [39] V. L. Bonch-Bruевич, S. V. Tyablikov, *The Green Function Method in Statistical Mechanics*, North-Holland, Amsterdam, 1962
- [40] C. A. Moskalenko, M. I. Smigliuk, B. I. Chinik, *Fiz. Tverdogo Tela* **10**, 351 (1968)
- [41] S. Adachi, *J. Appl. Phys.* **58**, R1 (1985)
- [42] P. Machnikowski, L. Jacak, *Phys. Rev. B* **71**, 115309 (2005)
- [43] L. Jacak, J. Krasnyj, A. Wójs, *Physica B* **229**, 279 (1997)
- [44] N. W. Ashcroft, N. D. Mermin, *Solid State Physics*, Holt, Rinehardt and Winston, New York, 1976
- [45] L. Jacak, J. Krasnyj, D. Jacak, W. Salejda, A. Mituś, *Acta. Phys. Pol. A* **99**, 277 (2001)
- [46] T. Story, R. R. Gałazka, R. B. Frankel, P. A. Wolff, *Phys. Rev. Lett.* **56**, 777 (1986)
- [47] H. Ohno, H. Munekata, T. Penney, S. von Molnar, L. J. Chang, *Phys. Rev. Lett.* **68**, 2664 (1992); H. Ohno, *Science* **281**, 951 (1998)
- [48] J. K. Furdyna, *J. Appl. Phys.* **64**, R29 (1988)
- [49] T. Dietl, H. Ohno, F. Matsukura, *Phys. Rev. B* **63**, 195205 (2001)
- [50] D. Ferrand, J. Cibert, A. Wasiela, C. Bourgoignon, S. Tatarenko, G. Fishman, T. Andrearczyk, J. Jaroszyński, S. Kolesnik, T. Dietl, B. Barbara, and D. Dufeu, *Phys. Rev. B* **63**, 085201 (2001)
- [51] H. Ohno, *Science* **281**, 951 (1998)
- [52] S. Das Sarma, E. H. Hwang, A. Kaminski, *Phys. Rev. B* **67**, 155201 (2003)
- [53] M. Csontos, G. Mihaly, B. Jankó, T. Wojtowicz, X. Liu, J. K. Furdyna, *Nature Materials* **4**, 447 (2005)
- [54] W. Jacak, J. Krasnyj, L. Jacak, S. Kaim, *Phys. Rev. B* **76**, 165208 (2007)
- [55] N. P. Kovalenko, J. Krasnyj, U. Krey, *Physics of Amorphous Metals*, Wiley-CH, Berlin, 2001
- [56] Ch. Kittel, *Quantum Theory of Solids*, John Willey, New York, 1968
- [57] A. I. Akhieser, V. G. Baryakhtar, S. V. Peletminskii, *Spin Waves*, North Holland, Amsterdam, 1968

- [58] T. Dietl, H. Ohno, F. Matsukura, Phys. Rev. B **63**, 195205 (2001)
- [59] J. König, H. H. Lin, A. H. MacDonald, Phys. Rev. Lett. **84**, 5628 (2000)
- [60] H. Ohno, A. Shen, F. Matsukura, A. Oiwa, A. Endo, S. Katsumoto, Y. Iye, Appl. Phys. Lett. **69**, 363 (1996)
- [61] J. König, T. Jungwirth, A. H. MacDonald, Phys. Rev. B **64**, 184423 (2001)
- [62] M. Berciu, R. N. Bhatt, Phys. Rev. B **66**, 085207 (2002)
- [63] J. Schliemann, J. König, A. H. MacDonald, Phys. Rev. B **64**, 165201 (2001)
- [64] W. Jacak, J. Krasnyj, L. Jacak, S. D. Kaim, Phys. Rev. B **76**, 165208 (2007)
- [65] J. Seufert, G. Bacher, M. Scheibner, A. Forchel, S. Lee, M. Dobrowolska, J. K. Furdyna, Phys. Rev. Lett. **88**, 027402 (2002)
- [66] H. Schömig, M. K. Welsch, G. Bacher, A. Forchel, S. Zaitsev, A. A. Maksimov, V. D. Kulakovskii, S. Lee, M. Dobrowolska, J. K. Furdyna, Physica E **13**, 512 (2002)
- [67] J. Seufert, M. Scheibner, G. Bacher, A. Forchel, S. Lee, M. Dobrowolska, J. K. Furdyna, Phys. Stat. Sol. (b) **229**, 727 (2002)
- [68] Ch. Kittel, *Quantum Theory of Solids* (John Willey, New York, 1968)
- [69] W. Jacak, J. Krasnyj, L. Jacak, Phys. Rev. B **78**, 073303 (2008)
- [70] L. Jacak, J. Krasnyj, W. Jacak, R. Gonczarek, P. Machnikowski, Phys. Rev. B **72**, 245309 (2005)

Charge States in Andreev Quantum Dots

Ivan A. Sadovskyy, Gordey B. Lesovik and
Valerii M. Vinokur

Additional information is available at the end of the chapter

<http://dx.doi.org/10.5772/60482>

Abstract

We study the charge states in Andreev quantum dot, the metallic quantum dot coupled to the superconducting ring. We show that breaking the electron-hole symmetry in a superconductor generates non-integer charge, localized in a metallic part of the Andreev quantum dot. We demonstrate that this non-integer charge varies continuously as a result of the electrostatic gating and/or change in the phase difference between the superconducting banks. We investigate charge fluctuations associated with the electron-phonon coupling and Coulomb interactions. We propose a recipe for measuring the charge enabling the design of a sensor for weak magnetic fields whose working element is the Andreev quantum dot.

Keywords: superconductivity, Andreev quantum dot, non-integer charge

1. Introduction

A relation between the charge and phase of the order parameter in superconductors is one of the central issues of physics of superconductivity. The nondissipative supercurrent is related to the gradient of the superconducting phase, in particular, Josephson current is caused by the phase difference φ at the banks of the contacts [1, 2]. The static charges are intimately connected with the singularities in the phase distribution. The point singularity associated with the zero of the order parameter, around which the phase, when encircling singularity, gains 2π are superconducting vortices [3], which can be viewed as filaments of the normal metal (vortex normal cores) surrounded by encircling supercurrents. The quasiparticle states that form in the core, so-called Caroli-de Gennes-Matricon or Andreev states, carry the small excess charge ek_F per unite length [4, 5], where e is the electronic charge and k_F is the Fermi wave vector of the underlying normal metal. This excessive charge stems from the violation of symmetry between electrons and holes. Since Andreev state are

the base for variety of the emerging superconducting devices, like, for example, Josephson transistors [6–8], the study of physics of the charge states associated with the Andreev levels is of prime importance not only from the fundamental science viewpoint but is critical for applications of superconductors.

We will focus on the charge states associated with the Andreev levels in a so-called Andreev quantum dot. The latter is a metallic quantum dot coupled via tunneling contacts to a superconducting ring [9, 10], see Fig. 1, where breaking the symmetry between electrons and holes gives rise to a localized charge [10, 11]. This charge can be continuously changed by variation of the phase difference between the superconducting banks φ and the gate voltage V_g , hence the charge is not necessarily an integer. In particular, a singly excited state (where the number of Bogoliubov quasiparticles is odd) carries an integer charge, whereas the ground state and a doubly excited states (with the even number of Bogoliubov quasiparticles) carry non-integer charge.

Condensed matter physics is mostly dealing with the situations where the charges appear as multiple integers of the electron elemental charge e . Notable examples where fractional charges appear are fractional Hall effect [12–14] and Luttinger liquid [15–17]. In either case fractional charge appears due to averaging over time. The charges at the Andreev dot that we will discuss here also appear due to averaging over time, but do not have some fixed fractionality and can be altered continuously by tuning external parameters such as superconducting phase difference and gate voltage. Continuously tunable charges in mesoscopic systems were discussed, e.g., in Refs. [18, 19]. There, the appearance of the non-integer charge is ensured by the peculiarity of corresponding wave function partially localized in the quantum dot; exponentially decaying wave function “tails” comprise the rest of an integer charge. Here we will discuss the non-integer charge completely localized in a quantum dot, while the rest is localized far away in the superconducting condensate. Non-integer charges we will be dealing with, resemble fractional charges associated with the excitations in superconductors and are discussed in the context of the charge relaxation in nonequilibrium superconductivity [20, 21]. The examples of measurable manifestations of the non-integer charge include the telegraph signal arising due to stochastic occupation of the Andreev levels [9, 10] and the dependence of the charge upon magnetic flux piercing a superconducting ring. This opens route for designing the Andreev dot-based device for measuring weak magnetic fields [22].

This chapter is organized as follows: In Sec. 2 we introduce preliminaries relating to the origin of the fractional charge in the Andreev quantum dot, and in Secs. 3 and 4 turn to the detailed analysis of the charge and energy states respectively. In Secs. 5–7 we describe the

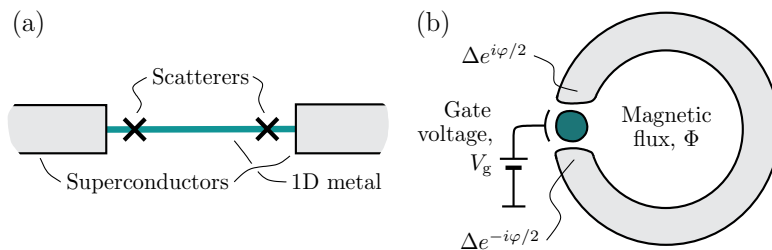


Figure 1. (a) Sketch of the Andreev quantum dot: A quantum dot connected to superconducting banks. (b) Andreev quantum dot driving by magnetic flux $\Phi = (\varphi/2\pi)\Phi_0$ threading the superconducting loop and by gate voltage V_g .

possible sources of the fluctuations of the fractional charge. Section 8 is devoted to effects of Coulomb interaction. In Sec. 9 we discuss the scalability of the charge. In Sec. 10 we describe the means for detecting the fractional charge, and in Sec. 11 the possibility of using the fractional charge in the Andreev quantum dot for detecting weak magnetic fields.

2. The origin of the fractional charge

Andreev reflection is at the heart of the physics of mesoscopic superconducting structures [23–25]. At the normal metal-superconductor (NS) interface an electron (hole) incident on the interface from the normal metal (N) at energies E less than the superconducting energy gap, $|E - E_F| < \Delta$ (E_F and Δ are the Fermi energy and the superconducting gap, respectively), cannot enter the superconductor (S) and is reflected as a hole (electron) moving in the direction opposite to that of incident electron (hole) into the normal metal. To form a hole, the electron in the $|k\rangle$ state pulls an electron in the $|-k\rangle$ state and transmits into the superconductor forming a Cooper pair. Note that at the ideal NS-interface the reflection of an electron is complete (i.e. the reflection coefficient is unity) and does not depend on the energy of the incident electron.

In the superconductor-normal metal-superconductor (SNS) contact, an electron impinging on one of the interfaces is Andreev reflected and converted into a hole moving in the opposite direction, thus generating a Cooper pair at the interface, and is converted back to an electron, leading to the destruction of the Cooper pair in the other superconductor, see Fig. 2(a). As a result of this cycle, a pair of correlated electrons is transferred from one superconductor to another, creating a supercurrent flow across the junction. The resulting state in a normal region maintains the electron-hole symmetry hence carrying an integer, if measured in the electron charge units, charge (we disregard hereafter a slight violation of the electron-hole symmetry of the order of Δ/E_F arising due to finiteness of the Fermi energy).

Adding a normal scatterer to each of the NS-interfaces would form so-called non-ideal normal metal-insulator-superconductor (NIS) interface, at which the scattering acquires both, Andreev and normal components, the latter being strongly energy-dependent, see Fig. 2(b). As a result in a SINIS junction the electron-hole symmetry breaks down. This is easily understood in terms of electron- and hole lifetimes within the normal region. In SNS contact these times coincide with the accuracy of Δ/E_F . The presence of scattering resonances breaks this symmetry drastically. Indeed, if the quasiparticle energy, ε , is close to resonance ε_D (both

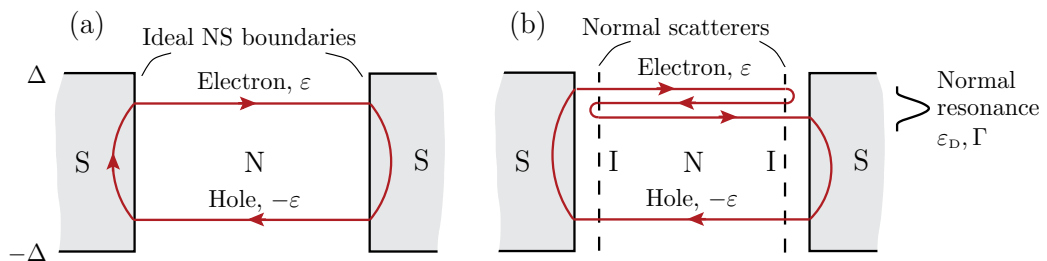


Figure 2. (a) Andreev reflection in the SNS junction with the ideal NS interfaces. (b) Andreev reflection in the SINIS junction: the scattering at the INI part is of the resonance character which results in violation of the electron-hole symmetry. The panel displays electron-like resonance, $\varepsilon_D > 0$.

ε and ε_D are measured from the Fermi level), more precisely, if $|\varepsilon - \varepsilon_D| < \Gamma$, where Γ is the resonance half-width, the probability of the normal reflection is appreciably enhanced, hence so does the time the quasiparticle dwells near the resonance. Shown in Fig. 2(b) is the electron-like resonance with $\varepsilon_D > 0$ where a quasiparticle spends the better share of time in the electron-like rather than in the hole-like state. Inversely, for $\varepsilon_D < 0$, the quasiparticle is predominantly a hole-like one.

More insight into Andreev states in a SINIS contact can be gained via the initial study a corresponding NININ structure where all the superconductors are substitute by normal metals. In this case every resonance turns into the corresponding Andreev level. Electron-like resonances above Fermi level, i.e. with $\varepsilon > 0$, correspond to electron-like Andreev states with the negative excitation charge, while hole-like resonances with $\varepsilon < 0$ correspond to hole-like Andreev levels with the positive excitation charge. These states can transform one into another via changing the gate potential V_g or the phase difference φ along the contact.

3. A single Andreev level

In this section we discuss a single quantum conducting channel for a spinless particle, i.e. a single Andreev level. We demonstrate that such a channel can carry a charge $Q \in [0 \dots 2e]$. Hereafter e is the negative charge of the electron, accordingly, $-e$ is the positive charge of the hole. We focus on the study of the charge Q as a function of the difference of the superconducting phase φ , and the position, ε_D , of the normal resonance with respect to the Fermi level. We thus adopt a model where both superconductor and metal are one-dimensional (1D), which captures all the essentials of SINIS behavior. Accounting for realistic peculiarity of the massive superconductor/normal metal contact would change quantitative characteristics of transport across SINIS, but not its qualitative behavior.

In order for only a single Andreev level contributed to a current, only a single resonance must fall into the superconducting gap energy interval, $\varepsilon_D \in [-\Delta \dots \Delta]$, and accordingly the resonances spacing, δ , well exceeded the superconducting gap,

$$\delta \gg \Delta. \quad (1)$$

This condition is equivalent to the requirement that the SINIS junction were short, i.e. that $L \ll \xi$, where L is the length of the normal segment, and $\xi = \hbar v_F / \Delta$ is the coherence length. Furthermore, the "tails" of the adjacent resonances should not appear within the $[-\Delta \dots \Delta]$ interval, therefore, we let also the half-widths of the adjacent resonances which are approximately the same as that of the resonance involved, Γ , were much less the resonance spacing, $\Gamma \ll \delta$. All these conditions are easily realized in experiment, see Fig. 3.

The Andreev quantum dots can be designed on the basis of single-wall carbon nanotubes [26–30] or molecule [31–33]. The nanotube can be attached suspending between the two superconducting leads, or else can be placed on the dielectric substrate, the superconducting contacts being sputtered on it. The normal scatterers can be realized via two extra gates that suppress electron density at the predesigned points creating two 1D scatterers with the transmission amplitudes t_L and t_R , see Fig. 3. The gates form the Andreev quantum dot at the nanotube. The main gate of the length of the order of the normal part of the junction creates

an extra potential V_g in the nanotube which tunes the position of the normal resonance with respect to the Fermi energy ε_D .

We start our description of the charge states in SINIS adopting the characteristics (positions and half-widths) of the resonances in the NININ junction, equivalent to the SINIS one. To this end let us consider the problem of the eigenvalues of the normal state Hamiltonian $\hat{\mathcal{H}}_0 \Psi = E \Psi$, defined by

$$\hat{\mathcal{H}}_0 = -\frac{\hbar^2}{2m} \frac{\partial^2}{\partial x^2} + U(x) - E_F. \quad (2)$$

The 1D potential describing the NININ junction,

$$U(x) = U_{ps,L}(x + L/2) + U_{ps,R}(x - L/2) + eV_g \theta(L/2 - |x|), \quad (3)$$

consists of two contributions, $U_{ps,L}$ and $U_{ps,R}$, from the point scatterers and of the gate potential V_g , which is taken to be much smaller than the Fermi energy, $eV_g \ll E_F$. The scatterers are endowed with the transmission and reflection amplitudes $t_\ell = \sqrt{T_\ell} e^{i\chi_\ell^t}$ and $\sqrt{R_\ell} e^{i\chi_\ell^r}$, respectively; $\ell = L$ (left), R (right), $R_\ell + T_\ell = 1$.

In Eq. (3) the Heaviside step function is $\theta(x) = 0$ for $x < 0$ and $\theta(x) = 1$ for $x > 0$. The eigenvalues of this problem are resonance energies

$$E_n = \varepsilon_L \left(n\pi - \frac{\chi_L^r}{2} - \frac{\chi_R^r}{2} \right)^2, \quad (4)$$

where $\varepsilon_L = \hbar^2/2mL^2$ is the energy defining the quantization along the contact. The levels (4) separation (spacing) is

$$\delta_n = \frac{E_{n+1} - E_{n-1}}{2} = 2\pi\sqrt{\varepsilon_L E_n} \approx \frac{2E_n}{n}, \quad (5)$$

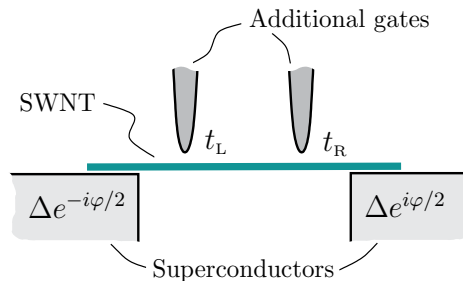


Figure 3. The Andreev quantum dot can be realized adding two gates to the SINIS structure, which deplete the electron density at the designed spots and form the effective barriers with the transmission amplitudes t_L and t_R .

and have half-widths

$$\Gamma_n = \frac{1 - \sqrt{R_L R_R}}{\sqrt[4]{R_L R_R}} \sqrt{\varepsilon_L E_n}. \quad (6)$$

If $T_L, T_R \ll 1$ formula (6) reduces to

$$\Gamma_n = \frac{T_L + T_R}{2} \sqrt{\varepsilon_L E_n} = \frac{T_L + T_R}{2} \frac{\delta_n}{2\pi}. \quad (7)$$

Gate potential shifts all the resonances over eV_g . Let us denote the position of the n -th resonance with respect to Fermi level E_F as $\varepsilon_D = E_n + eV_g - E_F$. Hereafter, the subscript n enumerating the resonances we will be omitted.

Now let us return from the ordinary normal quantum dot to the Andreev one, replacing the normal banks by the superconducting ones. To include the Andreev reflection processes in the SINIS, we solve Bogoliubov-de Gennes equations choosing the states with $\varepsilon_A \geq 0$,

$$\begin{bmatrix} \hat{\mathcal{H}}_0(x) & \hat{\Delta}(x) \\ \hat{\Delta}^*(x) & -\hat{\mathcal{H}}_0(x) \end{bmatrix} \begin{bmatrix} u(x) \\ v(x) \end{bmatrix} = \varepsilon_A \begin{bmatrix} u(x) \\ v(x) \end{bmatrix}, \quad (8)$$

with the piecewise smooth superconducting gap

$$\hat{\Delta}(x) = \Delta [\theta(-x - L/2) e^{-i\varphi/2} + \theta(x - L/2) e^{i\varphi/2}]. \quad (9)$$

Here $u(x)$ and $v(x)$ are the electron- and hole components of the wave function and ε_A is an excitation energy for the system, i.e. the energy acquired by the system upon adding a quasiparticle. The superconducting gap $\hat{\Delta}(x)$ describes bulk superconductors having the phase $-\varphi/2$ at the left bank and $\varphi/2$ at the right hand side one.

One can solve Eqs. (8) by matching plane wave solution for the normal and decaying solutions in a superconductor. We employ, however a more technique approach based on the scattering matrices approach, which utilizes the fact that the transfer-matrices of the series of the contacts is merely a product of all the respective sequential matrices corresponding to individual contact [34]. This is in fact a generalization of the wave functions matching approach but applied to NS boundaries only and including the characteristics of the normal part as parameters. Let us denote the amplitudes of transmission and reflection of the INI part as $\sqrt{T} e^{\chi^t}$ and $\sqrt{R} e^{\chi^r}$, respectively. In the Andreev approximation we find

$$\cos(S_+ - S_- - 2\alpha) = \sqrt{R_+ R_-} \cos \beta + \sqrt{T_+ T_-} \cos \varphi. \quad (10)$$

Here subscripts “ \pm ” refer to the probabilities and phases of reflection/transmission from/through the INI part corresponding to energies $\pm\varepsilon_A$. This parametrization presumes no electron-hole scattering within INI. The phase $\alpha = \arccos(\varepsilon_A/\Delta)$ is but the Andreev reflection phase at the ideal NS boundary at $\varphi = 0$. The phases $S_{\pm} = \chi_{\pm}^t + k_{e/h}L$ stand for the phase

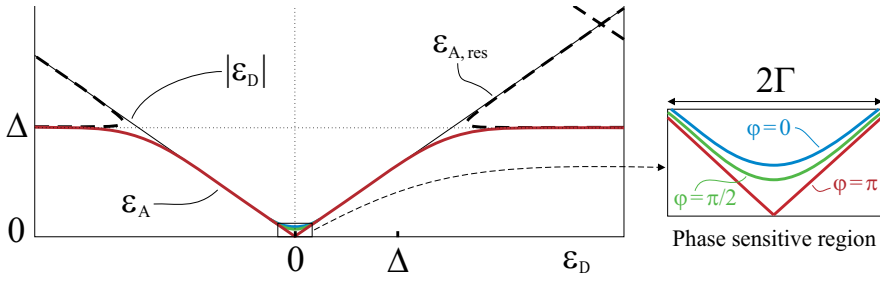


Figure 4. Andreev energy ε_A (thick solid line) and Andreev resonances $\varepsilon_{A,res}$ (dashed line) as functions of the position of the normal resonance ε_D . There are regions where both ε_A and $\varepsilon_{A,res}$ follow the behaviors of the normal resonances $|\varepsilon_D|$ shown by thin solid lines, holewise, with $\varepsilon_D < 0$ and electronwise with $\varepsilon_D > 0$ slopes. The inset on the right shows the magnified phase-sensitive region. When finding numerical solutions illustrated by the figure $\Gamma = 0.1\Delta$ was used and symmetric contact with $t_L = t_R$ was chosen.

gain of electron and holes in the normal region, where $k_{e/h} = \sqrt{2m(E_F \pm \varepsilon_A)}/\hbar$ are the respective wave vectors. For symmetric barriers the phase $\beta = (\chi_+^t - \chi_+^r) - (\chi_-^t - \chi_-^r)$ and an integer multiple of π and generates a smooth function $\sqrt{R_+R_-} \cos \beta$, changing its sign at each resonance [8, 35].

In the case of the SINIS contact, Eq. (10) acquires a form:

$$\begin{aligned} (R_L + R_R) \cos\left(2\pi \frac{I\varepsilon_A}{\delta}\right) - 4\sqrt{R_LR_R} \cos\left(2\pi \frac{\varepsilon_D}{\delta}\right) \sin^2 \alpha + T_L T_R \cos \varphi \\ = \cos\left(2\alpha - 2\pi \frac{\varepsilon_A}{\delta}\right) + R_LR_R \cos\left(2\alpha + 2\pi \frac{\varepsilon_A}{\delta}\right). \end{aligned} \quad (11)$$

The dependence of the Andreev energy ε_A upon the difference of the superconducting phases φ and the position of the normal resonance (i.e. upon the gate voltage) ε_D is found numerically and shown in Fig. 4.

One can analyze Eq. (11) in the following interesting situations. First, if the quantum dot is far from the resonance conditions, $|\varepsilon_D| \gg \Delta$, the Andreev energy is given by the expression

$$\varepsilon_A \approx \Delta \left(1 - \frac{\Gamma^2}{2\varepsilon_D^2}\right). \quad (12)$$

Second, if the resonance falls within the superconducting gap but is apart from the Fermi energy over than Γ , i.e. if $\Gamma \lesssim |\varepsilon_D| \lesssim \Delta$, the Andreev energy depends linearly on the position of the normal resonance:

$$\varepsilon_A \approx \left(1 - \frac{\Gamma}{\Delta}\right) |\varepsilon_D|. \quad (13)$$

Finally, if the resonance approaches to the Fermi level so that $|\varepsilon_D| \lesssim \Gamma$ and $\Gamma \ll \Delta$, the Andreev reflection grows sensitive to the superconducting phase difference φ and is given by

$$\varepsilon_A = \left(1 - \frac{\Gamma}{\Delta}\right) \sqrt{\varepsilon_D^2 + \tilde{\Gamma}^2}, \quad (14)$$

where

$$\tilde{\Gamma} = \Gamma \sqrt{\cos^2 \frac{\varphi}{2} + A^2}, \quad A = \frac{|T_L - T_R|}{2\sqrt{T_L T_R}}. \quad (15)$$

The latter case (often referred to as an infinite gap limit) is especially interesting to us as containing measurable $\varepsilon_A(\varphi)$ dependence. Restricting ourselves to the main order in Γ/Δ , we rewrite formula (14) as

$$\varepsilon_A = \sqrt{\varepsilon_D^2 + \tilde{\Gamma}^2}. \quad (16)$$

In this limit both wave function components, $u(x)$ and $v(x)$, are different from zero solely in the normal region

$$\begin{bmatrix} u(x) \\ v(x) \end{bmatrix} = \begin{cases} 0, & |x| > L/2, \\ \begin{bmatrix} C_e^{\rightarrow} e^{ik_e x} + C_e^{\leftarrow} e^{-ik_e x} \\ C_h^{\leftarrow} e^{ik_h x} + C_h^{\rightarrow} e^{-ik_h x} \end{bmatrix}, & |x| < L/2. \end{cases} \quad (17)$$

with the coefficients governing the relative contributions from the electronwise and holewise being

$$C_{e/h}^{\rightarrow} = C_{e/h}^{\leftarrow} = \sqrt{(1 \pm \varepsilon_D/\varepsilon_A)/2L}. \quad (18)$$

Let us discuss at some more length on the conditions under which Eqs. (16) and (17) hold. We need in fact two of them: (i) A large superconducting gap so that $\Delta \gg \Gamma$, which allows for disregarding the continuous spectrum and (ii) Small, as compared to the superconducting coherence length, the length of the contact, $L \ll \xi$. Note here that under these conditions the Andreev energy ε_A depends strongly upon φ in the window $|\varepsilon_D| \lesssim \Gamma$. Writing down these conditions via the parameters ordinarily relating to the coherence length $\hbar\xi = \hbar v_F/\Delta$ and the transparency of one of the barriers, one finds for the conditions (i) and (ii), respectively:

$$\frac{\Gamma}{\Delta} = T_1 \frac{\hbar v_F}{L\Delta} \ll 1, \quad (19)$$

$$\frac{L}{\xi} = \frac{L\Delta}{\hbar v_F} \ll 1. \quad (20)$$

We have taken a symmetric SINIS contact for the sake of simplicity. Both conditions (19) and (20) are satisfied simultaneously if we take e.g. $L/\xi = 0.1$ and $T = 0.01$. One sees immediately why one can neglect the wave function within the superconductors, see Eq. (17): the size of the region where the wave function dies out fast grows with ξ/L , whereas the amplitude square is proportional to Γ/Δ . Hence integrating the square of the wave function

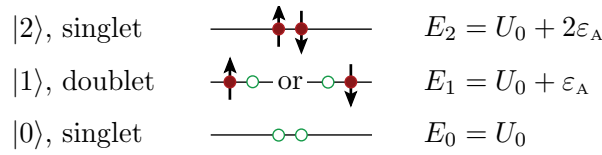


Figure 5. Classification of the energy levels in the SINIS junction.

over the length is proportional to ζ , one gets a quantity which is well less than that coming out from integrating over the normal region of smaller length.

In the limit of the infinite superconducting gap, we can neglect by the continuous spectrum and take into account only four states. The ground state is the quasiparticle-free state $|0\rangle$ with the energy

$$E_0 = U_0, \tag{21}$$

where U_0 is the c -number factor in the Bogoliubov transformation. We count all the energies from the Fermi energy E_F . The first excited state is $|1\rangle$ with one Bogoliubov particle is twice degenerate with respect to the spin (in order to discriminate different spin states we will be using notations $|\uparrow\rangle = \hat{a}_\uparrow^\dagger|0\rangle$, $|\downarrow\rangle = \hat{a}_\downarrow^\dagger|0\rangle$). Its energy is

$$E_1 = U_0 + \varepsilon_A, \tag{22}$$

which is obtained by adding the excitation energy ε_A to the energy of the ground state E_0 . The twice excited state with the two quasiparticles having the opposite spins $|2\rangle = \hat{a}_\uparrow^\dagger\hat{a}_\downarrow^\dagger|0\rangle$ has the energy

$$E_2 = U_0 + 2\varepsilon_A. \tag{23}$$

In the limit of the infinite gap, one can express the energy of the ground state via the Andreev energy:

$$U_0 = \varepsilon_D - \varepsilon_A. \tag{24}$$

We have omitted the contributions from the resonances that are far below the Fermi level, since they do not influence the formation of the superconductivity and their contribution into U_0 does not depend upon φ . Formulas (21)–(24) show that energies $E_{0/2} = \varepsilon_D \mp \varepsilon_A$ depend on the phase φ , while the energy $E_1 = \varepsilon_D$ does not. The energy levels are presented in Fig. 5.

4. The charge of the Andreev quantum dot

Now we turn to determining the charges of the ground and the excited states and the thermodynamic equilibrium charge. The Andreev state carries a non-trivial charge which can be found as the average of the charge operator in the state $|\nu\rangle$

$$\hat{Q} = e \sum_{\sigma} \int_{-L/2}^{L/2} \hat{\Psi}_{\sigma}^{\dagger}(x) \hat{\Psi}_{\sigma}(x) dx, \tag{25}$$

where the operator $\hat{\Psi}_\sigma$ is defined by the Bogoliubov transformations

$$\hat{\Psi}_\sigma(\mathbf{r}) = \sum_\nu \{u_\nu(\mathbf{r})\hat{a}_{\nu,\sigma} + \text{sign}\sigma v_\nu^*(\mathbf{r})\hat{a}_{\nu,-\sigma}^\dagger\}. \quad (26)$$

Correspondingly,

$$Q_\nu = \langle \nu | \hat{Q} | \nu \rangle. \quad (27)$$

The charge of the state $|\nu\rangle$ can be also found by differentiating the energy of this state ε_ν with respect to the gate potential,

$$Q_\nu = \frac{\partial E_\nu}{\partial V_g} = e \frac{\partial E_\nu}{\partial \varepsilon_D}. \quad (28)$$

Naturally, both approach yield the same. Hence

$$Q = Q_0 = e - Q_{\text{ex}}, \quad Q_1 = e, \quad Q_2 = e + Q_{\text{ex}}, \quad (29)$$

where Q_{ex} is the charge of the single excitation and is equal to the derivative of the Andreev energy $Q_{\text{ex}} = e \partial \varepsilon_A / \partial \varepsilon_D$, see Fig. 6.

For the arbitrary (but small as compared to the adjacent resonances spacing δ) values of Γ and ε_D , the charge is found by the implicit differentiation of Eq. (11), the resulting formula is quite cumbersome and will be analyzed in several particular cases.

The thermodynamic charge is determined by the formula

$$Q_{\text{eq}} = e + Q_{\text{ex}} [1 - 2f_{\mathbb{T}}(-\varepsilon_A)] = e + Q_{\text{ex}} [f_{\mathbb{T}}(\varepsilon_A) - f_{\mathbb{T}}(-\varepsilon_A)], \quad (30)$$

where $f_{\mathbb{T}}(E)$ is the Fermi function with the temperature \mathbb{T} ,

$$f_{\mathbb{T}}(E) = \frac{1}{(e^{E/k_{\text{B}}\mathbb{T}} + 1)}. \quad (31)$$

All these charges are localized near the quantum dot, mostly in the interval $[-L/2 \dots L/2]$. The excitation charge Q_{ex} is localized *solely* in this region and does not change upon expanding integration limits in Eq. (25). The equilibrium charge increases slightly upon increasing the integrating range over the coherence length ζ . This can be understood straightforwardly by looking at the times for the quasiparticle to span various parts of the contact. At the quantum point the quasiparticles dwell the lion share of the time $\tau_{\text{dot}} \sim \hbar/\Gamma$, whereas they spend much smaller time $\tau_{\text{sc}} \sim \zeta/v_F \sim \hbar/\Delta$ in the adjacent superconductor. Note that the charge ceases to be localized strictly in a normal region as soon as the Andreev energy becomes of order of the superconducting gap, $\varepsilon_A \approx \Delta$.

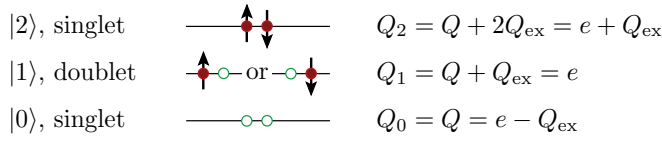


Figure 6. Systematics classification of the energy levels in the SINIS contact.

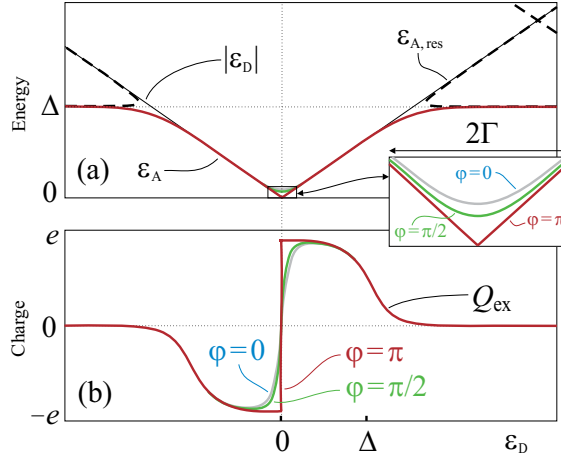


Figure 7. (a) Andreev energy, ε_A (the red curve), and Andreev resonances, $\varepsilon_{A,\text{res}}$ (dashed line), in the Andreev dot as functions of the position of the normal resonance ε_D . The half-width of the normal resonance is chosen as $\Gamma = 0.1\Delta$ and symmetric scatterers, $A = 0$, are adopted. Shown further are normal resonances, $|\varepsilon_D|$ (thin black solid line), hole-wise with the negative slope, $\varepsilon_D < 0$, electron-wise, with $\varepsilon_D > 0$, and in the inset the dependence upon superconducting phase φ along the quantum dot. (b) The excitation charge Q_{ex} is the derivative of the energy with respect to ε_D .

Analogously to the energy, the excitation charge can be analyzed in the different limiting cases:

$$Q_{\text{ex}} \approx \begin{cases} e \frac{\varepsilon_D}{\sqrt{\varepsilon_D^2 + \Gamma^2}}, & \varepsilon_D \lesssim \Gamma, \\ e \text{sign}(\varepsilon_D) \left(1 - \frac{\Gamma}{\Delta}\right), & \Gamma \lesssim \varepsilon_D \lesssim \Delta, \\ e \text{sign}(\varepsilon_D) \frac{\Gamma^2 \Delta}{\varepsilon_D^3}, & \Delta \ll \varepsilon_D. \end{cases} \quad (32)$$

The exact behavior of the $Q(\varphi)$ obtained numerically is shown in Fig. 7(b). One sees that the charge grows linearly with the slope approximately equal to $e/\Gamma \cos(\varphi/2)$. Note that the dependence becomes the sharp one near $\varphi = \pi$, where the resonance gets across the Fermi level and saturates as $e(1 - \Gamma/\Delta)$. As soon as the normal resonance departs from the interval below the gap, $|\varepsilon_D| \gg \Delta$, the excitation charge decays $\propto 4\Gamma^2\Delta/\varepsilon_D^3$. One sees that the fractional charge arises every time as the normal resonance crosses the Fermi level [10]. Note, furthermore, that in addition to the fractional charges corresponding to the ground state and doubly excited (paired) state, there appears an integer charge of a singly excited (unpaired) state $Q_1 = e$. We are going to focus hereafter on the most interesting case out of

listed in Eq. (32), corresponding $\varepsilon_D \lesssim \Gamma$, where the charge depends on the φ . We present it in an explicit form as

$$Q_{\text{ex}} = e \frac{\varepsilon_D}{\sqrt{\varepsilon_D^2 + \Gamma^2(\cos^2(\varphi/2) + A^2)}}. \quad (33)$$

5. Quantum fluctuations of the charge

All the above nontrivial charges result from the breaking down the electron-hole symmetry, and are formed as a superposition of electron-wise and hole-wise states with the states corresponding to integer charges. As such, the charges experience quantum fluctuations which are characterized by the mean square deviations

$$\delta Q_\nu = \sqrt{\langle \nu | \hat{Q}^2 | \nu \rangle - \langle \nu | \hat{Q} | \nu \rangle^2}. \quad (34)$$

An average of \hat{Q}^2 is given by $\langle \nu | \hat{Q}^2 | \nu \rangle = \sum_{\nu'} \langle \nu | \hat{Q} | \nu' \rangle \langle \nu' | \hat{Q} | \nu \rangle$, where the ν' -summation goes over all the states. We concentrate on fluctuations of the ground, $|0\rangle$, singly excited, $|\uparrow\rangle$, $|\downarrow\rangle$, and doubly-excited, $|2\rangle$, states. In the experiment the detector measures the charge during some time, τ , thus the measured charge is averaged in time $\bar{Q} = \int_0^\tau (dt/\tau) Q(t)$; implying that only the matrix elements between the states with the energy difference not exceeding \hbar/τ are to be taken into account. Assuming that the typical measuring frequencies are all $1/\tau \ll \Delta/\hbar$, we can restrict the summation over ν' to summation over the four states of the discrete spectrum $|0\rangle$, $|\uparrow\rangle$, $|\downarrow\rangle$, $|2\rangle$ (in the limit $\Gamma, |\varepsilon_D| \ll \Delta$). In this case these states constitute the complete basis of the Hilbert space, and the only non-diagonal non-zero matrix element is Q_{02} , $Q_{02} = \langle 0 | \hat{Q} | 2 \rangle = e\sqrt{1 - \varepsilon_D^2/\varepsilon_A^2}$. Then fluctuations of the charge corresponding to the states $|0\rangle$ and $|2\rangle$, we find

$$\delta Q_{0/2} = e\sqrt{1 - \varepsilon_D^2/\varepsilon_A^2} = \sqrt{Q_0 Q_2}, \quad (35)$$

and for $|0\rangle$ we have

$$\delta Q_1 = 0. \quad (36)$$

We see that the charge of the singly-filled state (having an integer charge) does not fluctuate, while the charges of the ground state and doubly excited state (having a fractional charge) fluctuate quite a lot. This illustrates graphically the fact that the cause of the fractional charge in the Andreev dot are fluctuations in the number of particles.

6. Charge fluctuations due to electron-phonon interaction

Now we consider the dynamics of the excitation of the Andreev states stemming from thermally induced re-population of the energy levels in the quantum dot. The process of re-population forms a telegraph signal reconfiguring charges in the states $|0\rangle$, $|1\rangle$, and $|2\rangle$, sketched in Fig. 8. Filling and decay of these states is accompanied by emission

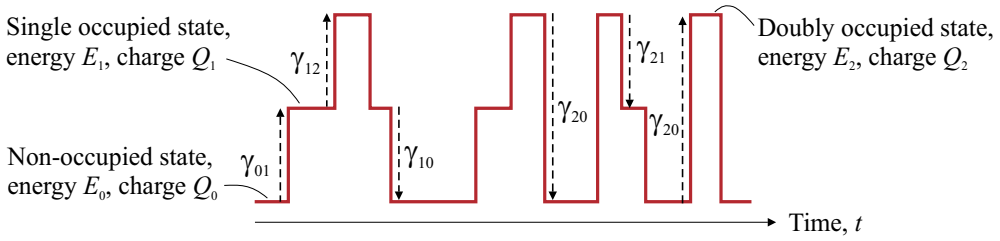


Figure 8. The structure of the telegraph process due to excitations of Bogoliubov quasiparticles by phonons. Transitions changing the system state over the even number of quasiparticles, $0 \leftrightarrow 2$ are fast, whereas the changes over the odd number of quasiparticles, $0 \leftrightarrow 1$ and $1 \leftrightarrow 2$, are slow.

and absorption of phonons [36]. The contribution into re-population comes from two processes, transitions between the ground and singly excited states with frequencies γ_{01} and $\gamma_{10} = \gamma_{01} \exp(\epsilon_A/\mathbb{T})$, respectively, and transitions between the ground- and twice excited states with frequencies γ_{02} and $\gamma_{20} = \gamma_{02} \exp(2\epsilon_A/\mathbb{T})$, respectively. Note that transitions $0 \leftrightarrow 1$ and $1 \leftrightarrow 2$ are equivalent and have same frequencies, $\gamma_{01} = \gamma_{12}$ and $\gamma_{10} = \gamma_{21}$. Transitions $0 \leftrightarrow 1$ occur via emission of the extra quasiparticle with the energy E belonging to continuous spectrum, $E > \Delta$.

One can find the frequencies γ_{01} and γ_{02} making use of Fermi golden rule with the Hamiltonian describing electron-phonon interaction

$$\hat{H}_{\text{el-ph}} = g \int dx \hat{n}_e (\partial_x u), \quad (37)$$

where u is the displacement, n_e is the electron density, and g is the electron-phonon coupling constant typically of order of 1 eV. We will consider 1D electron and phonon modes. The direct calculation of frequency γ_{02} due to electron-phonon interaction yields

$$\gamma_{02} \sim (g^2/\hbar m v_F^2) (a/k_{\text{ph}} L^2) N_{\mathbb{T}}(2\epsilon_A), \quad (38)$$

where $N_{\mathbb{T}}(\epsilon)$ is the Bose function of the phonon states corresponding the temperature \mathbb{T} , a is the lattice constant, $k_{\text{ph}} = 2\epsilon_A/s$ is the phono wave vector corresponding to the transition energy $2\epsilon_A$, and s is the sound velocity. Equation (38) is valid for 1D phonons provided their wavelength is less than the contact length, and, accordingly, $k_{\text{ph}} \gg 1/L$. In the opposite case, $k_{\text{ph}} \ll 1/L$ one has 0-dimensional situation giving rise to

$$\gamma_{02} \sim (g^2/\hbar m v_F^2) a k_{\text{ph}} N_{\mathbb{T}}(2\epsilon_A). \quad (39)$$

Numerical estimate with $g \sim 1\text{eV}$, $m v_F^2 \sim 1\text{eV}$, and $L \approx 500\text{nm}$ [27] yields $\gamma_{02} \sim N_{\mathbb{T}}(2\epsilon_A) 10^{12} \text{sec}^{-1}$ for $k_{\text{ph}} \sim 1/L$.

Calculation of the frequency γ_{01} requires additional summation over the states of the continuous spectrum with $E > \Delta$. This summation is dominated by the states with energies $E \sim \Delta$. Estimating the frequency of simultaneous filling the Andreev level and the state

belonging in the continuous spectrum which is accompanied by absorption of the phonon and decay of the Cooper pair, we find

$$\gamma_{01} \sim (g^2 T_1 / \hbar m v_F^2) (as / L v_F) \sqrt{k_B \mathbb{T} / \Delta} e^{-\Delta / k_B \mathbb{T}} [1 + e^{-\varepsilon_A / k_B \mathbb{T}}]. \quad (40)$$

Here $k_{\text{ph}} L \sim \Delta L / \hbar s \gg 1$ and T_1 is the transparency of a single barrier. We consider here a symmetric SINIS contact, $T_1 = T_2$. Using the typical values $k_B \mathbb{T} \approx 0.1 \Delta \approx 1 \text{ K}$ and $v_F / s \sim 10^3$, we estimate $\gamma_{01} \sim T_1 \exp(-\Delta / k_B \mathbb{T}) 10^{10} \text{ sec}^{-1}$.

Three-dimensionality of the phonon modes results in the additional factor

$$(\varepsilon_A / \hbar \omega_D)^3 (L/a) \sim 10^{-6}, \quad (41)$$

reducing frequency (38). The frequency (40) is reduced by the factor

$$(\Delta / \hbar \omega_D)^3 (L/a) \sim 10^{-3}, \quad (42)$$

where ω_D is Debye frequency and we assume $\varepsilon_A / \hbar \omega_D \sim 10^{-3}$.

One sees that the process $0 \leftrightarrow 2$ is more frequent than the process $0 \leftrightarrow 1$, since the latter includes the exponential factor $\exp(-\Delta / \mathbb{T})$, which allows reduction of the frequency γ_{01} , by lowering the temperature, see Fig. 8.

7. Fluctuations of the gate potential

An additional contribution to re-populating levels comes from the fluctuations of the gate voltage V_g . These fluctuations are defined by the interaction Hamiltonian $\hat{\mathcal{H}}_g = \int dx e \hat{n}_e V_g$. Making use of the technique analogous to that of the previous sections, one finds the respective transition frequencies. Transitions $0 \leftrightarrow 2$ occur with frequency

$$\tilde{\gamma}_{02} \sim (e^2 / \hbar C) N_{\mathbb{T}} (2\varepsilon_A), \quad (43)$$

where C is the contact capacitance to the gate. Taking $C \sim L = 500 \text{ nm}$, one finds the frequency of the gate fluctuations $\tilde{\gamma}_{02} \sim N_{\mathbb{T}} (2\varepsilon_A) 10^{11} \text{ sec}^{-1}$, which compares to the similar contribution from phonons γ_{02} . Transitions due to gate potential fluctuations accounting for the continuous spectrum yield frequencies of the transitions in which the quasiparticle number parity changes

$$\tilde{\gamma}_{01} \sim \hbar^{-1} (e^2 / C) \sqrt{k_B \mathbb{T} / \Delta} e^{-\Delta / k_B \mathbb{T}} [1 + e^{-\varepsilon_A / k_B \mathbb{T}}]. \quad (44)$$

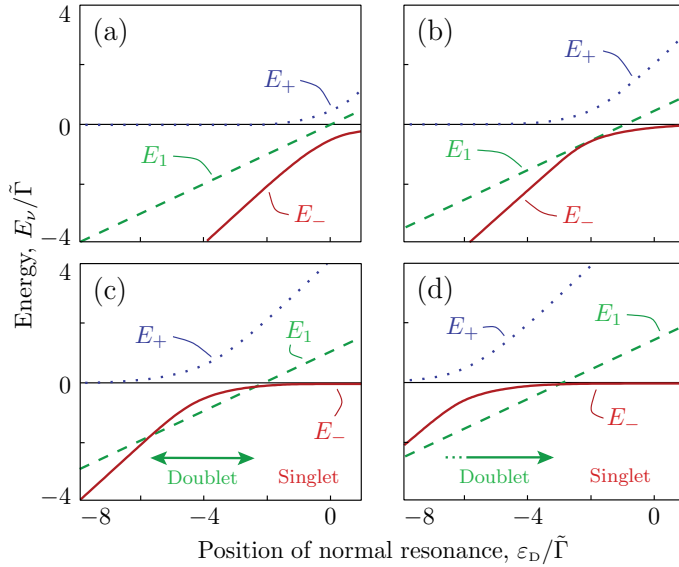


Figure 9. Energies E_- (the red solid line), E_1 (the green dashed line), and E_+ (blue dotted line) as functions of the position of the normal resonance ε_D , all energies being presented in the units $\tilde{\Gamma}$, see Eq. (15). The Coulomb energy $E_C = 0$ for (a), $E_C = \tilde{\Gamma}$ for (b), $E_C = 2\tilde{\Gamma}$ for (c), and $E_C = 3\tilde{\Gamma}$ for (d). At $E_C \geq \tilde{\Gamma}$, the region exists where the ground state is the doublet (shaded in gray). The width of the doublet domain is $2\sqrt{E_C^2 - \tilde{\Gamma}^2}$, the boundaries are blurred by the finite temperature T .

Plugging in the typical values of parameters $k_B T \approx 0.1\Delta \approx 1\text{ K}$ and $C \sim L$, we get $\tilde{\gamma}_{01} \sim \exp(-\Delta/k_B T) 10^{11} \text{ sec}^{-1}$. Similarly to the case of phonons, we observe that the process $0 \leftrightarrow 2$ always happens more often than $0 \leftrightarrow 1$ due to $\exp(-\Delta/k_B T)$ factor.

8. Coulomb interaction

To take into account the Coulomb interaction we have to take into account the charge screening at the quantum dot and mixing of the charge states. The screening due to an additional charge tunneling into the Andreev quantum dot is determined by the density of states. The corresponding energy scale is set by the gap between the adjacent resonances δ since each of them carries the charge $2e$. As a result the screening at the quantum dot is not important provided the Coulomb energy is smaller than the separation between the resonances, $E_C \ll \delta$. The scale $E_C \approx e^2/2C$ can be estimated taking the capacitance of the quantum dot $C = \epsilon L$, where ϵ is the dielectric permeability of the medium. On the other hand, the separation between the adjacent resonances $\delta = \hbar v_F/2L$, is inversely proportional to the normal part length L as well as E_C . The key parameter is the dimensionless ratio $\delta/E_C = \hbar v_F \epsilon / e^2$. Taking typical $\epsilon \sim 10$ and $v_F \sim 10^6 \text{ m/sec}$, we obtain $\delta/E_C \approx 30$, so we can order energies as $E_C \lesssim \Delta \lesssim \delta$. The paper [27] addressed the Andreev quantum dot formed by the nanotube of the length $L \approx 500 \text{ nm}$, corresponding the Coulomb energy $E_C \sim 1\text{ K}$. Thus the above chain of inequalities is experimentally feasible.

To investigate mixing of the charge states in the limit $E_C, \Gamma, |\varepsilon_D| \ll \Delta$, we again restrict ourselves to contribution of the four states: $|0\rangle, |\uparrow\rangle, |\downarrow\rangle$, and $|2\rangle$. The interaction is defined

by the operator

$$\hat{V} = E_C \frac{\hat{Q}^2}{e^2}. \quad (45)$$

In the basis of these for states, the diagonalization can be performed exactly. The non-zero matrix elements of \hat{V} are

$$V_{00} = E_C \frac{Q_0^2 + Q_{02}^2}{e^2}, \quad V_{11} = E_C, \quad V_{22} = E_C \frac{Q_2^2 + Q_{02}^2}{e^2}, \quad V_{02} = 2E_C \frac{Q_{02}}{e}. \quad (46)$$

New energy levels are determined from the consistency condition for the following system of equations:

$$\begin{bmatrix} \tilde{\varepsilon}_0 - E & & & V_{02} \\ & \tilde{\varepsilon}_{1\uparrow} - E & & \\ & & \tilde{\varepsilon}_{1\downarrow} - E & \\ V_{20} & & & \tilde{\varepsilon}_2 - E \end{bmatrix} \begin{bmatrix} D_0 \\ D_\uparrow \\ D_\downarrow \\ D_2 \end{bmatrix} = 0, \quad (47)$$

where we introduced notations $\tilde{\varepsilon}_\nu = \varepsilon_\nu + V_{\nu\nu}$ with $\nu = 0, \uparrow, \downarrow, 2$. The energy of the state with a single Bogoliubov quasiparticle $|1\rangle$ sifts over the constant equal the the Coulomb energy

$$E_1 = \varepsilon_D + E_C, \quad (48)$$

and the state itself $|1\rangle$ does not mix with the other states and retains its degeneracy with respect to spin. This state is called Kramers doublet. The ground state $|0\rangle$ and twice degenerate and twice excited $|2\rangle$ states do mix due to Coulomb interaction and generate two new singlet states $|-\rangle$ and $|+\rangle$. The new states are expressed through the coefficients $D_0, D_\uparrow, D_\downarrow$, and D_2 in Eq. (47) as follows: $|\pm\rangle = D_0^\pm |0\rangle + D_2^\pm |2\rangle$. The energies of new states are

$$E_\pm = \varepsilon_D + 2E_C \pm \sqrt{(\varepsilon_D + 2E_C)^2 + \tilde{\Gamma}^2}. \quad (49)$$

The energies of the doublet and singlet states depend on the position of the normal resonance ε_D and the difference of the superconducting phases φ differently, and at some values of ε_D and φ the situation can occur where $E_- > E_1$. Therefore the ground state can be created by either singlet, $|-\rangle$, or doublet, $|1\rangle$, states and the state $|+\rangle$ always remains doubly excited, see Fig. 9. If $E_C < \tilde{\Gamma}$, the ground state is always formed by the singlet $|-\rangle$. Otherwise, if $E_C \geq \tilde{\Gamma}$, the ground state is formed by the doublet $|1\rangle$ in the region

$$-2E_C - \sqrt{E_C^2 - \tilde{\Gamma}^2} < \varepsilon_D < -2E_C + \sqrt{E_C^2 - \tilde{\Gamma}^2}, \quad (50)$$

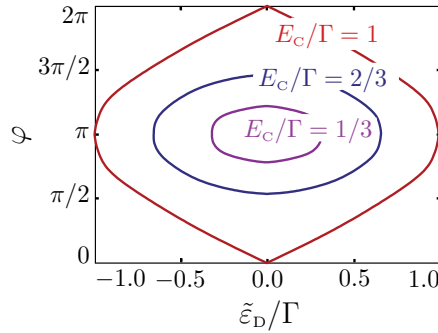


Figure 10. The doublet region in the coordinates $(\varphi, \tilde{\varepsilon}_D)$, where $\tilde{\varepsilon}_D = \varepsilon_D + 2E_C$ is position of the normal resonance shifted by the Coulomb interaction. The size of the doublet region grows upon the increase in the Coulomb energy E_C . $E_C/\Gamma = 1/3$ (magenta), $2/3$ (blue), and 1 (red).

or, which is the same,

$$(\varepsilon_D + 2E_C)^2 + \Gamma^2 \cos^2 \frac{\varphi}{2} + \Gamma^2 A^2 < E_C^2 \quad (51)$$

and remains a singlet $|-\rangle$ at all other values ε_D [37]. At the boundary of the region (50) occurs the transition from the singlet into the doublet state, the charge of the Andreev quantum dot and the current change abruptly as a jump. The boundary of the doublet region in the variables (φ, ε_D) is shown in Fig. 10.

The charges of the new states can be calculated as derivatives of the corresponding energies with respect to the gate voltage $Q_\nu = \partial E_\nu / \partial V_g$:

$$Q_\pm = e \left(1 \pm \frac{\varepsilon_D + 2E_C}{\sqrt{(\varepsilon_D + 2E_C)^2 + \Gamma^2}} \right), \quad Q_1 = e. \quad (52)$$

Everywhere except for the doublet region the charge of the ground state is equal to Q_- , while in the doublet region the charge is $Q_1 = e$. One can observe from Fig. 11(a) and 11(b), that if the Coulomb energy exceeds the critical value $E_C > E_C^* = \Gamma A$, the ground state reconstructs itself into a doublet one. The charge during this process jumps over $Q_- - Q_1$, at finite temperature the transition is being smoothed, see Fig. 11(c) and 11(d). The thermodynamic equilibrium charge at finite temperature, \mathbb{T} , is

$$Q_{\text{eq}} = \frac{Q_- e^{-E_-/k_B \mathbb{T}} + 2Q_1 e^{-E_1/k_B \mathbb{T}} + Q_+ e^{-E_+/k_B \mathbb{T}}}{e^{-E_-/k_B \mathbb{T}} + 2e^{-E_1/k_B \mathbb{T}} + e^{-E_+/k_B \mathbb{T}}}. \quad (53)$$

The charge of the Andreev quantum dot exhibits nontrivial dependencies on the difference of the superconducting phases between the banks. The discussed effects hold high potential for applications in various nanodevices.

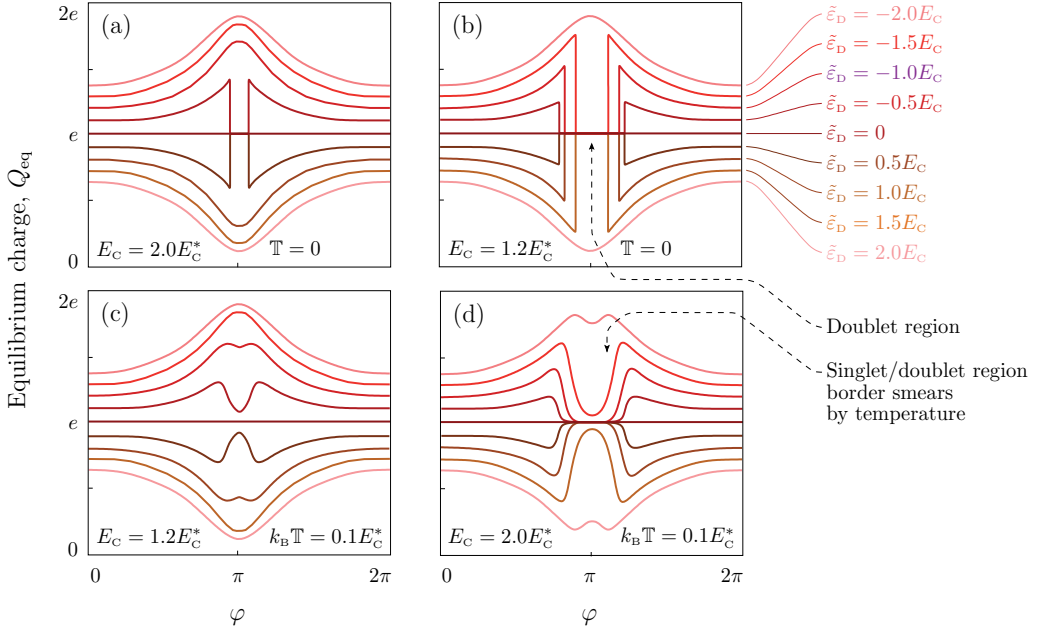


Figure 11. The equilibrium charge Q_{eq} as function of a difference of superconducting phases φ . The plots (a) and (b) correspond to zero temperature, i.e. Q_{eq} is equal to the charge of the ground state. Plots (c) and (d) correspond to temperature $k_B T = 0.1E_C^*$, where $E_C^* = \Gamma A$. The Coulomb energy is $E_C = 1.2E_C^*$ in panels (a) and (c), and $E_C = 2.0E_C^*$ in panels (b) and (d). The asymmetry of the quantum dot $A = 0.2$. The singularities in the centers of the plots correspond to the doublet region (50). In panels (c) and (d) the boundary of the doublet region is blurred by temperature T .

9. Scaling of the charge

We were assuming above that there exists a single conducting channel with the spin. Let us ask how would the charge scale if we had several conducting channels. For example, even in the case of the single-wall carbon nanotube, there is an orbital degeneracy and, in general, there are two channels with the spin. In the case of the multi-wall nanotube (or the normal metal) there may be more than one channel. In this case the Coulomb interaction between the different channels gives rise to the non-trivial charge states [30]. Here we restrict ourselves to a more simple case of multiple channels, but neglecting Coulomb effects. We investigate the SNS contacts endowed with the quadratic and linear dispersions in the normal part, corresponding to the contact superconductor-graphene-superconductor (SGS) [38].

We have demonstrated above that the phase-dependent part of the SINIS charge with the strong normal resonance change the sign upon traversing this resonance across the Fermi level. It is clear that in the absence of the Coulomb effects the contributions from the different channels are additive. This implies that if the part of the resonances are above Fermi level and other resonances are below it, then their contributions to the phase-sensitive part of the charge do compensate one another. As we have already mentioned, the situation where a group of the resonances appears either only above (or only below) the Fermi level is possible due to inhomogeneous distribution of the energy levels due to lateral quantization in the normal part [39].

Let us consider a short SNS contact (so that $L \ll \xi$) with the ideal NS boundaries without normal resonances. In the case of the absence of resonances the maximal sensitivity of a charge per one channel is much less than that in the presence of the resonances. At resonances the contribution into the charge from a single channel is of order of electron charge e [10, 22], whereas in the case of the ideal boundaries, it is of order $(\Delta/E_F)e \sim 10^{-4}e$ [11]. However, the contribution from these channels comes with the like sign, and there may be many of such channels.

The Andreev levels in the short SNS contact are given by

$$\varepsilon_{A,\nu}(\varphi, \mu) = \Delta \sqrt{1 - T_\nu \sin^2(\varphi/2)}, \quad (54)$$

where T_ν is the transparency of the normal region. This formula assumes that T_ν remains constant and does not depend on energy in the interval $[\mu - \Delta, \mu + \Delta]$, which is equivalent to inequality $\Gamma_\nu \gg \Delta$, where Γ_ν is the half width of the resonance having transparency T_ν . The width of the contact we denote by W . Now, the phase-sensitive part of the charge $Q(\varphi, \mu)$ hybridized in the contact can be calculated by summation over all the channels

$$Q(\varphi, \mu) = -2e \sum_{\nu=0}^{\infty} \frac{\partial}{\partial \mu} \varepsilon_{A,\nu}(\varphi, \mu). \quad (55)$$

The factor 2 results from the degeneracy with respect to spin. Note that in Eq. (55) we perform summation over both, propagating modes (when the energy of the lateral quantization is less than the Fermi energy and the solutions of the quasi-1D wave equation has a form of non-decaying waves), and over the dissipative modes (with the energies of the lateral quantization exceeding the Fermi energy and accordingly, decaying solutions of the wave equations). In the case of the linear dispersion only the propagation modes appear relevant.

9.1. Model rectangular potential

To begin with, let us present the distribution of the channels over the energies with the aid of the set of rectangular potentials

$$U_\nu(x) = [E_F - \mu_\nu] \Theta(L/2 - |x|) \quad (56)$$

(see inset in Fig. 12(a)) with the corresponding transparencies.

$$T_\nu(\mu) = \frac{4E_F\mu_\nu}{4E_F\mu_\nu + (E_F - \mu_\nu)^2 \sin^2 [(2m\mu_\nu/\hbar^2)^{1/2}L]}, \quad (57)$$

where E_F is the Fermi energy in the bulk superconductor, and $\mu_\nu = \mu - \pi^2 \hbar^2 \nu^2 / 2mW^2$ is the effective Fermi level in the normal part for ν -th mode, which one can tune changing

the gate potential V_g : $\mu = E_F - eV_g$. Positive μ_v correspond to the propagating modes, while the negative μ_v denote the decaying modes. The number of the propagating modes $N = [\sqrt{2m\mu_v W/\pi\hbar}]$, where square brackets [...] denote the integer part of the real part. Replacing summation over the modes by integration in Eq. (55), introducing the dimensionless parameters $\lambda = 2m\mu L^2/\hbar^2$, $\Lambda = 2mE_F L^2/\hbar^2$ and $x = \sqrt{|1 - \mu_v/\mu|} = \sqrt{\pi^2\hbar^2/2mW^2|\mu|v}$, we arrive at the following transparency

$$T(\lambda) = \frac{4\Lambda\tilde{\lambda}}{4\Lambda\tilde{\lambda} + [\Lambda - \tilde{\lambda}]^2 \sin^2 \tilde{\lambda}^{1/2}}, \quad (58)$$

and charge

$$Q(\varphi, \mu) = -2e \frac{2mLW\Delta}{2\pi\hbar^2} \int_0^\infty \frac{dx}{\sqrt{|\lambda|}} \left\{ \sqrt{1 - T \sin^2(\varphi/2)} - \frac{\sin^2(\varphi/2)}{\sqrt{1 - T \sin^2(\varphi/2)}} \lambda \frac{\partial T}{\partial \lambda} \right\}, \quad (59)$$

where $\tilde{\lambda} = \lambda(1 - x^2 \text{sign } \lambda)$.

The charge determined by the last formula is shown in the Fig. 12(a) for $\Lambda = 10^2$ and 12(b) for $\Lambda = 10^4$. Non-monotonic dependence upon the position of the gate stems from the resonances in the transparency (57). In the real experiment the potential is not sharp and its structure is significantly blurred.

9.2. Parabolic potential

The model that describes qualitatively the electrostatics of the gate results in the parabolic potential. This potential is universal in a sense that its transparency near the top depends only on its "curvature" $\partial_x^2 U_n(x)$. In a short contact where one can neglect by the difference between the mean free times of electrons and holes over the normal part, this universality maintains for SNS contact with the parabolic potentials inside.

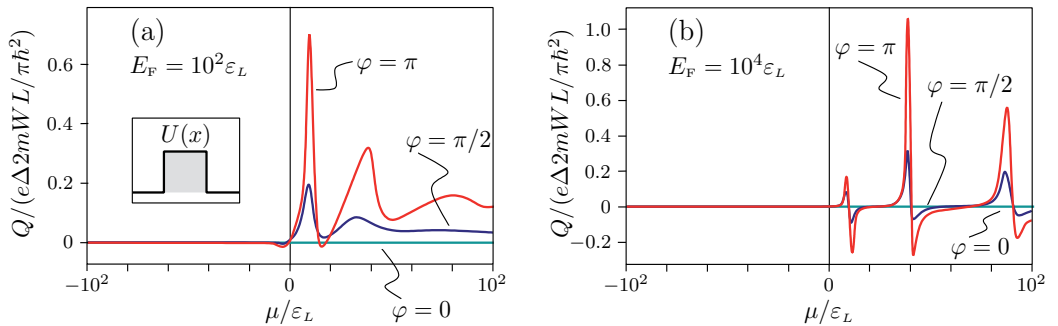


Figure 12. The phase-sensitive part of the charge $Q(\varphi, \mu)$ of the SNS contact as a function of the effective Fermi energy μ in the normal region at different superconducting phases $\varphi = 0, \pi/2, \pi$. (a) The Fermi energy in a superconductor $E_F = 10^2 \varepsilon_L$. (b) The Fermi energy $E_F = 10^4 \varepsilon_L$.

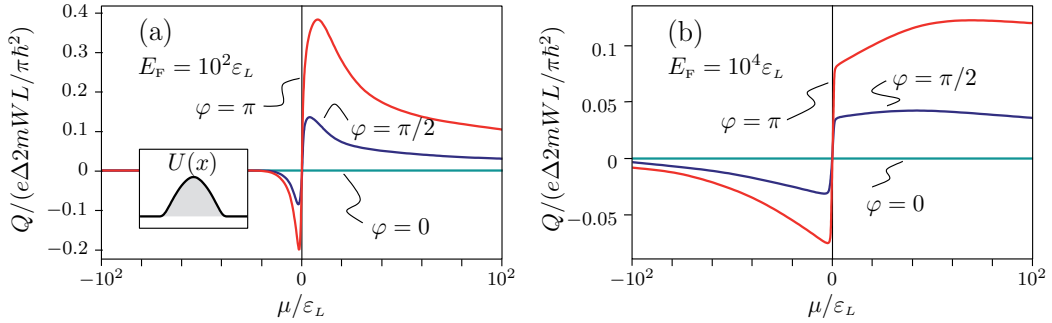


Figure 13. The same as in Fig. 12, but for the effective Fermi energy of a parabolic shape.

Let us consider the parabolic barrier corresponding the the ν -th mode:

$$U_\nu(x) = \left(E_F - \mu_\nu - \frac{m\Omega_\nu^2 x^2}{2} \right) \Theta(L/2 - |x|) \quad (60)$$

with the curvature at the maximum $\Omega_\nu = (4/\hbar)\sqrt{\varepsilon_L(E_F - \mu_\nu)}$, see inset in Fig. 13(a). As before, $\varepsilon_L = \hbar^2/2mL^2$. The potential is chosen to correspond the condition $U_\nu(\pm L/2 \mp 0) = 0$ at NS boundaries. The transparency near the maximum is given by the Kemble formula

$$T_\nu(\mu) = \frac{1}{1 + \exp(-2\pi\mu_\nu/\hbar\Omega_\nu)}. \quad (61)$$

Making use the same parametrization as for a rectangular barrier, we find

$$T(\lambda) = \frac{1}{1 + \exp(-2\pi\tilde{\lambda}/\sqrt{\Lambda - \tilde{\lambda}})} \quad (62)$$

(the formula for the charge looks alike). The phase-sensitive part of the charge is shown in Figs. 13(a) and 13(b). This part of the charge changes sign at $\mu = 0$ and mostly is monotonic as predicted. The “amplitude” of the phase-dependent part of the charge is expressed through the coherence length $\xi = \hbar v_F/\Delta$, giving rise to

$$Q \sim \frac{2|e|}{\pi} \frac{W}{\xi} \sqrt{\frac{E_F}{\varepsilon_L}} = \frac{2|e|}{\pi} \frac{W}{\xi}. \quad (63)$$

We see that the part of the charge we are interested in is proportional to the width of the normal part of the contact W , and that the magnitude of the effect is controlled mostly by the ratio W/ξ .

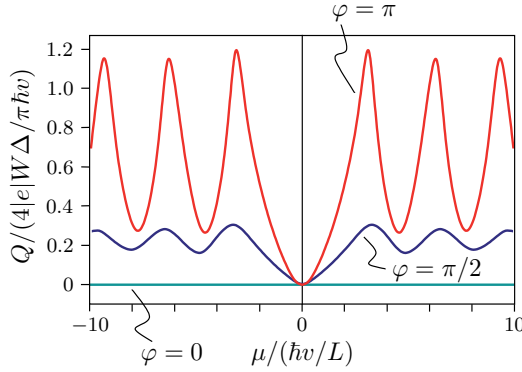


Figure 14. The charge of the SGS contact.

9.3. Graphene stripe with linear dispersion

The contacts of the SGS type are characterized by the linear dispersion. The critical currents across these contacts was studied theoretically [40, 41] and experimentally [38]. In the case of graphene we will be solving Dirac-Bogoliubov-de Gennes equations [42], rather than the usual Bogoliubov-de Gennes ones. For the wide, $W \gg L$, and short, $L \ll \xi$, rectangular sheets of graphene (here as well as in the previous subsection, L and W are the length and the width of the normal region, and $\xi = \hbar v / \Delta$ is the coherence length in superconductors.), the Andreev energy is given by Eq. (54) with the new transparency [40]:

$$T_v(\mu) = \frac{\mu_v^2}{\mu_v^2 + (\mu^2 - \mu_v^2) \sin^2[(\mu_v / \hbar v)L]}, \quad (64)$$

where $\mu_v^2 = \mu^2 - [\hbar v(\nu + 1/2)\pi/W]^2$. Here the real μ_v correspond to the propagating modes, while the imaginary ones, describe the decaying modes. The charge of the dot is given by the expression

$$\tilde{Q}(\varphi, \mu) = -4e \frac{\partial}{\partial \mu} \sum_{\nu=0}^{\infty} \varepsilon_{\Lambda, \nu}(\varphi, \mu). \quad (65)$$

The prefactor 4 arises in the last three formulas due to a double degeneracy with respect to spins and valleys in the graphene. We are still interested only by the phase-sensitive part of the charge. Introducing new variables, $x = (\nu + 1/2)\pi\hbar v / |\mu|W$, and $\lambda = \mu L / \hbar v$, we find

$$T(\lambda) = \frac{\tilde{\lambda}^2}{\tilde{\lambda}^2 + (\lambda^2 - \tilde{\lambda}^2) \sin^2 \tilde{\lambda}}, \quad (66)$$

where, as before, $\tilde{\lambda} = \lambda(1 - x^2 \text{sign } \lambda)$. For a wide contact we can replace summation by the integration to obtain:

$$\tilde{Q}(\varphi, \mu) = -4e \frac{W\Delta}{\pi\hbar v} \int_0^\infty dx \frac{\partial}{\partial \lambda} \left[\lambda \sqrt{1 - T \sin^2 \frac{\varphi}{2}} \right]. \quad (67)$$

The integral in Eq. (67) diverges, but, since we are interested only by the phase-sensitive part of the charge, we can extract unity from the integrand to get:

$$Q(\varphi, \mu) = -4e \frac{W\Delta}{\pi\hbar v} \int_0^\infty dx \left[\sqrt{1 - T \sin^2 \frac{\varphi}{2}} - 1 + \frac{\sin^2(\varphi/2)}{2\sqrt{1 - T \sin^2(\varphi/2)}} \lambda \frac{\partial T}{\partial \lambda} \right]. \quad (68)$$

This charge is shown in Fig. 14. One sees that the integral in Eq. (68) varies from zero to some number of order unity.

Let us compare the factors in front of the integrals in expressions for SNS and SGS contacts. Both are proportional to the width of the contact W , but in case SNS contact the factor does not depend on μ . Because of the rectangular graphene sheet we observe oscillations. The phase-sensitive part of the charge is of order $Q \sim 4|e|W\Delta/\pi\hbar v$. Expressing it through the superconducting coherence length ξ , we get

$$Q \sim \frac{4|e|}{\pi} \frac{W}{\xi}. \quad (69)$$

We see that the effect is again proportional to the width W and is controlled by the ratio W/ξ .

10. Measuring of the fractional charge

The charge can be measured by the capacitance technique tying the charge detector, such as single-electron transistor [21, 43] to the Andreev quantum dot. This approach suffers some difficulties due to, for example, fluctuations of the charges of substrate and the gate discussed in the Sec. 7. Another important problem is the such a measurement “feels” not the total charge Q of the Andreev quantum dot, but only its fraction $\alpha_c \alpha_s Q$.

The geometry factor α_c is determined by the detail of the measuring gate. Let the mutual capacitance of the quantum dot and the measuring contact be C_m , and the mutual capacitance of the Andreev quantum dot and the rest contacts as C_o . Then $\alpha_c = C_m/(C_m + C_o)$. The factor $\alpha_s = \alpha_s(Q)$ is determined by the dynamic feedback from the charge detector. Here we will assume $\alpha_c = \alpha_s = 1$, but bear in mind that the measurement would give us only a part of the charge. One of the most essential aspects of this work is the fact that the charge depends on the phase difference at the banks. Thus the important characteristic of the measurements is the differential sensitivity of the charge with respect to the phase.

$$S = \frac{2e}{\hbar} \frac{\partial Q}{\partial \varphi}. \quad (70)$$

Fluctuations of the charge due to re-population of the levels, generally speaking, interfere in the observation of the charge of the ground and the excited states, however, in certain regimes they can be used for the detecting the charge. The signal resolution of the up-to-date single electron transistors is about $\sim 10^{-5} |e|/\text{Hz}^{1/2}$ at frequencies $f < 10^9$ Hz [43]; therefore indeed the telegraph signal due to thermodynamic re-population of the Andreev state can be resolved, accordingly, the fractional charge due to thermodynamic re-population can be measured in the Andreev quantum dot. However, the process $0 \leftrightarrow 2$ can occur too fast, on the frequencies exceeding the resolution of the single-electron transistors. In this case the two alternative recipes for measuring the excitation charge can be proposed. One is to measure the averaged equilibrium charge Q_{eq} first at the temperature exceeding the level spacing and find $Q_{\text{eq}} = Q_1$, then at temperatures below the the level spacing, $Q_{\text{eq}} = Q_0$. The difference between the charges in these two experiments will give the excitation charge we look for $Q_1 - Q_0$, see Eq. (52). As a result we get the fractional charge, depending continuously upon the external parameter φ . The second way to to measure the charge at low temperatures resolving the slow process $0 \leftrightarrow 1$ and averaging it with respect the fast $0 \leftrightarrow 2$, see Fig. 8. The charge will be measured then in these two states, the state $|1\rangle$ and the state which is a thermodynamic equilibrium between $|0\rangle$ and $|2\rangle$. Let us calculate the difference between the average charges in these two states. The probabilities of filling states $|0\rangle$, $|1\rangle$, and $|2\rangle$ are equal to $p_0 = [1 - f_{\text{T}}(\varepsilon_{\text{A}})]^2$, $p_1 = 2f_{\text{T}}(\varepsilon_{\text{A}})[1 - f_{\text{T}}(\varepsilon_{\text{A}})]$, and $p_2 = f_{\text{T}}^2(\varepsilon_{\text{A}})$, respectively. The averaging over the rapidly fluctuating regime including states $|0\rangle$ and $|1\rangle$, yields $\langle Q \rangle_{0,2} = p_0 Q_0 + p_2 Q_2$, whereas the charge of a single excitation $\langle Q \rangle_1 = Q_1$. Then at low temperatures, where $f_{\text{T}}(\varepsilon_{\text{A}}) \ll 1$, we recover again the excitation charge $\langle Q \rangle_1 - \langle Q \rangle_{0,2} = Q_{\text{ex}}$.

11. Measurement of the flux by the Andreev quantum dot

In this section we will consider the dependence of the fractional charge of the Andreev quantum dot upon φ in some more detail. This dependence can be very sharp, so that one can think of using the Andreev quantum dot for design of the new type of the magnetometer of measuring the low magnetic fields. Usually there are superconducting quantum interferometers, SQUIDs, that are used for that purpose [21, 44–46]. While the SQUIDs utilize the dependence of the Josephson current upon the difference of superconducting phases φ (hence upon the magnetic magnetic flux Φ), we propose to use the dependence of the charge of the Andreev quantum dot upon φ .

The charge of the Andreev quantum dot can be measured by the sensitive magnetometer, for example, by the single-electron transistor. The best transistors can resolve the charges of order $10^{-5} |e|/\text{Hz}^{1/2}$ at given frequency, see, e.g. [43]. Simple estimates demonstrate that the change in the flux $\delta\Phi$ causes the variation of the charge δQ as $\delta Q = (2|e|/\Phi_0)\delta\Phi$, where $\Phi_0 = 2\pi\hbar/2|e|$ is the flux quantum. Taking the area of the superconducting loop equal 1 mm^2 , we obtain the sensitivity $10^{-14} \text{ T}/\text{Hz}^{1/2}$, which favorably compares to the sensitivity of the best SQUIDs, $10^{-14} \div 10^{-15} \text{ T}/\text{Hz}^{1/2}$ [45–48]. Let us call the sensitivity of the Andreev quantum dot the ratio $\delta Q/\delta\Phi$.

The differential sensitivity of the charge in the thermodynamic equilibrium to the magnetic flux threading the superconducting ring we define as the modulus of the partial derivative $\partial Q_{\text{eq}}/\partial\Phi$, taken at given magnitude of the flux Φ : $\mathcal{S} = \partial Q_{\text{eq}}/\partial\Phi$. Note that the sensitivity of the flux into the charge transformer described here, $\mathcal{S} = \mathcal{S}_{\Phi \rightarrow Q}$, exactly coincides with the sensitivity of the Josephson transistor [8], which converts the gate potential into the current

$S_{V \rightarrow I} = \partial I_{\text{eq}} / \partial V_g$. Making use of the Eq. (53), we obtain

$$S = F_{\mathbb{T}} \frac{\partial Q}{\partial \Phi} + Q \frac{\partial F_{\mathbb{T}}}{\partial \Phi}, \quad (71)$$

where $Q = (Q_+ - Q_-)/2$, the derivative

$$\frac{\partial Q}{\partial \Phi} = e \frac{2\pi}{\Phi_0} \frac{(\varepsilon_D + 2E_C)\Gamma^2 \sin \varphi}{4[(\varepsilon_D + 2E_C)^2 + \tilde{\Gamma}^2]^{3/2}} \quad (72)$$

defines the sensitivity of the charges of the states $|-\rangle$ and $|+\rangle$, and the function

$$F_{\mathbb{T}} = \frac{e^{-E_+/k_B\mathbb{T}} - e^{-E_-/k_B\mathbb{T}}}{e^{-E_-/k_B\mathbb{T}} + 2e^{-E_1/k_B\mathbb{T}} + e^{-E_+/k_B\mathbb{T}}}. \quad (73)$$

describes the dependence of the charge upon the temperature and accounts for the the doublet region (50).

One can see from Fig. 11 there exist two intervals where the dependence of $Q_{\text{eq}}(\varphi)$ is sharp. If φ increases from $\varphi = 0$, the charge increases (decreases) and achieves the maximum (minimum). In case $E_C < E_C^* = \Gamma A$ the maximum (minimum) of the charge is always at the point $\varphi = \pi$. In this case the whole curve is the interval I. If $E_C > E_C^*$ this extremum splits into two and there appears a dent in between the extrema, which we will be calling the interval II. The former interval corresponds to a singlet state of the Andreev quantum dot, while the better part of the latter interval corresponds to a doublet state (in the case of the zero temperature the whole second interval corresponds to a doublet region).

Let us begin with the description of the first interval. Let us fix the parameters Γ , A and E_C and seek for the maximum of the sensitivity S as function of φ and ε_D . The symmetries of the function $Q_{\text{eq}}(\varphi, \varepsilon_D)$ enable us to narrow the region of the search for maximum down to $0 \leq \varphi \leq \pi$, $\varepsilon_D + 2E_C > 0$. After that we analyze maximum as function of E_C , keeping A and Γ constant.

Interval I. In the case $E_C < \sqrt{3}E_C^*$ and zero temperature, $\mathbb{T} = 0$, the sensitivity is completely defined by $\partial Q_{\text{ex}} / \partial \Phi$ (72). In the limit $A \ll 1$ the function $|\partial Q_{\text{ex}} / \partial \Phi|$ achieves the maximum at $\varepsilon_D + 2E_C = \Gamma \cos(\varphi/2) = \Gamma A$, the maximum being

$$S_{\text{max}}^I = |e| \frac{2\pi}{\Phi_0} \frac{1}{6\sqrt{3}A}. \quad (74)$$

One sees that the smaller A imply larger sensitivity. In other words, more symmetric SINIS structure provides higher sensitivity. If $k_B\mathbb{T} \ll E_C^*$, the sensitivity is practically not temperature-dependent.

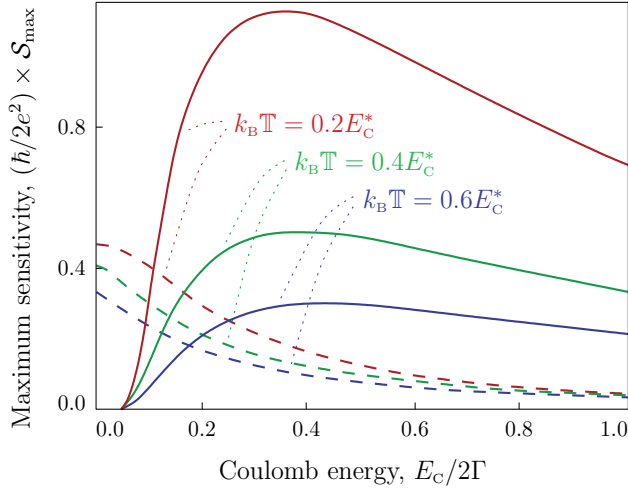


Figure 15. Maximal differential sensitivity in the interval I, S_{\max}^I (the dashed line) and in the interval II, S_{\max}^{II} (solid line) depending on the Coulomb energy E_C . The level of asymmetry $A = 0.2$; the corresponding critical Coulomb energy $E_C^*/\Gamma = 0.2$. The temperature varies from $k_B T = 0.2E_C^*$ to $k_B T = 0.6E_C^*$.

In the opposite case, $E_C > \sqrt{3}E_C^*$, the doublet region partially absorbs the interval I and maximum at zero temperature is achieved at the boundary of the doublet region. This yields the sensitivity

$$S_{\max}^I = |e| \frac{2\pi}{\Phi_0} \frac{\Gamma^2}{4E_C^3} \max_{\varphi} \left\{ \sqrt{E_C^2 - \Gamma^2} \sin \varphi \right\}. \quad (75)$$

The result is reduced to

$$S_{\max}^I = |e| \frac{2\pi}{\Phi_0} \frac{\Gamma^2}{4E_C^2} \quad (76)$$

in the limit $E_C \gg \Gamma$. The maximum is achieved at the point $\varepsilon_D + 2E_C = E_C$, $\varphi = \pi/2$. Note that formula (76) gives the correct estimate even in the case $E_C \approx \Gamma$.

Interval II. At zero temperature there is a jump in the charge at the boundary of the doublet region (interval II), therefore the sensitivity at this point is infinite. The finite temperature would smooth the jump, the sensitivity remaining finite. If $\Gamma \ll E_C \ll \Gamma^2/k_B T$, the sensitivity S achieves its maximum near the point $\varepsilon_D + 2E_C = E_C$, $\varphi = \pi/2$ and is equal to

$$S_{\max}^{II} = |e| \frac{2\pi}{\Phi_0} \frac{\Gamma^2}{16E_C k_B T}. \quad (77)$$

Note that this maximum is shifted at the finite temperature from the point of the phase transition towards the singlet over the quantity $\delta\varphi \sim E_C k_B T / 4\Gamma^2$. For the arbitrary E_C the expression for the S_{\max}^{II} is somewhat cumbersome. We have shown the numerically found dependence $S_{\max}^{II}(E_C)$ in Fig. 15, where we also presented the maximum of sensitivity in the

interval I. One sees that under the large Coulomb interaction the better sensitivity is achieved in the interval II.

Therefore the dependence of the charge of the Andreev quantum dot upon the the difference of the superconducting phases can be used, in principle, for the design of the new type of the of the quantum magnetometers working according to the scheme “magnetic flux \rightarrow charge of the Andreev dot \rightarrow charge detector \rightarrow current” instead of the usual scheme of customary SQUIDs “magnetic flux \rightarrow current.”

Let us estimate the sensitivity of the Andreev quantum point-based magnetometer, comparing them to the existing and widely used SQUIDs that can resolve at best the flux $10^{-6} \Phi_0/\text{Hz}^{1/2}$ at given frequency. The typical SQUID area is 2 mm^2 , implying the resolution of the magnetic field $10^{-15} \text{ T}/\text{Hz}^{1/2}$ at given frequency. Assume the area of the superconducting ring the same as in SQUIDs and take the resolution of the charge detector equal to $10^{-5} |e|/\text{Hz}^{1/2}$ [43]. In the limit of the small Coulomb interaction, the sensitivity is determined by the asymmetry of the quantum dot. At $A = 0.01$ Eq. (74) gives for the flux $2 \times 10^{-7} \Phi_0/\text{Hz}^{1/2}$ and for the field $2 \times 10^{-16} \text{ T}/\text{Hz}^{1/2}$. Upon increase of the Coulomb interaction the maximal sensitivity is located at the boundary of the doublet region and is determined by the magnitude of the Coulomb energy. Plugging in $E_C = 6\Gamma$, and using Eq. (76), we find the flux resolution $3 \times 10^{-4} \Phi_0/\text{Hz}^{1/2}$ and the field resolution $3 \times 10^{-13} \text{ T}/\text{Hz}^{1/2}$. The sensitivity that can be achieved upon transition from the singlet into the doublet region is restricted from above by the temperature of the measurements. Plugging in $k_B T = 0.02\Gamma$ and $E_C = 0.2\Gamma$ into Eq. (77), we find for the flux $10^{-7} \Phi_0/\text{Hz}^{1/2}$ and for the field $10^{-16} \text{ T}/\text{Hz}^{1/2}$.

In real devices the Coulomb interaction E_C can be less than Γ (see discussion in Refs. [10, 27]) or larger than Γ (see Refs. [28, 29]). The second case can be realized, for example, raising the Fermi level in the normal region. Nanomechanical effects also can either suppress or enhance the sensitivity of the Andreev quantum dot with respect to the phase difference [49].

12. Conclusions

We discussed in depth the charge of the Andreev quantum dot. We demonstrated that the charge is localized in the region of the dot and depends continuously upon the difference of the phases between the superconductors. We studied charge fluctuations due to both, electron-phonon interactions and due to fluctuations of the gate potential. We revealed that Coulomb interaction can cause the reconstruction of the singlet ground state in the doublet one. While in the singlet state the Josephson current is present and the charge does depend on the phase, in the doublet state the non-dissipative current is absent and the charge is integer. Upon increasing the charge energy, the “size” of the doublet region in the (φ, ε_D) coordinates increases as well.

We discussed a concept of a novel device for measurements of the magnetic flux, utilizing the Andreev quantum dot as a working element, and investigated its differential sensitivity. The estimates show that the expected theoretical sensitivity of the Andreev quantum dot magnetometer compares favorably with the characteristics of the existing SQUIDs.

Acknowledgements

We thank G. Blatter, T. Martin, T. Jonckheere, N.B. Kopnin, and V.V. Ryazanov for illuminating discussions. The work was supported by the Scientific Discovery through Advanced Computing (SciDAC) program funded by U.S. Department of Energy, Office of Science, Advanced Scientific Computing Research and Basic Energy Science (I.S.), U.S. Department of Energy, Office of Science, Materials Sciences and Engineering Division (V.V. and, partly, G.L. via Materials Theory Institute), and by the RFBR Grant No. 14-02-01287 (G.L.).

Author details

Ivan A. Sadovskyy¹, Gordey B. Lesovik², Valerii M. Vinokur¹

¹ Materials Science Division, Argonne National Laboratory, Argonne, Illinois, USA

² Landau Institute for Theoretical Physics, RAS, Chernogolovka, Moscow region, Russia

References

- [1] B.D. Josephson. Possible new effects in superconductive tunnelling. *Phys. Lett.*, 1: 251–253, 1962.
- [2] P.G. de Gennes. Boundary effects in superconductors. *Rev. Mod. Phys.*, 36(1):225–237, Jan 1964.
- [3] A.A. Abrikosov. On the magnetic properties of superconductors of the second group. *Sov. Phys. JETP*, 5(6):1174–1182, Dec 1957.
- [4] D.I. Khomskii and A. Freimuth. Charged vortices in high temperature superconductors. *Phys. Rev. Lett.*, 75(7):1384–1386, Aug 1995.
- [5] G. Blatter, M. Feigel'man, V. Geshkenbein, A. Larkin, and A. van Otterlo. Electrostatics of vortices in type-II superconductors. *Phys. Rev. Lett.*, 77(3):566–569, Jul 1996.
- [6] H. van Houten. Three-terminal quantum box resonant tunneling Josephson field-effect switch. *Appl. Phys. Lett.*, 58(12):1326–1328, 1991.
- [7] G. Wendin and V.S. Shumeiko. Josephson transport in complex mesoscopic structures. *Superlatt. and Microstruct.*, 20(4):569–573, Dec 1996.
- [8] D.D. Kuhn, N.M. Chtchelkatchev, G.B. Lesovik, and G. Blatter. Supercurrents through gated superconductor–normal-metal–superconductor contacts: The Josephson transistor. *Phys. Rev. B*, 63(5):054520, Jan 2001.
- [9] N.M. Chtchelkatchev and Yu.V. Nazarov. Andreev quantum dots for spin manipulation. *Phys. Rev. Lett.*, 90(22):226806, Jun 2003.
- [10] I.A. Sadovskyy, G.B. Lesovik, and G. Blatter. Continuously tunable charge in Andreev quantum dots. *Phys. Rev. B*, 75(19):195334, May 2007.

- [11] K. Engström and J. Kinaret. Phase-dependent charges in SNS systems. *Phys. Scr.*, 70(5): 326–329, 2004.
- [12] R.B. Laughlin. Anomalous quantum Hall effect: an incompressible quantum fluid with fractionally charged excitations. *Phys. Rev. Lett.*, 50(18):1395–1398, May 1983.
- [13] L. Saminadayar, D.C. Glattli, Y. Jin, and B. Etienne. Observation of the $e/3$ fractionally charged Laughlin quasiparticle. *Phys. Rev. Lett.*, 79(13):2526–2529, Sep 1997.
- [14] M. Reznikov, R. de Picciotto, T.G. Griffiths, M. Heiblum, and V. Umansky. Observation of quasiparticles with one-fifth of an electron's charge. *Nature*, 399(6733):238–241, May 1999.
- [15] X.G. Wen. Gapless boundary excitations in the quantum Hall states and in the chiral spin states. *Phys. Rev. B*, 43(13):11025–11036, May 1991.
- [16] A.V. Lebedev, A. Crépieux, and T. Martin. Electron injection in a nanotube with leads: finite-frequency noise correlations and anomalous charges. *Phys. Rev. B*, 71(7):075416, Feb 2005.
- [17] B. Trauzettel, I. Safi, F. Dolcini, and H. Grabert. Fractional charge in the noise of Luttinger liquid systems. In Peter Svedlindh, Dragana Popovic, and Michael B. Weissman, editors, *Fluctuations and noise in materials II*, volume 5843, pages 115–123. SPIE, 2005.
- [18] M. Büttiker and C.A. Stafford. Charge transfer induced persistent current and capacitance oscillations. *Phys. Rev. Lett.*, 76(3):495–498, Jan 1996.
- [19] P.S. Deo, P. Koskinen, and M. Manninen. Charge fluctuations in coupled systems: ring coupled to a wire or ring. *Phys. Rev. B*, 72(15):155332, Oct 2005.
- [20] C.J. Pethick and H. Smith. Relaxation and collective motion in superconductors: a two-fluid description. *Annals of Physics*, 119(1):133–169, 1979. ISSN 0003-4916. .
- [21] V.V. Schmidt. *The physics of superconductors: Introduction to fundamentals and applications*. Springer, 2002.
- [22] I.A. Sadovskyy, G.B. Lesovik, and G. Blatter. Magnetic flux detection with an Andreev quantum dot. *JETP Lett.*, 86:210, 2007.
- [23] A.F. Andreev. Thermal conductivity of the intermediate state of superconductors. *Sov. Phys. JETP*, 19:1228–1231, 1964.
- [24] A.F. Andreev. Thermal conductivity of the intermediate state of superconductors — II. *Sov. Phys. JETP*, 20:1490–1493, 1965.
- [25] A.F. Andreev. Electron spectrum of the intermediate state of superconductors. *Sov. Phys. JETP*, 22:455–458, 1966.
- [26] M.R. Buitelaar, T. Nussbaumer, and C. Schönberger. Quantum dot in the Kondo regime coupled to superconductors. *Phys. Rev. Lett.*, 89(25):256801, Dec 2002.

- [27] P. Jarillo-Herrero, J.A. van Dam, and L.P. Kouwenhoven. Quantum supercurrent transistors in carbon nanotubes. *Nature*, 439:953–956, Feb 2006.
- [28] J.A. van Dam, Yu.V. Nazarov, E.P.A.M. Bakkers, S. De Franceschi, and L.P. Kouwenhoven. Supercurrent reversal in quantum dots. *Nature*, 442:667–670, Aug 2006.
- [29] J.-P. Cleuziou, W. Wernsdorfer, V. Bouchiat, T. Ondarçuhu, and M. Monthieux. Carbon nanotube superconducting quantum interference device. *Nature Nanotech.*, 1:53–59, Oct 2006.
- [30] I.A. Sadovskyy, G.B. Lesovik, G. Blatter, T. Jonckheere, and T. Martin. Andreev quantum dot with several conducting channels. *Phys. Rev. B*, 85:125442, Mar 2012.
- [31] N. Roch, S. Florens, V. Bouchiat, W. Wernsdorfer, and F. Balestro. Quantum phase transition in a single-molecule quantum dot. *Nature*, 453(7195):633–637, 05 2008.
- [32] C.B. Winkelmann, N. Roch, W. Wernsdorfer, V. Bouchiat, and F. Balestro. Superconductivity in a single-C₆₀ transistor. *Nat. Phys.*, 5(12):876–879, 12 2009.
- [33] I.A. Sadovskyy, D. Chevallier, T. Jonckheere, M. Lee, S. Kawabata, and T. Martin. Josephson effect through an anisotropic magnetic molecule. *Phys. Rev. B*, 84:184513, Nov 2011.
- [34] G.B. Lesovik and I.A. Sadovskyy. Scattering matrix approach to the description of quantum electron transport. *Physics-Uspokhi*, 54(10):1007–1059, 2011.
- [35] N.M. Chtchelkatchev, G.B. Lesovik, and G. Blatter. Supercurrent quantization in narrow-channel superconductor–normal-metal–superconductor junctions. *Phys. Rev. B*, 62(5):3559–3564, Aug 2000.
- [36] D.A. Ivanov and M.V. Feigel'man. Phonon relaxation of subgap levels in superconducting quantum point contacts. *JETP Lett.*, 68(11):890–894, Dec 1998.
- [37] A.V. Rozhkov and D.P. Arovas. Interacting-impurity Josephson junction: variational wave functions and slave-boson mean-field theory. *Phys. Rev. B*, 62(10):6687–6691, Sep 2000.
- [38] H.B. Heersche, P. Jarillo-Herrero, J.B. Oostinga, L.M.K. Vandersypen, and A.F. Morpurgo. Bipolar supercurrent in graphene. *Nature*, 446:56–59, Mar 2007.
- [39] V.I. Fal'ko and G.B. Lesovik. Quantum conductance fluctuations in 3D ballistic adiabatic wires. *Solid State Comm.*, 84(8):835–837, 1992.
- [40] M. Titov and C.W.J. Beenakker. Josephson effect in ballistic graphene. *Phys. Rev. B*, 74(4):041401, Jul 2006.
- [41] J.C. Cuevas and A. Levy Yeyati. Subharmonic gap structure in short ballistic graphene junctions. *Phys. Rev. B*, 74(18):180501, Nov 2006.
- [42] C.W.J. Beenakker. Specular Andreev reflection in graphene. *Phys. Rev. Lett.*, 97(6):067007, Aug 2006.

- [43] A. Aassime, G. Johansson, G. Wendin, R.J. Schoelkopf, and P. Delsing. Radio-frequency single-electron transistor as readout device for qubits: charge sensitivity and backaction. *Phys. Rev. Lett.*, 86(15):3376–3379, Apr 2001.
- [44] J. Clarke. SQUIDs for low frequency measurements. In Brian B. Schwartz and Simon Foner, editors, *Superconductor applications: SQUIDs and machines*, pages 67–124, New York, 1977. Plenum Press.
- [45] J. Clarke and A.I. Braginski, editors. *Fundamentals and technology of SQUIDs and SQUID systems*, volume 1 of *The SQUID Handbook*. Wiley–VCH, Berlin, Germany, 2004.
- [46] J. Clarke and A.I. Braginski, editors. *Applications of SQUIDs and SQUID systems*, volume 2 of *The SQUID Handbook*. Wiley–VCH, Berlin, Germany, 2004.
- [47] R. Kleiner, D. Koelle, F. Ludwig, and J. Clarke. Electrostatics of vortices in type-II superconductors. *Proc. of the IEEE*, 92(10):1534–1548, Oct 2004.
- [48] H. Weinstock, editor. *Applications of Superconductivity*, volume 365 of *Series E: Applied Sciences*. Kluwer, Dordrecht, The Netherlands, 2000.
- [49] I.A. Sadovskyy, G.B. Lesovik, T. Jonckheere, and T. Martin. Nanomechanical effects in an Andreev quantum dot. *Phys. Rev. B*, 82:235310, Dec 2010.

Applications

Quantum Dots Prepared by Droplet Epitaxial Method

Ákos Nemcsics

Additional information is available at the end of the chapter

<http://dx.doi.org/10.5772/60823>

Abstract

In this work, we are dealing with the droplet epitaxially prepared quantum dots. This technology is not only an alternative way of the strain induced technique to prepare quantum dots, but it allows us to make various shaped nano structures from various material. The present paper deals not only with the so called conventional shaped quantum dot but also with the ring shaped dot, with the inverted dot and with dot molecules as well. Their thechnology, opto-electronical and the structural properties are also discussed.

Keywords: droplet epitaxy, GaAs, AlGaAs, AlAs, QD, MBE

1. Introduction

The electrons “boxed up” or confined in quantum confinement and the calculation of their energy levels, which are well known from textbooks, were regarded for decades as idealistic concepts far from practical reality. The molecular beam epitaxial (MBE) technology, developed for compound semiconductors, made the introduction of the low-dimension structures into the everyday scientific research possible. The structures confined in all three dimensions are called quantum dots (QDs).

For the fabrication of QDs or any zero-dimensional structures, various methods were developed. For a long time, the only known method for the production of epitaxially grown zero-dimensional system was the strain-induced method, based on lattice mismatch. Presently, the

most used technique is the lattice-mismatched technique by the Stranski–Krastanov mode [1–5]. QDs, such as InAs nanocluster prepared on GaAs surface, are the oldest known system. The droplet epitaxy (DE), however, is one of the latest methods for QD preparation. This method of preparation is not only an alternative way to the conventional method but also a production method for a number of zero-dimensional quantum structures such as ringlike QDs, double ringlike QDs, inverse QDs (filled nanoholes), or QD molecules. This technique is also fully compatible with MBE technology.

The subjects of this paper are the technologies used, growth kinetics, and some properties of the zero-dimensional nanostructures of different shapes, grown by DE. The fundamentals of DE were first demonstrated by Koguchi and his coworkers in the early 1990s [6–9]. One advantage is that it is not restricted by mismatch conditions; in addition to that is the possible fabrication of strain-free QDs and similar nanostructures by DE, against the Stranski–Krastanov-based growth method. The shape diversity makes it a preferable process for that application. The size, shape, and elementary distribution of the developed structures are dependent on the developing technology used. It is obvious that the physical parameters of the structures are important from both the theoretical and practical point of view.

In this paper, QDs grown by DE will be described, selected from III and V class materials. Here, the QDs are mostly GaAs with the use of AlGaAs as barrier material. This process consists of the following two basic steps: first, the metallic (e.g., Ga) nanosized droplets are generated on the surface by the Volmer–Weber growth mode, followed by the second step of droplet crystallization that is the transformation into GaAs QDs in arsenic atmosphere.

For the control of the process, the kinetics of the growth process knowledge is necessary, which is so far lacking the full theoretical description.

The DE technology for QD preparation has superiority over the nowadays widely used strain-induced method. The greatest advantage is that both lattice matched and mismatched can be used for QD fabrication. At the same time, the size and density of the QD's can be controlled independently, and the distribution is more uniform. However, the shapes of the QDs show a wide spectrum. This spectrum includes the conventionally shaped QDs, ringlike QDs, and complex multicomponent QD structures [9–13]. To avoid intermixing, low temperature can be applied at preparation. A wide variety substrate orientation has beneficial effect on the application.

Although the technique is quite recent, it is already successfully applied in a number of cases. QDs had significantly improved the general performance of the optoelectronic devices, like semiconductor lasers and optical amplifiers. DE fabricated QDs introduced further improvements for the beneficial reasons described previously [10].

Future quantum devices, based on quantum mechanical and electromagnetic interactions, require lateral QD configurations. With the modified DE method, aligned QD pairs and QD molecules can be produced without involving lithographic technology [14, 15].

2. The droplet epitaxial technique

2.1. Technological background and preliminaries of the droplet epitaxial technique

It is well known in our profession that the grown structure can be classified in three growth modes depending on the interaction among the constituents. These modes are the layer-by-layer growth or Frank–van der Merwe mode, the island growth or Volmer–Weber mode, and the intermediate mode (layer-plus-island growth) or Stranski–Krastanov mode (Figure 1) [16]. The morphology of the interface is determined by the interplay between deposition, desorption, and surface diffusion. If an atom or molecule from the environment arrives at a random position on the surface, the deposition process bonds with the surface atoms and sticks.

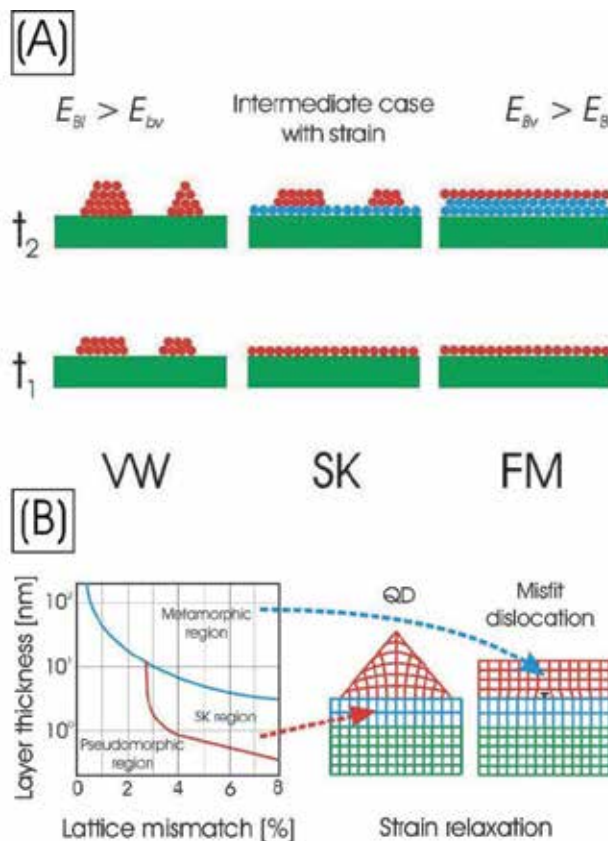


Figure 1. (A) Schematic illustration of the three growth modes. (B) Strain relaxation via QD formation and via generation of misfit dislocation.

The process competing with deposition is desorption. During the desorption process, some atoms deposited on the surface leave the interface. The probability of the desorption depends on how strongly the atom is bonded to the surface. The strength of the bonds depends either

on the type of atom or on the local atom arrangement of the surface where the atom sticks. The desorption can be negligible for many materials under typical MBE conditions. The deposited atoms diffuse on the crystal surface, searching for the energetically most favorable position. The diffusion length can be quite large and depends on the temperature and the binding energies to the substrate (E_{Bv} , binding in vertical direction).

In the Frank–van der Merwe mode, the interaction between the neighboring atoms (E_{Bv} , lateral directions) in the layer is weaker than that with the substrate atoms ($E_{Bv} > E_{Bl}$) [17]. In this growth mode, islands of monolayer (ML) height coalesce before a new layer can nucleate on top of them. In the Volmer–Weber mode, the situation is just the opposite, that is, the binding energy among the deposited atoms is stronger than to the substrate surface ($E_{Bl} > E_{Bv}$). In this case, the growth proceeds to many atomic layers at discrete islands before these islands merge.

In the Stranski–Krastanov mode, the process is initiated in a layer-by-layer fashion, but islanding commences after the growth of a certain layer thickness. In certain situations, layer-by-layer growth is desirable because of the need for multilayered structures with exact layer thickness and flat interfaces. This requires that the nucleation takes place as a single event on the substrate. In this growth mode, the lattice mismatch between the grown layer and the substrate material is the most common case.

The deformation takes place by the even layer to match the lattice of the substrate. In this case, elastic energy is generated in the structure, which deforms mainly the lattice of the grown layer. When this deformation energy overcomes a critical value, it can be relaxed in two ways. One possible way is to nucleate nanosized islands on the surface of the even layer, which is called the wetting layer. The absence of the lateral layer allows the atomic planes to laterally relax, reducing the elastic energy in the structure. According the first mentioned way, the so-called strain-induced QD can be grown. The other way is to generate misfit dislocations at the interface [18–21]. The dislocations in the substrate and at the interface can overgrow into the grown layer [23–25]. These defects are called threading dislocations.

Figure 1 shows the following two out of three growth modes, Volmer–Weber and Stranski–Krastanov for nanostructure production. One may ask why only the Stranski–Krastanov growth mode is widely used for QD production. The answer lies in the development of the MBE technology. The application of III–V materials opened the way for the production of heteroepitaxial structures, specifically the GaAs–AlGaAs–AlAs system, for its identical lattice parameter. The growth of InAs and InGaAs created particular technological difficulties due to the lattice mismatch. In the early 1990s, the success of InGaAs growth on GaAs, with differing indium content [26–27], brought about a big advance in this field. Initially, the thickness of the layers stayed under a critical value, but this limitation was successfully overcome. The strain-induced QD production has superseded the DE, dominating the field earlier.

The archetypal system of the clustered nanostructures is the lattice-mismatched system such as InAs on GaAs, where the strain-induced process leads to the formation of QD. The lattice-mismatched structure can relax either by the generation of misfit dislocation or by the nucleation of nanosized islands on the even layer (Figure 1). The essential driving force for

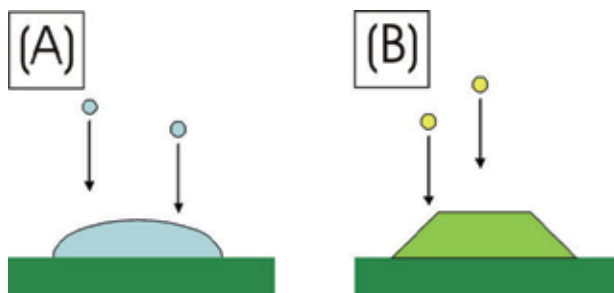


Figure 2. (A) First step of DE: generation of metallic droplet on the surface. (B) Second step: crystallization to create QD.

coherent QD formation, after an under layer formed, is the strain relaxation, whereby the energy gained from the increase in surface area via QD formation more than compensates the increase in interfacial free energy. It is generally accepted that one of the essential driving forces, for coherent lattice-mismatched QD formation, is strain relaxation.

The field of self-organized strain-induced QDs is dominated by two material system, InAs/GaAs (001) and Ge/Si (001). For instance, the MBE growth of about 1.5 MLs of InAs on GaAs results in the spontaneous formation of InAs QDs driven by the strain between the deposited InAs and the GaAs substrate. The driving force for the self-organized QD formation is the strain energy induced by the lattice mismatch of about 7%, in which the condition restricts the material choice. Two families of the shape such as pyramids and domes can be created during the defect-free QD transformations [28].

2.2. Principles of DE

The QD preparation in a self-assembled manner by using the DE technique is an advantageous alternative and extension to the strain-induced QD creation. The basic idea of the DE originated from Koguchi and his coworkers [29, 30]. In comparison with the technology of the strain-induced Stranski–Krastanov QD production, the DE is more flexible regarding the choice of the QD material and also regarding the shape and distribution of the resulted QDs and other unconventionally-shaped QD structures. For example, it is possible to create not only InAs QD on GaAs but also strain-free GaAs QD on AlGaAs surface. Furthermore, this technology of DE allows us to produce ringlike QD and further special-shaped nanosized structures and structure complexes [31–35].

In the case of the DE, the clustering on the surface is carried out with the help of Volmer–Weber like growth mode. The basic idea based on the separation of the III-column and V-column materials supply during the MBE growth (Figure 2). Here, the QD preparation consists of two main parts such as the formation of metallic nanosized droplet on the surface and its crystallization with the help of the non-metallic component of the compound semiconductor. It is very important to mention that this DE technique is entirely compatible with the MBE technology. This circumstance allows us to combine the DE method with the other conventional MBE processes.

First, the III-column elements such as Ga, In, Al, etc., are deposited. These metallic components form clusters that are nanosized droplets on the substrate surface. At the droplet formation, the main driving forces are the diffusion, the minimalization of the surface tension, and the Ostwald ripening [36–42]. The dominance of these driving forces depends on the technological circumstances. The second step of the DE technique is the crystallization of the metallic cluster by the molecular beam irradiation of the nonmetallic V-column element. It is important to suppress or to control the lateral diffusion of the group III elements from the cluster.

2.3. QD engineering

As known, the electronic and optoelectronic properties of the nanostructure depend strongly on the shape of the nanostructure. The technology used for growth can be controlled by the size, shape, and elementary distribution of the developing structure. These technological and physical parameters are very important from both theoretical and practical points of view. In the DE technique, because of the shape and distribution diversity, the key point is to discover growth mechanism and its relation with the parameters of the developed structures. Since the discovery of the DE, several scientific knowledge are gathered. However, until now, no full theoretical description of the underlying growth kinetic is available.

An interesting correlation between the GaAs QD shapes and their volume was observed by Heyn and coworkers [43, 44]. As a result of this discovery, they developed the first growth model for the DE of GaAs QDs [43, 44]. The experiment was carried out with the crystallization of Ga droplets on AlGaAs surface. Here, growth temperature ranged between 140°C and 300°C. On the arsenic terminated surface, the deposition of Ga with flux 0.025–0.79 ML/s was executed. It was clearly visible that growth temperature strongly influenced QD density.

The QD density dependence on temperature shows the scaling law [44]. Under 200°C, the slope of the temperature shows $E_a = 0.235$ eV. Over 200°C, data did not follow the scaling law, but QD density decreased. At this temperature, coarsening of the cluster begins. This effect goes back to the Ostwald ripening, which means the growth of large clusters at the expense of smaller ones, hence causing a decrease in the total cluster density.

Higher temperature combined with lower arsenic flux will result in a ringlike nanostructure. At longer waiting time and lower arsenic flux, these rings fall below the original substrate surface and the encircling surround. After the heat treatment of the sample with the clusters formed, the total lack of arsenic results in nanoholes. The creation of nanoholes can lead back to the thermal etching of the substrate by the liquid metallic component. At a typical process temperature of 570°C, etching starts approximately 20 s later than the beginning of the annealing step, followed by desorption approximately 100 s after. The depth of the nanoholes can be found by multiplying the etching time by the etching rate.

These nanoholes can be filled with low band-gap material to create the so-called inverted QD. Furthermore, the nanoholes can serve as templates for QD preparation. In the utilization of surface anisotropy, QD pairs can be grown. The nanohole and the nanomound can initialize QD molecules, where the QD per molecules ranged from two to six. In the case of InAs QDs on GaAs (001) surface, the number of QDs per GaAs mound can be effectively controlled by varying InAs ML coverage [45].

3. Droplet formation

3.1. The initial surface status

During the QD formation, the status of the substrate surface is very important. It is well known that surface reconstruction influences strongly the growing layer and the forming structure [16]. Surface reconstruction depends on the temperature and the ambient environment environment, too. As mentioned before, the DE technique is compatible with the MBE technology. It means that the growing surface can be continuously monitored with reflection high-energy electron diffraction (RHEED) to determine the status of the surface, e.g., the surface reconstruction. During the growth, the RHEED pattern and its specular spot intensity allows a real-time tracking of the surface status changes. Here, we are using the technological most important (001) surface orientation. The bipolar (001) surface of GaAs can be terminated by either Ga or As atoms with rich variety of reconstructions are formed depending on surface stoichiometries [16].

Before the droplet creation, we have to grow a layer from a wide band-gap material for barrier. This layer growth happened with a conventional MBE technology, which is carried out in arsenic ambient pressure. Hence, the initial status of the surface is arsenic terminated. After the layer growth, we have to change the temperature depending on the planned nanostructure shape. The deposited MLs are not equal with the droplet volume. Assume that Ga is deposited on AlGaAs surface at 200°C. Due to the strong binding energy of As to Ga and substrate, the first Ga ML is consumed for the formation of Ga terminated surface. This first ML volume does not contribute to the formation of the Ga droplets. It means the coverage of Ga located in the droplet is $Ft-A$. The total Ga surface coverage is $\Theta = Ft$, where it is resulted with flux F for a time t , and A is the incorporated value of ML.

Although no complete phase diagram of GaAs (001) has been mapped, certain surface phases are generally observed during growth or after growth and annealing. For example, the less As-rich surface exhibits a $(2 \times 4) / c(2 \times 8)$ pattern and arises from 0.75 ML of As. This reconstruction is normally present during the MBE of GaAs. Areas with (2×4) and $c(2 \times 8)$ symmetry can coexist. With larger coverage of As, a $c(4 \times 4)$ reconstruction with As coverage of 1.75 ML is observed [46, 47]. Depending on the substrate temperature and the Ga-to-As ratio during MBE, the GaAs (001) surface is known to display various surface reconstructions ranging from the As-rich $c(4 \times 4)\beta$, $c(4 \times 4)\alpha$, $c(2 \times 8)$, and (2×4) to the Ga-rich (6×6) , $c(8 \times 2)$, (4×6) , and (4×2) surface. The surface symmetry critically depends on the preparation conditions [46, 47].

In situ investigations of this large set of reconstructions with RHEED are well established. Using scanning tunneling microscopy (STM), most of these surface reconstructions could also be imaged in real space, and the structure and the structural models were refined, too. Most of the previous studies were based on the diffraction techniques and no direct observation for the (4×6) phase exists. The STM study reveals that (4×6) symmetry arises from the coexistence of (2×4) and (4×2) units [48]. We have seen before that the change in temperature and other parameters results in the continuous change in surface reconstruction. During the change of the temperature, not only the reconstruction but also the specular spot intensity changes. The results show that at lower temperature, the specular spot intensity is high, and at higher

temperature, the intensity is low. Furthermore, in the up and down and back directions, the temperature versus intensity function shows hysteretic behavior (Figure 3). The explanation of this phenomenon can lead us to the understanding of the intricate surface structures [49, 50].

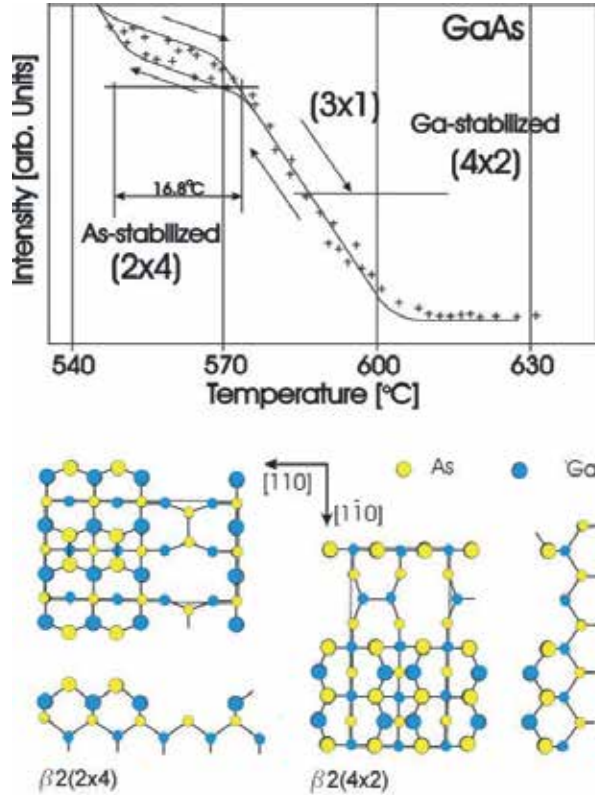


Figure 3. Ga and As stabilized GaAs (001) surface depending on the substrate temperature.

The initial step of the DE is the droplets creation on the surface. It is already well documented that the droplet nucleation requires Ga-terminated surface, which means that a part of Ga coverage incorporate into the surface. During the initial stage of Ga deposition, fundamental change happens in the surface reconstruction, which strongly influences the droplet formation. Before the Ga deposition, the surface reconstruction can be usually $c(4 \times 4)$, (2×4) , or (4×6) , where the values of As coverage are 1.75, 0.75, or 1.12 ML, respectively. The previous paragraphs show the complicity of the surface reconstruction and other difficult unsolved problems associated with the process. The part from the metallic surface deposition migrating into the droplet depends largely on the initial state of the surface.

3.2. Size and density of the droplets

The size and the density of the metallic droplets depend on the substrate temperature and on the deposited MLs. In the case of Ga droplets on AlGaAs surface under 200 °C, the cluster

density versus temperature follows scaling law. Over 200°C, the scaling law is broken. Under this temperature, the clusters begin to coalesce, which drastically reduce the cluster number. This decrease of cluster number is governed by the Ostwald ripening [36–42].

The reduction of the cluster number is affected by the diffusion length of the constituents. The condition required for the coalescence is the overlap of the diffusion length and the mean distance of the neighboring clusters. It is characterized by a local interaction between neighboring clusters of slightly different size. The smaller cluster starts to decompose to maintain the gradient of the radius equilibrium concentration toward the larger cluster due to the Gibbs–Thomson effect [51]. The appearance of such processes is critically dependent on the initial conditions.

The Ostwald ripening describes the driving force, which determines the size distribution of cluster ensemble on the surface [38–40, 42, 52]. This description supposes a driving force that depends on the mean radius of the islands. It is supposed that atoms detach more readily from smaller islands and condense rather to larger ones. Therefore, for a given amount of material on the surface, larger islands grow at the expense of smaller ones. The temporal evolution of the island radius (r) can be described by a differential equation: $dr/dt = b(T) / r^2(1/r - 1/r_c)$, where r_c is the critical cluster radius and $b(T)$ is a temperature-dependent parameter.

3.3. Droplet–surface interaction

In this section, we will discuss the interaction between the droplet and the substrate surface. Here, the dependence of the droplet shape and the so-called thermal etching are discussed. It is known that the droplet shape is determined by the wettability of the substrate surface, and this property can be described by contact angle. There are three types of situations: no wetting, partial wetting, and complete wetting, where these situations correspond somewhat with the three growth modes. The contact angle depends on some circumstances, such as the status of the carrier surface, the droplet size, and the temperature. This is because the nuclei may wet the substrate, strongly changing their geometry. The deposited material will not wet the substrate because this would be accompanied by an overall increase in free energy of the system. The liquid deposit will spread out to maximize the area of the interface. For all the other situations, a partial wetting with a contact angle θ should be considered, that is, $\gamma_s = \gamma_i + \gamma_e \cos\theta$, where γ_e and γ_s represent the surface free energies of deposited cluster and substrate, respectively, and γ_i is the interfacial free energy (Figure 4) [53].

In our DE case, we have to discuss a further interaction between the droplet and the carrier surface. This interaction is called thermal etching, droplet etching, or local droplet etching. The explanation of the process will be discussed with the help of Ga/GaAs/AlGaAs system. Where Ga droplet forms on AlGaAs surface.

It is known from the liquid phase epitaxy that thermal etching takes place at the interface Ga melt and AlGaAs surface [54–57]. In the first step in DE technology, Ga droplets are generated on the surface. Due to thermal etching, this droplet-shaped Ga melt can solve the arsenide from the substrate material. At the interface, the metallic components of the substrate mix with the Ga atoms of the droplet. During the QD formation, this thermal etching takes place, too.

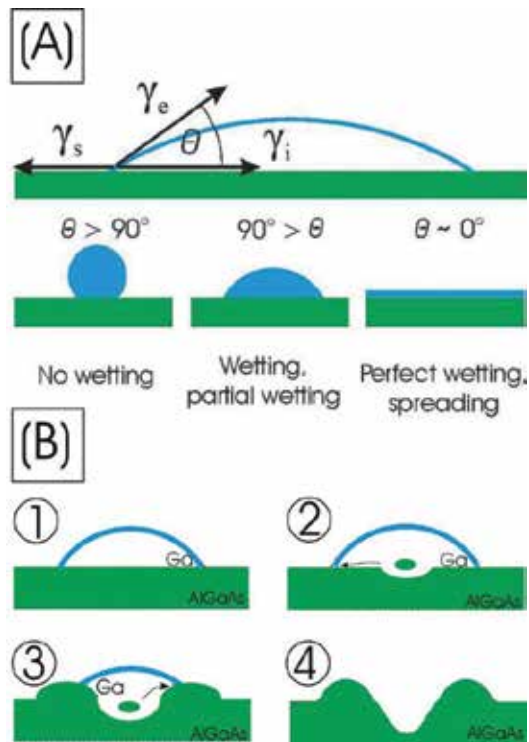


Figure 4. (A) The contact angle dependence on the surface tension and wettability. (B) Localized thermal etching of the compound semiconductor surface by a metallic droplet.

In the initial stage of the QD formation, enough time is available for the mixing of the atoms at the interface. In the case of GaAs QD on AlGaAs substrate, Al content can be observed in the GaAs QD. This phenomenon was confirmed by the author and coworkers [58]. This thermal etching effect can be observed also at evolution of the ringlike QDs.

Our observations show that the middle part of ringlike QDs is below the surface of the substrate surrounding the QDs. This phenomenon is also the consequence of thermal etching. At slow crystallization, etching can act longer; therefore, it results in deeper holes in the center. At high temperature, quite deep nanohole can be achieved [85].

Thermal etching can be utilized also for nanostructure preparation. With the help of droplets created on the substrate surface, the surface can locally be etched. At higher temperature, this etching phenomenon is more significant. After the local thermal etching, the remained deep craters are the so-called nanoholes. During the DE QD fabrication, the Ga deposition temperature is ranged between 100°C and 350°C typically. These temperatures are very low compared to usual MBE growth conditions. In this case, the droplet thermal etching is less significant. At significant higher temperature, the situation is different.

If the temperature ranged between 450°C and 620°C , the local thermal etching under the droplet is already considerable. After an annealing time, the droplet is replaced in a nanohole

surrounded with lobes. This local droplet etching shows a very promising technique for the structuring of the substrate surface without any lithographic processes. Furthermore, this patterning is also fully compatible with the MBE technology. In this way, nanohole was first presented by Wang and coworkers [59].

This finding opened a new way for the fabrication of another type of QD. This system was based on the filling of the nanohole, where the fill of the hole is carried out with lower band-gap material than the substrate. In this way created, nanohole filled inverted QDs are demonstrated by Heyn and coworkers [60–66]. In the process of nanohole filling, we utilize the Ga diffusion on the substrate surface. The temperature and orientation dependence of the Ga (and other metallic component) diffusion can be utilized at further nanostructure preparation.

4. Formation of QD

4.1. Preparation technology

The initialization of the alternatively grown conventionally shaped QD preparation, the basic idea of DE, originated from Koguchi and his coworkers [6, 30]. In this way, it is possible to create strain-free GaAs QD on AlGaAs surface. Along this discovery, further unconventionally shaped QD types were discovered [9, 32–35]. In the following, we will detail the DE-grown single hump-shaped QD in the case of GaAs/AlGaAs system. As discussed above, this process consists roughly of two main steps. First, metal (in our case Ga) droplets are generated on the surface in a Volmer–Weber-like growth mode. In the second step, crystallization takes place. Under arsenic pressure, the droplets transform into crystalline nanostructures. The shape of the nanostructures and their distribution depend on the initial droplet size and distribution and on the further technological parameters such as substrate temperature, arsenic pressure, waiting time, etc.

Here, typical experimental parameters for conventional QD preparation are described [43]. The GaAs QDs are grown on AlGaAs (001) surface. The growth experiments are performed in a solid source MBE system equipped with effusion cells for Ga and Al evaporation and valved cracker cell for arsenic ambient pressure. The evolution of growth front is in situ monitored with RHEED. First, on GaAs (001) wafer, pure GaAs layer is grown, and it is followed by an AlGaAs layer with Al content of 0.3. After the AlGaAs layer preparation, the sample is cooled down to 200°C. The $\theta = 3.75$ ML Ga is deposited with the flux of 0.75 ML/s without any As flux. After the Ga deposition, a 60-s waiting time is performed. The annealing is carried out at a temperature of 350°C and at an As pressure of 5×10^{-5} Torr. The growth process are tracked continuously in the direction of [110] with the help of RHEED [67]. In this direction, the RHEED pattern is more informative for the status of the QD evolution compared with the perpendicular [110] direction. After the growth process, the quantum objects can be ex situ investigated (AFM and TEM and PL methods), which can provide us further information to understand the growth kinetics.

During the QD preparation, the sequence of the RHEED pictures in the main growth stages is depicted in Figure 5. In the initial stage, the RHEED pattern showed sharp streaks (stage

at t_0). After the Ga deposition, the pattern diffused on the RHEED screen (stage at t_1). Almost at the same time with the offering of arsenic pressure, the RHEED pattern changed suddenly from diffused to spotty (stage at t_2). During the annealing phase, the pattern changed slowly (some minutes) from spotty to spots with tails (stage at t_3). The density of QDs is $3.6 \times 10^{10} \text{ cm}^{-2}$. It is shown that the characteristic RHEED pattern of QD is still recognizable even if the dot density is one order of magnitude less [43].

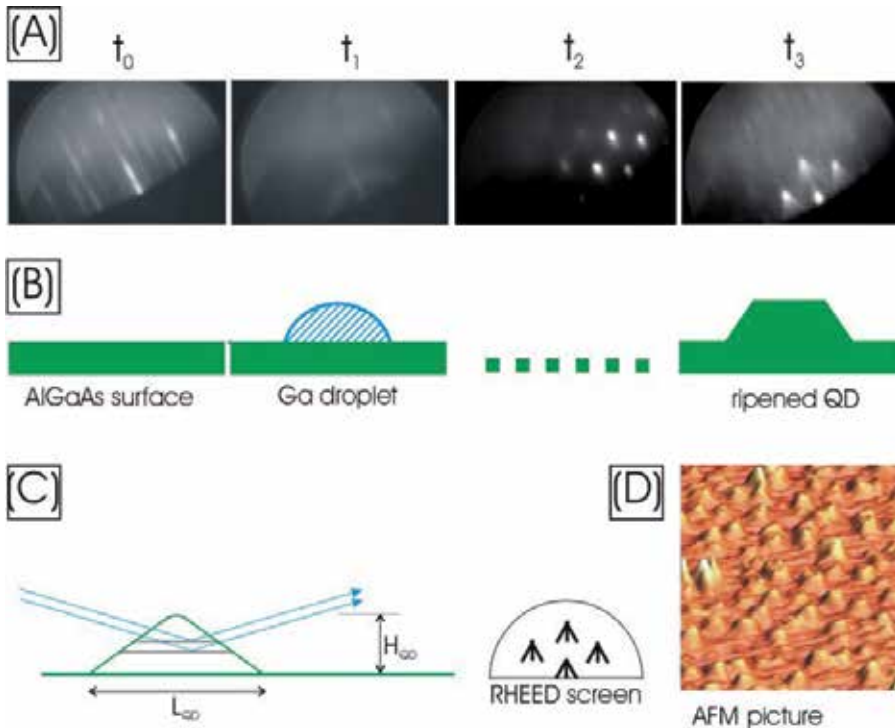


Figure 5. (A) During the QD evolution, the changing of the RHEED pattern and (B) its temporal evaluation. (C) Interaction of QD and electron beam. (D) AFM picture of DE-grown QDs.

4.2. Geometry and electronic structure of QD

As we demonstrated earlier, the shape of the QDs depends on the volume and also the density of QDs. According to the shape, there are two types of QDs. The larger type of QD is a truncated pyramid-like shape with side facets of 55° . The smaller QD is a pyramid-like form with a side facet of 25° [43, 44]. In the following, the geometry of the QD will be discussed in the case of the smaller type of QD.

The atomic resolution structure of a typical DE-grown QD is shown in Figure 6. (The image was taken with the electron beam parallel to the [110] zone axis of the AlGaAs single crystal substrate [43, 67–68].) The typical dimensions of the QD shown in Figure 6 are 54 nm base width and 5.5 nm height. The steepness of the QD side wall measured by TEM as well as by

AFM shows about 25° . Figure 6 also shows that all the lattice fringes of the AlGaAs substrate are continued in the GaAs QD without any distortion. It is well known that the lattice parameters of these two substances are practically the same. No crystal defects were observed within the QD or at the interface with the host crystal [68, 69].

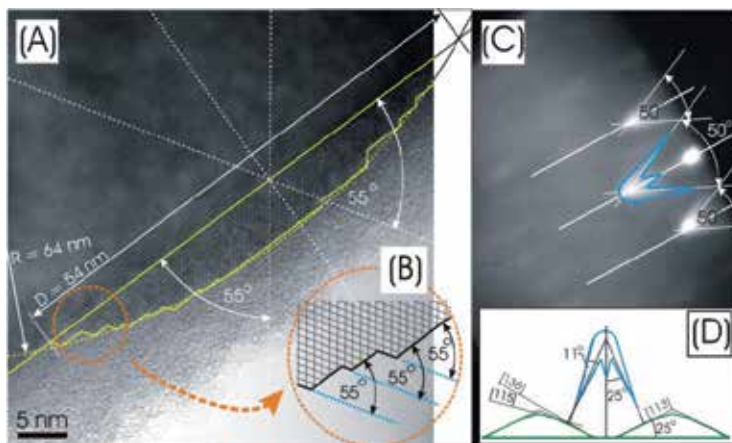


Figure 6. (A) Cross-sectional TEM image of a DE-grown QD, and (B) its stepped surface. (C) Broadened chevron tails and (D) their explanation.

The feature mentioned is shown in a darker contrast of the QD, also a few atomic surface layer of AlGaAs crystal between the QDs. The darker contrast on the AlGaAs surface can be interpreted as follows. The AlGaAs layer, at low temperature, shows As-rich $c(4\times 4)$ surface. Nominally, $\theta = 3.75$ ML Ga is deposited on the surface without arsenic flux. In the duration the Ga supply, a few ML of Ga is combined with excess arsenic surface atoms. Thus, a thin GaAs layer forms on the surface while the rest of the Ga forms nanodroplets. During the crystallization, the droplet and the surface layer go into similar composition. As a result, the QD and the surface layer shows similar darker contrast compared to the host material [69]. The existence of this GaAs surface layer was predicted earlier from the comparison of the PL measurement and the energy level calculation [32].

The chevron tails are connected with the faceting of QDs as it was verified in the case of diverse-shaped DE QDs [10]. In case of DE, it can be shown from the AFM measurement and from the tilted TEM picture that the shape and size of QDs are very uniform [69], and their side angle is about 25° [43, 68], which corresponds to the half opening angle of the chevron tails (Figure 6). Despite the same shape of the QDs, the chevron tails are not sharp but broad [68]. The observed side angle near to 25° corresponds to the (113) crystallographic plane [67, 68].

A cross-sectional TEM image shows that the side of the QD is not a single crystalline plane but has stepped shape (faceting). The steps consist of planes parallel with interface (parallel with {002} crystal planes) and planes with 55° to the interface, corresponding to {111} planes. The envelope curve of the QD cross section is a circle segment with a radius of $R = 64$ nm [68].

The electronic structure of the DE-grown GaAs QDs was investigated by PL spectroscopy [70, 71]. Furthermore, lasing was demonstrated in such structure [72]. After postgrown annealing, improved optical performance was demonstrated [72]. In the case of DE-grown QDs, the better optical properties compared to strain-induced QDs originated from the technology. The DE-grown QDs are prepared at very low substrate temperatures, which are unfavorable in view of the incorporation of undesired background impurities and crystal defects.

4.3. Some aspects to the kinetics of QD growth

The growth kinetic can primarily be investigated by the in situ RHEED tracking. In the annealing phase of QD production, the diffused RHEED pattern becomes spotty nearly simultaneously with the opening of arsenic source. The sufficient arsenic quantity and the low temperature make the build in (infiltration) of As in the Ga phase (i.e., crystallization) possible [73]. This process of infiltration takes about 2–3 min to the sharp chevron image. A crystallized shell comes into being on the Ga droplets. The spotty RHEED pattern originates from the transmission electron diffraction. The electron beam goes through the crystalline GaAs shell layers over the droplet. If there are crystallite formation or droplets on the surface, it is observed that bulk scattering of the grazing beam can occur and the RHEED pattern may become dominated by spots rather than streaks due to transmission electron diffraction (Figure 5) [67].

The scattering from several planes strongly modulates the intensity along the reciprocal lattice rod. Thus, the streaks observed from two-dimensional surface are not observed when transmission dominates [67]. For the transmission case, the reciprocal lattice is an array of points each broadened owing to the finite size of the scattering region. During the annealing, the As diffuses inside of droplets, while excess As builds in (infiltrates) in the shell [73, 74]. Thus, the droplet crystallizes slowly. In the given moment, the rounded shell will be broken by the cornered crystallite grown inside of the structure. At the same time, a chevron-shaped spot develops on the RHEED screen [43, 48, 67, 68].

The angle between two RHEED streaks starting from same reciprocal lattice point is about 55° , as shown in final stage of the QD evolution. These so-called chevron tails are attributed perpendicularly to the facets of the QD [67, 69]. The volume of the QDs is large enough to receive transmission pattern during the electron scattering. The main lateral expansion L_{QD} and height H_{QD} of QD – according to the AFM measurement – are 50 and 5 nm, respectively (see Figure 6). The mean free path of the electrons λ in GaAs between the crystal planes without collision at the typical incidence angle of RHEED (about 2°) is less than 20 nm. Thus, in our case, there are several (ca. 9) lattice planes to receive transmission character [67].

The analytical TEM investigation provides further contribution to the evolution kinetics. In our TEM investigations, we detected Al content in GaAs QD [48]. Here, this study shows the high-resolution micrograph of a similar QD together with Ga and Al elemental maps of the same area. These images clearly show that the QDs contain both Ga and Al. The presence of Al within the QDs is supported by the explicit protrusion of bright contrast on the Al map at regions corresponding to the QDs. This feature originated from a dissolution process [67]. This process is very important for QR production. This phenomenon will be discussed in the next section.

On the basis of the measurements, the following kinetics explanation seems plausible [68, 69]. The process of GaAs crystallization starts at the edge of the droplet, initialized by the three-phase line (TPL) at this point, serving as discontinuity for the seeding [100]. Although in principle interaction can take place at any point of the droplet, due to the thermal movement, the species, arriving to the edge, will start the seeding of the crystallization process. The described mechanism for this process has been accepted by several authors too. [11, 67]. (Otherwise, it would be difficult to explain the formation of the ringlike QD. In the case of a dot, the seed grows inward, while in the case of ring, it tends to grow outward, which is maintained by the Ga migration.) Since we are dealing with dot shape, the dominant process is arsenic diffusion.

The crystal seed grows inward into the droplet, and also upward simultaneously. This process of growth can only be explained quantitatively because, in the case of nanosizes, the observed bulk processes and properties like diffusion and binding energy cannot be applied. Although similar crystallization processes have been observed, no attempt has been made to explain them until now (see Figure 7) [68]. The growth of the GaAs crystal occurs in direction opposite to the penetration of Al. The crystallization of GaAs can start only after the opening of arsenic cell, while the dissolution of AlAs species occurs immediately upon the deposition of droplets. The process at the surface is quicker than process at the interface. Thus, the process at the surface is the dominant during the processing time of the QD production.

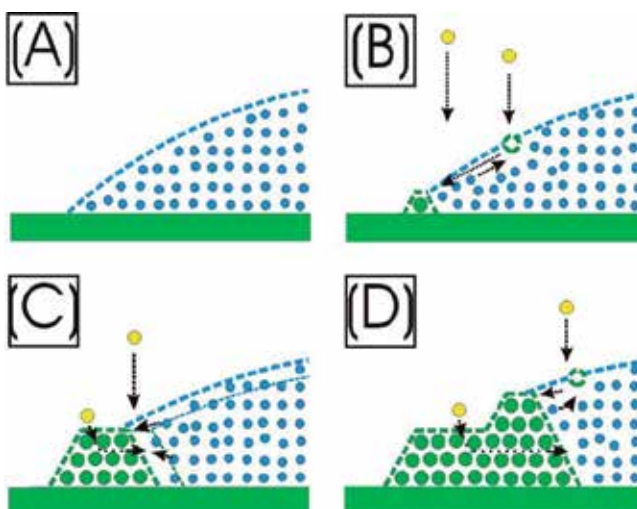


Figure 7. Explanation of the stepped surface evolution.

We explained the evolution kinetics of the stepped outer surface of the QD [68]. The summary of the kinetic is as follows. The intersection of the crystal surface with the droplet is the TPL, which serves as an initial place of crystallization [68]. When a Ga atom of the droplet meets an arsenic atom, they form a GaAs molecule. These GaAs species, making a Brown-like movement over the droplet surface, can reach the TPL, where the crystallization starts (Figure 6). The

crystal seed at the TPL will grow on the account of further arriving arsenic species. The outer facet angle of the crystallization center at the edge will be the favorable 55° because it has enough time to find the optimal position (the low index facet). The crystallization seed grows partly upward and also partly in the direction of the droplet inside. During the process of solidification, a circular monocrystalline phase is formed at the droplet edge inheriting the orientation of the perfect substrate. During the process of solidification, the amount of Ga atoms in the droplets decreases so the droplet size decreases too. The outer side of the QD consists of steps of few MLs, where the front panel and the terrace of the step are (111) and (001) planes, respectively.

It is known in fcc crystals that the surface energy of (111) facet is less than that of (001) facet; thus, the latter grows predominantly during crystallization. This takes place by the lateral shift of the low energy (111) step facets with the simultaneous areal growth of (001) facets. With the size decrease of the droplet, its edge moves inward, thus creating a new TPL or crystallization seed at the new place, and the whole process continues as before with the original droplet and substrate. The only difference is that the crystallization takes place along a circle of less and less diameter.

5. Ringlike QD preparation

5.1. Growth technology of ringlike QD

The preparation process responsible for the DE formation of ringlike QDs is described in the case of GaAs nanostructures on AlGaAs (001) surface. The growth experiments are performed similarly as described in the previous section, but the technological parameters somewhat differs. On GaAs (001) wafers, first pure GaAs layer is grown, and it is followed by an AlGaAs layer with Al content of 0.3.

Then the GaAs sample with AlGaAs layer must be cooled down to 300°C . On the surface, Ga is deposited as described in former section. Then $\theta = 3.75$ ML gallium is deposited with the flux of 0.19 ML/s without any arsenic flux. During the annealing, the temperature remained the same (300°C), but the As pressure was 4×10^{-6} Torr. The production of the quantum objects was tracked continuously in the direction of $[1\bar{1}0]$ with the help of RHEED [67].

Further, two types of ringlike nanostructures were generated with different amounts of deposited Ga. One of them was generated at 570°C on AlGaAs (001) surface applying 6.4 ML Ga. In this case, the AFM measurement shows ringlike QD with deep hole in the middle of the structure and very large clusters [95]. The other type of the nanostructures was prepared similarly, but the deposited Ga was less than that in the former case. The Ga coverage was 3.2 ML. In this case, the AFM picture shows special-shaped nanostructure with very deep crater in the middle surrounded by ringlike bulge formations and also shallow nanocraters, with plane rims (without bulge) [75, 76].

After the growth process, quantum objects are investigated using the AFM method, and the first mentioned types of nanostructure are studied with PL technique, too. Temperature-

dependent PL spectra measured on the GaAs ringlike QD samples are compared with the conventionally shaped QDs.

The technology can continuously be tracked by RHEED. The initial stage of the surfaces is the same as in the case of conventional QD. The RHEED pattern of the initial surface shows sharp streaks (stage t_0 on Figure 8). After the Ga deposition, the pattern diffuses on the RHEED screen similarly as in the case of QDs (stage t_1). The deposited Ga is in liquid phase. The disappearance of the RHEED pattern originates from the appearance of the liquid phase of Ga droplet on the surface. However, after the Ga deposition, the change of the observed RHEED pattern is quite different. After the offering of arsenic background of 4×10^{-6} Torr, the RHEED pattern develops very slowly, over 5 min. Contrary to the case of conventionally shaped QDs, which is almost at the same time of the arsenic cell opening, the RHEED pattern changed suddenly. The developed pattern contains in the middle a streak with a small spot and around elongated larger spots. According the AFM measurement, the density of the ringlike structures is $1.5 \times 10^9 \text{ cm}^{-2}$. In this case, the effect of open surface on RHEED is larger than in the case of QD [69]. It is shown that the characteristic RHEED pattern of QD is still recognizable even if QD density is one order of magnitude less [43].

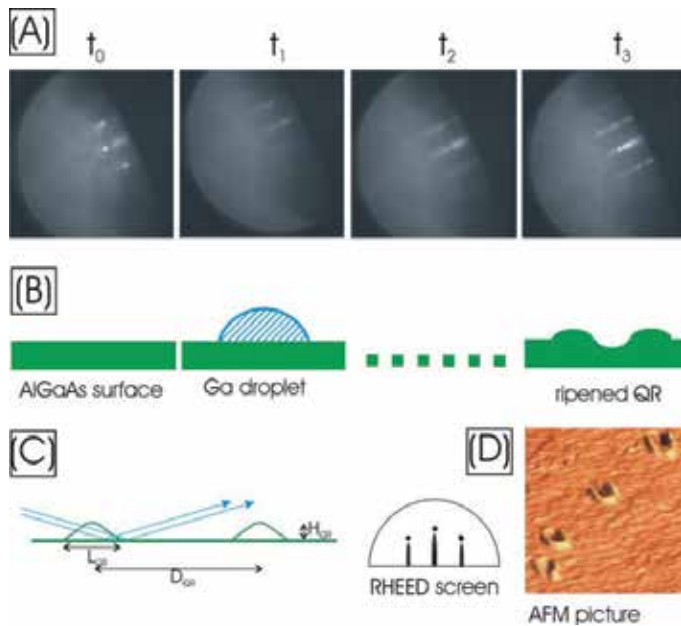


Figure 8. (A) During the evolution of ringlike DE-grown QD, the changing of the RHEED pattern and (B) its temporal evaluation. (C) Interaction of ringlike QD and electron beam. (D) AFM picture of DE-grown ripened nanostructures.

5.2. Geometry and electronic structure of the ringlike QD

The shapes of ringlike QDs are various. The main parameters are the following: ring-middle diameter, width of the ring base, and height. As we will show, the facet angle is determined

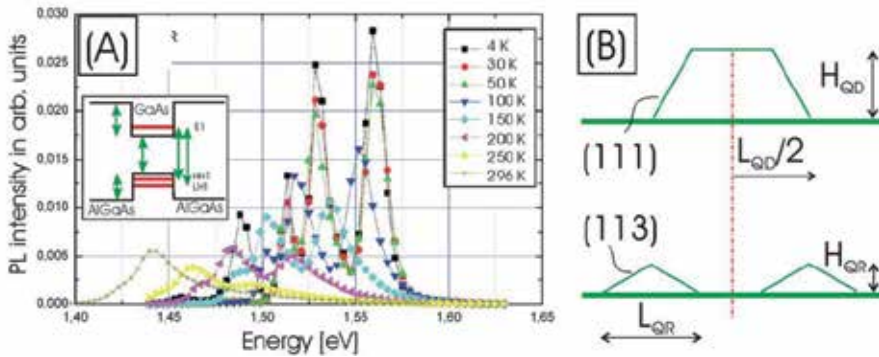


Figure 9. Temperature-dependent PL spectra of ringlike QD. (B) The explanation, why the ringlike QD has significantly sharper PL peaks compared to conventionally shaped QD.

by the volume. The further shape parameter is the level of the ring middle. The ring middle can lie higher or deeper than the original substrate surface. At lower annealing temperature and at less arsenic ambient pressure, the droplet metamorphosis results in ringlike nanostructure with smaller crater in the middle [78–81]. For example, at 4.75 ML Ga deposition, under 1×10^{-5} Torr arsenic pressure and 350°C annealing for 10 min, the resulted structures are ring with shallow crater [79].

In another case, if the ring center lies deeper [75, 77], the structure is called a nanohole. In this case, thermal etching is dominant. If the annealing temperature is higher and the arsenic ambient pressure is smaller, then we receive ring structure with low-lying center. For example, at 8 ML deposited Ga, at 520°C annealing and under various arsenic pressure, we can get nanostructures with various deepness in the middle. If the arsenic pressures are 3×10^{-6} , 2×10^{-6} , 1×10^{-6} , and 1×10^{-7} Torr, then the holes are ca. 3, ca. 7, ca. 8.5, and 9.5 nm deep, respectively [62, 75, 76, 82].

The electronic structure is strongly governed by the shape of the nanostructure. Here, the advantages of the ringlike QD compared to the conventionally shaped QD are described using temperature-dependent PL spectra. Under measurement, the temperature ranges between 4 K and 300 K. The samples are excited by Ar^+ ion laser at 488 nm wavelength. The resolution was better than 0.5 nm [83].

The PL spectra of the uncovered GaAs ringlike QD grown on AlGaAs surface are shown in Figure 9. At 4 K, the spectrum has five peaks. They can be explained as bound exciton (1.5129 eV), exciton bound to acceptor (1.4892 eV), and its longitudinal optical phonon replica (1.4577 eV). Further on at higher energies, two peaks appear (1.5308 and 1.5602 eV). The PL spectra were also recorded as a function of temperature. To verify the identification of the peaks, the temperature dependence of the band-gap energy of GaAs and that of the bound exciton were compared. At 4 K in the case of conventionally shaped QD with identical volume, three peaks can only be seen at lower energy range. It is visible that the quantum confinement in ringlike QD is larger than that in QD at same nanostructure volume. In the following, this phenomenon will be explained [83].

The base diameter of the QD (L_{QD}) investigated is much larger, and its height (H_{QD}) is also larger but comparable. Thus, here no quantum effects are expected. Therefore, it was impossible to detect a peak shift or peak broadening for QD. At the same volume, for ringlike structure, the laterally wide (L_{QR}) nanostructure had a height (H_{QR}) significantly less than 7 nm. Consequently, the supposition of quantum confinement produces proper result [83].

The PL spectra show characteristic peak width, depending on the temperature and the size distribution of these structures. At the same temperature, a broader size variation results in a broader PL peak. Under similar growth conditions, the PL peaks of ringlike structures have significantly narrower full width at half maximum (FWHM) (less than one third) than that of the conventionally shaped QDs [78, 84].

The sharper PL peaks can be explained by follows. As it is known, both kinds of QDs is formed from a gallium droplet. Assume that the volume and its variation of the initial droplets are the same in both cases. The facet of the nanostructures is size dependent and cannot be arbitrarily sized [43]. For the QD, let's start from the greater (111) facet (the approx. diameter ($2r = L_{\text{QD}}$) is 100 nm [43]). For the ringlike QD, only the (113) facet can be taken into account because of the smaller volume (the approximate width (L_{QR}) is 60 nm [43, 44, 83], dedicated to a circle segment). Due to the crystallographic constraints, the geometry of the formed QDs is determined. The height-to-diameter ratio cannot be arbitrary; it can be defined by a single parameter.

If r ($r = L_{\text{QD}}/2$) is the radius of the base circle belonging to the initial droplet, the volume of the developing QD, as a function of r , is given by $V = 1.58r^3$. For the ringlike nanostructure, from the equality of the volumes, the w ($w = L_{\text{QR}}$) parameter can be calculated as $w = 0.71r$. (This means that the nano-object with a parameter of $2r = 100$ nm has (111) facets, and the other one with a parameter of $w = 0.71 \times 100 \sim 70$ nm or less has (113) facets. It corresponds to the above presented measured data.) It means, that the height of the nanostructure influences commonly the quantum behavior. The heights of the QD and QR structures can be expressed as a function of their volumes: $m_{\text{QD}} = V^{1/3}/1.34$ and $m_{\text{QR}} = V^{1/3}/6.56$, respectively. Assuming the same variations of the volumes, it can be seen that the variation of the height for QR is much smaller than for QD; consequently, the corresponding FWHM of the PL peak is smaller [83].

5.3. Some aspects to the formation of ringlike nanostructure

The primer information to discover the formation kinetic originates from RHEED tracking [67]. After the deposition of Ga on AlGaAs (001) surface, the RHEED picture is becoming diffused due to the amorphous nature of the phase present on the surface. The annealing phase begins after the offering of arsenic component ($p_{\text{As}} = 4 \times 10^{-6}$ Torr, $T_{\text{sub}} = 300^\circ\text{C}$). After releasing the arsenic, some time is needed for the development of the characteristic sharp pattern, representative of the crystalline structure. This is an indication that the liquid state on the surface stays longer and that the material transfer processes helps the formation of the ringlike structures. For detailed technological parameters of the different DE nanostructures, we refer the readers to the literature [32–35, 43–45, 62].

After the completion of the growth, the QR structures were investigated with AFM. The perspective AFM image and the top view with line scans are shown in Figure 10. The dimensions of QRs were determined from individual line scans. The density of the nanostructures determined from AFM pictures was $1.5 \times 10^9 \text{ cm}^{-2}$. It is visible that the middles of the nanostructures are deeper than the original surface level [85]. It can be shown, from the AFM measurement that although the shapes and sizes of QRs are fairly uniform, we can observe small deviations from these averages. It is often observed that the smaller diameter rings have deeper depressions in the center and the larger diameter rings have shallower ones in the middle. (In the illustrations, the smaller and larger objects are labeled with "S" and "L", respectively.) The QRs have slightly elongated shapes due to the different binding properties in $[110]$ and $[\bar{1}\bar{1}0]$ directions [86].

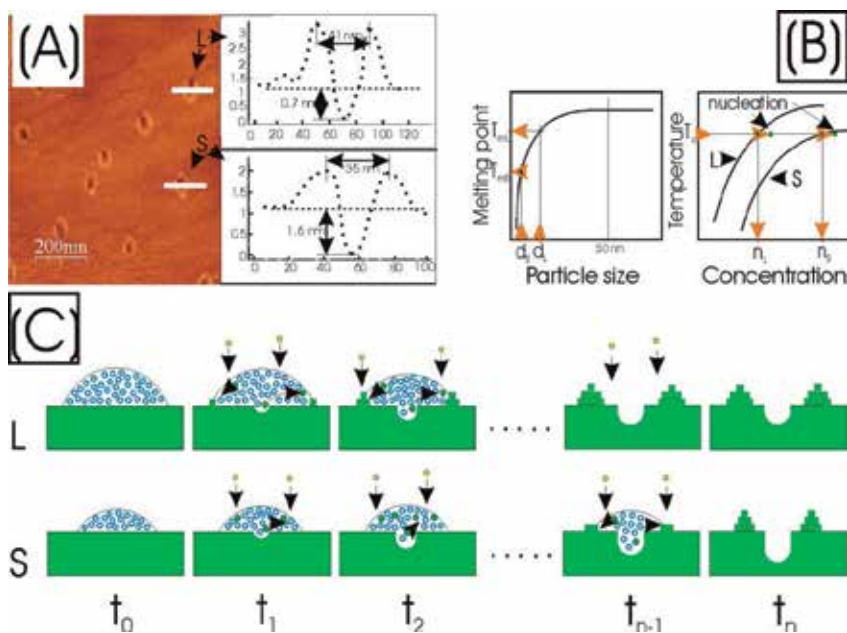


Figure 10. (A) Cavity dependence on the droplet size. (B) Functions of melting point and solubility. (C) Temporal evaluation of the smaller and larger ringlike QDs.

These facts are contradictory to the aspect ratios of ringlike QDs, and the explanation can help to understand the kinetics of the DE quantum structure formation. The explanation to this extraordinary behavior is as follows [85]. It is an obvious assumption that the larger droplets are leading to the development of rings of larger diameter and equally the smaller droplets to smaller rings. The intersection of the crystal surface with the droplet edge is the so-called TPL, which is the initial place of crystallization [85]. The TPL of larger diameter initiates a larger droplet, and equally, the smaller diameter forms from a smaller droplet. It is known from the liquid phase epitaxy that thermal etching takes place at the interface of the Ga melt and AlGaAs surface. This phenomenon was confirmed by analytical TEM for DE QD [69]. The Ga melt can

solve the arsenide molecules (e.g., GaAs). These arsenide molecules originate partly from the thermal etching of the AlGaAs substrate surface and partly from the reaction of the external (from effusion source) arsenic atoms. (When a Ga atom of the droplet meets an arsenic atom from the environment, they form a GaAs molecule.) These molecules, due to thermal movement in the droplet, can reach the TPL, where the crystallization takes place. During the process of solidification, the material migrates from the middle to the edge of the nanostructure. A circular crystalline phase is formed at the droplet edge. The proposed kinetics for the formation is shown schematically in Figure 10.

It is known that the melting point decreases with the reduction of the particle size. The normalized melting curve versus the diameter of the particle (Figure 10) shows that when the particle size is less than 50 nm, then the melting point depends very strongly on size. In the nanorange, this dependence on the size is stronger than for the bulk. What makes it more complicated is the fact that the melting point depends on the particle shape as well. In this case, the Ga droplet's shape is a segment of a sphere. Its width in the middle falls in the range of 10–20 nm. Here, the change in the melting point is particularly sharp [85].

Around the edges the structure is thin. The experimentally obtained melting curves for near spherical metal nanoparticles show similarly. We use these curves for the qualitative assessment. This indicates that the melting point of the large and that of the small Ga droplets can differ considerably. The solubility curves for different particle sizes (Figure 10) show that at the same temperature, the larger droplet has lower saturating concentration than the smaller one. The meaning of this is that crystallization in the larger droplet will take place earlier, at lower arsenide concentration than in a smaller one. The smaller droplet will crystallize later, during arsenide concentration.

The temporal evaluation of the smaller and larger ringlike QDs is shown in lower part of the figure onset (Figure 10) [85]. In other words, in the larger droplets, the probability of the formation of the crystallization seeds is higher; therefore, the crystallization takes place earlier so less time is spent on material transportation, causing the development of the depression in the middle. When the droplets are small, the probability is less, and crystallization starts later, leaving more time for the formation of deeper depression in the center of the ring. This process is influenced by other factors as well. The melting temperature of the nanostructure is dropping with its diminishing size, staying longer in liquid state at the same temperature, spending more time on the formation of deeper in the center [85].

The above-described finding can be proven by further experiments (in Section 5.1, ringlike nanostructure production is described where the amounts of the deposited Ga were 3.2 and 6.4 ML, respectively). The explanation is as follows [85, 87, 88]: At a given temperature, there is a critical droplet size (CDS) under which the solution begins. After the Ga deposition, droplets form, followed by the growth of the larger droplets at the expense of smaller ones according the Ostwald ripening. When the droplet is smaller than the CDS, the substrate solution begins. In the case of Ga 6.4 ML, the formation of small holes and large clusters can be observed. The sizes of the droplets formed are above the CDS. After the deposition, the differentiation of the droplets begins. The smaller droplets reach critical size and start solving the substrate. This state is frozen via opening the arsenic cell.

When the deposited Ga is 3.2 ML, we can observe shallow holes with plane rims. The explanation is as follows [85, 87, 88]. In this case, the quantity of the deposited Ga is small. The formed droplets are under CDS. Therefore, the solution starts under the droplets immediately after the droplet formation. Under the small droplets, the solution is faster, but the material of liquid Ga is used up in a short time. The reduction in material is due to, first, the solution and, second, the migration of materials toward the larger droplets. After a short time, at the smaller droplets, the solution stops, while it carries on further under the larger ones. The larger droplets will not be spent, and therefore the surrounding ring will freeze after the opening of the arsenic cell.

6. Specular-shaped QDs and complexes

6.1. The inverted QDs

The ringlike QD is an unconventional QD, which has advantages over the conventional QD. As we have shown, the DE technique is a many-sided tool in this field. It allows us to fabricate further interesting nanostructures. Here, we will further discuss unconventional-shaped QDs and their complexes. In the present subsection, we will focus on an alternative QD preparation technique. This is not only an alternative preparation but the QD with inverted technology can also have advantages at special application.

A further recent method for the fabrication of strain-free QD is the nanohole filling. The nanohole is created by localized thermal etching, and it is filled subsequently [95]. This is a QD with inverted technology. The localized thermal etching takes place at conventional MBE growth temperatures, and we expect only very low level of crystal defects. The nanoholes are created in a self-organized fashion by local material removal [89]. For the inverted QD fabrication, nanoholes are generated using Al droplets on AlAs surface. Subsequently, the holes are filled with GaAs layer to form QDs of controlled height [90]. The nanoholes are filled with GaAs in pulsed mode.

Here, we show a cross-sectional study of an inverted QD [66]. The technology of this QD is as follows. The structure is grown on GaAs (001) surface. On the surface, AlGaAs and AlAs layer sequence is grown. The AlGaAs layer has 0.23 Al content. The AlAs and the AlGaAs layers are 5.5 and 19.5 nm, respectively. After the growth of every AlAs layer, 3.2 ML Al is deposited at 650°C without any arsenic flux. The deposited Al MLs form droplets on the surface. This is followed by an annealing step of 180 s, during which the droplets transform into nanoholes.

Following that, the holes are partially filled by the deposition of 0.6 nm thick GaAs in a growth-interrupted fashion. During the hole filling, the substrate temperature is 600°C. Depending on the foreseen high of the QD, some growth of 0.5 s and pause of 30 s sequences are carried out. Finally, the GaAs QD can be covered with AlGaAs. The scheme and the TEM image of the inverted QD structure are shown in Figure 11. The above-described pulsed technique allows us to create not only single QDs but also vertically aligned QD pairs [91].

The distances on the TEM image correspond with the intended layer thicknesses. The picture shows GaAs QD embedded in AlGaAs barrier material. Furthermore, the TEM image shows a thickening of the AlAs layer in the surrounding the nanohole. Elementary maps taken using electron energy loss spectroscopy confirm that the thickened region consists of AlAs. We identify the additional AlAs on top of the flat AlAs layer as the wall that surrounds the nanohole opening. Furthermore, the TEM image on Figure 11 shows that the next AlAs layer grown on top of the inverted QD layer is bended upward at the location of the QD, resulting in the formation of a kind of hill [66].

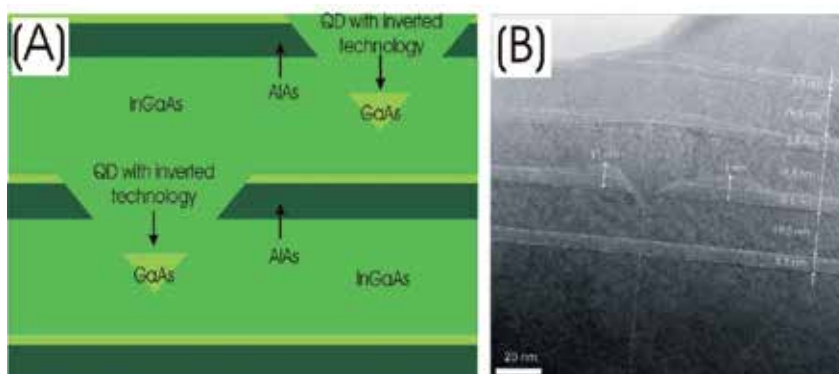


Figure 11. (A) Scheme of the sample with inverted QDs. (B) Cross-sectional TEM image of a GaAs QD embedded in InGaAs layer.

6.2. The laterally aligned QD pairs

Two semiconductor QDs in close proximity, which can each spatially confine an individual charge carrier in a discrete energy level, interact quantum mechanically with each other. In particular, the wave functions of the charge carriers confined in each QDs of the pair begin to overlap, resulting in an efficient tunneling. Furthermore, the wave functions may become mixed to develop molecular orbital. Moreover, resonance in the optical range leads to the formation coupled QD pairs with the help of dipole–dipole interaction. These research leads toward quantum information processing. The QD pairs and their systems offer, at least conceptually, the potential of implementing scalable arrays of qubits.

In this part, we are dealing GaAs QD pairs prepared on AlGaAs surface with the usage of the anisotropy of the (001) oriented surface. We will show two preparational series. One of them is carried out under lower temperature, at less amount of deposited MLs. The other ones is prepared under higher temperature at higher amount of deposited Ga.

In the first case, AlGaAs with Al content of 0.27 is grown on the GaAs (001) surface. After this, Ga droplets are created at 330°C temperature on the substrate. The crystallization happens at 200°C, under accurate control of the arsenic flux [104]. The ripened structure basically consists of two QDs aligned in the $[0 \bar{1} 1]$ crystallographic direction. The average base size and height of each QD are 45 and 10 nm, respectively. The QDs are separated by an average distance of

39 nm between their apexes, as measured by AFM. The density of the structure is $2 \times 10^8 \text{ cm}^{-2}$ [104]. For the study of its optical properties, the QD pairs are embedded in AlGaAs barrier layer.

The second technology is carried out on GaAs surface. First, AlGaAs layer is grown with 0.3 Al amount. At 550°C substrate temperature, a large amount of Ga is deposited to create droplets on the surface. The structure is “arsenized” by fine control of the flux [99]. The resulting dots are rather large. The individual pairs have an interdot distance of about 130 nm and are aligned along the $[0\bar{1}1]$ direction. The dots with a height of 10 nm reside on a shallow base with a diameter of 300 nm. The density of the structure is $2.3 \times 10^8 \text{ cm}^{-2}$ [99]. For optical characterization, the QD pairs are buried by the deposition of AlGaAs layer.

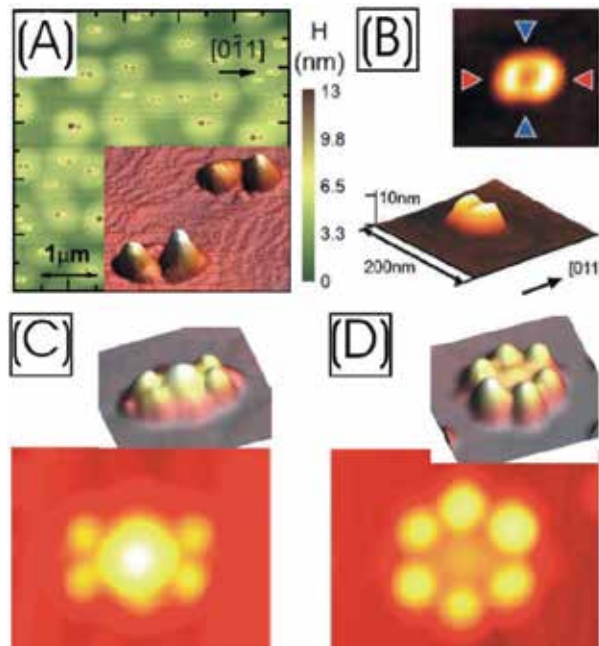


Figure 12. QD pairs grown at high substrate temperature with large amounts of Ga MLs. (Illustration originated from R. Pomraenke et al.; Phys. Rev. B 77 (2008) 075314) [105].) (B) QD pairs grown at low substrate temperature with low amounts of Ga MLs. (Illustration originated from M. Yamagiwa et al.; Appl. Phys. Lett. 89 (2006) 113115) [104].) (C and D) Growth of quad- and hexa-QD molecules initiated by GaAs mound. (Illustrations originated from J.H. Lee et al.; Appl. Phys. Lett. 89 (2006) 202101) [110].)

In the first case, the micro-PL spectra of a single QD pair show the ensemble of emissions, which may indicate the existence of a tunnel coupling between the members of the pair. However, it must be mentioned that these emission lines are still not fully understood [104]. At the second experiment, the PL study is performed at a rather larger inter-dot separation. Here the formation of coherently coupled molecular QD states is suppressed, and excitonic interactions between neighboring QDs within each members are weak [105]. The process of the QD pair evolution is also not fully understood. Instead of the hemispherical shape of the

initial droplet, the ripened structure is anisotropic. The explanation is based on the anisotropic surface potential of the GaAs (001) surface (Figure 12).

6.3. Configuration of QD ensembles

Until now, the most widely studied system of interacting self-assembled QDs is a vertically stacked QD molecule. However, this system is limited by its one-dimensional nature and is not easily scalable. Alternatively, a variety of techniques can be used to modify the substrate to nucleate laterally coupled QD molecules in two dimensions by MBE technology. Various shape droplets can subsequently serve as templates for further growth, without the need for further surface preparation.

The DE-like created nanohole and also the homo-DE-grown island can serve as an initialization place for the growth of further nanostructures. The nanohole as a template for QD molecules is demonstrated by Songmuang and coworkers [106]. The nanohole can serve as a template for QD pair too [107]. Salamo and coworkers proposed a new way for the preparation of QD molecules [92-94, 110]. They adopt a hybrid growth approach, utilizing both DE and strain-induced growth to overcome some limitations of the Stranski-Krastanov QD growth mode alone on a planar GaAs surface [102]. Using MBE, a self-assembled InGaAs QD molecule is realized around GaAs mound formed by DE on GaAs (001) surface [102].

The number of QDs per GaAs mound can be effectively controlled by varying the InAs ML coverage. The number of QDs per template ranges from two to six. The technology is as follows. On GaAs (001) surface, 3 ML Ga is deposited at 500°C without any arsenic flux to form Ga droplets. Subsequently, 80 s of annealing occurs, and the substrate temperature is decreased to 150°C. The Ga droplet is crystallized under 1.3×10^{-5} Torr equivalent pressure for 100 s. During this time, nanoscale GaAs mound forms as template. The substrate temperature is raised again to 500°C, and InAs deposition follows. If the deposited InAs are 1.4, 1.6, and 2.0 ML, then the created nanostructures are bi-QD molecule, quad-QD molecule, and hexa-QD molecule [108].

During the QD molecule preparation, the height of the GaAs mound decreases from the original value, and also the diameter decreases. It appears that the InAs growth started mixing with the Ga atoms from the GaAs mounds, resulting in InGaAs shoulders on initial templates. This technique allows to fabricate the so-called quantum-rod pair and lip-shaped structures too [108]. The technology is extended with incident angle-controlled molecular beam technique [109].

Acknowledgements

In alphabetical order, the author would like to thank J. Balázs, J. Bozsik, A. Csík, M. Csutorás, L. Dobos, Z. Hajnal, Ch. Heyn, W. Hansen, P. Kucsera, J. Makai, C. Manzoni, B. Pécz, B. Pődör, I. Réti, K. Sakoda, S. Sanguinetti, A. Stemmann, J. Takács, G. Tényi, L. Tóth, and A. Ürmös for their fruitful cooperation and to the “Concert-Japan ERA-NET FemtoTera” Project for financial support via OTKA-NN 114457 Found.

Author details

Ákos Nemcsics^{1,2}

1 Institute for Microelectronics and Technology, Óbuda University Budapest, Hungary

2 CER, Institute for Technical Physics and Materials Science, Hungarian Academy of Sciences, Budapest, Hungary

References

- [1] D. Leonard, M. Krisnamurthy, C. M. Reaves, S. P. Denbaas, P. M. Petroff; *Appl. Phys. Lett.* 63 (1993) 3203.
- [2] V. Bressler-Hill, S. Varma, A. Lorke, B. Z. Noshov, P. M. Petroff, W. H. Weinberg; *Phys. Rev. Lett.* 74 (1995) 3209.
- [3] W. Yang, H. Lee, T. J. Johnson, P. C. Sercel, A. G. Norman; *Phys. Rev. B* 61 (2000) 2784.
- [4] O. Stier, M. Grundmann, D. Bimberg; *Phys. Rev. B* 59 (1999) 5688.
- [5] Ch Heyn, A. Bolz, T. Maltezopoulos, R. L. Johnson, W. Hansen; *J. Cryst. Growth* 278 (2005) 46.
- [6] N. Koguchi, S. Takahashi, T. Chikyow; *J. Cryst. Growth* 111 (1991) 688.
- [7] T. Mano, K. Watanabe, S. Tsukamoto, H. Fujioka, M. Oshima, N. Koguchi; *Jpn. J. Appl. Phys.* 38 (1999) L1009.
- [8] J M Lee, D H Kim, H Kong, J C Woo, S J Park; *J. Cryst. Growth* 212 (2000) 67.
- [9] T Mano, T Kuroda, K Mitsuishi, M Yamagiwa X J Guo, K Furuya, K Sakoda, N Koguchi; *J. Cryst. Growth* 301–302 (2007) 740.
- [10] T. Mano, S. Tsukamoto, H. Fujioka, M. Oshima, N. Koguchi; *J. Cryst. Growth* 227–228 (2001) 1069.
- [11] Z. Gong, Z. C. Nin, S. S. Huang, Z. D. Fang, B. Q. Sun, J. B. Xia; *Appl. Phys. Lett.* 87 (2005) 093116.
- [12] T. Kuroda, T. Mano, T. Ochiai, S. Sanguinetti, K. Sakoad, G. Kigo, N. Koguchi; *Phys. Rev. Lett.* 72 (2005) 205301.
- [13] S. Hwang, Z. Nin, Z. Fang, H. Ni, Z. Gong, J. B. Xia; *Appl. Phys. Lett.* 89 (2006) 031921.
- [14] M. Yamagiwa, T. Mano, T. Kuroda, T. Tateno, K. Sakoda, G. Kido, N. Koguchi; *Appl. Phys. Lett.* 89 (2006) 113115.

- [15] J. H. Lee, Zh. Wang, N. W. Strom, Yu. I. Mazur, G. J. Salamo; *Appl. Phys. Lett.* 89 (2006) 202101.
- [16] H. Lüth: *Surfaces and Interfaces of Solid Materials*; Springer Verlag, Berlin (1998).
- [17] J. Tersoff, F. K. LeGoues; *Phys. Rev. Lett.* 72 (1994) 3570.
- [18] J. M. Gérard, O. Cabrol, J. Y. Marzin, N. Lebouché, J. M. Moison; *Mat. Sci. Eng. B* 37 (1996) 8.
- [19] D. Bimberg, M. Grundmann, N. N. Ledentsov: *Quantum Dot Heterostructures*, John Wiley, New York (1999).
- [20] B. A. Joyce, D. D. Vvedensky: Growth modes and morphologies on GaAs surfaces, (in *Thin Films: Heteroepitaxial Systems*, Eds.: W. K. Lin, M. B. Santos) World Sci., Singapore (1999) p 368.
- [21] V. A. Shchukin, D. Bimberg; *Rev. Mod. Phys.* 71 (1999) 1125.
- [22] P. Ribas, V. Krishnamoorthy, R. M. Park; *Appl. Phys. Lett.* 57 (1990) 1040.
- [23] E. A. Fitzgerald; *Mater. Sci. Rep.* 7 (1991) 621.
- [24] Á. Némcsics, F. Riesz, L. Dobos; *Thin Solid Films* 343 (1989) 520.
- [25] Á. Némcsics, F. Riesz; *Phys. Stat. Sol. C* 0 (2003) 893.
- [26] R. Schnurpfeil, K. Restöft, A. Müller, Á. Némcsics, R. Manzke, M. Skibowski; *J. Electr. Spectr. Rel. Phen.* 68 (1994) 175.
- [27] Á. Némcsics, J. Olde, M. Geyer, R. Schnurpfeil, R. Manzke, M. Skibowski; *Phys. Stat. Sol. A* 155 (1996) 427.
- [28] S. Lee, I. Daruka, C. S. Kim, A. L. Barabási, J. L. Metz, J. K. Furdyna; *Phys. Rev. Lett.* 81 (1998) 3479.
- [29] N. Koguchi, S. Takahashi, T. Chikyow; *J. Cryst. Growth* 111 (1991) 688.
- [30] N. Koguchi, K. Ishige; *Jpn. J. Appl. Phys.* 32 (1993) 2052.
- [31] T. Mano, T. Kuroda, K. Mitsuishi, M. Yamagiwa, X. J. Guo, K. Furuya, K. Sakoda, N. Koguchi; *J. Cryst. Growth* 301–302 (2007) 740.
- [32] T. Mano, S. Tsukamoto, H. Fujioka, M. Oshima, N. Koguchi; *J. Cryst. Growth* 227–228 (2001) 1069.
- [33] Z. Gong, Z. C. Nin, S. S. Huang, Z. D. Fang, B. Q. Sun, J. B. Xia; *Appl. Phys. Lett.* 87 (2005) 093116.
- [34] T. Kuroda, T. Mano, T. Ochiai, S. Sanguinetti, K. Sakoad, G. Kigo, N. Koguchi; *Phys. Rev. Lett.* 72 (2005) 205301.
- [35] S. Hwang, Z. Nin, Z. Fang, H. Ni, Z. Gong, J. B. Xia; *Appl. Phys. Lett.* 89 (2006) 031921.

- [36] W.Z. Ostwald; *Z. Phys. Chem.* 34 (1900) 975.
- [37] M. Zinke-Allmang, L.C. Feldman, S. Nakahara; *Appl. Phys. Lett.* 51 (1987) 975.
- [38] M. Zinke-Allmang, L.C. Feldman, W. van Saarloos; *Phys. Rev. Lett.* 68 (1992) 2358.
- [39] G.Z. Pan, K.N. Tu; *Appl. Phys. Lett.* 68 (1996) 1654.
- [40] G.R. Carlow, M. Zinke-Allmang; *Phys. Rev. Lett.* 78 (1997) 4601.
- [41] K. Shorlin, S. Krylov, M. Zinke-Allmang; *Physica A* 261 (1998) 248.
- [42] A. Raab, G. Springholz; *Appl. Phys. Lett.* 77 (2000) 2991.
- [43] Ch. Heyn, A. Stemann, A. Schramm, H. Welsch, W. Hansen, Á. Nemcsics; *Appl. Phys. Lett.* 90 (2007) 203105.
- [44] Ch. Heyn, A. Stemann, A. Schramm, H. Welsch, W. Hansen, Á. Nemcsics; *Phys. Rev. B* 76 (2007) 075317.
- [45] J.H. Lee, Z.M. Wang, N.W. Strom, Y.I. Mazur, G.J. Salamo; *Appl. Phys. Lett.* 89 (2006) 202101.
- [46] A. Ohtake; *Surf. Sci. Rep.* 63 (2008) 295.
- [47] Q.K. Xue, T. Hashizume, T. Sakurai; *Prog. Surf. Sci.* 56 (1997) 1.
- [48] D.K. Biegelen, R.D. Brinans, J.E. Northrup, L.E. Swartz; *Phys. Rev. B* 41 (1990) 5701.
- [49] Á. Nemcsics, J. Takacs; *Acta Polytechn. Hung.* 7 (2010) 109.
- [50] Á. Nemcsics, J Takacs; *Semiconductors* 45 (2011) 91.
- [51] M. Zinke-Allang, L.C. Feldman, M.H. Grabow; *Surf. Sci. Rep.* 16 (1992) 377.
- [52] V. A. Shcukin, D. Bimberg; *Rev. Mod. Phys.* 71 (1999) 1125.
- [53] M. Wautelet, D. B. Beljonne, J.-L. Brédas, J. Cornil, R. Lazzaroni, P. Lecére, M. Alexander, P. Dubois, P. Gills, Y. Gossuin, R. Muller, A. Ouakssim, A. Roch, D. Duviver, J. Robert, R. Gouttebaron, M. Hecq, F. Monteverde: *Nanotechnologie*; Oldenbourg Verlag, München (2003).
- [54] I. Grossy, M.B. Small; *J. Cryst. Growth* 11 (1971) 157.
- [55] H. Ijmin, S. Gonda; *J. Cryst. Growth* 33 (1976) 215.
- [56] N.S. Peev; *J. Cryst. Growth* 98 (1989) 499.
- [57] E. Lendvay, T. Görög, V. Rakovics; *J. Cryst. Growth* 72 (1985) 616.
- [58] Á. Nemcsics, L. Tóth, L. Dobos, Ch. Heyn, A. Stemann, A. Schramm, W. Hansen; *Superlatt. Microstr.* 48 (2010) 351.
- [59] Zh. M Wang, B.L. Liang, K A Sablon, G.J. Salamo; *Appl. Phys. Lett.* 90 (2007) 113120.

- [60] Ch. Heyn, A. Stemann, W Hansen; *Appl. Phys. Lett.* 95 (2009) 1731100.
- [61] Ch. Heyn, A. Stemann T Köppen Ch Strelow, T Kipp, M Grave, S Mendach, W Hansen; *Appl. Phys. Lett.* 94 (2009) 183113.
- [62] Ch Heyn, A Stemann, R Eiselt, W Hansen; *J. Appl. Phys.* 105 (2009) 054316.
- [63] A. Stemann, Ch. Heyn, T. Köppen, T. Kipp, W. Hansen; *Appl. Phys. Lett.* 93 (2008) 123108.
- [64] Ch. Heyn, A. Stemann, W. Hansen; *J. Cryst. Growth* 311 (2009) 1839.
- [65] Ch Heyn, A. Stemann, T. Köppen, Ch. Strelow, T. Kipp, M. Grave, S. Mendach, W. Hansen; *Nanoscale Res. Lett.* 5 (2010) 576.
- [66] Á. Nemcsics, Ch. Heyn, L. Tóth, L. Dobos, A. Stemann, W. Hansen; *J. Cryst. Growth* 335 (2011) 58.
- [67] Á. Nemcsics, Ch. Heyn, A. Stemann, A. Schramm, H. Welsch, W. Hansen; *Mat. Sci. Eng. B* 165 (2009) 118.
- [68] Á. Nemcsics, L. Tóth, L. Dobos, A. Stemann; *Microel. Reliab.* 51 (2011) 927.
- [69] D. Choi, M. Warusawithana, C.O. Chui, J. Chen, W. Tsai, D.G. Schlom, J.S. Harris; *Mat. Res. Symp. Proc* 996 (2007) H5–H31.
- [70] H. Lee, R. Lowe-Webb, W. Yang, P.C. Sercel; *Appl. Phys. Lett.* 72 (1998) 812.
- [71] K. Watanabe, N. Koguchi, Y. Gotoh; *Jpn J Appl. Phys* 39 (2000) L79.
- [72] T. Mano, T. Kuroda, M. Yamagiwa, G. Kido, K. Sakoda, N. Koguchi; *Appl. Phys. Lett.* 89 (2006) 183102.
- [73] Á. Nemcsics; *Semiconductor* 39 (2005) 1352.
- [74] I. Mojzes, T. Sebestyén, P. B. Barna, G. Gergely, D. Szigethy; *Thin Solid Films* 61 (1979) 27.
- [75] N. Koguchi, S. Takahashi, T. Chikyow; *J. Cryst. Growth* 111 (1991) 688.
- [76] N. Koguchi, K. Ishige; *Jpn. J. Appl. Phys.* 32 (1993) 2052.
- [77] J.M. Garcia, D. Grandos, J.P. Silveira, F Briones; *Microel. Journal* 35 (2004) 7.
- [78] T. Mano, T. Kuroda, M. Yamagiwa, G. Kido, K. Sakoda, N. Koguchi; *Appl. Phys. Lett.* 89 (2006) 183102.
- [79] C. Zhao, Y.H. Chen, B. Xu, P. Jin, Z.G. Wang; *Appl. Phys. Lett.* 91 (2007) 033112.
- [80] S. Sanguinetti, T. Mano, A. Gerosa, C. Somaschini, S. Bietti, N. Koguchi, E. Grilli, M. Guzzi, M. Gurioli, M. Abbarachi; *J. Appl. Phys.* 104 (2008) 113519.
- [81] C. Somaschi, S. Bietti, N. Koguchi, S. Sanguinetti; *Appl. Phys. Lett.* 97 (2010) 203109.

- [82] A Stemmann, T Köppen, M Grave, S Wildfang, S Mendach, W Hansen, Ch Heyn; *J. Appl. Phys.* 106 (2009) 064315.
- [83] Á. Nemcsics, J. Balázs, B. Pődör, J. Makai, A. Szemann; *Phys. Stat. Sol. C* 8 (2011) 2826.
- [84] K. Watanabe, S. Tsukamoto, Y. Gotoh, N. Koguchi; *J. Cryst. Growth* 227 (2001) 1073.
- [85] Á. Nemcsics, A. Stemmann, J. Takács; *Microel. Reliab.* 52 (2012) 430.
- [86] Á. Nemcsics; *J. Cryst. Growth* 217 (2000) 223.
- [87] Á. Nemcsics; *AIP Conf. Proc.* 1598 (2014) 79.
- [88] Á. Nemcsics; *Acta Politechn. Hung.* 8 (2011) 5.
- [89] Ch. Heyn, A. Stemmann, T. Köppen, Ch. Strelow, T. Kipp, M. Grave, S. Mendach, W. Hansen; *Appl. Phys. Lett.* 94 (2009) 183113.
- [90] Z.M. Wang, B.L. Liang, K.A. Sablon, G.J. Salamo; *Appl. Phys. Lett.* 90 (2007) 113120.
- [91] V. Pollojärvi, A. Stemmann, M. Guina, A. Stemmann, Ch. Heyn; *Nanotechnology* 22 (2011) 105603.
- [92] J.H. Lee, S. Sablon, Z.M. Wang, G.J. Salamo; *J. Appl. Phys.* 103 (2008) 054301.
- [93] M. Hanke, M. Dubsloff, M. Schmidbauer, Z.M. Wang, Y.I. Mazur, P.M. Lytvyn; *Appl. Phys. Lett.* 95 (2009) 023103.
- [94] M. Dubsloff, M. Hanke, M. Burghammer, S. Schröder, R. Hoppe, C.G. Schroeder, Y.I. Mazur, Z.M. Wang, J.H. Lee, G.J. Salamo; *Appl. Phys. Lett.* 98 (2011) 213105.
- [95] Ch. Heyn; *Phys. Rev. B* 83 (2011) 165302.
- [96] R. Viswanatha, S. Saha-Dasgupta, D.D. Sarma; *Phys. Rev. B* 72 (2005) 045333.
- [97] G. Bastarg; *Wave Mechanics Applied to Semiconductor Heterostructures*, Les Éditions, Les Ulis (1990).
- [98] T. Mano, T. Kuroda, S. Sanquinetti, T. Ochiai, T. Tateno, J. S. Kim, T. Noda, M. Kawabe, K. Sakoda, G. Kido, N. Koguchi; *Nano Lett.* 5 (2005) 425.
- [99] H. Lee, R. Lowe-Webb, W. Yang, P.C. Sercel; *Appl. Phys. Lett.* 72 (1998) 812.
- [100] K. Watanabe, N. Koguchi, Y. Gotoh; *Jpn J Appl. Phys.* 39 (2000) L79.
- [101] T. Mano, T. Kuroda, M. Yamagiwa, G. Kido, K. Sakoda, N. Koguchi; *Appl. Phys. Lett.* 89 (2006) 183102.
- [102] G.A. Satunkin; *J. Cryst. Growth* 255 (2003) 170.
- [103] T. Mano, K. Watanabe, S. Tsukamoto, H. Fujikoa, M. Oshima, N. Koguchi; *J. Cryst. Growth* 209 (2000) 504.

- [104] M. Yamagiwa, T. Mano, T. Kuroda, T. Tateno, K. Sakoda, G. Kido, N. Koguchi; *Appl. Phys. Lett.* 89 (2006) 113115.
- [105] R. Pomraenke, C. Lienau, Y.I. Mazur, Z.H. Wang, B. Liang, G.G. Tarasov, G.J. Salamo; *Phys. Rev. B* 77 (2008) 075314.
- [106] R. Sonmuang, S. Kiravittaya, O.G. Schmidt; *Appl. Phys. Lett.* 82 (2003) 2892.
- [107] P.A. Gonzalez, J.M. Sanchez, Y. Gonzalez, B. Alen, D. Fuster, L. Gonzalez; *Cryst. Growth Des.* 9 (2009) 2525.
- [108] K.A. Sablon, J.H. Lee, Z.M. Wang, J.H. Scultz, G.J. Salamo; *Appl. Phys. Lett.* 92 (2008) 203106.
- [109] M.K. Yakes, C.D. Cress, J.G. Tiscler, A.S. Bracker; *Nano* 4 (2010) 3877.
- [110] J.H. Lee, Zh.M. Wang, Yu, I. Mazur, G.J. Salamo; *Appl. Phys. Lett.* 89 (2006) 202101.

Physical Reasons of Emission Varying in CdSe/ZnS and CdSeTe/ZnS Quantum Dots at Bioconjugation to Antibodies

Tetyana V. Torchynska

Additional information is available at the end of the chapter

<http://dx.doi.org/10.5772/60821>

Abstract

Photoluminescence, its excitation power dependence, and Raman scattering spectra have been studied in CdSe/ZnS and CdSeTe/ZnS QDs for the nonconjugated states and after the QD conjugation to the anti-Interleukin-10, Human papilloma virus and Pseudo rabies virus antibodies. The QD bioconjugation to charged antibodies stimulates the “blue” energy shift of PL bands related to exciton emission in the CdSe or CdSeTe cores. The “blue” energy shift of PL spectrum in bioconjugated CdSe/ZnS QDs has been attributed to the electronic quantum confined effects stimulated by decreasing the effective QD size at its bioconjugation to charged antibodies. It was shown that the attachment of a charge deals with the antibody to the exterior shell of CdSe/ZnS QDs, leads to blocking away a fraction of core’s volume. The energy band diagrams of CdSeTe/ZnS QDs in the nonconjugated and bioconjugated states have been designed, which permit to explain the types of optical transitions in QDs and their transformations at the QD bioconjugation. It is shown that the change of energy band profile and the “blue” shift of QD energy levels, owing to the change of potential barrier at the QD surface, are the dominant reasons of PL spectrum transformation in the double core CdSeTe/ZnS QDs conjugated to charged antibodies. Better understanding the QD bioconjugation to specific antibodies is expected to produce the major advances in biology and medicine and can be a powerful technique for early medical diagnostics.

Keywords: CdTeSe/ZnS quantum dots, CdSe/ZnS quantum dots, emission, bioconjugation

1. Introduction

In the last two decades, the colloidal core/shell quantum dots (QDs) of II-VI semiconductors (CdSe, CdS, CdSeTe, and ZnS) attracted an enormous scientific attention owing to the fundamental scientific aspects and future promising applications in optoelectronics, photonics, biology, and medicine. The modern developments in nanotechnology allow numerous promising applications in the field of biology and medicine, which in the future may bring an unprecedented effect in nanomedicine [1, 2].

The development of biocompatible nanoparticles for molecular imaging and targeted therapy is an area of enormous current interest. This novel technique as expected will allow targeted drug delivery to cells with certain parameters, as well as improvements in diagnostics and localization of affected tissues in the human body. When conjugated with biomolecular affinity ligands, such as antibodies, peptides, or small molecules, these nanoparticles can be used to target malignant specific tumors [3-5].

The key issue for nanoparticles intended for biological use is to ensure their stability, which suggests the formation of core-shell structures with a certain enveloping layer required to isolate a nanoparticle [6]. The core defines the main properties of the system—it may be the material with outstanding luminescence or magnetic properties for the precise detection of particle's location inside the body. On the other hand, the core can be used as a reservoir for the medicine used in targeted drug delivery applications. The application of semiconductor QDs as luminescent markers in biology and medicine is expected to produce the major advances in molecular diagnostic [1], gene technology [2], toxin detections [7], drug delivery [8], at obtaining tissue imaging in vivo etc [3, 9].

Note that luminescent markers usually used earlier, such as organic dyes, fluorescent proteins, or lanthanide chelates, have some restrictions, such as broad spectrum bands, low photo bleaching threshold, poor photochemical stability, and degradation [10]. In contrary, the II-VI semiconductor core/shell QDs are characterized by the high-photoluminescence (PL) quantum yield (up to 75%) [11-13]. Surface-passivized II-VI QDs are highly stable against photo bleaching and are characterized by narrow, symmetric emission peaks with the half width about 25-30 nm [6].

New luminescent markers are needed for the better assessment of treatments for many types of cancers. The antibodies, which can be found in circulating blood, may help in the early detection of cancer. The development of a blood test, using the optical methods, which permits early diagnosis, would be a great advance in the management of cancer disease. Note that the core/shell CdSeTe/ZnS QDs with near-infrared (IR) emission (780-800 nm) are very interesting for biological applications owing to the possibility of animal imaging in vivo due to the low absorption of IR light by an animal tissue [6, 14, 15]. At the same time, the chemical behavior of Cd/Se/Te components of QDs in the biological system is still unclear. The last question is very important due to the toxicity of these components for the human body [16-18].

The conjugation of biomolecules with semiconductor core/shell QDs has been achieved using functional groups (linkers) on the QD surface [19-21], and/or with the help of electrostatic

interaction between the QDs and the biomolecules [12, 22, 23]. A set of publications, related to the study of QD bioconjugation using PL spectroscopy, revealed that the emission intensity of QDs decreased [12, 24, 25] or increased [22, 26] owing to the energy exchange between the QDs and the biomolecules. Thus, the QD luminescence intensity depends on the concentration of attached biomolecules, promising the QD application as a protein sensor as well [6]. However, the limits of biomolecule detection are not very sensitive. Moreover, the influence of bioconjugation processes on QD optical properties and the bioconjugation mechanisms are not yet completely understood.

It is desirable to have the additional information concerning the conjugation process such as a spectral shift of QD emission or changing the PL band half width, or using nonlinear optical phenomena: two-photon-induced fluorescence, second harmonic generation, or sum frequency generation [27]. Simultaneously, the other optical methods can be useful for the bioconjugation detection such as the Raman scattering method [28] or coherent anti-Stokes Raman scattering (CARS) [27]. This chapter presents the study of the transformation of PL and Raman scattering spectra of the core/shell CdSe/ZnS QDs with visible emission (605 or 655 nm) and CdSeTe/ZnS QDs with near IR emission (780-800 nm) at the bioconjugation to different types of antibodies.

2. QD bioconjugation process and experimental details

Core-shell quantum dots (QDs) commercially available covered by the amine (NH₂)-derivatized polyethylene glycol (PEG) polymer were used in a form of colloidal particles diluted in a phosphate-buffered saline (PBS) with a 1:200 volumetric ratio. CdSe/ZnS QDs with emission peaked at 605 nm (2.05 eV) and 655 nm (1.89 eV) and CdSeTe/ZnS QDs with emission at 780-800 nm (1.55-1.60 eV) have been investigated. QDs have been studied by means of photoluminescence and Raman scattering methods in nonconjugated states and after the conjugation to different types of antibodies (Ab). All optical measurements are performed on the dried droplets of the original solution of nonconjugated and bioconjugated QDs. At the first the PL spectra of QDs are studied in the nonconjugated state. Then some part of QDs has been conjugated to the antibodies using the QD conjugation kits [29, 30]. These kits contain amine-derivatized polymer-coated QDs and the amine-thiol cross-linker SMCC. The samples of QDs (bioconjugated and nonconjugated) in the form of a 5-mm spot were dried on a surface of crystalline Si substrates (Figure 1) as described earlier by Torchynska [22] and Vega Macotela et al. [24].

The types of antibodies (Ab) used for the bioconjugation to the CdSe/ZnS QDs with emission at 605 nm (2.05 eV) and 655 nm (1.89 eV) are as follows:

- i. Mouse monoclonal [8C9] antihuman papilloma virus Ab, HPV 16-E7, bacterially derived fusion protein containing anti-HPV 16 early protein E7 Ab (Invitrogen, isotype (IgG1))
- ii. Anti-interleukin-10 (IL-10) antibodies (antihuman IL-10, Rt IgG1, stock concentration of 1 mg/ml, clone JES3-9D7, code RHCIL1000)

- iii. Pseudorabies virus (PRV) Ab, immunoglobulin G antibodies (affinity purified with Protein G Sepharose from rabbit antiserum to pseudorabies virus, stock concentration of 1 mg/ml in PBS)

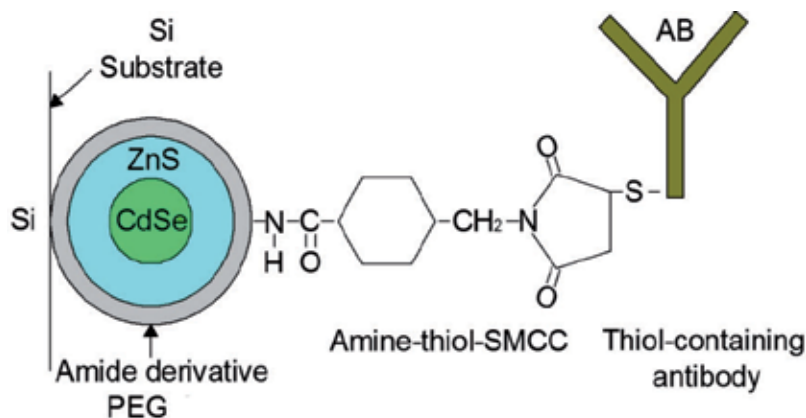


Figure 1. Bioconjugated CdSe/ZnS QDs on the Si substrate.

CdSeTe/ZnS QDs with near IR emission at 780-800 nm (1.59-1.60 eV) have been conjugated to different types of antibodies as well:

- i. Mouse monoclonal [8C9] antihuman papilloma virus Ab, anti-HPV 16-E7, bacterially derived fusion protein containing anti-HPV 16 early protein E7 Ab (Invitrogen, isotype (IgG1))
- ii. Mouse monoclonal [C1P5] antihuman papilloma virus HPV16 E6 + HPV18 E6 Ab, HPVE6 (Abcam, ab70, isotype IgG1, gel-purified HPV18 E6-beta-galacto-sidase fusion protein)
- iii. Pseudorabies virus (PRV) Ab, immunoglobulin G antibodies (affinity purified with Protein G Sepharose from rabbit antiserum to Pseudorabies virus, stock concentration of 1 mg/ml in PBS)
- iv. Anti-IL-10 antibodies (antihuman IL-10, Rt IgG1, stock concentration of 1 mg/ml, clone JES3-9D7, code RHCIL1000)

The protocol of bioconjugation details can be found in refs. [29, 30]. Bioconjugated CdSe/ZnS QDs have been called as 605P+IL-10, 655P+IL-10, 605P +HPV E7, 655P +HPV E7, 605P+PRV, and 655P+PRV, and the bioconjugated CdSeTe/ZnS QDs have been called as (i) 800P+HPV E7, (ii) 800P+HPV E6, (iii) 800P+PRV, and (iv) 800P+IL-10.

The majority of PL spectra were measured at the excitation by a He-Cd laser with a wavelength of 325 nm and a beam power of 76 mW at 300 K using a PL setup on a base of spectrometer SPEX500 described by Torchynska [22] and Vega Macotela et al. [24]. Raman scattering spectra were measured at 300 K by means of the spectrometer Lab-Raman HR800 Horiba Jovin-Yvon

in the range of Raman shifts of 100-600 cm^{-1} at the excitation by a solid-state laser with a wavelength of 532 nm and a beam power of 20 mW [26, 28].

3. The bioconjugation study of CdSe/ZnS QDs

3.1. CdSe/ZnS QDs bioconjugated to anti-IL-10 Ab

Figures 2 and 3 demonstrate the PL spectra of the three samples of nonconjugated (605N, 655N) QDs and three samples of bioconjugated (605P, 655P) QDs.

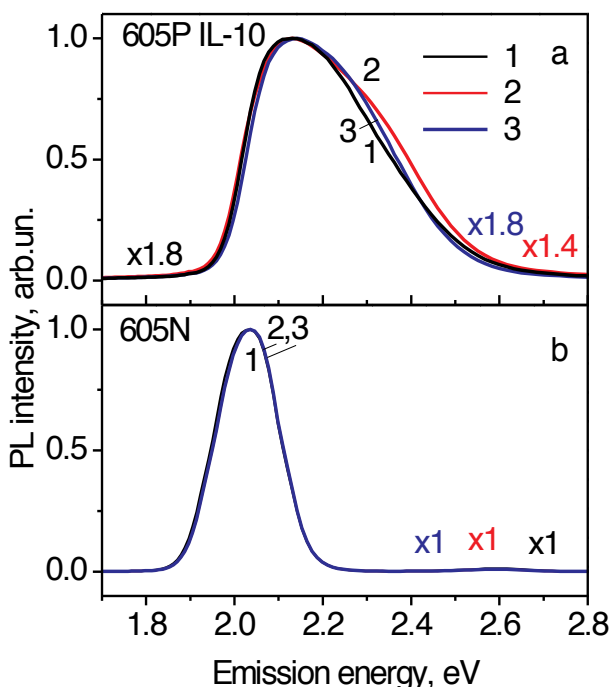


Figure 2. Normalized PL spectra of three 605P (a) and three 605N (b) QD samples at 300 K. Numbers at the curves ($\times 1$, $\times 1.4$, and $\times 1.8$) show the multiplication coefficients used at the normalization of PL spectra.

The PL spectra of CdSe/ZnS QDs are characterized by the Gaussian shape PL band in the nonconjugated states with the peaks at 2.04 eV (Figure 2) and 1.90 eV (Figure 3) related to exciton emission in corresponding CdSe cores [31]. At the bioconjugation of studied QDs, the PL intensity decreases, the emission peak shifts to higher energies, a PL half width increases, and the shape of PL bands became asymmetric with high-energy tails (Figures 2 and 3). The PL energy shift at the bioconjugation of QDs to antibodies can be attributed to the following: (i) the impact of anti-IL-10 Ab or PBS buffer emission excited by UV light, (ii) the oxidation or degradation of CdSe cores owing to core/shell atom intermixing [32], (iii) the impact of compressive strains that appears at the bioconjugation [33, 34], or (iv) the emission of excitons

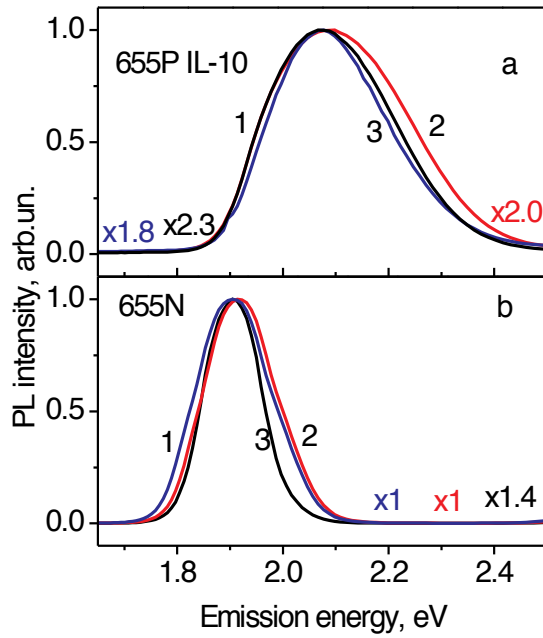


Figure 3. Normalized PL spectra of three 655P (a) and three 655N (b) QD samples at 300 K. Numbers at the curves ($\times 1$, $\times 1.8$, and $\times 2.0$) show the multiplication coefficients used at the normalization of PL spectra.

bound to the QD excited states in QDs [31]. To distinguish between proposed reasons, the PL spectra of anti-IL-10 Ab and PBS were studied at UV light excitation (Figure 4).

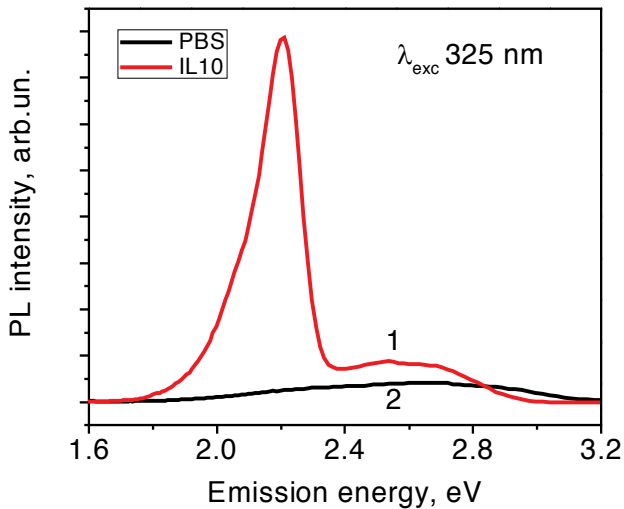


Figure 4. PL spectra of anti-IL-10 Ab (1) and PBS (2) without QDs.

The PL spectrum of anti-IL-10 Ab is characterized by the PL band with a maximum at 2.21 eV and a small shoulder in the range 2.4-3.0 eV (Figure 4, curve 1). The PL spectrum of PBS is shown in Figure 4, curve 2. The PL intensity of PBS in the range 2.2-3.2 eV is 15-fold smaller than the emission intensity of 2.21 eV PL band related to anti-IL-10 Ab. Simultaneously, the PL intensity of anti-IL-10 Ab emission (2.21 eV) is 10-fold smaller than the PL band intensity of CdSe/ZnS QDs at UV excitation. Hence, we can conclude that the “blue” shifts of PL spectra in bioconjugated QDs (605P and 655P) do not connect with the luminescence of anti-IL-10 Ab or PBS. However, the emission of anti-IL-10 Ab can influence on the shape of tails in PL spectra of bioconjugated QDs.

Raman scattering spectra were investigated with the goal to study the impact of compressive strains [33, 34] and the oxidation or degradation processes at the QD bioconjugation [32, 35], as well as to confirm the existence of electric charges in IL-10 Ab. Raman scattering spectra of 605N and 605P CdSe/ZnS QDs present the low-intensity Raman peaks at 211.9, 235.8, 302.8, 345.3, 424.8, 434.6, and 490 cm^{-1} (Figure 5).

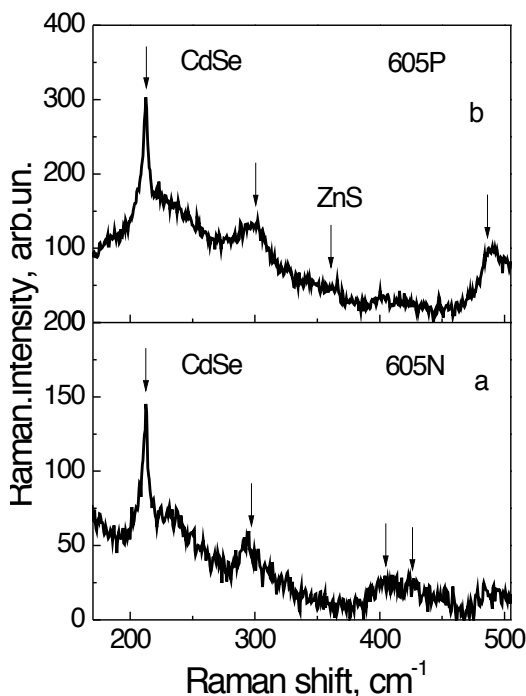


Figure 5. Raman scattering spectra of nonconjugated (a) and bioconjugated (b) QDs.

The peak at 211.9 cm^{-1} (and two phonon overtone at 424.8 cm^{-1}) corresponds to LO phonons in the CdSe core. The shift of LO phonon Raman peak (211.9 cm^{-1}) from its position in the bulk CdSe crystal (213 cm^{-1}) has related to the phonon confinement effect in small QDs [6, 35]. The peak at 345.3 cm^{-1} is due to the LO phonon scattering in the ZnS shell (Figure 5). The shift of

LO phonon Raman peak (345.3 cm^{-1}) from its position in the bulk ZnS crystal (352 cm^{-1}) is related to the phonon confinement effect in thin ZnS shell [6, 35, 36]. Raman spectra in the diapason of $0\text{-}500 \text{ cm}^{-1}$ include the peaks related to the Si substrate as well (Figure 1). Raman scattering spectra of Si present the overtones of acoustic phonons: $235.8, 302.8, 434.6,$ and 458.6 cm^{-1} (Figure 5). The peaks at $230, 302, 435,$ and 469 cm^{-1} were attributed early to two TA phonon overtones at the L, X, and Σ critical points of the Si Brillouin zone [36-38].

The Raman study shows that Raman peaks related to LO phonons in the CdSe core (Figure 5) have not varied at the QD bioconjugation. Meanwhile, if the QD bioconjugation is accompanied by the compressive strain applied, and by the degradation or oxidation of cores, the Raman peaks have to change. Finally, we can conclude that the mentioned processes have not been realized at the QD bioconjugation to anti-IL-10 Ab.

Note that the CdSe core Raman peak intensity increases twofold in bioconjugated QDs as it is shown in Figure 5. The enhancement of optical field at the surface of bioconjugated QDs and increasing the Raman peak intensity can be attributed to the surface-enhanced Raman scattering (SERS) [28,39]. This fact means that anti-IL-10 Abs have the electric charges (dipoles), which interact with an electric field of excitation light at the SERS effect [39-41].

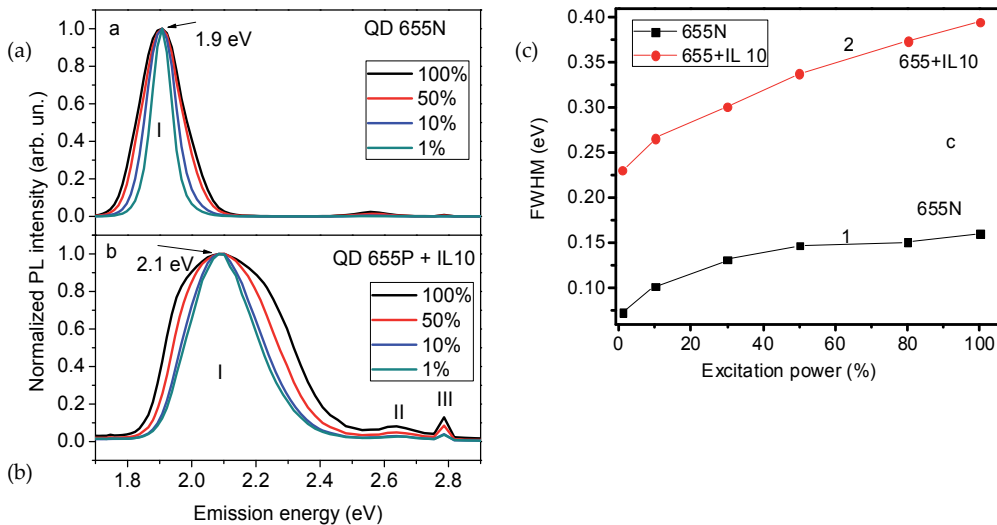


Figure 6. (a,b). Normalized PL spectra of 655N (a) and 655P-IL-10 (b) QDs at different excitation light intensities 100%, 50%, 10%, and 1%, respectively. The 100% intensity corresponds to 76 mW. Coefficients at the normalization of PL spectra for 655N QDs (a) are $\times 1.00, \times 1.10, \times 1.75,$ and $\times 9.11$ and for 655P QDs (b) are $\times 1.28, \times 1.59, \times 3.38,$ and $\times 31.18$. (c). FWHMs of main PL bands in PL spectra of 655N (1) and 655P-IL-10 (2) QDs versus excitation light power.

To study the impact of excitons at QD excited states on the emission of bioconjugated QDs, the PL spectra were measured at different UV light (325nm) excitation intensities. The PL spectra of 655N QDs kept a Gaussian shape of PL band (1.90 eV) at all excitation intensities (Figure 6a). The full width at half maximum (FWHM) of PL band at the first increases with raising excitation intensities owing to the enlargement of the number of excited

QDs and their size distribution. Then the FWHM saturates at higher excitation intensities (Figure 6c, curve 1).

The PL spectra of bioconjugated QDs represent a set of PL bands: (i) PL band (I) with a peak at 2.10 eV connected with QD core emission; (ii) PL band (II) at 2.64 eV, apparently, is related to PBS emission; and (iii) PL band (III) with the peak at 2.78 eV (Figure 6b).

The high-energy PL band III is attributed to a CdSeS alloy appeared at the CdSe/ZnS interface [31]. The confirmation of the existence of such alloy has been obtained at the Raman scattering study in CdSe/ZnS QDs (see Figure 5). The formation of high-energy tails of PL band I together with increasing the PL band II and III intensities have been detected by raising the excitation light power (Figure 6b). Simultaneously, the intensity of a low-energy part of band I increases versus excitation power due to the increasing excited QD numbers and QD size distribution, as it has been seen in nonconjugated QDs. The FWHM of band I in bioconjugated QDs increases monotonously without saturation versus excitation intensity (Figure 6c, curve 2). This study has shown that the PL band I intensity increases with excitation power owing to the increasing emission of excitons localized at the excited states in bioconjugated QDs. The mentioned effect can explain the asymmetric shape of band I and the increasing FWHM (Figure 6c, curve 2) in bioconjugated QDs. Note that the exciton emission via excited states cannot explain “blue” shift (~ 200 meV) in the PL band I peak and appearing the PL band III in the PL spectra of QDs bioconjugated to anti-IL-10 Abs.

3.2. CdSe/ZnS QDs bioconjugated to HPV E7 and PRV Ab

The PL spectra of CdSe/ZnS QDs with emission 605 nm and 655 nm nonconjugated and bioconjugated to PRV and HPV E7 antibodies have been presented in Figures 7 and 8, respectively. The PL spectra of QDs in a nonconjugated state are characterized by the one Gaussian shape PL band peaked at 2.05 eV (Figure 7a) and 1.90 eV (Figures 7b and 8a) and related to exciton emission in corresponding CdSe cores. The PL spectra of bioconjugated QDs have changed essentially: the core PL band shifts into the high-energy spectral range (“blue” shift). Simultaneously, the PL intensity of core emission decreases at the bioconjugation, its half width increases, and the shape of PL band becomes asymmetric with the essential high-energy tails (Figures 7 and 8).

As we have shown above, the processes of oxidation, the CdSe material degradation, or the appearance of elastic strains have been not realized at the bioconjugation of QDs [31, 42]. The “blue” energy shift of PL bands in bioconjugated QDs can be assigned to the emission of HPV E7 or PRV antibodies or PBS at high-energy UV excitation and/or the emission of excitons localized at the excited QD states.

The PL spectra of HPV E7 Ab, PRV Ab, and PBS have been studied at UV excitation as well (Figure 9). As it is clear from Figure 9, the PL spectra of antibodies and PBS are characterized by PL bands in the spectral range of 2.0-3.2 eV. The intensity of PL band in the spectral range 2.0-3.2 eV related to PBS is five- or eightfold smaller than the intensity of PL band related to antibodies. Simultaneously, the intensity of PL band related to the antibodies 10-fold smaller than the PL intensity of CdSe/ZnS QD emission at the UV excitation. Thus, we can conclude

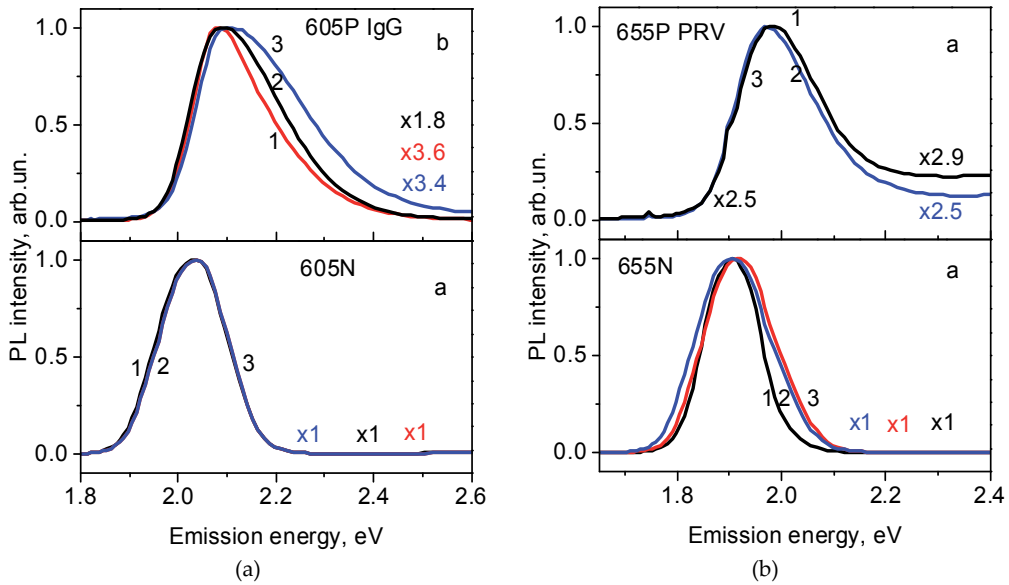


Figure 7. (a). Normalized PL spectra of three different 605N (a) and 605P-PRV (b) QD samples measured at 300 K. Numbers at the curves ($\times 1$, $\times 1.8$, $\times 3.4$, and $\times 3.6$) indicate on the multiplication coefficients used at the normalization. (b). Normalized PL spectra of three different 655N (a) and 655P-PRV (b) QD samples measured at 300 K. Numbers at the curves ($\times 1$, $\times 2.5$, and $\times 2.9$) indicate on the multiplication coefficients used at the normalization.

as well that the “blue” energy shift of PL spectra in bioconjugated QDs does not connect with the emission of HPV E7 Ab, PRV Ab or PBS.

To study the role in the emission of excitons, localized at QD excited states in bioconjugated QDs, the PL spectra were measured at different excitation light intensities (Figure 8a, b). The PL spectra of nonconjugated 655N QDs kept the Gaussian shape of core PL band (1.90 eV) for all excitation intensities used (Figure 8a). The FWHM of this PL band at the first increases versus excitation intensity, due to raising the excited QD numbers and QD size distribution, and then the FWHM saturates at higher excitation intensities (Figure 8c, curve 1).

The PL band intensity in QDs, bioconjugated to HPV E7 Abs, increases versus excitation light power together with the formation of high-energy tails (Figure 8b). The PL band intensity at a low-energy side increases owing to rising the excited QD numbers and QD size distribution by the same way as in nonconjugated QDs. The FWHM of PL band in bioconjugated QDs increases monotonously versus excitation intensity without the saturation effect (Figure 8c, curve 2). Thus, the PL band intensity at a high-energy side increases versus excitation light power due to raising the role of exciton emission via excited states in bioconjugated QDs. This effect can explain an asymmetric shape of PL bands and increasing the FWHMs (Figure 8c, curve 2) in bioconjugated QDs. However, the emission of excitons localized at the excited QD states cannot explain shifting the main PL peak to higher energy in the PL spectra of bioconjugated CdSe/ZnS QDs.

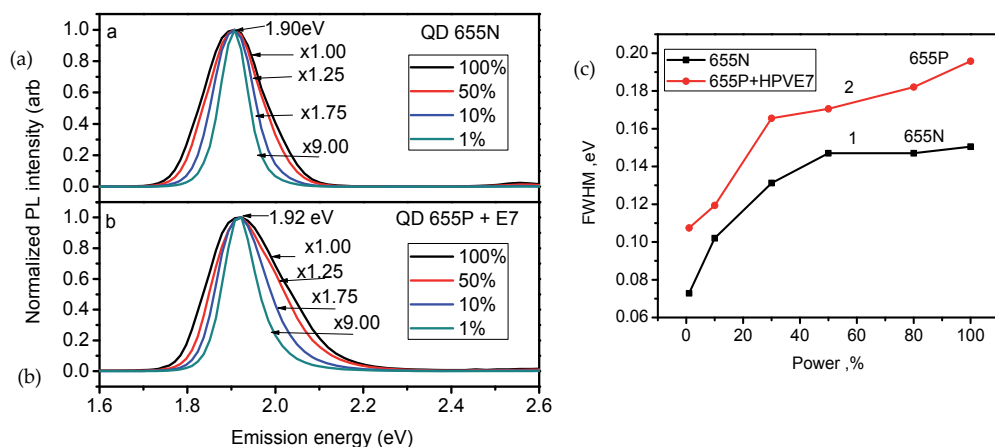


Figure 8. (a,b). Normalized PL spectra of 655N (a) and 655P-HPV E7 (b) QD samples measured at 300 K at the excitation intensities 100%, 50%, 10%, and 1%. The excitation intensity of 100% corresponds to 76 mW. (c). The FWHM variation of PL bands in 655N (1) and 655P-HPV E7 (2) QDs versus excitation light power. 100% corresponds to the power 76 mW.

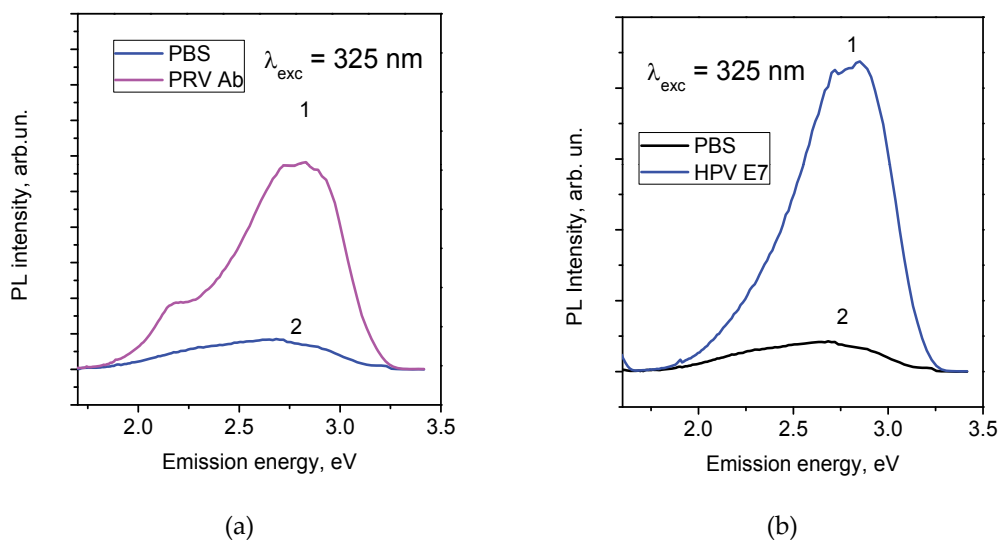


Figure 9. (a) PL spectra of PRV Ab (1) and PBS (2) without QDs. (b) PL spectra of HPV E7 Ab (1) and PBS (2) without QDs.

4. Discussion of the CdSe/ZnS QD bioconjugation

The experimental results presented above have shown that the influence of exciton emission via excited QD states or the emission of antibodies and PBS as well as the oxidation or degradation processes in QD cores can be avoided from the consideration as the reasons of “blue” PL peak shift at the QD bioconjugation. Let us discuss other reasons for the PL

energy shift at the bioconjugation of QDs to antibodies. These factors could be assigned to (i) the quantum-confined Stark effect stimulated by the charge of antibodies [43, 44], (ii) the quantum-confined effect related to the shift of QD energy levels and stimulated by the change of electric potential at the QD surface [45], or (iii) decreasing the effective QD size in bioconjugated QDs [46].

The Stark effect is shifting and splitting of energy levels in atoms and molecules due to the presence of external electric field. The Stark shift of energy levels, ΔE , as a function of electric field, ξ , can be presented as a sum of linear (first order Stark effect) and quadratic (second order Stark effect) functions of an electric field: $\Delta E = \mu_{\text{QD}} \xi + 0.5 \alpha_{\text{QD}} \xi^2 + \dots$, where E is an energy of optical transition, and μ_{QD} and α_{QD} are projections of excited-state dipole and polarizability, respectively, along the electric field [43, 44]. This relation includes both the polar and polarizable parts of emitting state. Actually, the Stark shift in the emission of QD ensembles was found earlier to be purely quadratic versus applied electric field [39]. The dependences of the quantum-confined Stark shift versus QD sizes and electric fields in the CdS, CdSSe, and CdSe QDs were studied theoretically [44] and experimentally [43] in the early 90th. Only the “red” Stark energy shift was predicted theoretically for CdS and CdSSe QD ensembles at applying an external electric field [44]. Thus, we can conclude that the quantum-confined Stark effect could not explain the observed experimental “blue” energy shift of PL bands at the QD bioconjugation to studied antibodies.

Another reason for the “blue” shift of PL peak in bioconjugated QDs can be connected with the change of potential barrier at the surface of QDs bioconjugated to the charged antibodies. The position of energy levels in QDs for the strong quantum-confined regime depends on the value of potential barrier [45]. It was shown that the impact of a finite potential barrier on the electron-hole energy states increases with decreasing the dot radius. The lower potential barrier reduces and higher potential barrier increases the energy levels and these changes are more relevant for high-energy states [45]. However, the comparison of the PL spectrum transformation presented in Figures 2 and 3 or Figure 7a, b has shown that the value of “blue” PL energy shift at the QD bioconjugation to anti-IL-10 or PRV Abs is more essential for QDs with the biggest sizes (6.4 nm) and emission at 655 nm. Thus, the “blue” PL band energy shifts at the CdSe/ZnS QD bioconjugation to antibodies do not connect with the variation of the potential barrier at the QD surface.

The other reason for the “blue” shift of QD energy levels at the quantum-confined condition, owing to decreasing the effective QD size in bioconjugated QDs, was considered by Torchynska et al. [46]. When QD is bioconjugated, its energy balance changes very much. The energy variation comes from the fact that the attachment of biomolecules to the external QD surface will result in the generation of van der Waals forces. The extra charge attached to the exterior shell will form a blocking electric field, which “truncates” the effective volume of QDs (Figure 10). In this situation, it is natural to expect energy varying of emitted light. At the same time, the stronger confinement will produce a blue shift of the QD emission spectrum.

The question about the accurate calculation of the truncated volume is a complicated one. For a point charge, the equipotential surfaces will be spheres, which will make the blocked volume corresponding to a spherical segment. The remaining effective volume will lose its spherical

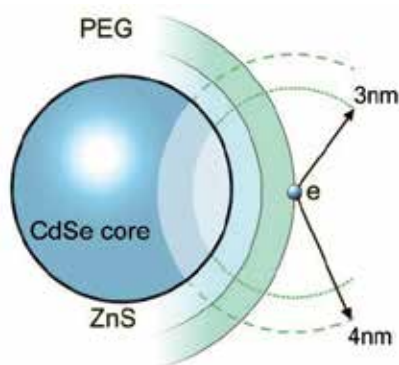


Figure 10. A schematic depiction of CdSe/ZnS QD with the 6.4 nm CdSe core, encased in the ZnS and poly-ethylene glycol (PEG) protective shells. A charge generated upon bioconjugation is shown attached to the PEG shell to the right. We consider two radii of the blocking sphere of $d = 3$ and 4 nm, respectively.

shape. We proposed to approximate it with a cylinder with a height c and a circular base of the diameter a . The Schrödinger equation for such system was solved using the mirror boundary conditions [46, 47], providing the ground state energy relative to the material band gap [47]:

$$E_{GS_c} - E_g = \frac{\hbar^2}{2m} \left(\frac{0.268}{a^2} + \frac{0.25}{c^2} \right) \quad (1)$$

The parameters of a cylinder can be estimated for different strength of the blocking field. We consider two cases with the blocking field extending for the distance $d = 3$ and 4 nm from the charge attached to the protective PEG layer covering nanoparticle (Figure 9). For these cases, the parameters of the effective cylinder are as follows: $a = 1.6 R$, $c = 1.55 R$ (for 4 nm blocking radius) and $a = 1.65 R$, $c = 1.6 R$ (for 3 nm blocking radius), where $R = 3.2$ nm is the radius of the CdSe core of the particle. Using these values, one can obtain the expressions for the ground state of conjugated nanoparticle with 4 nm blocking [46]:

$$E_{GS_c} - E_g \approx \frac{\hbar^2}{9.6mR^2} \quad (2)$$

and also for conjugated nanoparticle with 3 nm blocking distance [46]:

$$E_{GS_c} - E_g \approx \frac{\hbar^2}{11.1mR^2} \quad (3)$$

In a real system, the absorbed energy that triggered the formation of an exciton can be partially dissipated, so that the peak of PL spectra will occur at lower energy, producing Stokes shift

E_{St} . Therefore, the total blue shift observed in the system can be defined as a ratio between peak positions of a bioconjugated sample $h\nu_c$ versus nonconjugated sample $h\nu_0$:

$$\frac{E_{GS_c} - E_g}{E_{GS_0} - E_g} = \frac{h\nu_c + E_{St} - E_g}{h\nu_0 + E_{St} - E_g} \quad (4)$$

Using the experimental data shown in Figure 3, one can see that $h\nu_0 = 1.89$ eV and $h\nu_c = 2.08$ eV; the typical Stokes shift is $E_{St} = 56.0$ meV [48]. Using the band gap $E_g = 1.74$ eV for the bulk CdSe at 300 K [49], one can obtain the ratio for the experimental shift equal to 2.16 from equation (4). The ratios calculated with Eqs. (1), (2), (3), and (4) are 3.30 (for blocking distance $d = 4$ nm) and 2.88 (for $d = 3$ nm), which is considerably close to the experimental value in view of simplifications made in treating the truncation of nanoparticle's core volume.

Thus, we have proposed to use the mirror boundary condition for simplifying solution of the Schrödinger equation for a spherical CdSe/ZnS core/shell QDs. It was shown that the "blue" shift in the PL spectrum observed in the experiment with bioconjugated QDs can be explained by the attachment of a charge deals with the antibody to the exterior shell of QDs, blocking away a fraction of core's volume. Representing the truncated effective part of core as a cylinder, we obtained a blue shift values with a considerable accuracy in relation to the experimental data. Thus, the "blue" energy shift of PL spectrum in the bioconjugated CdSe/ZnS QDs has been attributed to the electronic quantum-confined effects stimulated by the charged antibodies.

5. The bioconjugation study of CdSeTe/ZnS QDs

5.1. CdSeTe/ZnS QDs bioconjugated to anti-IL-10 Ab

The PL spectra of CdSeTe/ZnS QDs for the nonconjugated (800N) and bioconjugated (800P+IL-10) states are shown in Figure 11. The PL spectrum of 800N QDs is characterized by Gaussian shape PL band with a peak at 1.59-1.60 eV (Figure 11, curves 1 and 2) connected with exciton emission in CdSeTe cores. The PL peak shifts to higher energies ("blue" shift) up to 1.90 eV (Figure 11, curves 3 and 4), and the shape of PL bands becomes asymmetric with low-energy shoulders (at 1.75 eV) in the PL spectra of bioconjugated QDs (Figure 11, curves 3 and 4). Simultaneously, the PL intensity of QDs decreases in the case of the bioconjugation to anti-IL-10 Ab (Figure 11, curves 3 and 4).

The PL spectra of anti-IL-10 Ab and PBS have been measured at the UV light excitation early (Figure 4). The PL spectrum of anti-IL-10 Ab is characterized by the PL band with a peak at 2.21 eV and a small PL shoulder in the range 2.3-3.0 eV (Figure 4, curve 1). The intensity of the PL band related to PBS (Figure 4, curve 2) is 15-fold smaller than the emission intensity of 2.21 eV PL band connected with anti-IL-10 Abs. Note that the 2.21 eV PL band intensity in anti-IL-10 Abs is 10-fold smaller than the emission intensity of excitons in CdSeTe/ZnS QDs at UV

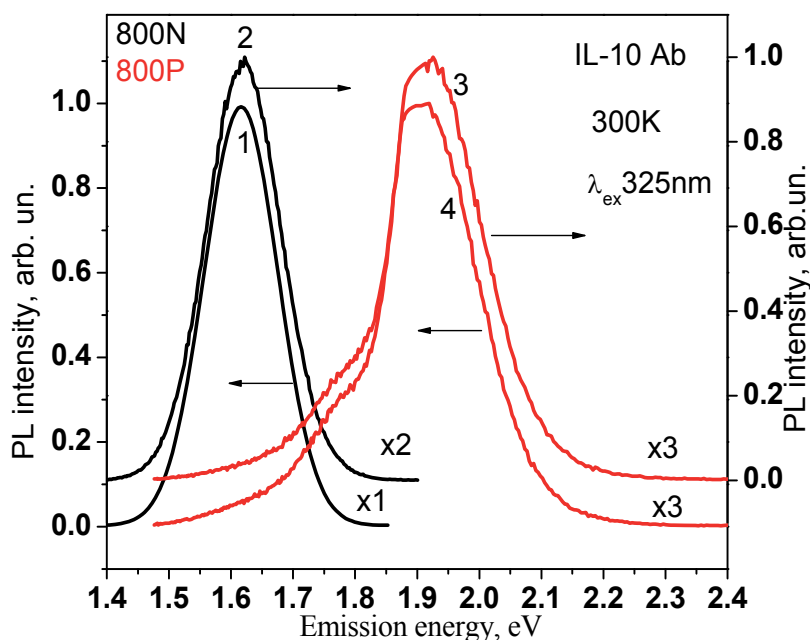


Figure 11. Normalized PL spectra of two 800N (curves 1 and 2) and two 800P+ IL-10 (curves 3 and 4) QD samples at 300 K. PL spectra are shifted along *y* axis to prevent their overlapping. Numbers (x1, x2, x3) indicate the multiplication coefficients used at the normalization. Excitation light wavelength is 325 nm.

light excitation (Figure 11). Thus, the new PL bands peaked at 1.75 and 1.90 eV that appeared in the PL spectra of bioconjugated QDs do not related to the emission of anti-IL-10 Abs or PBS.

To study the impact of the excitation quanta energy on the shape of PL bands, the PL spectra of nonconjugated and bioconjugated QDs have been measured using the different excitation wavelengths of 532 nm, 488 nm, and 325 nm (Figure 12). The difference in PL intensities is related to the power of lasers used, but the shape of PL bands in the nonconjugated and bioconjugated QDs is similar. Note that the PL intensity of QD emission is higher at the UV excitation (325 nm).

The Raman scattering spectra of CdSeTe/ZnS QDs are investigated as well. The Raman spectrum of nonconjugated CdSeTe/ZnS QDs represents a complex Raman peak of QDs at 202.5 cm^{-1} and the Raman peak at 519.6 cm^{-1} connected with the first-order Raman scattering involving optic phonons in the Si substrate (Figure 13a). The Raman peak of QDs is a superposition of two Raman peaks at 191.2 and 202.5 cm^{-1} (Figure 13a), which correspond to the LO phonons in the CdSe₅₀Te₅₀ core and CdSe₈₀Te₂₀ core's cover layer [31, 50]. In addition, the Raman spectrum represents two peaks at 177.0 and 280 cm^{-1} . The peak at 177.0 cm^{-1} could be assigned to a surface phonon (SP) in QD cores [6]. The Raman peak at 280 cm^{-1} is probably due to the CdZnSeS alloy that appears at the CdSeTe/ZnS interface at the temperature of ZnS shell growth [6, 50-52].

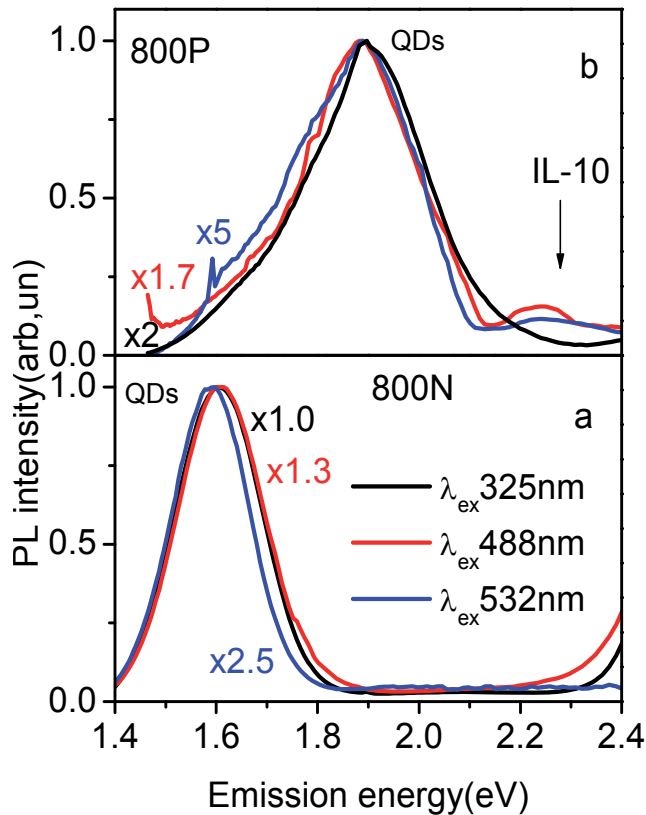


Figure 12. PL spectra of 800N (a) and 800P+ IL-10 (b) CdSeTe/ZnS QDs measured at 300 K and excited by the light with wavelengths: 532 nm (1), 488 nm (2), and 325 nm (3).

The Raman scattering investigation shows (Figure 13a, b) that the Raman peaks related to the LO phonons in the double CdSeTe core and in the alloy at the interface did not vary at the QD bioconjugation. This fact testifies that the “blue” PL energy shift in bioconjugated CdSeTe/ZnS QDs (Figures 11 and 12) has been not connected with compressive strains or with the degradation of CdSeTe QD core owing to core/shell intermixing or core oxidation at the QD bioconjugation.

5.2. CdSeTe/ZnS QDs bioconjugated to the HPV and PRV antibodies

Normalized PL spectra of nonconjugated and bioconjugated CdSeTe/ZnS QDs have been presented in Figures 14, 15, and 16 for the different antibodies used: (i) mouse monoclonal anti-HPV E7 Ab, (ii) mouse monoclonal HPV E6 Ab, and (iii) pseudorabies virus (PRV) Ab.

QD emission spectra in nonconjugated state are characterized by the two Gaussian shape PL bands. The main PL band (I) with a maximum at 1.57-1.60 eV (Figures 14-16, curve 1) is connected with exciton emission in the CdSeTe core. The small intensity PL band (II) with a

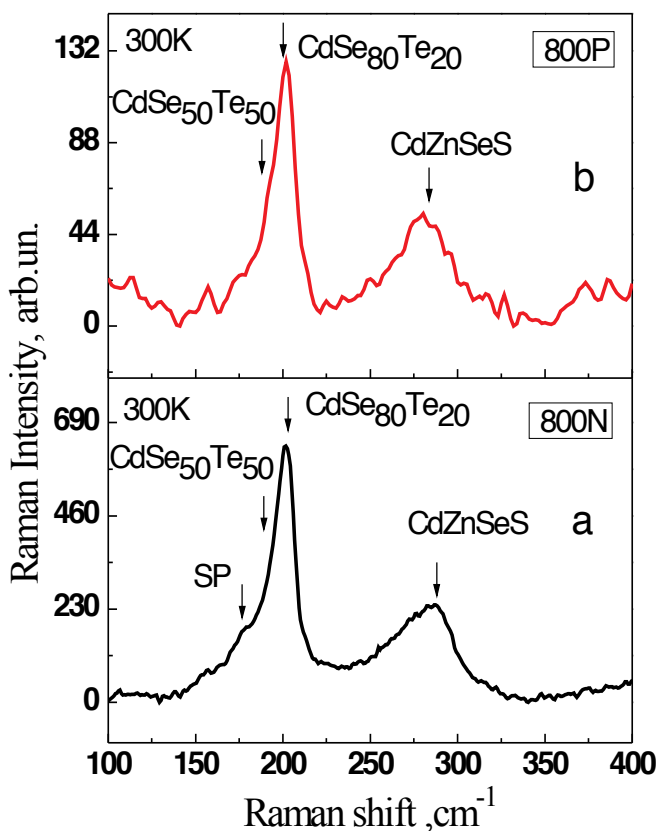


Figure 13. Raman scattering spectra of 800N (a) and 800P+ IL-10 (b) QDs.

peak at 2.50 eV is attributed to exciton emission in the intermediate alloy CdZnSeS layer at the core/shell interface [50-52]. This intermediate layer was introduced at the process of QD growth with the aim to decreasing the mismatch between the CdSeTe and the ZnS crystal lattices. The PL intensity of 2.50 eV band varies owing to the variation, apparently, a volume of intermediate alloy layers in the different QD ensembles (Figures 14-16). The small intensity PL band at 2.50-2.90 eV (Figure 15) can be connected with the emission of PBS (see Figures 4 and 9) that exists in the nonconjugated QD ensembles as well.

The main PL peak (I) shifts to higher energy in the PL spectra of bioconjugated QDs up to: 1.881 eV (Figure 14, curve 2), 1.887 eV (Figure 15, curve 2), or even 1.937 eV (Figure 16, curve 2). Simultaneously, the PL band shape becomes asymmetric with essential low-energy shoulders. The analysis has revealed that the main PL band in bioconjugated QDs is complex and can be represented by a superposition of two PL bands (Figure 15, curves 3 and 4): the low-energy band with a peak at 1.60 eV and the high-energy band centered at 1.887 eV in Figure 15. At the same time, the PL intensity of main PL band I decreases and the additional PL band appears in the spectral range 2.2-3.0 eV.

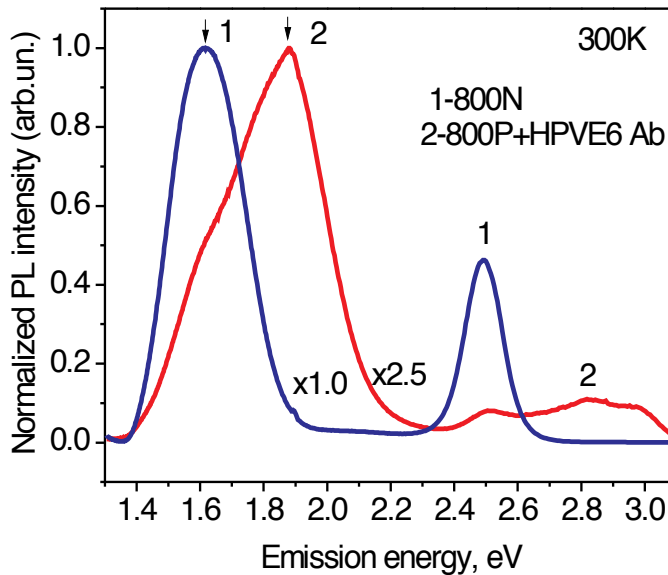


Figure 14. Normalized PL spectra of nonconjugated 800N (1) and bioconjugated 800P (2) QDs to HPV E6 Ab measured at 300 K. Numbers at the curves ($\times 1.0$ and $\times 2.5$) present the multiplication coefficients used at the normalization of experimental PL spectra.

6. Discussion of the CdSeTe/ZnS QD bioconjugation

Let us discuss again the physical reasons of PL spectrum transformation at the QD bioconjugation to antibodies. As we mentioned above, these reasons can be related to (i) the emission of antibody molecules or PBS at UV excitation; (ii) the compressive strain applied to QDs at the bioconjugation [33]; (iii) the compound material degradation owing to core/shell intermixing [53] or oxidation [32] at the QD bioconjugation; (iv) the quantum-confined Stark effect [43, 44], stimulated by electric charges of antibodies; (v) the dominated emission of excitons localized at the excited QD states; (vi) the change of energy band profile at the application of electric field of charged Abs; and (vi) the quantum-confined effect owing to the shift of QD energy levels stimulated by the change of potential barrier at the QD surface [45] or by decreasing the effective QD size in bioconjugated QDs [46]. To make the decision concerning the most probable physical reasons of the PL transformation in CdSeTe/ZnS QDs, let us analyze all of these factors in details.

(i) The emission of HPV or PRV antibodies and PBS can be excited together with QD emission at the PL excitation by UV light (325 nm). The PL spectra of pure HPV and PRV antibodies, and PBS without QDs have been investigated (Figure 17).

The wide emission bands have been detected in the spectral range 2.0-3.2 eV in PL spectra of both the antibodies and PBS (Figure 17). The PL intensity of PBS emission is 50-fold smaller, and the PL intensities of antibody's emissions are 5- or 10-fold smaller in comparison with the PL intensity of the main PL bands I in bioconjugated CdSeTe/ZnS QDs. Thus, the emission of

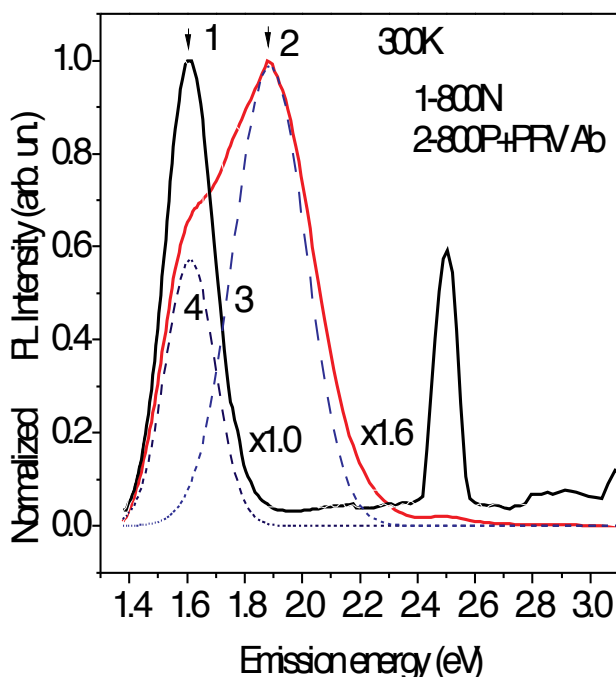


Figure 15. Normalized PL spectra of nonconjugated 800N (1) and bioconjugated 800P QDs (2) to PRV Ab measured at 300 K. Numbers ($\times 1.0$ and $\times 1.6$) present the coefficients used at the normalization of PL spectra. Dashed curves (3 and 4) show the deconvolution of curve 2 on two PL bands.

antibodies or PBS at the high-energy UV light excitation can influence only on the shape of high-energy tails in PL spectra of bioconjugated QDs. This impact is seen clearly in Figures 14, 15, and 16 (curve 2), where the high-energy PL band appears in the spectral range 2.2-3.2 eV.

(ii-iii) If the compressive strain appears at QD bioconjugation, the Raman peaks have shifted in Raman spectra in comparison with those for nonconjugated QDs. The Raman scattering spectrum of nonconjugated CdSeTe/ZnS QDs represents a complex Raman peak of QDs at 202.5 cm^{-1} and another Raman peak at 519.6 cm^{-1} related to the Si substrate (Figures 13a and 18a).

The QD peak is a superposition of Raman peaks at 191.2 and 202.5 cm^{-1} (Figure 18a), which correspond to Raman scattering involving the LO phonons of the CdSe₅₀Te₅₀ core and CdSe₈₀Te₂₀ core's cover layer [31, 50]. The detailed estimations of material compositions in the double CdSeTe QD core on the base of Raman peak analysis were published earlier by Quintos Vazquez et al. [31]. The Raman spectrum demonstrates as well the peak at 280 cm^{-1} , which can be assigned to light scattering by LO phonons in the CdSeZnS intermediate alloy layer. The Raman peak at 406 cm^{-1} is related to two-phonon Raman scattering in the CdSeTe core [50]. The intensity of Raman signals in bioconjugated CdSeTe/ZnS QDs increases in comparison with those in nonconjugated QDs [54]. This effect was attributed early to the surface-enhanced

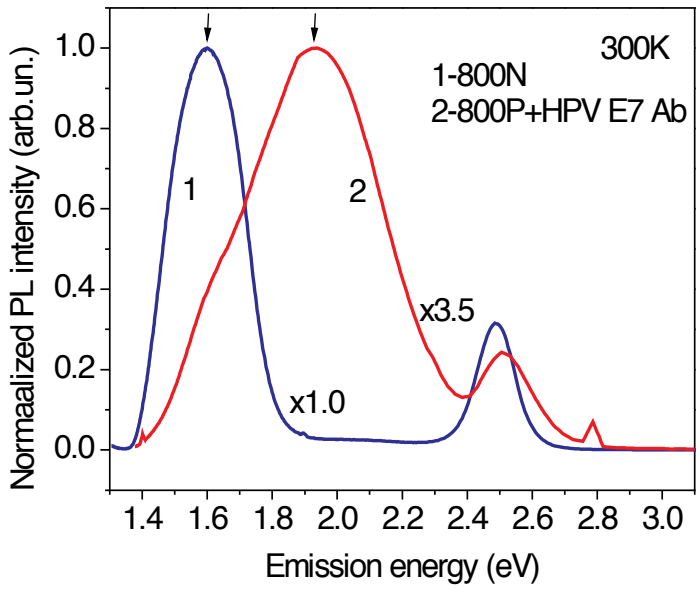


Figure 16. Normalized PL spectra of nonconjugated 800N (1) and bioconjugated 800P QDs (2) to HPV E7 Ab at 300 K. Numbers at the curves ($\times 1.0$ and $\times 3.5$) correspond to multiplication coefficients used at the normalization of experimental PL spectra.

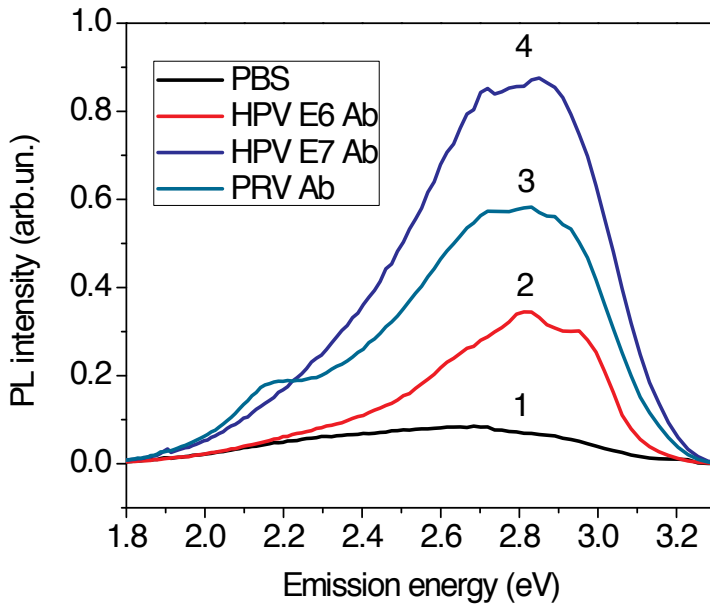


Figure 17. PL spectra of PBS (1), HPV E6 Ab (2), PRV Ab (3), and HPV E7 Ab (4) without QDs.

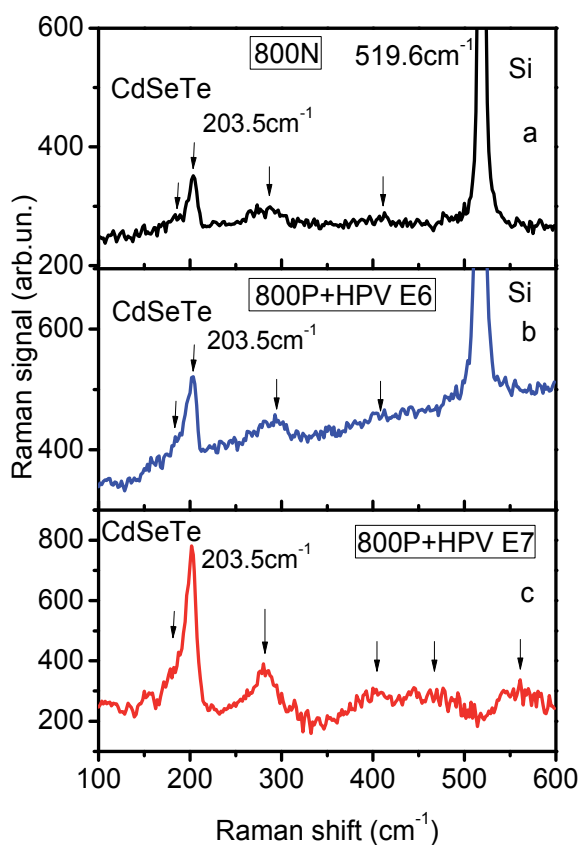


Figure 18. Raman scattering spectra of nonconjugated 800N (a) and bioconjugated 800P (b, c) QDs to HPV E6 (b) and HPV E7 (c).

Raman scattering (SERS) [22, 39, 54] due to the interaction of the electromagnetic field of excitation light with the electric charges (dipoles) of antibodies. The realization of the SERS effect at Raman scattering in bioconjugated QDs testifies that the antibodies have the electric charges.

The SERS effect is responsible for appearing the low-intensity Raman peaks (463 and 580 cm^{-1}) in Raman spectra of bioconjugated QDs (Figure 18c). These Raman signals are related to the Si substrate and were assigned early to scattering involving TO phonons (463 cm^{-1}) and the combination of TA and TO phonons at the X direction in the Si Brillouin zone [36]. The Raman scattering study shows (Figure 18b, c) that the positions of Raman peaks in Raman spectra of the double CdSeTe core and intermediate CdSeZnS layer have not been varied at the CdSeTe/ZnS QD bioconjugation. Permanent positions of Raman signals in QDs testify that the bioconjugation process has not connected with the compressive strains to QDs, with the compound degradation owing to core/shell intermixing or the QD core oxidation at the bioconjugation.

(iv) The quantum-confined “red” Stark energy shift was predicted theoretically for emission in the ensembles of CdS or CdSSe QDs [43, 44]. The quantum-confined Stark effect can be avoided from our discussion as well because the “blue” PL energy shift is detected in studied CdSeTe/ZnS QDs at the bioconjugation.

(v) To analyze the role of excitons bounded at the excited states in the CdSeTe core, the dependence of PL spectrum transformation versus excitation light intensities has been studied (Figure 19a-c). As it is clear from Figure 19a, the shape of PL bands in nonconjugated CdSeTe/ZnS QDs (800N) has not changed at varying the excitation light intensities.

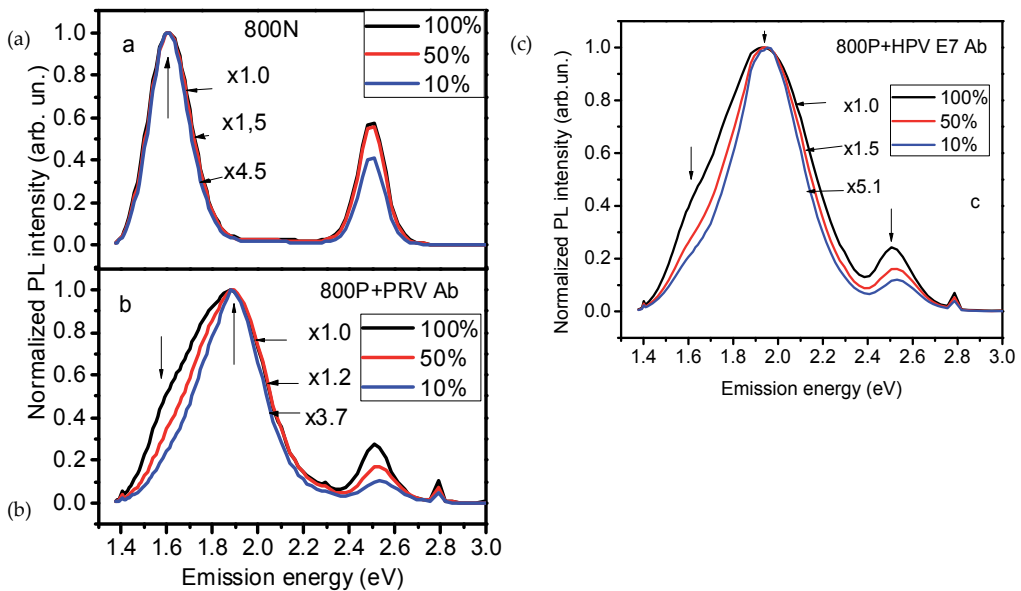


Figure 19. Normalized PL spectra of nonconjugated (a) and bioconjugated QDs to PRV Ab (b) and to HPV E7 Ab (c) measured at different excitation light powers at 300 K.

Meanwhile, the shape of the PL spectra of bioconjugated QDs varies versus excitation light power (Figure 19b, c). The PL intensity decreases mainly in the low-energy (1.60 eV) and high-energy (2.50 eV) ranges that have been seen clearly. The mentioned PL bands do not connect with the emission of excitons localized at the excited states in the CdSeTe core. Thus, the emission of excitons localized at the excited states in bioconjugated CdSeTe/ZnS QDs is not responsible for the transformation of PL spectra versus excitation light power.

(vi) Let us consider the energy band diagram of CdSeTe/ZnS QDs with the aim to analyze the varying energy band profile at the bioconjugation. The energy diagram of the double core CdSeTe/ZnS QDs with emission at 800 nm was calculated early by Quintos Vazquez et al. [31]. The band gaps and electronic affinities for the CdSe₅₀Te₅₀, CdSe₈₀Te₂₀, and ZnS bulk crystals [31, 55] have been represented in Figure 20.

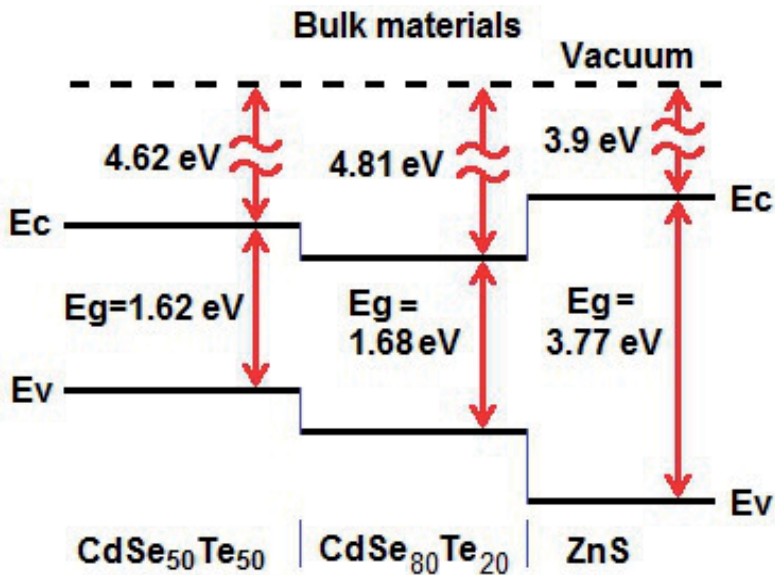


Figure 20. Energy band diagram for the CdSeTe alloys and ZnS bulk crystal.

To create the energy diagram of nonconjugated CdSeTe QDs (Figure 21), the variation of energy band gaps for the CdSe₅₀Te₅₀ core and CdSe₈₀Te₂₀ core cover layer with their sizes is estimated using the effective mass approximation model [31]. The big size of the double core/shell CdSeTe/ZnS QDs (emission, 800 nm) permits to apply the effective mass approximation approach [6].

The ground energy of electron-hole pairs and the energy of the first absorption transition are estimated as follows [56]:

$$E_{1S1S} = E_g + \frac{\hbar^2 \pi^2}{2\mu\alpha^2} - 1.786 \frac{e^2}{\epsilon\alpha} - 0.248R_y \quad (5)$$

where E_g is the energy band gap of bulk material, α is a QD radius, μ is the reduced mass, $\mu^{-1} = m_e^{*-1} + m_h^{*-1}$, m_e^* and m_h^* are the effective masses of electrons and holes, and ϵ is the high-frequency permittivity. The term $\frac{e^2}{\epsilon\alpha}$ in Eq. (5) describes the electron-hole Coulomb interaction, and the fourth term is a minor correction.

To analyze the energy band gap, the following parameters have been used for the bulk CdSe: $E_g = 1.730$ eV at 300 K, $m_e^* = 0.13 m_0$, $m_h^* = 0.45 m_0$, and the high-frequency permittivity $\epsilon = 8.2$ [50, 51]. Using the parameters for the bulk CdTe: $E_g = 1.50$ eV at 300 K, $m_e^* = 0.11 m_0$, and $m_h^* = 0.35 m_0$ [50, 57], the values of energy band gaps and effective masses for the bulk CdSe_{0.8}Te_{0.2} and CdSe_{0.5}Te_{0.5} alloys have been obtained by the linear interpolation. To estimate the position of PL excitation peaks connected with the electron-hole ground states in QD, the value of Stokes

shift is taken in account, which equals 50 meV [6]. Estimated energy band gaps for the $\text{CdSe}_{0.5}\text{Te}_{0.5}$ and $\text{CdSe}_{0.8}\text{Te}_{0.2}$ alloys have been used for the design of the energy diagram of the double core/shell QDs (Figure 21).

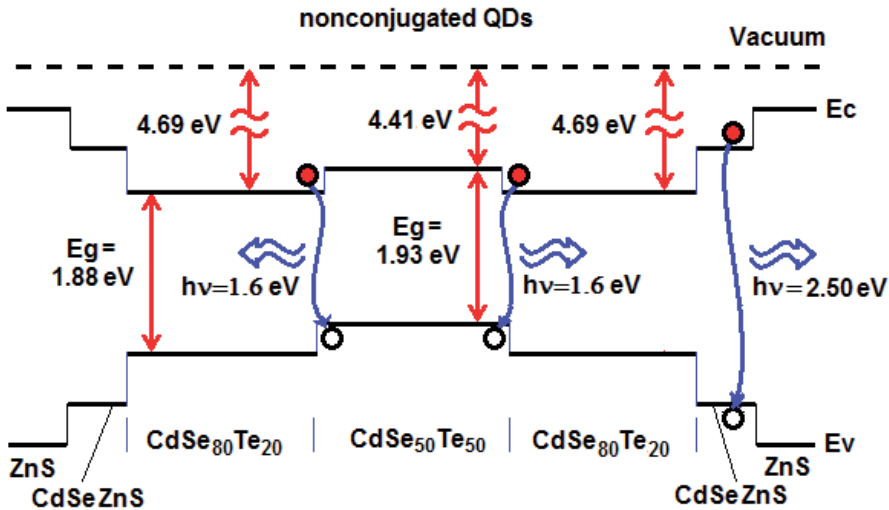


Figure 21. The energy band diagram of nonconjugated double core CdSeTe/ZnS QDs.

The energy band diagram of nonconjugated CdSeTe/ZnS QDs (Figure 21) explains the types of the optical transitions and emission energy of 1.60 eV detected in the PL spectra of nonconjugated QDs. As it is clear from Figure 21, owing to the type II quantum well ($\text{CdSe}_{80}\text{Te}_{20}/\text{CdSe}_{50}\text{Te}_{50}/\text{CdSe}_{80}\text{Te}_{20}$) in double core QDs, the wide band gap core and the core's covered quantum well layer with the energy band gaps of $E_g = 1.93$ and 1.88 eV, respectively, enable to emit IR emission with a PL peak at 1.60 eV in nonconjugated QDs (Figures 11, 14, 15, and 16). This 1.6-eV emission owes to the recombination of electrons, from the $\text{CdSe}_{80}\text{Te}_{20}$ conduction band, with holes localized in the $\text{CdSe}_{50}\text{Te}_{50}$ valence band (Figure 21).

To explain the PL band "blue" shift into the higher energy range (1.88-1.94 eV) in bioconjugated CdSeTe/ZnS QDs (Figures 11, 14, 15, and 16), let us to consider the transformation of band diagram at applying the external electric field of charged antibodies. In this case, the energy band profile varies as it is presented in Figure 22. Actually, in the bioconjugated QDs, the two types of optical transitions are possible: the recombination of excitons located at the ground states in the $\text{CdSe}_{50}\text{Te}_{50}$ core and/or the recombination of electrons, from the $\text{CdSe}_{80}\text{Te}_{20}$ conduction band, with holes localized in the $\text{CdSe}_{50}\text{Te}_{50}$ valence band (Figure 22).

The transformation of PL spectra versus excitation light intensities (Figure 19) has confirmed the proposed QD energy band diagrams. Actually, at low excitation light intensity, the recombination (1.88 eV) of excitons at the ground $\text{CdSe}_{50}\text{Te}_{50}$ core states dominates in the PL spectrum (Figure 22). At obtaining the last value (1.88 eV), the Stock shift of 50 meV is taken into account [6, 29, 30]. When excitation intensity increases, the indirect recombination

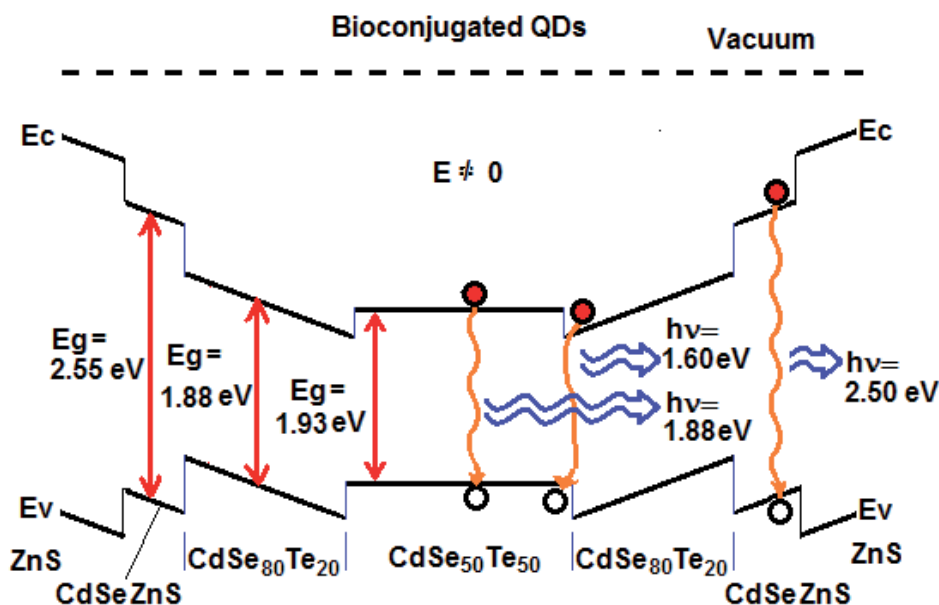


Figure 22. Energy band diagram of QDs bioconjugated to 800P+HPV E6 Ab.

transition (electrons from CdSe₈₀Te₂₀ with holes in CdSe₅₀Te₅₀) and exciton emission in the intermediate CdSeZnS layer can be realized. Hence, the energy band profile variation in the double core CdSeTe/ZnS QDs at the bioconjugation to charged antibodies permits to explain the PL spectrum peculiarities of bioconjugated QDs.

(vii) Finally, let us discuss the difference in PL band positions in CdSeTe/ZnS QDs bioconjugated to different antibodies (Figures 14-16, curve 2). The main PL peaks in bioconjugated QDs are as follows: 1.881 eV for 800P+HPV E6 Ab (Figure 14, curve 2), 1.887 eV for 800P+PRV Ab (Figure 15, curve 2), and 1.937 eV for 800P+HPV E7 Ab (Figure 16, curve 2). The difference in PL peaks can be related to the difference in electric potentials (potential barriers) at the surface of bioconjugated QDs. It is known that the position of energy levels in QDs, for the strong quantum confinement regime, depends on the value of potential barriers at the surface [45]. The comparison of PL intensities, detected for the pure antibodies (Figure 17), and the corresponding PL peaks in bioconjugated QDs (Figures 14-16, curve 2) have shown that the antibody HPV E7 with highest emission intensity (Figure 17, curve 4) stimulates the biggest PL band shift up to 1.937 eV (Figure 16, curve 2). The PL intensity, measured for the pure antibodies (Figure 17), depends on their concentrations in PBS. Thus, it is possible to conclude that the shift of PL spectra depends on a number of charged antibodies bioconjugated to CdSeTe/ZnS QDs [58]. Moreover, this PL shift increases by enlarging the antibody concentration in PBS. The potential barrier increasing at the QD surface has shifted the QD emission into the higher energy range owing to the shift of QD energy levels [58].

Thus, the PL spectrum transformation of CdSeTe/ZnS QDs, bioconjugated to studied antibodies, is related to the two effects: (i) the change of energy band profiles and (ii) the quantum-

confined effect owing to the shift of QD energy levels stimulated by the change of electric potentials (potential barrier) at the surface of QDs bioconjugated to charged antibodies. The potential barrier increasing has shifted the QD energy levels and QD emission into the higher energy range.

7. Conclusion

Photoluminescence, its excitation power dependence, and Raman scattering spectra have been studied in CdSe/ZnS and CdSeTe/ZnS QDs for the nonconjugated states and after the QD conjugation to the anti-IL-10, human papilloma virus, and pseudorabies virus antibodies. The QD bioconjugation to charged antibodies stimulates the “blue” energy shift of PL bands related to exciton emission in the CdSe or CdSeTe cores.

The “blue” energy shift of PL spectrum in bioconjugated CdSe/ZnS QDs has been attributed to the electronic quantum-confined effects stimulated by decreasing the effective QD size at its bioconjugation to charged antibodies. It was shown that the attachment of a charge, deals with the antibody, to the exterior shell of CdSe/ZnS QDs leads to blocking away a fraction of core’s volume.

The energy band diagrams of CdSeTe/ZnS QDs in the nonconjugated and bioconjugated states have been designed, which permit to explain the types of optical transitions in QDs and their transformations at the QD bioconjugation. It is shown that the change of energy band profile and the “blue” shift of QD energy levels, owing to the change of potential barrier at the QD surface, are the dominant reasons of PL spectrum transformation in the double core CdSeTe/ZnS QDs conjugated to charged antibodies. A better understanding of the QD bioconjugation to specific antibodies is expected to produce the major advances in biology and medicine and can be a powerful technique for early medical diagnostics.

Acknowledgements

The work was partially supported by CONACYT (project 130387) and by SIP-IPN (projects 20140648 and 20150601), Mexico. The author would like to thank Dr. Janna Douda for the QD bioconjugation to antibodies and Dr. Jose Luis Casas Espinola for the PL measurements.

Author details

Tetyana V. Torchynska

Address all correspondence to: ttorch@esfm.ipn.mx

National Polytechnic Institute, ESFM, Mexico D.F., Mexico

References

- [1] T. Jamieson, R. Bakhshi, D. Petrova, R. Pockock, M. Imani, A.M. Seifalian, *Biomaterials* 28, 4717 (2007).
- [2] D. Gerion, W.J. Parak, S.C. Williams, D. Zanchet, C.M. Micheel, A.P. Alivisatos, *J Am. Chem. Soc.* 124, 7070 (2002).
- [3] X.H. Gao, Y.Y. Cui, R.M. Levenson, L.WK. Chung, S.M. Nie, *Nat. Biotechnol.* 22, 969 (2004).
- [4] Z. Liu, W.B. Cai, L.N. He, N. Nakayama, K. Chen, X.M. Sun, X.Y. Chen, H.J. Dai, *Nat. Nanotech.* 2, 47 (2007).
- [5] R. Weissleder, K. Kelly, E.Y. Sun, T. Shtatland, L. Josephson, *Nat. Biotechnol.* 23, 1418 (2005).
- [6] T. Torchynska, Yu. Vorobiev. *Semiconductor II-VI Quantum Dots with Interface States and Their Biomedical Applications*, *Advanced Biomedical Engineering*, Gaetano D. Gargiulo and Alistair McEwan (Eds.), InTech Publisher, Croatia, pp. 143-182, 2011.
- [7] L.J. Yang, Y.B. Li, *Analyst* 131, 394 (2006).
- [8] I. Brigger, C. Dubernet, P. Couvreur, *Adv. Drug Deliv. Rev.* 54, 631 (2002).
- [9] Y. Ebenstein, T. Mokari, U. Banin, *J. Phys. Chem. B* 108, 93 (2004).
- [10] F. Wang, W.B. Tan, Y. Zhang, X. Fan, M. Wang, *Nanotechnology* 17, R1-R13 (2006).
- [11] M. Kuno, D.P. Fromm, H.F. Hamann, A. Gallagher, D.J. Nesbitt, *J. Chem. Phys.* 115, 1028 (2001).
- [12] A.R. Clapp, I.L. Medintz, J.M., Mauro, Br.R. Fisher, M.G. Bawendi, H. Mattoussi, *J. Am. Chem. Soc.* 126, 301 (2004).
- [13] N. Tessler, V. Medvedev, M. Kazes, S.H. Kan, U. Banin, *Science* 295, 1506 (2002).
- [14] Th.E. Rasmussen, L. Jauffred, J. Brewer, S. Vogel, E.R. Torbensen, B.Ch. Lagerholm, L. Oddershede, E.C. Arnsfang, *J. Mod. Phys.* 4, 27 (2013).
- [15] K. Koenig, *J. Microsc.* 200, 83 (2000).
- [16] H.M.E. Azzazy, M.M.H. Mansour, S.C. Kazmierczak, *Clin. Biochem.* 40, 917 (2007).
- [17] C.H. Lin, L.W Chang, H. Chang, M.H. Yang, Ch.Sh. Yang, W.H. Lai, W.H. Chang, P. Lin, *Nanotechnology* 20, 215101 (2009).
- [18] B.A. Fowler, *Toxicol. Appl. Pharmacol.* 238, 294 (2009).

- [19] W.J. Parak, D. Gerion, D. Zanchet, A.S. Woerz, T. Pellegrino, Ch. Micheel, Sh. C. Williams, M. Seitz, R.E. Bruehl, Z. Bryant, C. Bustamante, C.R. Bertozzi, A. P. Alivisatos, *Chem. Mater.* 14, 2113 (2002).
- [20] A. Wolcott, D. Gerion, M. Visconte, J. Sun, Ad. Schwartzberg, Sh. Chen, J. Z. Zhang, *J. Phys. Chem. B* 110, 5779 (2006).
- [21] D. Gerion, F. Pinaud, Sh.C. Williams, W.J. Parak, D. Zanchet, Sh. Weiss, A. P. Alivisatos, *J. Phys. Chem. B* 105, 8861 (2001).
- [22] T.V. Torchynska, *Nanotechnology* 20, 095401 (2009).
- [23] X. Ji, J. Zheng, J. Xu, V.K. Rastogi, T.Ch. Cheng, J.J. DeFrank, R.M. Leblanc, *J. Phys. Chem. B* 109 (2005) 3793.
- [24] L.G. Vega Macotela, J. Douda, T.V. Torchynska, R. Peña Sierra, L. Shcherbyna, *Phys. Status Solidi (c)* 7, 724 (2010).
- [25] W. Guo, J. Jack Li, J.A. Wang, X. Peng, *Chem. Mater.* 15, 3125 (2003).
- [26] T.V. Torchynska, J. Douda, P.A. Calva, S.S. Ostapenko, R. Peña Sierra, *J. Vac. Sci. Technol.* 27(2), 836 (2009).
- [27] T.Y. Ohulchanskyy, A.M. Pliss, P.N. Prasad, *Biophotonics: harnessing light for biology and medicine*, B. Di Bartolo and J. Collins (Eds.), *Biophotonics: Spectroscopy, Imaging, Sensing, and Manipulation*, Springer Science+Business Media B.V., 2011, p. 3.
- [28] T.V. Torchynska, J. Douda, S.S. Ostapenko, S. Jimenez-Sandoval, C. Phelan, A. Zajac, T. Zhukov, T. Sellers, *J. Non-Crystal. Solids*, 354, 2885 (2008).
- [29] <http://www.lifetechnologies.com/ua/en/home/brands/invitrogen.html>
- [30] [30]<http://www.lifetechnologies.com/ua/en/home/life-science/cell-analysis/qdots-microspheres-nanospheres.html?ICID=ta-lm-quantumdots-QuantumDot&Microspheres>
- [31] A.L. Quintos Vazquez, T.V. Torchynska, J.L. Casas Espinola, J.A. Jaramillo Gómez, J. Douda, *J. Luminesc.* 143, 38 (2013).
- [32] A.Y. Nazzal, X. Wang, L. Qu, W. Yu, Yu. Wang, X. Peng, M. Xiao, *J. Phys. Chem. B* 108, 5507 (2004).
- [33] R.W. Meulenberg, T. Jennings, G.F. Strouse, *Phys. Rev. B* 70, 235311 (2004).
- [34] M. Dybiec, G. Chomokur, S. Ostapenko, A. Wolcott, J.Z. Zhang, A. Zajac, C. Phelan, T. Sellers, G. Gerion, *Appl. Phys. Lett.* 90, 263112 (2007).
- [35] X. Gao, W.C.W. Chan, Sh. Nie, *J. Biomed. Opt.* 7(4), 532 (2002).
- [36] P.A. Temple, C.E. Hathaway, *Phys. Rev. B* 7, 3685 (1973).
- [37] F.A. Johnson, R. Loudon, *Proc. R. Soc. A* 281, 274 (1964).

- [38] N.E. Korsunskaya, I.V. Markevich, T.V. Torchinskaya, M.K. Sheinkman, *Phys. Status Solidi (a)* 60, 565 (1980).
- [39] T.V. Torchynska, A. Diaz Cano, M. Dybic, S. Ostapenko, M. Morales Rodriguez, S. Jimenes Sandoval, Y. Vorobiev, C. Phelan, A. Zajac, T. Zhukov, T. Sellers, *Phys. Status Solidi (c)* 4, 241 (2007).
- [40] T.V. Torchynska, J. Douda, R. Peña Sierra, *Phys. Status Solidi (c)* 6, S143 (2009).
- [41] A. Diaz Cano, S. Jiménez Sandoval, Y. Vorobiev, F. Rodriguez Melgarejo, T. V. Torchynska, *Nanotechnology* 21, 134016 (2010).
- [42] V. Torchynska, J.L. Casas Espinola, A. Díaz Cano, J. Douda, K. Gazarian, *Physica E*, 51, 60 (2013).
- [43] S.A. Empedocles, M.G. Bawendi, *Science* 278, 2114 (1997).
- [44] D.J. Norris, A. Sacra, C.B. Murray, M.G. Bawendi, *Phys. Rev. Lett.* 72, 2612 (1994).
- [45] D.B. Tran Thoai, Y.Z. Hu, S.W. Koch, *Phys. Rev. B* 41, 6079 (1990).
- [46] T.V. Torchynska, Y.V. Vorobiev, V.P. Makhniy, P.P. Horley, *Physica B*, 453 68 (2014).
- [47] P.P. Horley, P. Ribeiro, V.R. Vieira, J. González-Hernández, Yu.V. Vorobiev, L.G. Trápaga-Martínez, *Physica E* 44, 1602 (2012).
- [48] D.J. Norris, M.G. Bawendi, *Phys. Rev. B* 53, 16338 (1996).
- [49] C. Kittel, *Introduction to Solid State Physics*, 6th ed., John Wiley, New York, 1986.
- [50] *Physics of II-VI compounds*, A.N. Georgobian and M.K. Sheinkman (Eds.), Publisher "Nauka," Moscow, Russia, 1986, 300 p.
- [51] *Physics and chemistry of II-VI compounds*, M. Aven, J.S. Prener (Eds.), North-Holland, Amsterdam, 1967, p. 625.
- [52] T.V. Torchynska, *J. Luminesc.* 137, 157 (2013).
- [53] X. Xia, Z. Liu, G. Du, Y. Li, M. Ma, *J. Phys. Chem. C* 114, 13414 (2010).
- [54] T.V. Torchynska, J.L. Casas Espinola, J.A. Jaramillo Gómez, J. Douda, K. Gazarian *Physica E*, 51, 55 (2013).
- [55] A.G. Milnes, D.L. Feucht, *Heterojunctions and Metal-Semiconductor junctions*, Academic Press, New York, 1972.
- [56] Y. Kayanuma, *Phys. Rev. B* 38, 9797 (1988).
- [57] N.E. Korsunskaya, I.V. Markevich, T.V. Torchinskaya, M.K. Sheinkman, *J. Phys. Chem. Solids* 43, 475 (1982).
- [58] T.V. Torchynska, *Physica E* 68, 87 (2015).



Edited by Vasilios N. Stavrou

The book *Quantum Dots - Theory and Applications* collects some new research results in the area of fundamental excitations, decoherence, charge states, epitaxial techniques and photoluminescence experiments related to devices made with quantum dots. This book is divided in two sections. First section includes the fundamental theories on excitons, trions, phase decoherence, and charge states, and the second section includes several applications of quantum dots.

Photo by NiPlot / iStock

IntechOpen

